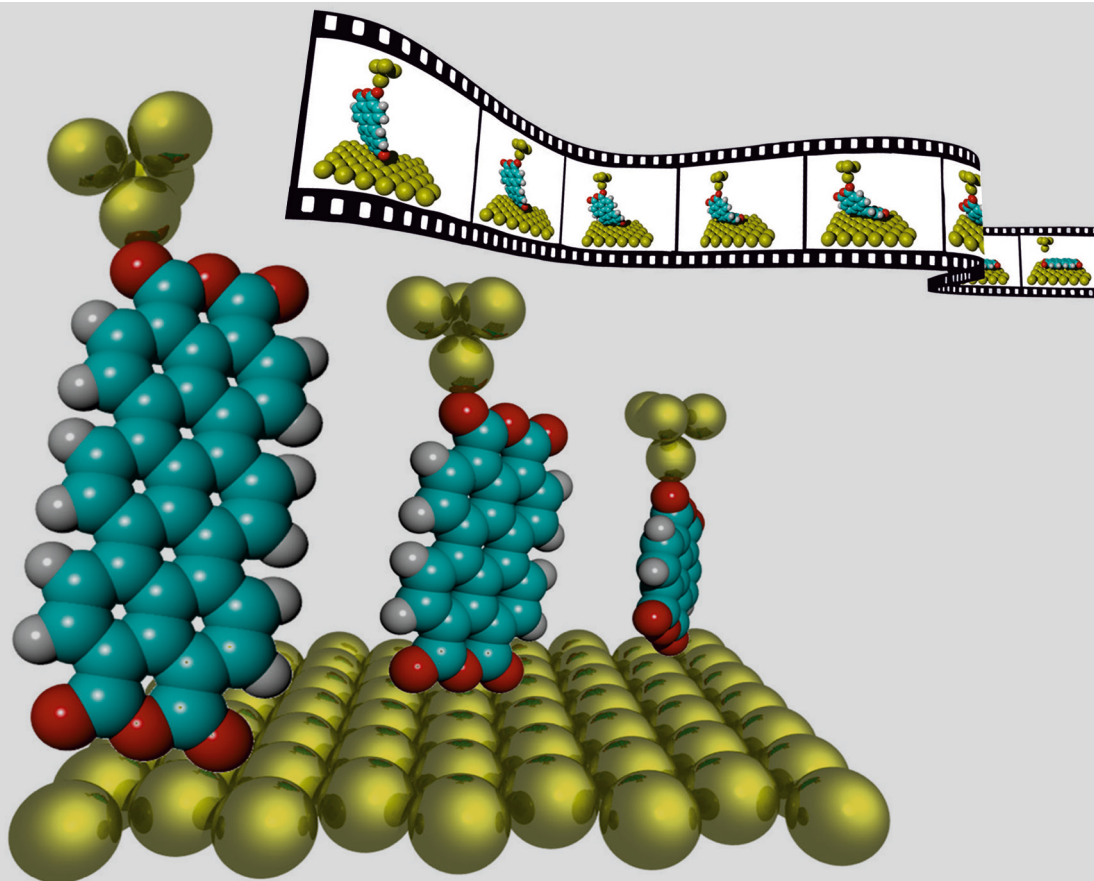


# STM-based quantum transport through molecular wires

Norman Fournier



Schlüsseltechnologien /  
Key Technologies  
Band/ Volume 108  
ISBN 978-3-95806-059-3



**STM-based quantum transport  
through  
molecular wires**

Von der Fakultät für Mathematik, Informatik und Naturwissenschaften der  
RWTH Aachen University zur Erlangung des akademischen Grades eines  
Doktors der Naturwissenschaften genehmigte Dissertation

vorgelegt von

Diplom-Physiker

**Norman Fournier**

aus Kehl am Rhein

Berichter: Prof. Dr. Stefan Tautz  
Prof.dr. J.M. van Ruitenbeek

Tag der mündlichen Prüfung: 04. September 2014

Diese Dissertation ist auf den Internetseiten der Universitätsbibliothek  
online verfügbar



Forschungszentrum Jülich GmbH  
Peter Grünberg Institut (PGI)  
Functional Nanostructures at Surfaces (PGI-3)

# STM-based quantum transport through molecular wires

Norman Fournier

Schriften des Forschungszentrums Jülich  
Reihe Schlüsseltechnologien / Key Technologies

Band / Volume 108

---

ISSN 1866-1807

ISBN 978-3-95806-059-3

Bibliographic information published by the Deutsche Nationalbibliothek.  
The Deutsche Nationalbibliothek lists this publication in the Deutsche  
Nationalbibliografie; detailed bibliographic data are available in the  
Internet at <http://dnb.d-nb.de>.

Publisher and Distributor:	Forschungszentrum Jülich GmbH Zentralbibliothek 52425 Jülich Tel: +49 2461 61-5368 Fax: +49 2461 61-6103 Email: <a href="mailto:zb-publikation@fz-juelich.de">zb-publikation@fz-juelich.de</a> <a href="http://www.fz-juelich.de/zb">www.fz-juelich.de/zb</a>
Cover Design:	Grafische Medien, Forschungszentrum Jülich GmbH
Printer:	Grafische Medien, Forschungszentrum Jülich GmbH
Copyright:	Forschungszentrum Jülich 2015

Schriften des Forschungszentrums Jülich  
Reihe Schlüsseltechnologien / Key Technologies, Band / Volume 108

D 82 (Diss. RWTH Aachen University, 2014)

ISSN 1866-1807

ISBN 978-3-95806-059-3

The complete volume is freely available on the Internet on the Jülicher Open Access Server (JuSER)  
at [www.fz-juelich.de/zb/openaccess](http://www.fz-juelich.de/zb/openaccess).

Neither this book nor any part of it may be reproduced or transmitted in any form or by any  
means, electronic or mechanical, including photocopying, microfilming, and recording, or by any  
information storage and retrieval system, without permission in writing from the publisher.

# Acknowledgements

This work would not have been realized without the help of many people, therefore I want to thank them for their support.

I wish to express my sincere thanks to Prof. Dr. Stefan Tautz for giving me the opportunity to work on the wonderful topic of molecular wires in his institute and for the intense discussions and the great support during the writing of this thesis. Very special thanks go to Dr. Ruslan Temirov for being an excellent supervisor. Without his knowledge, support and encouragement this work would have been much more difficult to achieve.

Many thanks go to Dr. Christian Wagner for the fruitful discussions about physics in general and especially his force-field simulations, which contributed a lot to my understanding of this work. Further I would like to thank Georgy Kichin for always helping me in the laboratory when support was needed. Also many thanks go to Matthew Green for proofreading of the second chapter.

I thank all PGI-3 members for creating a pleasant atmosphere which made working here in Jülich a great joy.

Finally I thank my parents, sister and brother for their love and support. Last but not least my gratitude goes to my girlfriend Eva for her patience, enthusiasm and motivation during the last three years.





# Abstract

The further miniaturization of electronic devices is a strong driving force in science. In the last few decades, devices based on organic materials have been studied. One goal is to create applications performed nowadays by silicon-based CMOS technology with organic materials. In these studies the interest is placed upon diverse properties of the organic molecules, such as their electronic, geometric, thermal, optical, and electroluminescence characteristics. One of the main problems of these studies is the lack of geometrical control of the systems during the measurements. As the physical properties critically depend on the exact geometry, contradictory results are found in literature.

To overcome this lack of control, this work introduces a new method which enables transport studies on single molecules with highly controlled junction geometries. The concept of this method, which is based on scanning probe techniques, will be presented as well as its realization. The method will be applied to molecule-metal junctions with molecules of different lengths which are contacted by different metal electrodes. It will be shown that highly reproducible experiments can be performed. Furthermore, the physical interpretation of the measurements will be discussed. It will be demonstrated that the profound knowledge of the geometry in these junctions helps to achieve a better understanding of the transport properties.



# Contents

<b>1</b>	<b>Introduction</b>	<b>1</b>
<b>2</b>	<b>Experimental methods</b>	<b>5</b>
2.1	Introduction . . . . .	5
2.2	Scanning tunneling microscopy . . . . .	5
2.2.1	The tunneling effect . . . . .	5
2.2.2	Bardeen's theory . . . . .	7
2.2.3	Tersoff-Hamann theory . . . . .	8
2.2.4	The scanning tunneling microscope . . . . .	9
2.2.5	Preparation of the tip . . . . .	9
2.2.6	Imaging and manipulation of single molecules with STM . . . . .	11
2.3	Scanning tunneling spectroscopy . . . . .	15
2.3.1	Working principle of the STS . . . . .	15
2.3.2	Spectroscopy at bare metal surfaces . . . . .	16
2.3.3	Electron-vibration coupling in STS . . . . .	17
2.3.4	The lock-in amplifier . . . . .	20
2.3.5	Calibration of the lock-in amplifier . . . . .	22
2.4	Noncontact atomic force microscopy . . . . .	23
2.4.1	Working principle of the AFM . . . . .	24
2.4.2	Controlling the junction with the AFM . . . . .	26
2.5	Sample preparation . . . . .	27
2.5.1	Preparation of the crystals . . . . .	27
2.5.2	Deposition of the molecules . . . . .	28
2.5.3	The molecular islands . . . . .	30
<b>3</b>	<b>Theory of transport</b>	<b>37</b>
3.1	Introduction . . . . .	37
3.2	Ballistic transport . . . . .	37
3.2.1	Landauer formula . . . . .	40
3.2.2	Transmission probability . . . . .	41
3.3	Molecule in a vacuum junction . . . . .	43
3.3.1	Coherent resonant tunneling in a double-barrier . . . . .	44
3.3.2	Incoherent tunneling . . . . .	46
3.3.2.1	Resonant current . . . . .	47

## Contents

3.3.2.2	Off-resonant current . . . . .	48
3.4	Molecular vibrations . . . . .	53
3.5	The Kondo effect . . . . .	54
3.6	Conclusions . . . . .	56
<b>4</b>	<b>Electronic structure of <math>\pi</math>-conjugated molecules</b>	<b>57</b>
4.1	Introduction . . . . .	57
4.2	Electronic structure of the seven systems . . . . .	59
4.2.1	Electronic structure of the Ag(111) systems . . . . .	59
4.2.2	Electronic structure of the Au(111) systems . . . . .	62
4.3	Investigation of NTCDA on Ag(111) . . . . .	67
4.4	Geometric and electronic structure of NTCDA on Ag(111) . . . . .	69
4.4.1	The commensurate phase . . . . .	69
4.4.2	The incommensurate phase . . . . .	73
4.4.3	The compressed phase . . . . .	75
4.5	Mapping the electronic structure within a molecule . . . . .	76
4.5.1	Electronic structure within a type A molecule . . . . .	77
4.5.2	Electronic structure within a type B molecule . . . . .	86
4.6	Temperature dependence of the Kondo resonance . . . . .	88
4.6.1	Temperature dependence of the peak height . . . . .	89
4.6.2	Temperature dependence of the peak width . . . . .	89
4.7	Differential conductance map of NTCDA on Ag(111) . . . . .	93
4.8	Conclusions . . . . .	100
<b>5</b>	<b>Highly reproducible lifting of <math>\pi</math>-conjugated molecules</b>	<b>103</b>
5.1	Force-controlled lifting of molecular wires . . . . .	105
5.2	Measurement of the Binding Energies of the Organic-Metal Perylene-Teracarboxylic-Dianhydride/Au(111) Bonds by Molecular Manipulation Using an Atomic Force Microscope . . . . .	111
<b>6</b>	<b>Systematic study of transport through a homologous series of <math>\pi</math>-conjugated molecules</b>	<b>117</b>
6.1	Introduction . . . . .	117
6.2	Transport measurements on single molecules . . . . .	118
6.2.1	Measurement routine . . . . .	118
6.2.2	Highly reproducible measurement . . . . .	119
6.3	Processing the data . . . . .	123
6.3.1	Sorting the data by classes . . . . .	123
6.3.2	Aligning the individual curves within class B . . . . .	130
6.3.3	Finding a curve which represents an individual system best . . . . .	135
6.3.3.1	Class A: Determine a generic curve . . . . .	135



## Contents

6.3.3.2	Class B: Determine the measured curve with the largest correlation with all other curves . . . . .	137
6.3.4	Exponential decay in the tunneling barrier . . . . .	148
6.4	Results: Molecular wires on Ag(111) . . . . .	155
6.4.1	Manipulations of class B on Ag(111) . . . . .	155
6.4.1.1	Two transport regimes . . . . .	162
6.4.1.2	The conductance peak . . . . .	170
6.4.1.3	Molecules in wire configuration on Ag(111) of class B . . .	174
6.4.2	Manipulations of class A on Ag(111) . . . . .	176
6.4.2.1	The hysteresis in class A manipulations . . . . .	177
6.4.2.2	Transport in class A manipulations . . . . .	182
6.4.2.3	The conductance peak . . . . .	184
6.4.2.4	Molecules in wire configuration on Ag(111) of class A . . .	189
6.4.2.5	Differences between class A and B on Ag(111) . . . . .	191
6.5	Results: Molecular wires on Au(111) . . . . .	191
6.5.1	Manipulations of class B on Au(111) . . . . .	194
6.5.1.1	Influence of the electrodes material on the conductance of the junction . . . . .	198
6.5.2	Manipulations of class A on Au(111) . . . . .	203
6.5.2.1	Transport in class A manipulations on Au(111) . . . . .	205
6.5.2.2	Influence of the electrodes material on the frequency shift . . .	207
6.6	Conclusions . . . . .	210
<b>7</b>	<b>Summary</b> . . . . .	<b>213</b>
<b>A</b>	<b>Supplemental materials</b> . . . . .	<b>217</b>
	<b>Bibliography</b> . . . . .	<b>283</b>



# 1 Introduction

The state of the art in the semiconductor industry is a 22 nm CMOS transistor [1]. For 2014 a 14 nm transistor was announced by Intel at their annual investors meeting in Santa Clara in may 2011 [2]. These transistors are multiple gate field-effect transistors (MuGFET), which are build in a 3-D architecture by photolithography [3]. It is believed that the miniaturization of the CMOS transistors is coming to an end with transistors of about 10 nm. The main reason for this threshold are leak currents due to quantum tunneling and thermal excitation, which lead to energy dissipation in the transistors [4,5]. Also the photolithographic fabrication of these devices reaches its limits as the 157 nm lithography failed in 2003 [6].

In the last decades alternatives to CMOS technology were proposed, such as single electron transistors (SET) [7], carbon nanotubes (CNT) [8] or single molecule transistors [9]. Especially in the field of organic materials new devices have proven their applicability, such as the organic photovoltaic cell (OPVC) [10], the organic field-effect transistor (OFET) [11] and the organic light emitting diode (OLED) [12]. Their performance was massively improved since then [13–15]. All these devices were built of thin films of organic materials. The advantages of organic semiconductors are their lighter weight, the mechanical flexibility of organic devices and the simple and low cost production via ink-jet printing, spin coating, or stamping [16]. Moreover, the complex structure of molecules and the variety of interactions between them offers a whole bunch of intrinsic functionalities which could be used in a variety of electronic devices [17].

The ultimate miniaturization can be attained with devices build of single molecules. In their famous paper, Aviram and Ratner [18] describe the possibility to use single molecules in electronic circuits. Since then a lot of effort was dedicated to investigate the electron transport through single molecules. One can separate the experiments carried out into the following groups: scanning probe techniques (SPT), fixed electrodes and mechanically formed molecular junctions [19]. In the SPT a scanning tunneling microscope (STM) or atomic force microscope (AFM) is used to image, manipulate,

## 1 Introduction

contact and probe single molecules [20–23]. Fixed electrodes are made on insulating substrates by electromigration, electrochemical etching or deposition [19]. Into the gap between the electrodes molecules are deposited and conductance measurements can be performed [9, 24, 25]. Mechanically formed break junctions are realized with either mechanically controlled break junctions (MCBJ) or by break junctions based on scanning probe microscopy (SPM) [26–30]. It was found that the control of the exact molecule-electrode contact geometry on an atomistic level during a measurement is very difficult [31]. As this contact is crucial for the conductance behavior, large variations in the conductance measurements are observed [32]. As a consequence the transport measurements of different studies vary substantially, even when the same electrode-molecule system is observed [31, 33, 34]. In this thesis an experimental method will be presented which overcomes at least partly this difficulty to control the junction. This was done in the following way:

The metal-molecule-metal junction structure is controlled by attaching the tip of a scanning tunneling microscope (STM) to a specific part of the molecule. The structure of the junction formed in this manner has still a structural improbability. This is mainly caused by the undefined tip structure. To limit the improbability of the junction structure the noncontact atomic force microscope (NC-AFM) based on a qPlus sensor was used to monitor the mechanical properties during the transport measurements. Using force-field simulations these mechanical properties are connected to structural information. With this structural information the transport measurements can be selected and sort into categories (classes). In this way the structural control is enhanced. Further by scanning tunneling spectroscopy (STS) the electronic structure of the molecules was probed. This electronic structure was measured with the tip above the adsorbed molecule or with the tip in contact to the molecule to measure the so-called transport spectroscopy. In chapter 2 the experimental techniques just mentioned are described as well as their specific application in this thesis.

As the control over the junction is achieved, reproducible transport measurements were carried out. To understand the transport behavior, the concepts of ballistic transport and double barrier tunneling have to be introduced. It is found that the molecular orbitals rearrange after contact formation with the metal electrode [32, 35, 36]. This rearrangement characterizes the transport properties to a large extent. In chapter 3 the concepts of ballistic transport and double barrier tunneling are presented, it is shown that the charge transport through the molecule can be described by coherent double barrier tunneling. Furthermore, the concepts of molecular vibrations and the Kondo effect are

introduced.

As mentioned above the transport through the tip-molecule-substrate junction is defined to large extent by the rearrangement of the molecular orbitals upon contact to the metal [32, 35, 36]. When the molecule gets into contact, its electronic structure changes. The orbitals are shifted and broadened [37, 38]. The overlap of the molecular orbitals with the substrate, i.e the coupling, then defines the transport behavior. In chapter 4 a systematic study of the electronic spectra of four different molecules on two different substrates is presented. Thereby an interesting electronic structure was observed for the system NTCDA on Ag(111). It was found that the electronic structure formed by NTCDA is composed of two distinguishable molecules within the submonolayer. This structure was investigated by STS. It is suggested that the structure is the result of the Kondo effect which was formally observed for the system PTCDA on Ag(111) [39–41]. By comparing the experimental results to DFT calculations side peaks in the scanning tunneling spectra were identified as originating from electron-vibrations coupling.

To investigate the transport through the molecules the experimental approach described earlier was used. A single molecule was isolated from the molecular island, contacted with the STM tip with atomistic precision and finally lifted up and lowered down with respect of the substrate. This routine is describe in chapter 5. In the first experiments it was shown that one can simultaneously measure the conductance and the force of the junction during this up and down movement of the molecule [42]. Later this technique was improved and highly reproducible lifting and lowering cycles were realized [43]. The highly reproducible transport measurement are remarkable considering that the tip was oscillating to measure the force in the noncontact AFM mode simultaneously to the STM measurement. The frequency shift was used to control the junction geometry and to determine the adsorption energy for the system NTCDA/Au(111) and PTCDA/Au(111). This was done by comparing the experimental data to simulations. By this the total adsorption energy as well as the different interactions between the molecule and the substrate are quantized.

Finally in chapter 6 the results of the transport measurements are presented. The four  $\pi$ -conjugated molecules NTCDA, PTCDA, TTCDA and QTCDA were probed on the two metal substrates Ag(111) and Au(111). By performing thousands of molecule manipulations large statistics for all the systems were collected and analyzed. It was found that all experimental data can be split basically into two different classes of behavior. The first one called class A is characterized by a strong Kondo resonance at the Fermi



## *1 Introduction*

energy when the molecule is contacted by Ag(111) electrodes and a hysteresis in the force and conductance data. Class B is characterized by a highly stable junction configuration which provided maximum reproducibility. It is assumed that the different behavior of the two classes is the result of a bistable versus a stable junction configuration, as a consequence of different tip apex atoms. Apart from this separation into two classes it was found that the conductance behavior is fundamentally different for the two electrode materials Ag(111) and Au(111). Further a clear dependency of the conductance behavior on the length of the molecule is observed. This is a consequence of the different degree of bending of the molecules during the manipulation process.

## 2 Experimental methods

### 2.1 Introduction

In this thesis transport measurements on single molecules are presented. The measurements are distinguished by high control and reproducibility. This was achieved by the use of scanning probe microscopy (SPM).

In this chapter the theoretical concepts of the experimental techniques and the details of the sample preparation are discussed. In the first part scanning tunneling microscopy (STM), scanning tunneling spectroscopy (STS) and atomic force microscopy (AFM) are presented. Further their application to our transport measurements is addressed. In the second part the preparation of the crystal and the deposition of the molecules is discussed. Finally STM images of the molecular islands are presented and the unit cells of the investigated systems are determined.

### 2.2 Scanning tunneling microscopy

The basis of scanning tunneling microscopy (STM) is the tunneling effect. The first experimental observation of the tunneling effect in the 1960s was on metal/oxide/metal sandwiches [44–46]. This phenomenon was described by Bardeen’s perturbation theory [47]. In 1981 Binnig and Rohrer invented the STM [48, 49]; its theoretical description was proposed by Tersoff and Hamann in 1983 [50, 51].

#### 2.2.1 The tunneling effect

If a particle hits a potential wall, and its energy  $E$  is inferior to the energy of the potential wall  $\Phi$ , it cannot pass through it in a classical mechanics picture. In a quantum mechanical picture the particle has a finite probability to pass through the wall (see Fig. 2.1). This phenomenon is called the tunneling effect, a consequence of the wave-like

## 2 Experimental methods

nature of a particle. The particle is described by a wave function  $\Psi$ , which must be continuous. Inside the barrier the wave function decays exponentially. On the other side of the barrier the wave function must still be continuous, hence there is a finite probability for the particle to tunnel through the barrier.

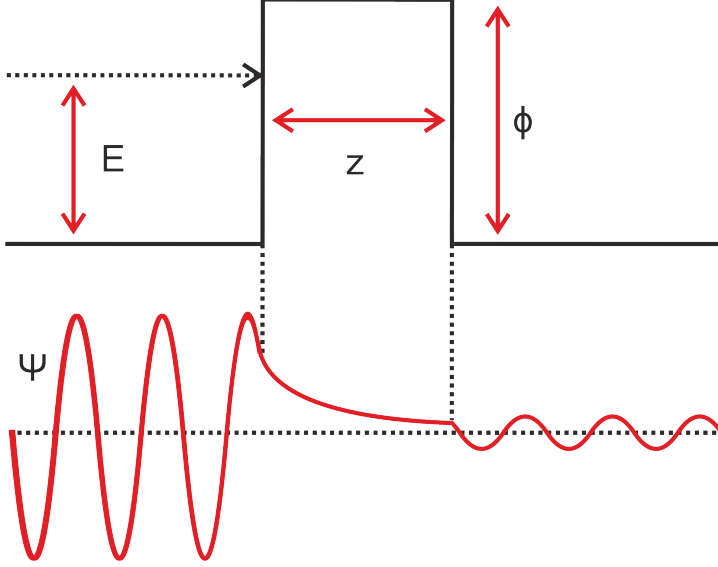


Figure 2.1: Tunneling barrier and wave function of a particle hitting a barrier. In the upper part the tunneling barrier with height  $\Phi$  and width  $z$  and the incoming particle with energy  $E$  is sketched. In the lower part the particle's wave function with the exponential decay inside the barrier is sketched.

The probability to pass a barrier is given by the Schrödinger equation. For a particle of mass  $m$  with an energy  $E$  hitting a barrier of energy  $\Phi$  and width  $z$ , the transmission probability is given by:

$$T = \frac{1}{1 + \frac{\Phi^2 \sinh(\sqrt{\frac{2m(\Phi-E)}{\hbar^2}} z)}{4E(\Phi-E)}} \quad (2.1)$$

The transmission probability decays exponentially in the tunneling barrier, depending on the effective tunneling barrier height  $(\Phi - E)$  and the barrier width  $z$ . The first tunneling experiments were performed on planar metal/oxide/metal tunneling junctions [44–46]. Applying a bias voltage  $V$  the tunneling current was measured. It was found that the

## 2 Experimental methods

tunneling current  $I$  is proportional to  $e^{-2\kappa z}$ , with the decay constant  $\kappa = \sqrt{\frac{2m}{\hbar^2} \frac{\Phi_L + \Phi_R - eV}{2}}$ , where the effective barrier height  $\frac{\Phi_L + \Phi_R - eV}{2}$  is given by the work functions of the two metals  $\Phi_L$  and  $\Phi_R$  (see Fig. 2.2).

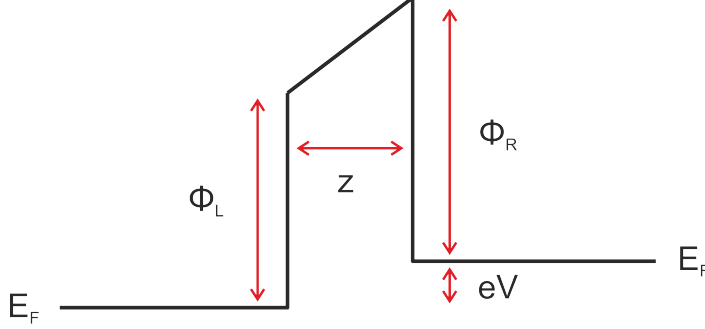


Figure 2.2: Tunneling barrier of width  $z$  between two planar metal electrodes with the work functions  $\Phi_L$  and  $\Phi_R$  and Fermi level  $E_F$ . The bias voltage  $V$  is applied between the two metal electrodes.

### 2.2.2 Bardeen's theory

John Bardeen presented in 1961 a description of the tunneling effect between two planar electrodes [47]. It is based on a time-dependent perturbation theory. The tunneling current can be expressed as follows:

$$I = \frac{2\pi e}{\hbar} \sum_{\mu, \nu} [f(E_\mu) - f(E_\nu - eV)] |M_{\mu, \nu}|^2 \delta(E_\mu - E_\nu) \quad (2.2)$$

This is a sum over all states  $\Psi_\mu$  and  $\Psi_\nu$  of the electrodes, where  $f(E)$  is the Fermi function,  $e$  is the charge of an electron and  $V$  is the bias voltage applied to the electrodes.  $M_{\mu, \nu}$  is the tunneling matrix element between the two states  $\Psi_\mu$  and  $\Psi_\nu$ , which have eigenenergies  $E_\mu$  and  $E_\nu$ . This tunneling matrix is an integral over a surface within the tunneling barrier, which represents the overlap of the two states  $\Psi_\mu$  and  $\Psi_\nu$ . The matrix element is given by the following expression:

$$M_{\mu, \nu} = -\left(\frac{\hbar^2}{2m}\right) \int d\vec{S} * (\Psi_\mu^* \vec{\nabla} \Psi_\nu - \Psi_\nu \vec{\nabla} \Psi_\mu^*) \quad (2.3)$$

## 2 Experimental methods

As mentioned above, equation 2.2 is the sum over all states  $\Psi_\mu$  and  $\Psi_\nu$  of the electrodes. This sum can be substituted by an integral by defining the density of states (DOS)  $\rho(E)$ , which is the number of states per unit interval of energy. Equation 2.2 can than be written as:

$$I = \frac{2\pi e}{\hbar} \int_{-\infty}^{+\infty} [f(\epsilon) - f(\epsilon - eV)] |M^2| \rho_L(\epsilon) \rho_R(\epsilon - eV) d\epsilon \quad (2.4)$$

This equation can be simplified as the Fermi function can be represented by a step function at low temperatures:

$$I = \frac{2\pi e}{\hbar} \int_0^{eV} |M^2| \rho_L(E_F + \epsilon) \rho_R(E_F + \epsilon - eV) d\epsilon \quad (2.5)$$

The tunneling current is thus function of the density of states (DOS) of both electrodes multiplied with the tunneling matrix element, which describes the overlap of the electronic states.

### 2.2.3 Tersoff-Hamann theory

In 1983 after the advent of the scanning tunneling microscope (STM) the theory of Bardeen was applied to the system of a tip (a sharp wire) and a sample (planar electrode) [50, 51]. Taking the limits of low temperatures and small voltages, as are typically used in STM, the tunneling current is given by:

$$I = \frac{2\pi}{\hbar} e^2 V \sum_{\mu, \nu} |M_{\mu, \nu}|^2 \delta(E_\nu - E_F) \delta(E_\mu - E_F). \quad (2.6)$$

By further assuming that the STM tip apex is composed of an s-orbital the tunneling matrix element can be estimated and the tunneling current can be expressed in the following way:

$$I \propto \int_{E_F}^{E_F + eV} \rho(\vec{r}_0, \epsilon) d\epsilon \quad (2.7)$$

with the local density of states (LDOS)  $\rho(\vec{r}_0, \epsilon)$ , which is the density of states of the sample at the position  $\vec{r}_0$  of the tip. If the assumptions just mentioned are fulfilled the



## 2 Experimental methods

tunneling current is proportional to the local density of states (LDOS) near the Fermi energy. To get a STM image which only shows the modulus squared of the sample wave functions at the Fermi energy and none of the spatial derivatives, it is essential to have a tip with an s-orbital [52–55]. In this way the STM image shows the lateral distribution of the LDOS at the sample surface.

### 2.2.4 The scanning tunneling microscope

The scanning tunneling microscope (STM) was invented by Gerd Binnig and Heinrich Rohrer in 1981 at IBM Zürich [48, 49]. It allows the imaging of conducting surfaces with atomic resolution [56–58].

In Fig. 2.3 a schematic representation of a STM is shown. A sharp metal wire, henceforth referred to as the tip, is scanned above the sample surface at a distance of a few Å. This motion is controlled by three piezoelectric elements. A voltage is applied between tip and sample and the resulting tunneling current is measured. This tunneling current depends exponentially on the distance between tip and sample surface. Considering typical work function values the rule of thumb is that for one additional Å the current drops by one order of magnitude. Two scanning modes are usually used for imaging:

**constant current mode** The feedback loop is set such that the tunneling current between tip and sample is constant. In this way the tip follows the contour of a constant density of states (DOS). The signal retrieved from this mode is the vertical position of the tip, which allows a topographic image to be displayed.

**constant height mode** The feedback loop is set such that the distance between tip and sample is constant. The tunneling current measured in this mode as a function of the lateral tip position is used to make an image.

The STM used for the experiments presented here is the commercial Besocke beetle type LT-STM/AFM produced by SPS-CREATEC GmbH [59]. It is operated at low temperatures ( $T_{\text{sample}} \approx 5$  K) under ultra high vacuum (UHV).

### 2.2.5 Preparation of the tip

We used a tip made from Pt/Ir wire with a diameter of 15 µm (see Fig. 2.4). The inert platinum-iridium was chosen instead of tungsten, as it oxidizes much less and is thus

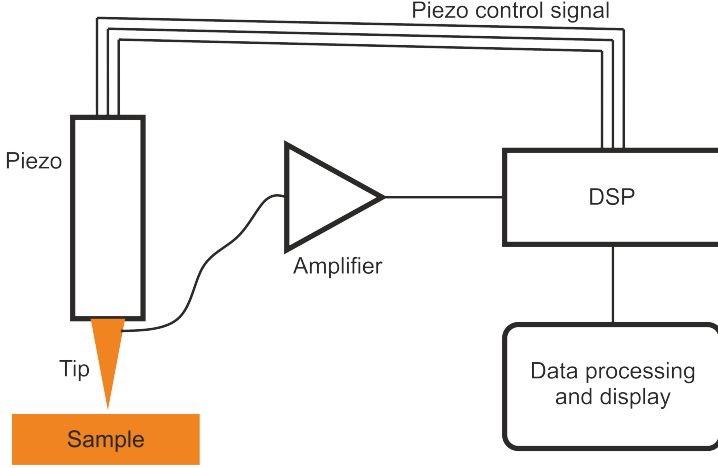


Figure 2.3: Schematic representation of a scanning tunneling microscope (STM). A sharp wire (tip) is scanned at a few Å distance above the sample surface. This motion is controlled by piezoelectric elements. A bias voltage is applied between tip and sample and the tunneling current is measured. Two scanning modes are usually used, constant current mode and constant height mode.

more stable over a long period of time [60, 61]. This was especially important as the tip could not be annealed inside the vacuum chamber once glued to the qPlus sensor. The tip was prepared by a focused ion beam (FIB) [62–64]. This was done with the help of D. Park and J. Mayer from RWTH Aachen. The working principle of a focused ion beam (FIB) is as follows:

Similar to a scanning electron microscope (SEM) a beam of particles is accelerated by applying a strong electric field [65]. In the case of FIB, gallium ions ( $\text{Ga}^+$ ) are used, in contrast to electrons used in SEM. Typically the gallium ion beam energy is in the range of 10 keV to 50 keV. The FIB can be used for imaging, sputtering and deposition. A tip which is in a vacuum chamber ( $\approx 10^{-7}$  mbar) can be sputtered by the beam. For this purpose high beam energies are used. When the ion beam hits the tip, the ions transfer their energy to the electrons and atoms of the target. By this tip material is removed.

Before imaging the surface or manipulating a molecule the tip apex structure had to be refined. This was done by dipping the tip carefully into the crystal. Typical parameters for this vertical manipulation of the tip are a voltage of 0.1 V and a displacement from the

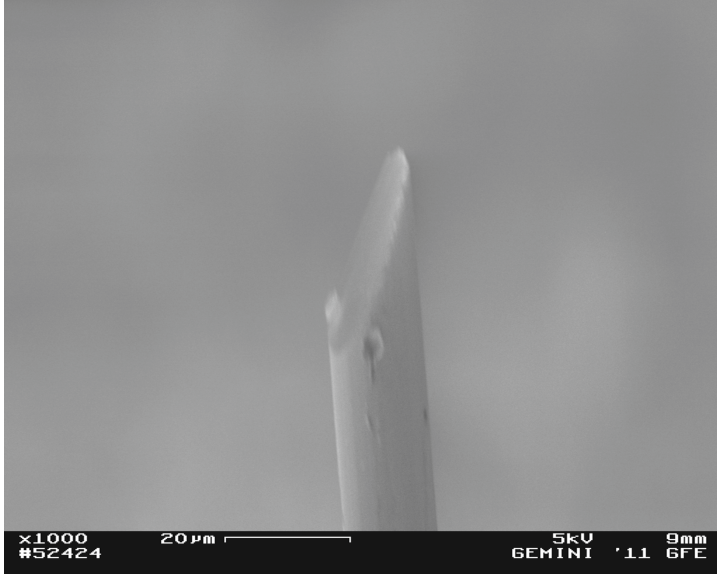


Figure 2.4: SEM image of a Pt/Ir wire with a diameter of  $15\text{ }\mu\text{m}$  cut by FIB. This is the Pt/Ir tip used for the transport measurements presented in this thesis.

stabilization point of  $10\text{ }\text{\AA}$ . By this procedure the apex of the tip was covered by the metal atoms of the sample crystal. This dipping procedure was repeated until the tip was sharp. Sharp manifesting as superior contrast in STM images.

### 2.2.6 Imaging and manipulation of single molecules with STM

In the experiments presented in this thesis the STM was used to image and manipulate molecules on metal substrates. The imaging and manipulation procedure as used in this work are described in this section.

The samples were prepared for the experiments by deposition of organic molecules onto metal substrates (see section 2.5). By annealing the sample after the deposition molecular islands would form. Ideally the molecular islands covered the metal substrate by 10% to 30%. In this way sufficient molecules and clean metal space for tip preparation were available. The tip preparation was crucial as only a clean and sharp metal tip would allow reproducible transport measurements. To measure the transport through single molecules, first the molecule had to be isolated from a molecular island and then secondly

## 2 Experimental methods

dragged with the STM tip a few nm away from the island border [42, 43]. Furthermore the single molecule had to be at a sufficient distance from any defects to perform transport measurements.

After a sample preparation the sample was brought into the STM chamber and the tip was approached towards the surface. Then the system was given time to find its thermal equilibrium which was around 5° K. This usually took about 12 hours. This was necessary as the feedback loop was open during the transport measurements and thus the drift had to be minimized as much as possible. After this the sample was scanned until an overview scanning image of  $3200 \text{ \AA} \times 3200 \text{ \AA}$  (see Fig. 2.5a) showed the desired molecular coverage of 10% to 30%.

Within this large overview scan a smaller scanning image of about  $200 \text{ \AA} \times 200 \text{ \AA}$  (see Fig. 2.5b) was scanned. This smaller scanning image typically showed a molecular island border and free metal substrate. From this molecular island border a single molecule could then be isolated. This detaching procedure of the molecule was done by a lateral manipulation with the tip. For this purpose the feedback loop was closed. Typical lateral manipulation parameters were:

- tunneling current  $I = 50 \text{ nA}$
- bias voltage  $V = 10 \text{ mV}$
- preamplifier gain  $G = 10^7 \text{ V/A}$

The lateral manipulation was done in the following way:

- molecule S jutting out of the border was chosen within the  $200 \text{ \AA} \times 200 \text{ \AA}$  scanning image
- two points A and B were chosen
- point A was the position of one of the carboxylic oxygen atoms of molecule S
- point B was the position where to drag molecule S, typically around  $100 \text{ \AA}$  to  $150 \text{ \AA}$  away from the molecular island border
- tip displacement in z-direction (vertical to the sample) was chosen
- tip moves laterally to point A, vertically towards the carboxylic oxygen
- by transferring a molecule-substrate bond to the tip the molecule is bound to the tip

## 2 Experimental methods

- tip moves laterally to point B and then vertically to the stabilization height breaking the tip-molecule bond

After this manipulation procedure the molecule usually was at point B (see Fig. 2.5c). However this detaching procedure was not always successful. The success rate depended on the type of molecule and metal substrate. It also happened that the molecule was not moved at all, broke during the lateral manipulation, jumped onto the tip or several molecules were moved to point B. Critical parameters for a successful manipulation were the atomistic shape of the tip, the extent to which the molecule jutted out of the island (the more the better) and the lateral manipulation parameters. Of particular importance were the exact contact point and the height at which the molecule was dragged.

These manipulation parameters varied for each type of molecule, as well as for the two metal substrates used, Ag(111) and Au(111). With silver electrodes it was generally easier to isolate a molecule. The reason is the stronger covalent bond between the silver and carboxylic oxygen atom, compared to the gold and carboxylic oxygen atom. The higher success rate for bigger molecules was probably due to the fact that it was less likely that they jumped onto the tip during the manipulation. The reason could be, that the aggregate position of the four highly reactive carboxylic oxygen atoms is larger for a long molecule. Also the shape of the tip influenced the manipulation parameters. A sharp tip, as was also preferable for imaging made a lateral manipulation more likely to be successful.

When a molecule was successfully detached from the island the system was given five minutes to minimize drifting of the tip because of piezo creep. Then the transport measurement could start by contacting the single molecule with the tip and performing vertical manipulation [39, 40, 42, 43]. The details of this vertical manipulation for the transport measurements are described in the chapters 4 to 6.

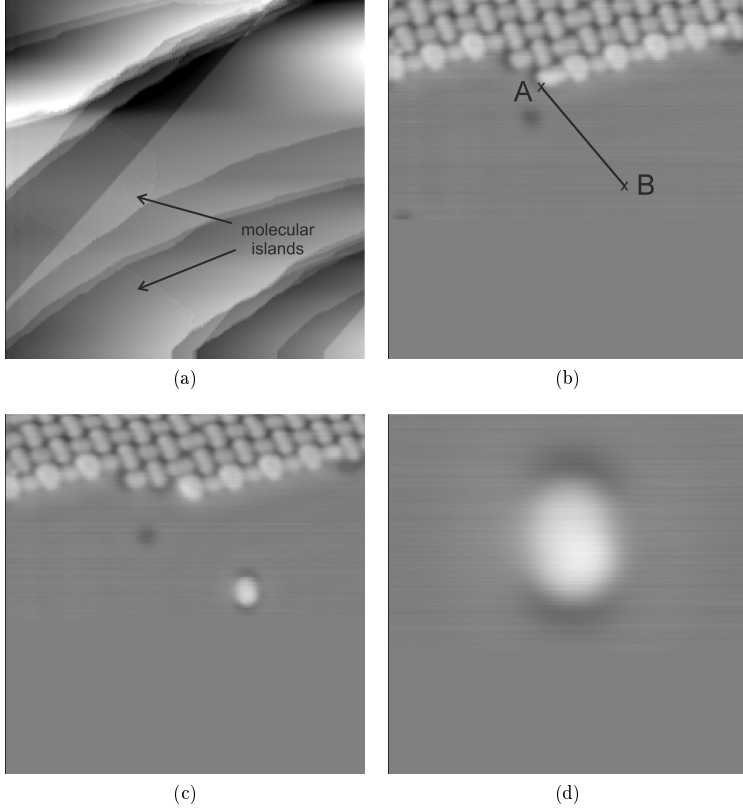


Figure 2.5: Creating a single TTCDA molecule on Ag(111). (a) Large overview scan with two TTCDA islands in the lower left and center left of the image.  $3200 \text{ \AA} \times 3200 \text{ \AA}$ ,  $0.1 \text{ nA}$ ,  $278 \text{ mV}$ . (b) TTCDA island border. The line indicates the path of the lateral manipulation. Point A and B are the starting and endpoint of the manipulation as described in the text.  $200 \text{ \AA} \times 200 \text{ \AA}$ ,  $0.1 \text{ nA}$ ,  $278 \text{ mV}$ . (c) Same TTCDA island border as in (b) and detached single TTCDA molecule.  $200 \text{ \AA} \times 200 \text{ \AA}$ ,  $0.1 \text{ nA}$ ,  $278 \text{ mV}$ . (d) The detached TTCDA molecule.  $50 \text{ \AA} \times 50 \text{ \AA}$ ,  $0.1 \text{ nA}$ ,  $278 \text{ mV}$ .

### 2.3 Scanning tunneling spectroscopy

As was shown in equation 2.7 the first derivative of the tunneling current, i.e. the differential conductance, is proportional to the local density of states (LDOS):

$$\frac{dI}{dV}(\epsilon) \propto \rho(\vec{r}_0, \epsilon) \quad (2.8)$$

at the position  $\vec{r}_0$  of the tip with the energy  $\epsilon = eV_{\text{bias}}$ , where  $V_{\text{bias}}$  is the voltage applied between tip and sample. This proportionality is used in scanning tunneling spectroscopy (STS) to probe the LDOS of a surface. In comparison to other spectroscopic methods such as photo emission spectroscopy (PES), with STS it is possible to probe the filled as well as the unfilled states of a sample. Also, in STS the sample can be probed locally, i.e. a single molecular entity can be probed [66–69]. In contrast to this in PES the signal is integrated over a large area of typically several  $\mu\text{m}$ , with some techniques as nano-ESCA reaching spatial resolution in the order of 100 nm [70, 71].

#### 2.3.1 Working principle of the STS

The STS allows to measure current-voltage ( $I - V$ ) characteristics. This is done by measuring the tunneling current  $I$  between tip and sample as a function of the bias voltage  $V$ . By STS information about the local density of states (LDOS) at the surface of a sample is gained [72].

A scanning tunneling spectra is obtained by placing the tip above the spot to be probed, e.g. a molecular orbital. Then the feedback loop is opened. This allows the tip to remain in the same position during the measurement. For the measurement the bias is swept through an interval of typically  $\pm 1 \text{ eV}$  to  $\pm 2 \text{ eV}$ . At higher bias voltage the risk of a tip crash increases and field emission might set in [73]. Ideally the tip is prepared such that it has no features in the DOS of the energy range probed, i.e. its density of states (DOS) is constant. This has to be checked before probing a molecule by doing a STS on clean metal. The (111) surfaces of noble metals are known to have a Shockley surface state [74]. Probing such a metal surface, the most prominent feature in the spectra should be the surface state (see Fig. 2.7).

In Fig 2.6 a schematic representation of a tunneling barrier with an applied bias voltage  $V_{\text{bias}}$  is shown. Electrons tunnel from the tip to the sample. The electrons can only tunnel into empty states of the sample within the energy range  $E_F$  to  $E_F + eV$ . The

higher the energy difference between the electron in the tip and the Fermi energy of the sample, the higher the probability for the electron to tunnel from the tip to the sample (indicated by the red arrows).

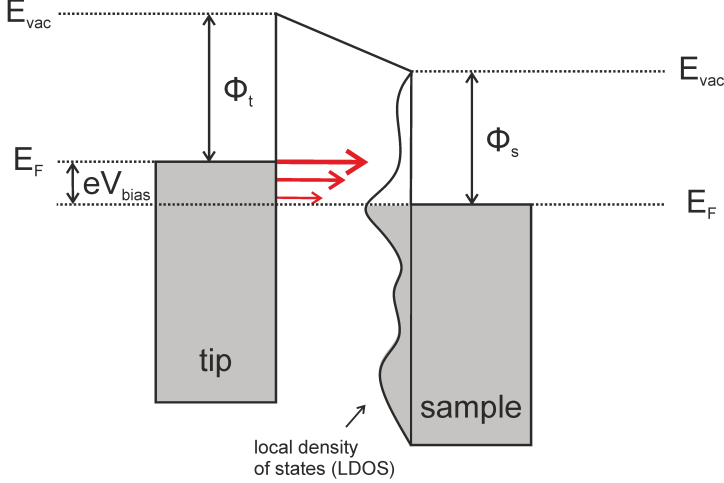


Figure 2.6: Schematic representation of a tunneling barrier with an applied bias voltage  $V_{bias}$ . The electrons tunnel from filled states in the tip to empty states in the sample in the energy range  $E_F$  to  $E_F + eV$ .  $\phi_s$  and  $\phi_t$  are the work functions of the sample and the tip, i.e. the energy difference between the Fermi energy  $E_F$  and the vacuum energy  $E_{vac}$ . The differential conductance  $dI/dV$  measured in STS is proportional to the local density of states (LDOS) on the sample at the position of the tip.

### 2.3.2 Spectroscopy at bare metal surfaces

As discussed before the shape of the tip apex atom orbital influences the tunneling current significantly [52–55]. To minimize this influence the apex tip atom orbital desired for STS should be an s-orbital. To check the shape of the tip apex atom orbital a spectrum is taken from the (111) surface of the noble metal. The tip is prepared until the STS of the metal has the Shockley surface state as its most prominent feature. In Fig 2.7 two spectra measured on the bare Ag(111) and Au(111) samples are shown. The spectra taken on the Ag(111) sample shows a surface state at  $-65$  mV (see Fig. 2.7a) as was found by Burgi *et al.* [75]. The measured surface state of the Au(111) sample is with  $-490$  mV (see Fig. 2.7b) in the energy range as reported earlier [76, 77].



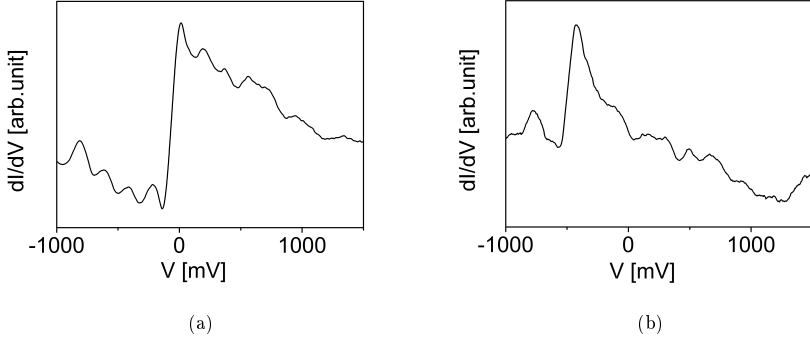


Figure 2.7: Scanning tunneling spectra of the bare Ag(111) and Au(111) samples. (a) The STS of Ag(111) shows the Shockley surface state at  $-65$  mV as was found earlier by Burgi *et al.* [75]. (b) The STS of Au(111) shows the Shockley surface state at  $-490$  mV which is within the energy range of experiments reported earlier [76, 77].

### 2.3.3 Electron-vibration coupling in STS

In chapter 4 electron-vibration coupling will be discussed. Therefore its influence on scanning tunneling spectroscopy is worked out here. When a molecule is probed by STS and electron-vibration coupling is observed, then the LDOS  $\rho(\vec{r}_0, \epsilon)$  at the position  $\vec{r}_0$  of the tip will change. This change is observed at the vibrational threshold  $\epsilon = \epsilon_F + \hbar\Omega$  which is defined by the frequency  $\Omega$  of the molecular vibration [78]. This can be expressed by the following equation:

$$\rho(\vec{r}_0, \epsilon) \rightarrow \rho(\vec{r}_0, \epsilon) + \delta\rho(\vec{r}_0, \epsilon) \quad (2.9)$$

with the change of the LDOS  $\delta\rho(\vec{r}_0, \epsilon)$ . This change of the LDOS has a continuously varying part and a discontinuity at the vibrational threshold  $\hbar\Omega$ . When it is assumed that there is only one vibrational mode  $\Omega$ , this discontinuous part can be called  $\Delta\rho(\vec{r}_0)$ . This discontinuous part of the LDOS results in a discontinuity  $\eta(\vec{r}_0)$  in the differential conductance:

$$\eta(\vec{r}_0) = \Delta\sigma(\vec{r}_0)/\sigma(\vec{r}_0, \epsilon) \quad (2.10)$$

## 2 Experimental methods

with the differential conductance  $\sigma = dI/dV$  at the position  $\vec{r}_0$  of the tip at the vibrational threshold  $\epsilon = \epsilon_F + \hbar\Omega$ . The discontinuous part of the change of the LDOS  $\Delta\rho$  can be separated into two contributions - an inelastic contribution  $\Delta\rho_{\text{inel}}$  (see Fig. 2.8a) which is characterized by the excitation of a real vibron with energy  $\hbar\Omega$  and an elastic contribution  $\Delta\rho_{\text{el}}$  (see Fig. 2.8b) which is characterized by the emission and readsorption of a virtual vibron:

$$\Delta\rho(\vec{r}_0) = \Delta\rho_{\text{inel}}(\vec{r}_0) + \Delta\rho_{\text{el}}(\vec{r}_0) \quad (2.11)$$

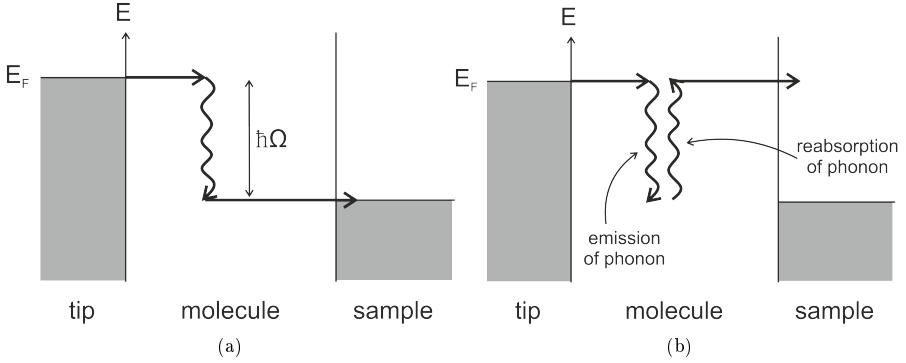


Figure 2.8: Tunneling processes by electron-vibration coupling. a) In the inelastic process the electron loses energy by emitting a vibron. b) In the elastic process the energy of the electron is conserved.

The discontinuous part of the change of the LDOS is responsible for the step in the differential conductance  $dI/dV$  at the vibrational threshold  $\epsilon = \hbar\Omega$ . This is depicted in Fig. 2.9. At the vibrational threshold a step in  $dI/dV$  is observed, which results from the additional tunneling channel opening as the vibron of energy  $\epsilon = \hbar\Omega$  is excited.

The LDOS of the electron eigenstate can be expressed as follows:

$$\rho(\vec{r}_0, \epsilon) = \sum_{\mu} |\langle \mu | \vec{r}_0 \rangle|^2 * \delta(\epsilon - \epsilon_{\mu}) \quad (2.12)$$

with the initial eigenstate in the tip  $|\vec{r}_0\rangle$  and the final eigenstate in the sample  $|\mu\rangle$ . If a transition to a electronic state  $|\lambda\rangle$  is allowed because of electron-vibration coupling, then

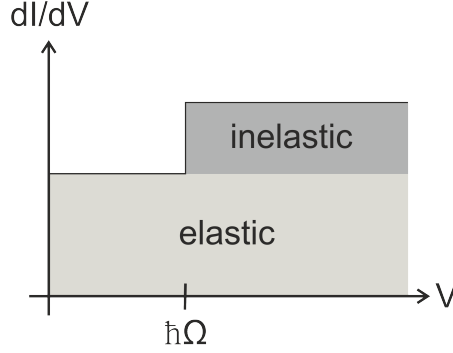


Figure 2.9: As the vibrational threshold is reached an additional tunneling channel is opening, resulting in a step in the differential conductance. This step in the differential conductance is determined by the discontinuous part of the change of the LDOS  $\Delta\rho_{\text{inel}}(\vec{r}_0)$ .

the LDOS can be expressed as:

$$\rho(\vec{r}_0, \epsilon) = \sum_{\mu} |\langle \mu | \sum_{\lambda} \frac{\Delta v_{\text{eff}} |\lambda\rangle \langle \lambda|}{\epsilon_{\mu} - (\epsilon_{\lambda} - \hbar\Omega) + iO^+} |\vec{r}_0\rangle|^2 * \delta(\epsilon - \epsilon_{\mu}) \quad (2.13)$$

where  $v_{\text{eff}}$  is the effective one-electron potential and  $\epsilon_{\lambda}$  the energy of the electronic state. This transition is depicted in Fig. 2.10a. With this, the inelastic contribution can be expressed as was shown by Lorente *et al.* [78], based on the work of Caroli *et al.* [79]:

$$\Delta\rho_{\text{inel}}(\vec{r}_0) = \delta Q^2 \sum_{\mu} \left| \sum_{\lambda} \frac{\langle \mu | v' | \lambda \rangle \langle \lambda | \vec{r}_0 \rangle}{\epsilon_{\mu} + \hbar\Omega - \epsilon_{\lambda} + iO^+} \right|^2 * \delta(\epsilon_{\text{F}} - \epsilon_{\mu}) \quad (2.14)$$

with the electron-vibration coupling,  $v'$ , which is the first derivative of the effective one-electron potential,  $v_{\text{eff}}$ , regarding the vibrational displacement  $Q$ , and  $\delta Q^2 = \hbar/(2M\Omega)$  the mean-square amplitude of  $Q$  and the mass  $M$ .

For the elastic contribution Lorente *et al.* [78] derived the following equation:

$$\Delta\rho_{\text{el}}(\vec{r}_0) = -2\delta Q^2 \sum_{\mu} \left| \pi \sum_{\lambda} \langle \mu | v' | \lambda \rangle \langle \lambda | \vec{r}_0 \rangle * \delta(\epsilon_{\mu} + \hbar\Omega - \epsilon_{\lambda}) \right|^2 * \delta(\epsilon_{\text{F}} - \epsilon_{\mu}) \quad (2.15)$$

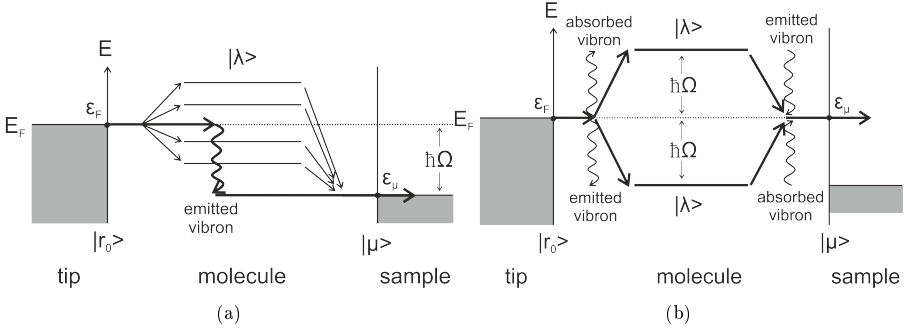


Figure 2.10: Electronic transition by electron-vibration coupling. a) The inelastic contribution is characterized by a virtual transition. The electron loses energy by emitting a vibron. b) The elastic contribution is characterized by a real transition to an electronic state. The electron loses no net energy between tip and sample.

This is depicted in Fig. 2.10b. In the elastic contribution the electron loses no energy between tip and sample. The transition through the electronic state  $|\lambda\rangle$  is real.

### 2.3.4 The lock-in amplifier

To measure the differential conductance a lock-in amplifier was used. Lock-in amplifiers are able to measure very small AC signals down to a few nano volts [80]. These measurements are possible even if the signal is covered by large noise. This is done by a technique called phase-sensitive detection. Its basic operating principle is to filter out parts of the signal at a known reference frequency and phase, the rest of the signal is then suppressed.

This is done by superimposing a voltage modulation on top of the bias voltage applied to the tunnel junction (see Fig. 2.11a). The resulting tunneling current through the junction, the modulation signal, is amplified and multiplied with a reference signal of the same frequency  $f$  as the modulation signal but shifted by the phase  $\phi$  (see Fig. 2.11b). This product of the signals is integrated by a low pass for the time  $TC$ . The resulting averaged signal is a DC signal proportional to the initial tunneling current if the frequency  $f$  of the modulation and the reference signal are of the same frequency. By a sensitivity  $S$  the gain to amplify this DC signal is defined. To get absolute differential

## 2 Experimental methods

conductance values this resulting signal has to be calibrated using the tunneling current, this is explained in the next section.

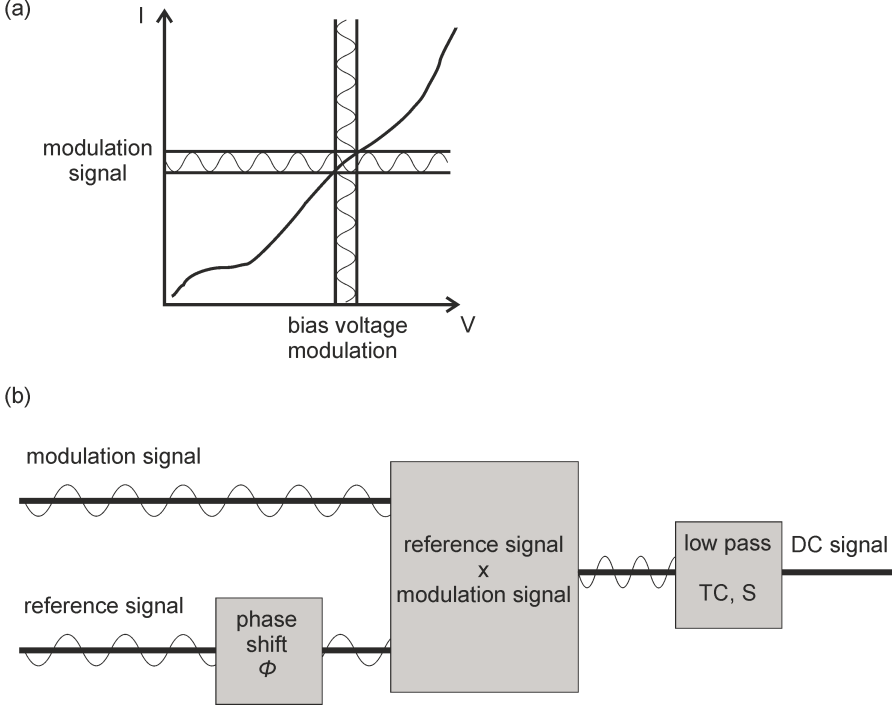


Figure 2.11: Working principle of the Lock-in amplifier. (a) A voltage modulation is superimposed to the bias voltage  $V$ . The resulting current  $I$  is called the modulation signal. (b) The modulation signal is multiplied with a reference signal of the same frequency  $f$  as the modulation, but shifted by the phase  $\phi$ . The multiplied signal is integrated by a low pass which results in a DC signal.

To get a good signal-to-noise ratio the parameters of the modulation and the reference signal had to be carefully chosen. The frequency  $f$  of the modulation and reference signal had to be chosen such that it did not match the noise in the tunneling current signal. In the course of this thesis the frequency was changed several times, as the noise condition of the whole setup changed. The increasing quality in the transport measurement was to a great extent a consequence of the ability to use smaller and smaller frequencies. At the beginning high frequencies of about  $f \approx 5$  kHz were used. As the noise conditions became

## 2 Experimental methods

better smaller frequencies of  $f < 1$  kHz were used. The use of smaller frequencies made the transport measurements less noisy, as the crosstalk with the qPlus sensor oscillating at  $f_0 = 30\,300$  Hz was reduced (see section 2.4).

The amplitude  $A$  of the modulation was constant during all the measurements. The phase of the reference signal  $\phi$  with respect of the modulated tunneling current signal had to be adjusted each time the preamplifier gain  $G$  was changed (typically  $G = 10^7$  V/A or  $10^8$  V/A), such that the signal-to-noise ratio was maximized. The time constant  $TC$  defines the time the signal gets integrated in the low pass filter. The higher the frequency was the shorter the time constant could be. It was chosen such that there was no hysteresis in the resulting signal. The lock-in amplifier  $S$  was chosen in a way that the resulting signal used the whole range of the DAC.

The commercial Stanford Research Systems SR830 DSP Lock-in Amplifier was used in this thesis to measure the differential conductance ( $dI/dV$ ). To measure the second derivative of the differential conductance  $d^2I/dV^2$  a second lock-in amplifier of the same type was connected to the first lock-in amplifier in series. The following parameters were the ones used most of the time for the experiments:

- modulation amplitude  $A = 5$  mV
- modulation frequency  $f = 933.3$  Hz
- phase  $\phi = -30$  with preamplifier gain  $G = 10^8$  V/A
- sensitivity of first lock-in  $S_1 = 500$  mV
- time constant of first lock-in  $TC_1 = 3$  ms
- sensitivity of second lock-in  $S_2 = 50$  mV
- time constant of second lock-in  $TC_2 = 30$  ms

### 2.3.5 Calibration of the lock-in amplifier

The lock-in amplifier puts out the differential conductance in DAC values. We want to display the differential conductance data in units of the quantum of conductance  $G_0 = 2e^2/h$ . This quantum of conductance is derived from the Landauer formalism [32, 81]. To display the data in units of the quantum of conductance a conversion factor  $\alpha$  was derived from spectroscopic measurements.

## 2 Experimental methods

This was done by measuring a scanning tunneling spectrum. The measured tunneling current  $I$  was numerically differentiated with respect to the applied bias voltage. This derivative of the tunneling current must be identical to the differential conductance  $dI/dV$  from the lock-in amplifier. With a conversion factor  $\alpha$  the two signals can be matched. This conversion factor  $\alpha$  depends on the preamplifier gain  $G$  and the gain of the lock-in amplifier (sensitivity)  $S$ . It can be calculated by following equation:

$$\alpha(G, S)[G_0/\text{DAC}] = \frac{1}{2^{19}}[\text{V}/\text{DAC}] * 12900[\text{A}/\text{V}] * 200[G_0/\text{A}^2] * \frac{1}{G}[\text{A}/\text{V}] * S[\text{V}]. \quad (2.16)$$

With the conversion factor  $\alpha$  the conductance values are converted from DAC units to  $G_0 = 2e^2/h$  units:

$$\frac{dI}{dV}[G_0] = \alpha(G, S)[G_0/\text{DAC}] * \frac{dI}{dV}[\text{DAC}]. \quad (2.17)$$

To rule out other influences on the factor  $\alpha$  the calibration routine was repeated every few weeks. Apart from the just mentioned dependency on the preamplifier gain and the gain of the lock-in amplifier no fluctuation of  $\alpha$  was observed.

## 2.4 Noncontact atomic force microscopy

The atomic force microscope (AFM) was invented in 1986 by Gerd Binnig, Calvin Quate and Christoph Gerber [82]. It allows to image conducting as well as non-conducting surfaces with atomic resolution [83–86]. The surface is probed by measuring the deflection of a force sensor.

The setup we use is the combined LT-STM/AFM from SPS-CREATEC GmbH [59] mentioned earlier. This means that almost all the components are shared by the STM and the AFM. This is realized by the use of a qPlus sensor as force sensor (see Fig. 2.12(a)), a tuning fork to which the Pt/Ir tip is glued [87].

### 2.4.1 Working principle of the AFM

The force sensor is scanned by piezoelectric elements above the sample. In dependency of the lateral position the force signal is measured. With this force signal an image can be made. In our setup we use a qPlus sensor, which allows us to perform STM and AFM measurements simultaneously. In Fig. 2.12b the qPlus sensor setup is shown schematically [87]. The qPlus sensor consist of a commercial tuning fork with two prongs of length  $L = 2.4$  mm. To one of the prongs (blue electrode) the tip is connected. The tunneling current is measured at the sample. The deflection of the force sensor is measured by piezoelectric detection between the two prongs of the tuning fork [88]. The advantage of this piezoelectric detection in comparison with light detection is the lower temperature of the setup, as the sensor does not get heated up by photon bombardment. The qPlus sensor is made of quartz material and thus has a high stiffness ( $k_0 \approx 1800$  N/m) compared to silicon cantilevers [88]. This allows oscillations at small amplitudes, which in turn enables high resolution measurement of the short-range forces. Furthermore the small amplitudes allow tunneling current to be measured, next to the deflection.

The qPlus sensor deflection is influenced by attractive and repulsive forces [89]. The attractive forces are van der Waals interaction, electrostatic forces and chemical forces. The repulsive forces are hard-sphere repulsion, Pauli exclusion interaction and electron-electron Coulomb interaction. The forces acting on the qPlus sensor result in a frequency shift  $\Delta f$  of the tuning fork resonance frequency  $f_0$ . This frequency shift  $\Delta f$  is proportional to the derivative of the forces acting on the qPlus sensor. This can be expressed as follows [42]:

$$\Delta f = \frac{d^2V}{dz^2} \frac{f_0}{2k_0} = -\frac{dF_z}{dz} \frac{f_0}{2k_0} \quad (2.18)$$

with the potential energy of the junction tip-sample  $V$ , the vertical component of the force  $F_z$ , the distance tip-sample  $z$  and the spring constant  $k_0$ .

The resonance frequency  $f_0$  depends critically on the weight of the tip attached to the quartz fork. The tuning forks used for the qPlus sensor have a resonance frequency of  $f_0^{\text{bare}} = 32\,768$  Hz [88]. With the Pt/Ir tip the force sensor used for this thesis had a resonance frequency of  $f_0 = 30\,300$  Hz. The frequency was checked every few weeks, the observed fluctuation was very small in the order of  $\pm 5$  Hz.



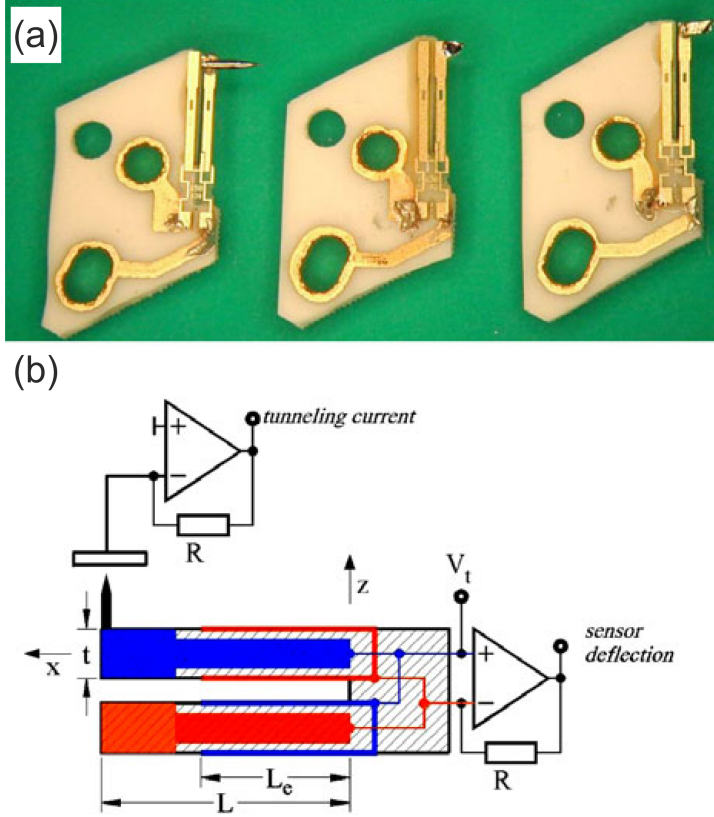


Figure 2.12: The qPlus sensor. (a) Three qPlus sensors with different tips glued to them. (b) Schematic representation of the qPlus sensor and the wiring for the simultaneous measurement in the STM and AFM mode (from reference [87]).

### 2.4.2 Controlling the junction with the AFM

The AFM was used in the experiments to control the geometry of the tip-molecule-substrate junction. This was done by measuring the frequency shift  $\Delta f$  of the qPlus sensor and comparing it to simulations (see chapter 5) [43]. In order to perform the vertical manipulation of the molecule with an oscillating tip, it was crucial to have a small oscillation amplitude  $A_{\text{real}}$ . On the other hand the oscillation had to be large enough to get a good signal-to-noise ratio.

In contrast to the tunneling current measured by STM, the forces measured by AFM are long-ranged. It is therefore even more important to have a sharp tip for force measurements, such that only the local interaction is measured. It is possible that a tip has good STM properties, but bad AFM properties. The quality of the tip within respect of the frequency shift measurement was judged upon the frequency shift at the stabilization point. A tip was considered as good, when its frequency shift  $\Delta f$  at the stabilization point was 5 Hz or less. To get such a tip, it was sometimes necessary to dip the tip up to 100 Å into the substrate.

To check the performance of the AFM measurement a calibration had to be done at least each time the sample or the sensor had been moved. This was necessary since the performance depended critically upon the exact contact geometry between the qPlus sensor and the body of the LT-STM/AFM. The calibration was made by scanning the resonance curve of the force sensor. A resonance curve with no side peaks was required. If there were side peaks, next to the resonance curve, the qPlus sensor had to be repositioned by the nitrogen cooled manipulator. After repositioning the resonance curve was checked again. If side peaks appeared again the procedure was repeated once more.

The amplitude of the oscillation  $A_{\text{real}}$  was kept constant during a measurement by the feedback loop. This amplitude  $A_{\text{real}}$  was set in the software with  $A_{\text{set}}$ . The relation between  $A_{\text{set}}$  and  $A_{\text{real}}$  varied over time, as it depended on uncontrollable parameters. This made it necessary to carefully determine this relation every time an experiment was performed by making a calibration as described by Simon *et al.* [90]. In this way the real oscillation of the qPlus sensor  $A_{\text{real}}$  was known during a measurement. It was found that a threshold of the oscillation existed under which the frequency shift was not measured properly during a vertical manipulation. This threshold was at  $A_{\text{set}} = 0.4$  mV. The real amplitude  $A_{\text{real}}$  corresponding to this amplitude fluctuated between 0.2 Å to 0.4 Å.

## 2 Experimental methods

The typical AFM parameters set in the software which were used for the manipulation experiments presented in chapter 6 were:

- oscillation amplitude  $A_{\text{set}} = 0.4 \text{ mV}$
- resonance frequency  $f_0 = 30\,300 \text{ Hz}$
- resonance phase  $\phi = -150$
- maximum frequency shift  $\Delta f_{\text{max}} = 100 \text{ Hz}$

### 2.5 Sample preparation

In this section the experimental details of the sample preparation are presented. First, the different sample preparation routines for the Ag(111) and Au(111) crystal are discussed. Then the method used for the molecular deposition, which is based on a deposition from the sample storage, is presented. In the last part STM images of the molecular islands are presented and discussed.

#### 2.5.1 Preparation of the crystals

The preparation of the samples was carried out in a preparation chamber at ultra high vacuum (UHV) which was separated from the STM chamber. The crystals were prepared by sputtering and annealing cycles. The preparation procedure of the Ag(111) and Au(111) crystals differed. In table 2.1 the preparation parameters are listed.

The sputtering was done by bombardment of the crystal with  $Ar^+$  ions. For both metals an energy of 800 eV was used for about 20 min. The annealing procedure for the two metals differed. The annealing of the Ag(111) sample was done at a temperature of 820 K for 30 min. The Au(111) sample had to be annealed first for 20 min at 700 K and then for a longer period of 60 min at 450 K. In this way the surface herringbone reconstruction was rebuilt [91]. These preparation cycles were repeated one or several times depending on the cleanliness of the sample.

## 2 Experimental methods

Sample	$S_{\text{time}}$ [min]	$S_{\text{energy}}$ [eV]	$A_{\text{time}}$ [min]	$A_{\text{temp}}$ [K]
Ag(111)	20	800	30	820
Au(111)	20	800	20	700
			60	450

Table 2.1: Typical parameters used for the preparation of the Ag(111) and Au(111) samples. Both samples were sputtered with  $Ar^+$  ions for  $S_{\text{time}} = 20$  min with an energy of  $S_{\text{energy}} = 800$  eV. The annealing of the silver sample was done for  $A_{\text{time}} = 30$  min at  $A_{\text{temp}} = 820$  K. The gold sample was first annealed for 20 min at 700 K. The long annealing period  $A_{\text{time}}$  for the Au(111) sample at  $A_{\text{temp}} = 450$  K afterward is necessary to rebuilt the surface herringbone reconstruction [91]. These preparation cycles were repeated several times depending on the cleanliness of the sample.

### 2.5.2 Deposition of the molecules

Once a sample was cleaned molecules were deposited on it. The molecule deposition procedure did not depend on which metal it was deposited. The molecules were evaporated from a crucible which was mounted on a sample holder. This sample holder was placed on the sample storage. The crucible was heated by applying a voltage to the button heater. To deposit molecules a metal crystal was moved above the crucible with a manipulator for the deposition time  $t_{\text{depo}}$  and then removed. By using a quadrupole mass spectrometer (QMS) the molecular flux was controlled during the whole deposition process.

The crucible on the sample holder had the advantage that the molecular powder in the crucible could be changed easily by transferring a sample holder with another powder from the outside into the vacuum chamber. Also it offered the ability to work with a very small molecular flux, as the crystal could be brought into close proximity of the crucible (3 cm to 4 cm). This was especially of importance for the deposition of TTCDA and QTCDA as the total amount of molecular powder available was very limited.

For the experiments a submonolayer coverage of molecules was needed, with the molecules assembled in molecular islands. The coverage was controlled by two parameters, the deposition time  $t_{\text{depo}}$  and the crucible temperature  $T_{\text{oven}}$ . To form molecular islands the molecules had to diffuse on the crystal after they were deposited. This was done by annealing the sample after the deposition for  $t_{\text{ann}} = 60$  s to a annealing temperature  $T_{\text{ann}} = 470$  K. During the deposition the crystal was kept at room temperature to

## 2 Experimental methods

prevent contamination by the adsorption of the residual gas in the preparation chamber.

Another important parameter is the pressure  $P_{\text{PC}}$  in the preparation chamber during the deposition. This pressure is an indicator for the molecular flux as well as the cleanliness of the molecular powder. In table 2.2 the parameters just described, used for our depositions, are listed. The pressure  $P_{\text{PC}}$  in the table refers to the pressure measured at the end of the deposition process.

Molecule	$T_{\text{oven}}$ [K]	$t_{\text{depo}}$ [s]	$P_{\text{PC}}$ [mbar]
NTCDA	500	5	6E-10
PTCDA	570	60	1E-09
TTCDA	710	10	3E-08
QTCDA	690	1800	8E-10

Table 2.2: Typical parameters used for the deposition of molecules. The deposition was realized by moving a metal crystal for the deposition time  $t_{\text{depo}}$  above a crucible. The crucible was mounted on a sample holder and heated to  $T_{\text{oven}}$  by applying a voltage to a button heater. By long annealing cycles of the crucible, the pressure in the preparation chamber  $P_{\text{PC}}$  was kept low during the deposition. By this a clean submonolayer of molecules was prepared.

The deposition of NTCDA and PTCDA was a very clean process, i.e. almost no contamination was found on the sample after deposition. Also almost no defects were found in the molecular islands. This suggests that the molecules did not decompose upon heating. The TTCDA islands usually showed more defects. Also the islands borders were contaminated by other types of particles. But the amount of impurities was still small enough to perform the experiments described later. In contrast the QTCDA evaporation was accompanied by the deposition of a large amount of another type of particle. These particles could be fragments of QTCDA or a contamination in the molecular powder. It is possible that some of the molecules decomposed during the heating of the crucible. Also one could imagine that particles in the powder could be a side product of the synthesis.

To reduce the flux of this second type of particle the deposition temperature  $T_{\text{depo}}$  was kept as low as possible. The consequence was a very long deposition time for QTCDA. Nevertheless, it was not possible to find a temperature at which only intact QTCDA molecules were evaporated. Long annealing cycles of the crucible did not clean the deposition process. On the Ag(111) crystal the second type of particle could be separated

from the QTCDA molecules by annealing. Both particle species agglomerated in individual islands. This made it possible to investigate QTCDA on Ag(111). In the case of the QTCDA deposition on Au(111) it was not possible to separate the molecules from the fragments by annealing (see Fig. 2.14d).

### 2.5.3 The molecular islands

After the preparation the coverage and the cleanliness of the sample was checked. A good sample was considered to have a coverage of about 10% to 30% of molecules arranged in islands. This low coverage was necessary to have enough space of clean metal on the sample to make tip preparations. A perfect tip shape was the prerequisite for the molecule manipulations as discussed in chapter 6.

In Fig. 2.13 four molecular structures as they were imaged by STM on Ag(111) are shown. The red parallelograms depict the unit cells which will be discussed in the following. In Fig. 2.13a an ordered structure of NTCDA/Ag(111) is shown. It is characterized by two types of molecules with different electronic structures (for more details see chapter 4). The molecules are arranged in a brick-wall-like structure in this commensurate phase as was observed earlier [92]. Next to this two more phases were observed which are not shown here, but discussed in details in section 4.4. The lattice parameters of the commensurate phase determined by STM are  $a = 15.1 \text{ \AA}$ ,  $b = 12.1 \text{ \AA}$  and  $\alpha = 91^\circ$ . This is in good agreement with the lattice parameters found by Stahl *et al.* [92] with STM and LEED:  $a = 15 \text{ \AA}$ ,  $b = 11.6 \text{ \AA}$  and  $\alpha = 90^\circ$ . Fig. 2.13b shows PTCD/Ag(111) imaged with a bias voltage of  $V = -340 \text{ mV}$ . The two bright lobes, i.e. the highest density of states (DOS), are in the region of the hydrogen atoms. The contrast seen here is caused by the lowest unoccupied molecular orbital (LUMO) [66]. This herringbone structure has the lattice parameters  $a = 17.8 \text{ \AA}$ ,  $b = 13 \text{ \AA}$  and  $\alpha = 93^\circ$ . This results in a slightly smaller unit cell than the ones reported of earlier by Glöckler *et al.* [93], determined by LEED and Kilian *et al.* [94], determined by SPA-LEED. They found the following lattice parameters:  $a = 19 \text{ \AA}$ ,  $b = 12.6 \text{ \AA}$  and  $\alpha = 89^\circ$ . In Fig. 2.13c an ordered structure of TTCDA/Ag(111) is shown. The molecules are arranged in a square phase, with four molecules in the unit cell. The molecular layer is interspersed with defects. The lattice parameters determined from STM are  $a = 27.9 \text{ \AA}$ ,  $b = 26.6 \text{ \AA}$  and  $\alpha = 98^\circ$ . Usually the borders of the TTCDA islands are populated by defects, which had to be removed by tip manipulation before accessing the TTCDA molecules and performing the experiments discussed in chapter 6. Fig. 2.13d shows QTCDA/Ag(111) which is forming a herringbone

## 2 Experimental methods

structure similar to PTCDA/Ag(111). The amount of defects in the island is smaller than in the TTCDA islands on Ag(111). This results as QTCDA could be separated from the defects by annealing on Ag(111). The lattice parameters of the QTCDA/Ag(111) unit cell are  $a = 23.3 \text{ \AA}$ ,  $b = 19.4 \text{ \AA}$  and  $\alpha = 92^\circ$ . No earlier measurement with TTCDA or QTCDA molecules was found in literature.

In Fig. 2.14 four ordered molecular structures as imaged by STM on Au(111) are shown. The red parallelograms depict the unit cells which will be discussed in the following. In Fig. 2.14a NTCDA/Au(111) is shown. The herringbone reconstruction of the Au(111) surface is well visible through the molecular layer. By STM the lattice parameters of this phase were determined to  $a = 15 \text{ \AA}$ ,  $b = 9.1 \text{ \AA}$  and  $\alpha = 96^\circ$ . This results in a area per molecule which is about 25% smaller than in the case of NTCDA/Ag(111), i.e. the NTCDA molecules are much closer packed on Au(111) than on Ag(111). Fig. 2.14b shows PTCDA/Au(111) in the herringbone structure as was observed earlier [95, 96]. The lattice parameters of the unit cell determined by STM are  $a = 18.6 \text{ \AA}$ ,  $b = 12.7 \text{ \AA}$  and  $\alpha = 92^\circ$ . This results in about the same area per PTCDA molecule as measured on Ag(111) (see table 2.3). Fenter *et al.* [97] measured PTCDA/Au(111) by X-ray diffraction (XRD) and found the following lattice parameters for a rectangular unit cell:  $a = 19.91 \text{ \AA}$ ,  $b = 11.96 \text{ \AA}$  and  $\alpha = 90^\circ$ , which is in good agreement with the parameters determined in this work. In Fig. 2.14c TTCDA/Au(111) is shown. The molecules are oriented perpendicular to each other in a square phase. The lattice parameters of the unit cell are  $a = 27.8 \text{ \AA}$ ,  $b = 26.4 \text{ \AA}$  and  $\alpha = 97^\circ$ . Also for TTCDA the area per molecule is about the same on both metal substrates (see table 2.3). In Fig. 2.14d the result of the QTCDA deposition on Au(111) is shown. The QTCDA molecules are oriented in long chains. In between the QTCDA chains another type of particle is arranged in chains as well. Different annealing temperatures and annealing times were tried to separate both types of particles. In contrast to the case of QTCDA/Ag(111) it was not possible to separate both types of particles. In consequence this smaller type of particle used to stick at the QTCDA molecules, when they were dragged away from the islands by the STM tip to perform the experiments discussed in chapter 6. In table 2.3 the lattice parameters and the area per molecule for each system are summarized.

To check the chemical structure of the molecules TTCDA and QTCDA the well established technique scanning tunneling hydrogen microscopy (STHM) was used [98–100]. In Fig. 2.15 two STHM images are shown [98–100]. These images were measured with the tip functionalized by a CO molecule. In Fig. 2.15a a TTCDA island on Au(111) is shown. The three naphthalene units which form the carbon backbone of the molecule are

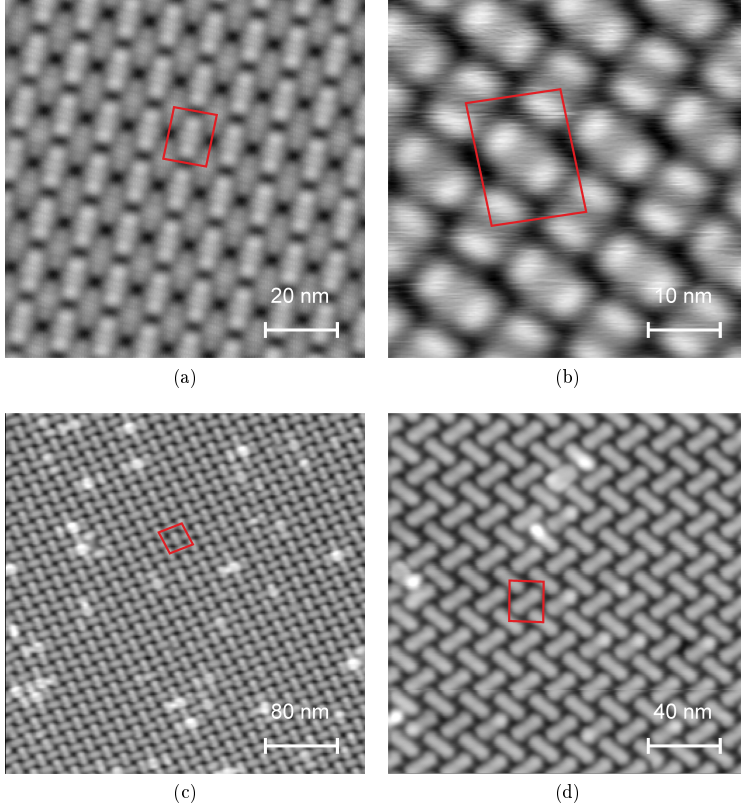


Figure 2.13: STM images of molecular islands on Ag(111). By the red parallelograms the unit cells as discussed in this section are depicted. (a) NTCDA on Ag(111). Molecules with two different types of electronic structures (see chapter 4) are arranged in stripes. They form a brick-wall-like structure.  $100 \text{ \AA} \times 100 \text{ \AA}$ , 0.1 nA, 50 mV. (b) PTCDA on Ag(111) in a herringbone structure. The LUMO contrast is shown, with the two bright lobes, i.e. the highest density of states (DOS), above the hydrogen atoms of the molecules [66].  $50 \text{ \AA} \times 50 \text{ \AA}$ , 0.1 nA,  $-340 \text{ mV}$ . (c) TTCDA on Ag(111). The molecules are arranged in a square phase. The amount of defects is much higher than in the NTCDA or PTCDA islands.  $400 \text{ \AA} \times 400 \text{ \AA}$ , 0.1 nA, 278 mV. (d) QTCDA on Ag(111) also forms a herringbone structure like PTCDA. The number of defects is smaller than in the TTCDA islands.  $200 \text{ \AA} \times 200 \text{ \AA}$ , 0.1 nA, 278 mV.



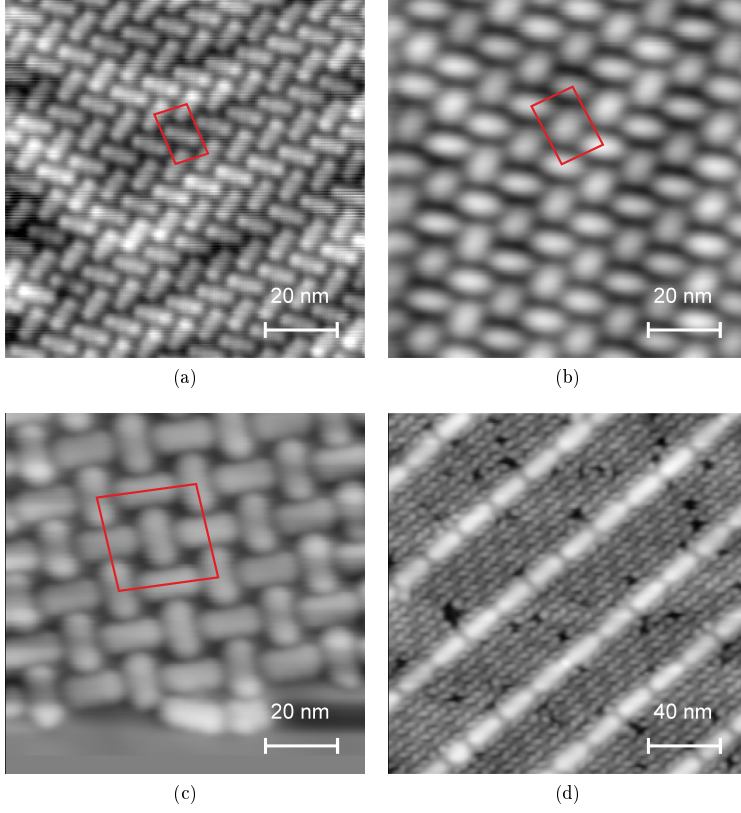


Figure 2.14: STM images of molecular islands on Au(111). By the red parallelograms the unit cells as discussed in this section are depicted. (a) NTCDA on Au(111) with the well visible herringbone reconstruction of the metal underneath.  $100 \text{ \AA} \times 100 \text{ \AA}$ ,  $0.1 \text{ nA}$ ,  $1666 \text{ mV}$ . (b) PTCDA on Au(111) forms a herringbone structure.  $100 \text{ \AA} \times 100 \text{ \AA}$ ,  $0.1 \text{ nA}$ ,  $300 \text{ mV}$ . (c) TTCDA on Au(111), with the molecules arranged perpendicular to each other in a square phase.  $100 \text{ \AA} \times 100 \text{ \AA}$ ,  $0.025 \text{ nA}$ ,  $-11 \text{ mV}$ . (d) QTCDA on Au(111) forms long chains. In between of the QTCDA molecules another type of particle is also arranged in chains. It was not possible to separate them from the QTCDA molecules by annealing. Thus the molecule manipulations could not be performed with QTCDA on Au(111).  $200 \text{ \AA} \times 200 \text{ \AA}$ ,  $0.1 \text{ nA}$ ,  $316 \text{ mV}$ .

## 2 Experimental methods

Substrate	Molecule	a [Å]	b [Å]	$\alpha$ [°]	Area [Å <sup>2</sup> ]	No. of mol.	$\frac{\text{Area}}{\text{Molecule}}$ [Å <sup>2</sup> / mol.]
Ag(111)	NTCDA	15.1	12.1	91	183	2	92
	PTCDA	17.8	13.0	93	231	2	116
	TTCDA	27.9	26.6	98	735	4	184
	QTCDA	23.3	19.4	92	452	2	226
Au(111)	NTCDA	15.0	9.1	96	136	2	68
	PTCDA	18.6	12.7	92	235	2	118
	TTCDA	27.8	26.4	96	729	4	182

Table 2.3: The coordinates of the unit cells of the different systems probed with STM. The unit cell of the system NTCDA/Ag(111) refers to the commensurate phase, the other two phases are discussed in section 4.4. QTCDA/Au(111) is not found isolated from another type of particle, therefore no unit cell was determined.

indicated by red ellipses. In Fig. 2.15b a single QTCDA molecule on Au(111) is shown, which is characterized by four naphthalene units. The molecule is bound to a defect, in this way the single molecule did not move when scanned with the functionalized tip. Because of the defect the STM image was not fully scanned. This had to be done in order to preserve the tip, as it was found that scanning above such a defect often resulted in losing the CO molecule on the tip.

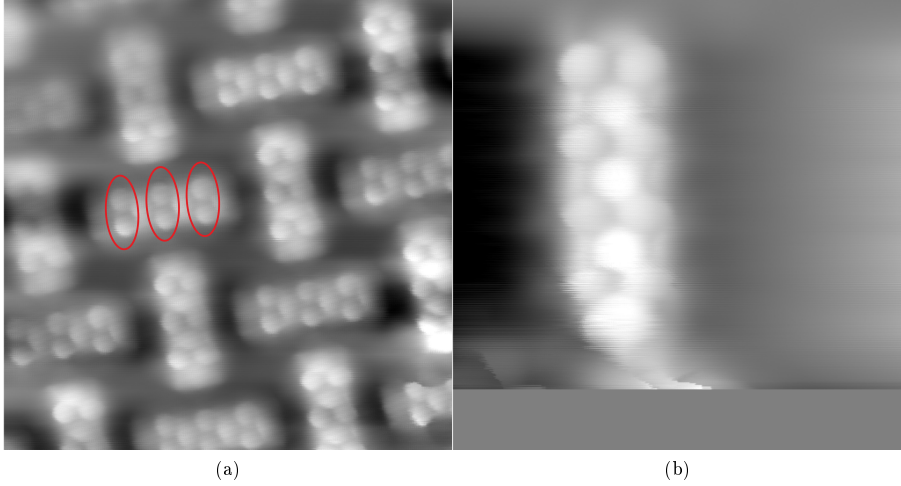


Figure 2.15: Scanning tunneling hydrogen microscopy (STHM) images made with a CO molecule bound to the tip [98–100]. (a) STHM image of a TTCDA island on Au(111). Clearly visible are the three naphthalene units forming the carbon backbone of the molecule (see red ellipses).  $50 \text{ \AA} \times 50 \text{ \AA}$ ,  $0.1 \text{ nA}$ ,  $-11 \text{ mV}$ . (a) STHM image of a single QTCDA molecule on Au(111) bound to a defect. As defects tend usually to change the tip, the image was not fully scanned. In this way the CO molecule on the tip was preserved. Also here the four characteristic naphthalene units are visible.  $25 \text{ \AA} \times 25 \text{ \AA}$ ,  $0.05 \text{ nA}$ ,  $-10 \text{ mV}$ .



## 3 Theory of transport

### 3.1 Introduction

In this chapter the theoretical concepts to understand the charge transport through molecular junctions are worked out. In the first part the description of the charge transport through mesoscopic conductors, e.g. a molecule, is described. Introducing the Landauer formalism the concept of ballistic transport is introduced. In the second part the concept of double barrier tunneling, as is found in molecular junctions, is discussed. Finally the vibration-electron coupling and the Kondo effect are introduced, as they will be observed in the experiments discussed in chapter 4.

### 3.2 Ballistic transport

The conductance of a conductor contacted by two contacts (see Fig. 3.1a) can be expressed with the material dependent conductivity  $\sigma$  by the following equation [101]:

$$G = \sigma W/L \quad (3.1)$$

where  $W$  is the width of the conductor and  $L$  its length. According to this equation, the conductance is growing infinitely as the length of the conductor  $L$  is reduced. It is found however that the conductance is saturating at  $G_c$  when the length of the conductor is much smaller than the mean free path  $L_m$ . The resistance limiting the conductance is resulting from the interface between the conductor and the contacts. Therefore this resistance is referred to as contact resistance  $G_c^{-1}$ . This contact resistance is the consequence of the current, which is carried by infinite modes in the contacts, having to be redistributed on a few modes in the conductor (see Fig. 3.1b). Furthermore reflectionless contacts have to be assumed, i.e. an electron can move from a narrow conductor to a wide contact with negligible probability of reflection.

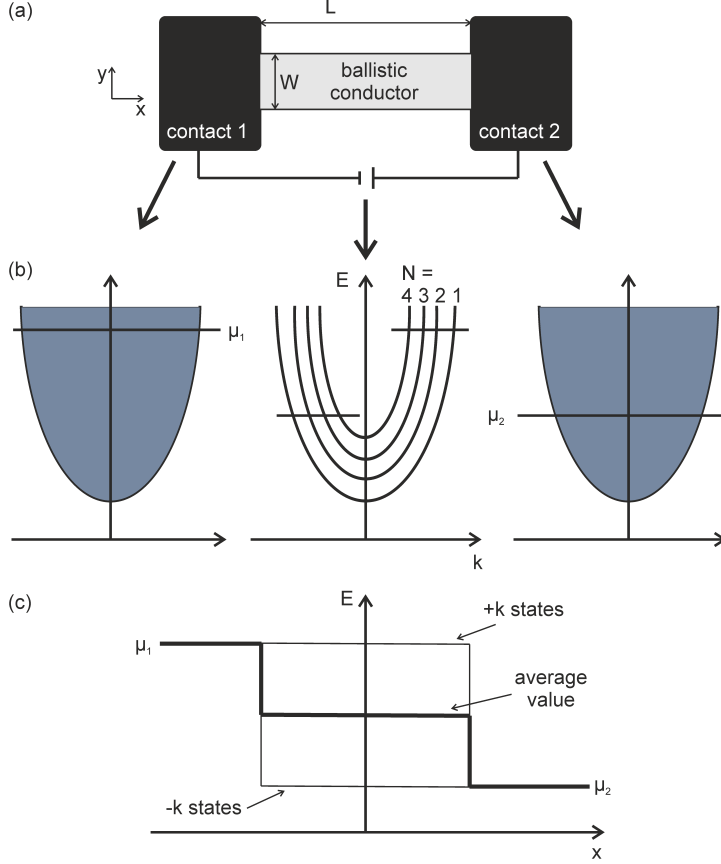


Figure 3.1: (a) Ballistic conductor with length  $L$  and width  $W$ . If the length of the conductor is smaller than the mean free path  $L < L_m$ , the conductance of the conductor is saturating at a value  $G_c$ . This is a result of the contact resistance  $G_c^{-1}$ . (b) The contacts left and right of the conductor have an infinitely number of modes. In the ballistic conductor the number of transverse modes is discrete. The current through the ballistic conductor is carried by the  $+k$  states of the transverse modes in the energy range between  $\mu_1$  and  $\mu_2$ . (c) The distribution of the electrochemical potential. The voltage drop occurs at the interface between contacts and conductor (after [101]).

### 3 Theory of transport

The current is carried by a few transverse modes  $N$  in the conductor (see Fig. 3.1b). With the dispersion relation  $E(N, k)$  a cut-off energy  $\epsilon_N = E(N, k = 0)$  can be attributed to each mode. The number of modes  $M$  at a certain energy  $E$  is given by

$$M(E) = \sum_N \vartheta(E - \epsilon_N) \quad (3.2)$$

The current through the conductor can be calculated by summing up the current transported by each mode  $N$ . An electron gas with an electron density  $n$  moving with the velocity  $v$  result in the current  $I = env$ . The electron density of a  $+k$  state in a conductor of length  $L$  is  $(1/L)$ . With this the current can be expressed as follows:

$$I^+ = \frac{e}{L} \sum_k v f^+(E) = \frac{e}{L} \sum_k \frac{1}{\hbar} \frac{\delta E}{\delta k} f^+(E) \quad (3.3)$$

with a function  $f^+(E)$ , which describes the occupation of the  $+k$  states and the charge of an electron  $e$ . By replacing the sum  $\sum_k$  with an integral  $2$  (for spin)  $\ast \frac{L}{2\pi} \int dk$  the current is:

$$I^+ = \frac{2e}{h} \int_{\epsilon}^{\infty} f^+(E) dE \quad (3.4)$$

with the Planck constant  $h$  and the cut-off energy  $\epsilon$ . With the number of modes  $M$  at a certain energy  $E$  (see equation 3.2) the current can be expressed as:

$$I^+ = \frac{2e}{h} \int_{-\infty}^{\infty} f^+(E) M(E) dE. \quad (3.5)$$

If the number of modes is constant in the energy range between  $\mu_1$  and  $\mu_2$  the current can be expressed as follows:

$$I = \frac{2e^2}{h} M \frac{\mu_1 - \mu_2}{e} \quad (3.6)$$

The contact resistance can then be written with the voltage  $(\mu_1 - \mu_2)/e$  as:

$$G_c^{-1} = \frac{h}{2e^2 M} \approx \frac{12.9 \text{ k}\Omega}{M} \quad (3.7)$$

where the contact resistance is decreasing with the number of modes  $M$ . The voltage drop occurs at the interface of the contacts and the conductor as can be seen in Fig. 3.1c.

### 3.2.1 Landauer formula

In the previous section an ideal ballistic conductor was considered, i.e. a conductor where the electrons can move without being scattered in the conductor. To account for the scattering events the transmission probability  $T$  has to be introduced. This transmission probability  $T$  gives the probability an electron has, entering the conductor on one side, to exit the conductor on the other side.

We can assume that left of the conductor the  $+k_x$  states are occupied by electrons at the electrochemical potential  $\mu_1$  and right of the conductor the  $-k_x$  states are occupied by electrons at the electrochemical potential  $\mu_2$  (see Fig. 3.1b). If the temperature is zero, than the current is driven by electrons in the energy range between  $\mu_1$  and  $\mu_2$ .

If the current from the left side into the conductor is given by:

$$I_1^+ = \frac{2e}{h} M [\mu_1 - \mu_2], \quad (3.8)$$

than the current from the conductor out to the right side is equation 3.8 times the transmission probability  $T$ :

$$I_2^+ = \frac{2e}{h} MT [\mu_1 - \mu_2]. \quad (3.9)$$

If the transmission probability  $T$  is not unity, than part of the current is reflected at the right interface of the conductor:

$$I_1^- = \frac{2e}{h} M(1 - T) [\mu_1 - \mu_2]. \quad (3.10)$$

With this the net current  $I = I_1^+ - I_1^- = I_2^+$  through the conductor is given by equation 3.9. Together with the voltage across the conductor  $\frac{\mu_1 - \mu_2}{e}$  the conductance can be expressed by the Landauer formula [101]:



$$G = \frac{I}{(\mu_1 - \mu_2)/|e|} = \frac{2e^2}{h}MT. \quad (3.11)$$

with the number of modes  $M$ , the transmission probability  $T$  and the conductance quantum  $\frac{2e^2}{h}$ . This means the conductance does not depend on the width  $W$  of the conductor, but instead the conductance is discrete and depends on the number of transverse modes  $M$ . Further the contact resistance is independent of the length of the conductor  $L$ . If all electrons entering from one side exit the other side of the conductor ( $T = 1$ ), equation 3.7 for the contact resistance is recovered.

### 3.2.2 Transmission probability

The transmission probability  $T$  of a conductor of length  $L$  is typically not unity as the electrons can scatter [101]. Its dependence on the length can be expressed as:

$$T(L) = \frac{L_0}{L + L_0} \quad (3.12)$$

with the characteristic length  $L_0$  which is on the order of the mean free path, i.e. the average distance of an electron between two scattering events.

Considering two conductors connected in series (see Fig. 3.2a) one could assume that the net transmission  $T_{12}$  through the series is

$$T_{12} = T_1 T_2 \quad (3.13)$$

This is wrong, as it would mean that the transmission is going down exponentially with the length of the series of conductors  $T(L) = \exp[L/L_0]$  and that Ohm's Law (see equation 3.1) is not true. To get the real transmission  $T_{12}$ , the probabilities of all path have to be added, i.e. the path which the electrons undergo which are multiply reflected by the resistors in the series (see Fig. 3.2b). The phase relation between the path can be neglected assuming that the phase-relaxation length is much shorter than the distance between two resistors. The net transmission is then gained by summing up the transmission with no reflection, with two reflections, with four reflections and so on:

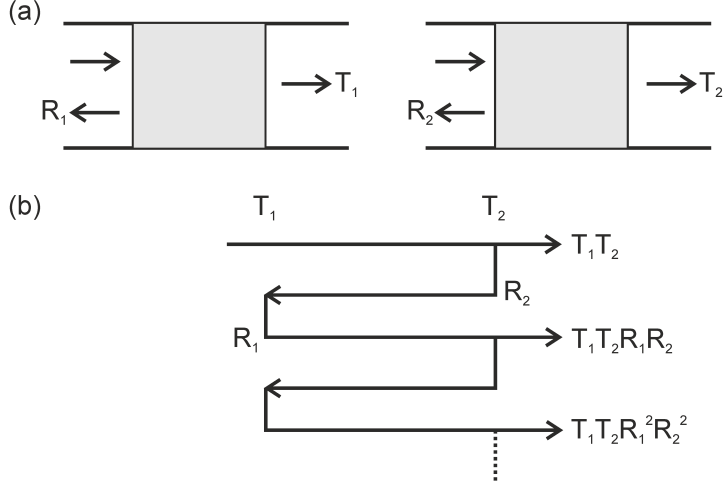


Figure 3.2: (a) Two conductors connected in series with transmission probability  $T_1$  and  $T_2$  and reflection probability  $R_1$  and  $R_2$ . (b) When all phase information are neglected, the net transmission can be calculated by summing up the transmission with no reflection, with two reflections, with four reflections and so on. (after [101]).

$$\begin{aligned}
 T_{12} &= T_1T_2 + T_1T_2R_1R_2 + T_1T_2R_1^2R_2^2 + \dots \\
 &= \frac{T_1T_2}{1 - R_1R_2}
 \end{aligned}
 \tag{3.14}$$

This can be rewritten using  $T_1 = 1 - R_1$  and  $T_2 = 1 - R_2$ :

$$\frac{1 - T_{12}}{T_{12}} = \frac{1 - T_1}{T_1} + \frac{1 - T_2}{T_2}
 \tag{3.15}$$

From this the transmission probability of  $N$  conductors in series, each with an individual transmission probability  $T$  is given by:

$$T(N) = \frac{T}{N(1 - T) + T}
 \tag{3.16}$$

With the density of scattering events  $\nu = N/L$ , i.e. the number of scatterers  $N$  in a conductor of length  $L$ , equation 3.12 is recovered:

$$T(L) = \frac{L_0}{L + L_0} \quad (3.17)$$

Finally the total resistance can be written as a combination of the contact resistance and the resistance of the conductor:

$$G^{-1} = \frac{h}{2e^2 M} \frac{1}{T} = \frac{h}{2e^2 M} + \frac{h}{2e^2 M} \frac{1-T}{T} \quad (3.18)$$

### 3.3 Molecule in a vacuum junction

In chapter 2 the scanning tunneling microscope (STM) was introduced. The working principle of the STM is based on the tunneling effect, i.e. transport which is characterized by the probability of a particle to cross a potential barrier which is classically forbidden. It was found that this transmission probability decays exponentially inside the barrier. The effective tunneling barrier height, which is defined as the energy difference between the particle energy  $E$  and the potential barrier  $\Phi$ , as well as the barrier width  $z$  define the transmission probability. With the mass of the particle  $m$  the tunneling current is then given as:

$$I \propto e^{-2\kappa z} \quad \text{where} \quad \kappa = \sqrt{\frac{2m}{\hbar}(\Phi - E)} \quad (3.19)$$

By introducing a molecule into the vacuum gap we observe the system which was probed in this thesis. As the molecule is contacted by the electrodes charge flow, charge rearrangement and geometric reorganization takes place [32]. A simplified picture of the electronic structure after contact formation is given in Fig. 3.3 [102].

In Fig. 3.3a the Fermi level of the metal electrodes is lying in between the lowest unoccupied molecular orbital (LUMO) and the highest occupied molecular orbital (HOMO). The Fermi level can not only lie in the middle of the two orbitals, but anywhere in between them. The transport through such a junction is defined by two properties. The coupling between the electrodes and the molecule  $\Gamma$  and the charging energy of the molecule  $U$ . When  $\Gamma < U$  the coupling is weak, for  $\Gamma > U$  strong coupling is observed. In Fig. 3.3a-c the molecule-electrode coupling  $\Gamma$  is increasing from left to right. The increase of the coupling is reflected by a broadening of the energy levels of the molecule. This

happens as the molecular energy levels mix with the metal states. For some coupling a Kondo resonance (see section 3.5) may be observed.

In Fig. 3.3d-g the transport through a quantum dot (QD) is depicted. This picture can be used to understand the transport through a metal-molecule-metal junction. This can be done as the transport properties of a molecule and a QD in the conductance behave very often similar [102]. To have a significant current flow the molecular orbitals have to be brought to the Fermi level  $E_F$  such that resonant tunneling is enabled. By mechanical gating or a gate voltage  $V_g$  (3.3e) the energy levels can be brought in resonance and hence electrons can tunnel through the junction. Another possibility is to bring the Fermi level  $E_F$  of the electrodes up to a molecular orbital by applying a bias voltage (3.3f). When vibrational modes appear, resulting from interaction of electrons and molecular vibrations, additional transport channels can be opened. This is the consequence of incoherent tunneling (see section 3.4).

#### 3.3.1 Coherent resonant tunneling in a double-barrier

A double-barrier, as will be discussed in this section, consists of two potential barriers which are separated by a few nanometers [101]. The double-barrier is observed in molecular junction, where the first barrier is the tip-molecule contact and the second barrier is the molecule-substrate contact [103]. One could assume that the current through such a double-barrier can be understood on the basis of a single-barrier. According to Ohm's Law to get the same current through a double-barrier as through a single-barrier the voltage has to be doubled. This is not the case!

The different characteristic between the conductance through a single-barrier and a double-barrier is the consequence of the energy quantization between the barriers. If the spacing between the two barriers is small enough, than only a single energy state  $E_T$  is allowed between the barriers (see Fig. 3.4). This state acts like a filter and only lets through electrons at the energy  $E_T$ . By applying a voltage between the two barriers the energy of this single state can be changed. With this it is possible to probe the density of states of the right and left electrode at different energies. At some voltage  $V = V_T$  the energy of the state between the barriers lies below the conduction band of the electrode. In consequence the current-voltage ( $I - V$ ) curve shows a sharp drop, as no more state is in the probed energy range. By further lowering the voltage the current can increase again. This effect is called negative differential resistance (NDR). It was first observed by

### 3 Theory of transport

Chang *et al.* [104] in a double-barrier structure made by a thin GaAs layer sandwiched between two GaAlAs barriers.

To calculate the  $I - V$  characteristics the Landauer formula as given in 3.11 has to be modified. This has to be done, as the transmission probability can depend on the energy. In fact it is found, that at non-zero temperature and non-zero bias the transmission has to be described by the transmission function  $\bar{T}(E) = M(E)T(E)$ . With the Fermi functions  $f_1(E)$  and  $f_2(E)$  for the two contacts the current can be described as follows:

$$I = \frac{2e}{h} \int \bar{T}(E)[f_1(E) - f_2(E)]dE \quad (3.20)$$

by approximating the Fermi functions to step functions equation 3.20 can be simplified to

$$I = \frac{2e}{h} \int_{\mu_1}^{\mu_2} \bar{T}(E)dE \quad (3.21)$$

The transmission function is given by:

$$\bar{T}(E) = \sum_m T_L(E - \epsilon_m) = \frac{\Gamma_1 \Gamma_2}{\Gamma_1 + \Gamma_2} \sum_m A(E - E_m) \quad (3.22)$$

where

$$E_m = E_\Gamma + \epsilon_m \quad (3.23)$$

with the longitudinal resonance energy  $E_\Gamma$ , the transverse mode  $m$  with its energy  $\epsilon_m$ , the coupling of an electron in the barrier to the left and right contact  $\Gamma_1$  and  $\Gamma_2$ , i.e. the rate at which an electron leaks out from the barrier into the right or left contact. The Lorentzian function  $A(\epsilon)$  is defined as follows:

$$A(\epsilon) = \frac{\Gamma}{\epsilon^2 + (\Gamma/2)^2} \quad (\Gamma \equiv \Gamma_1 + \Gamma_2) \quad (3.24)$$

The transmission function has now to be integrated as shown in equation 3.21 to get the current. The integration is done from  $\epsilon_m$  to  $\mu_1$  as no transmission is possible if the total

### 3 Theory of transport

energy is smaller than the energy of the transverse mode ( $E < \epsilon_m$ ). With this we get the current carried by one transverse mode:

$$I_m = \frac{2e}{h} \int_{\epsilon_m}^{\mu_1} \bar{T}(E) dE = \frac{2e}{h} \frac{\Gamma_1 \Gamma_2}{\Gamma_1 + \Gamma_2} \int_{\epsilon_m}^{\mu_1} A(E - E_m) dE \quad (3.25)$$

Thus the current per transverse mode is equal to the area its Lorentzian function is covering in the energy range between  $\epsilon_m$  and  $\mu_1$ . If the Lorentzian function covers the whole energy range, then the current is maximized, this is the so-called resonant condition (see Fig. 3.5a). The maximum current per mode is then given by:

$$I_P = \frac{2e}{h} \frac{\Gamma_1 \Gamma_2}{\Gamma_1 + \Gamma_2} \quad (3.26)$$

This means that the current per mode is approximately  $I_P$  if the mode is resonant and zero if the mode is non-resonant (see Fig. 3.5b).

#### 3.3.2 Incoherent tunneling

In the previous sections coherent tunneling processes were discussed. This means that the electrons traveling through the double-barrier did not lose their phase memory. The prerequisite for coherent tunneling is that the time the electron spends in the double-barrier is short compared to the scattering time  $\tau_\varphi$ . In molecular junctions however it is observed that the tunneling electron interacts with the vibrations of the molecule. This electron-vibration interaction can change the transport from coherent to incoherent [105]. In the following the incoherent tunneling processes will be described, a distinction between the resonant (see Fig. 3.4a) and the off-resonant (see Fig. 3.4c) transport will be made.

To distinguish between coherent and incoherent transmission the scattering rate  $\Gamma_\varphi$  is introduced [101]. It is proportional to the scattering time  $\tau_\varphi$ :

$$\Gamma_\varphi \equiv \hbar/\tau_\varphi \quad (3.27)$$

with  $\hbar = \frac{h}{2\pi}$  the reduced Planck constant or Dirac constant. Comparing this scattering rate to the coupling parameters  $\Gamma_1$  and  $\Gamma_2$  the transport can be characterized as mainly coherent if:

$$\Gamma_1 + \Gamma_2 \gg \Gamma_\varphi \quad (3.28)$$

or incoherent if:

$$\Gamma_1 + \Gamma_2 \leq \Gamma_\varphi \quad (3.29)$$

### 3.3.2.1 Resonant current

In Fig. 3.6 the electron paths in a double-barrier are depicted. Only a part of the electrons can pass the double-barrier coherently. Some electrons get scattered, e.g. by electron-vibration coupling [105]. The coherent resonant current per mode is given as (compare with equation 3.26):

$$I_{\text{coh}} = \frac{2e}{\hbar} \frac{\Gamma_1 \Gamma_2}{\Gamma_1 + \Gamma_2 + \Gamma_\varphi} \quad (3.30)$$

The scattered current per mode is very similar to the coherent resonant current per mode. The only difference is the replacement of  $\Gamma_2$  by  $\Gamma_\varphi$ . This is reasonable, as the scattered electrons can be thought of passing through a third barrier with coupling  $\Gamma_\varphi$ . The scattered current is then given as:

$$I_s = \frac{2e}{\hbar} \frac{\Gamma_1 \Gamma_\varphi}{\Gamma_1 + \Gamma_2 + \Gamma_\varphi} \quad (3.31)$$

These scattered electrons are reinjected. This reinjected current gets split and moves to barrier '1' and '2' with the ratio  $\Gamma_1 : \Gamma_2$ . The part of the reinjected current which goes through barrier '2' is the incoherent current:

$$I_{\text{incoh}} = \frac{\Gamma_2}{\Gamma_1 + \Gamma_2} I_s = \frac{\Gamma_\varphi}{\Gamma_1 + \Gamma_2} I_{\text{coh}} \quad (3.32)$$

The total current through the double-barrier is then given by summing the coherent and the incoherent current:

$$I_0 = I_{\text{coh}} + I_{\text{incoh}} = \frac{2e}{\hbar} \frac{\Gamma_1 \Gamma_2}{\Gamma_1 + \Gamma_2} \quad (3.33)$$

This is the same current that was determined in the case of resonant tunneling without scattering events (see equation 3.26). This means that the scattering has no influence on the current in the case of resonant tunneling.

### 3.3.2.2 Off-resonant current

The off-resonant current is very small, as was observed e.g. by Chang *et al.* [104]. It is found in experiments however that the valley current in NDR is higher than theory predicts (see e.g. [106]). This is the consequence of electron scattering and thus incoherent transport [107]. The transport behavior differs between the resonant and the non-resonant condition. The main difference is that in the resonant condition the resonance lies fully in the energy range of the electrons, while in the non-resonant condition the resonance lies outside the energy range of the electrons (see Fig. 3.5).

If we treat the non-resonant condition as the resonant condition the current can be described as was shown in equation 3.30 to 3.33. The coherent current is then given by:

$$I_{V,\text{coh}} = \frac{2e}{\hbar} K \Gamma_1 \quad \text{where} \quad K \approx \int_0^{\mu_1} \frac{\Gamma_2 dE}{(E - E_\Gamma)^2} \quad (3.34)$$

And the scattering current is given by replacing  $\Gamma_2$  with  $\Gamma_\varphi$ :

$$I_s = \frac{2e}{\hbar} g \Gamma_1 \quad \text{where} \quad g \approx \int_0^{\mu_1} \frac{\Gamma_\varphi dE}{(E - E_\Gamma)^2} \quad (3.35)$$

In contrast to the resonant condition, in the non-resonant condition all reinjected electrons (see Fig. 3.6) exit the double-barrier via barrier '2'. This is the consequence of no states being available at barrier '1' at the energy of the reinjected electrons  $E_\Gamma$ . Therefore the incoherent current is the same as the scattering current in the non-resonant condition:

$$I_{V,\text{incoh}} = \frac{2e}{\hbar} g \Gamma_1 \quad \text{where} \quad g \approx \int_0^{\mu_1} \frac{\Gamma_\varphi dE}{(E - E_\Gamma)^2} \quad (3.36)$$

The total off-resonance current is then given by summing the coherent and the incoherent current. This can be done if low temperatures are assumed, as in this case no



### 3 Theory of transport

electron that lost energy by emitting a photon can absorb a photon to gain energy again:

$$I_V = I_{V,\text{coh}} + I_{V,\text{incoh}} = \frac{2e}{\hbar} [K\Gamma_1 + g\Gamma_1] \quad (3.37)$$

This equation can not be correct, as it would mean that there is still a current even when barrier '2' is so thick that the coupling of the resonance to the contact is zero ( $\Gamma_2 = 0$ ). To overcome this problem equation 3.36 has to be modified such, that the incoherent current gets zero ones the resonant level is filled up with electrons. This is done by introducing a occupation factor  $f_\Gamma$  for the resonant level:

$$f_\Gamma = \frac{g\Gamma_1}{g\Gamma_1 + \Gamma_2} \quad (3.38)$$

With this factor the occupation of the resonant level in dependence of the coupling to both contacts can be determined. The occupation of the resonant level is zero if  $\Gamma_2 \gg g\Gamma_1$ . When  $\Gamma_2 \approx g\Gamma_1$  the resonant level starts to fill up and the current is decreasing. The incoherent current can then be expressed as follows with the occupation factor  $f_\Gamma$ :

$$I_{V,\text{incoh}} = \frac{2e}{\hbar} g\Gamma_1 (1 - f_\Gamma) = \frac{2e}{\hbar} \frac{g\Gamma_1\Gamma_2}{g\Gamma_1 + \Gamma_2} \quad (3.39)$$

The total off-resonant current is then expressed as follows:

$$I_V = I_{V,\text{coh}} + I_{V,\text{incoh}} = \frac{2e}{\hbar} [K\Gamma_1 + \frac{g\Gamma_1\Gamma_2}{g\Gamma_1 + \Gamma_2}] \quad (3.40)$$

With this one can compare the peak and the valley current, i.e. the current in the resonant (see equation 3.33) and in the non-resonant condition (see equation 3.40). The current depend on the coupling parameters as follows:

$$I_{\text{res}} \sim \frac{1}{\Gamma_1} + \frac{1}{\Gamma_2} \quad \text{and} \quad I_{\text{off-res}} \sim \frac{1}{g\Gamma_1} + \frac{1}{\Gamma_2} \quad (3.41)$$

This means that the ratio between the resonant and the off-resonant current critically depends on the coupling parameters  $\Gamma_1$ ,  $\Gamma_2$  and  $\Gamma_\varphi$ .

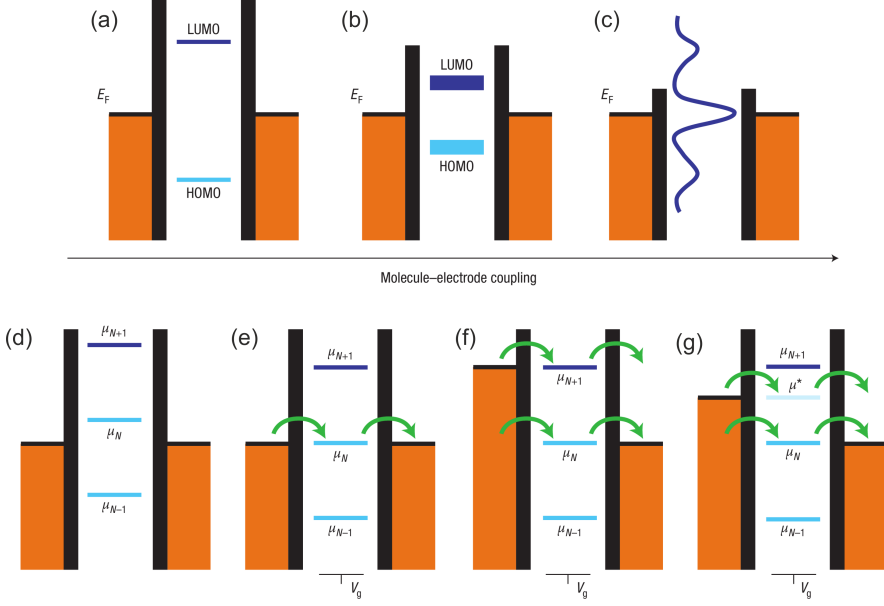


Figure 3.3: Schematic representation of the energies of a molecule in the tunneling junction. As the molecule gets into contact with the metal electrodes, charge is flowing until the Fermi level of the metal is in between the HOMO-LUMO gap of the molecule. (a)-(c) The HOMO-LUMO gap gets smaller and the orbitals are broadened when the coupling  $\Gamma$  between molecule and electrodes is increasing. (d)-(g) To enable the electron transport the energy levels of the molecule have to be aligned with the Fermi level  $E_F$  of the electrode. Vibrational modes  $\mu^*$  can create additional transport channels (from reference [102]).

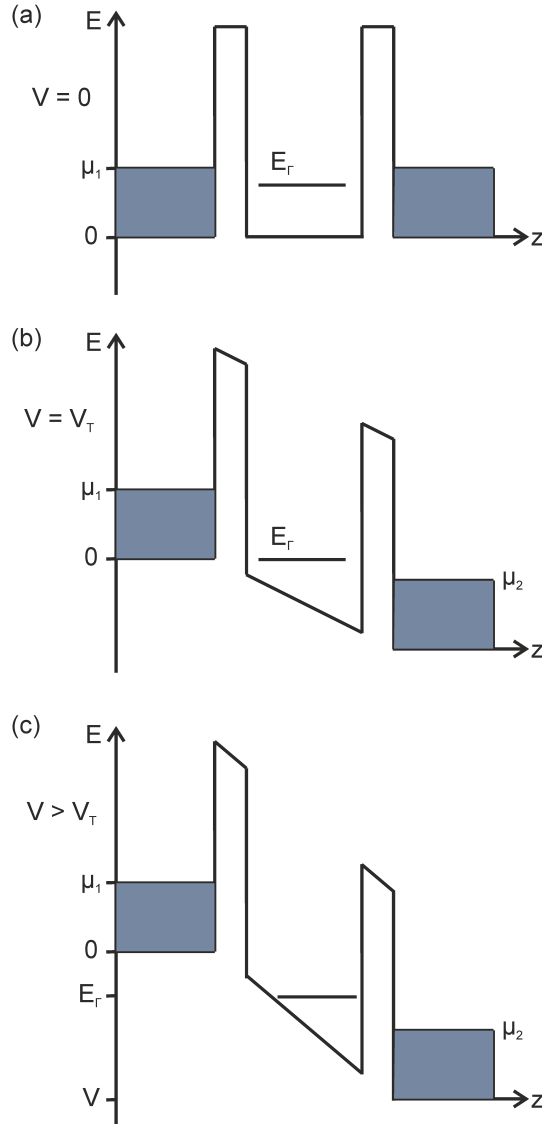


Figure 3.4: Double barrier with (a) no bias applied to the contacts, (b) a bias applied, such that the electrons tunnel through the barrier at the bottom of the conduction band and (c) a bias applied, such that the only energy state in the barrier is off-resonance (after [101]).

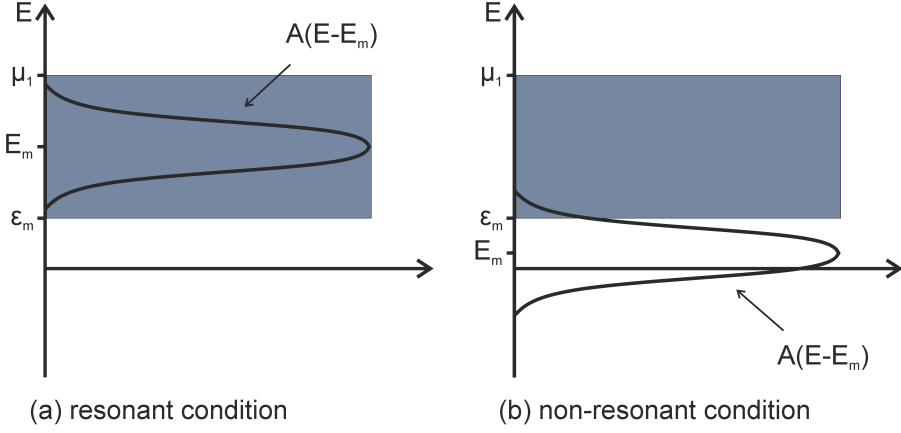


Figure 3.5: The area under the Lorentzian shaped transmission function gives the current carried by a mode. (a) In the resonant condition the current is maximized, as the Lorentzian shaped transmission function covers the whole energy range from the transverse mode energy  $\epsilon_m$  to the electrochemical potential  $\mu_1$ . (b) In the non-resonant condition the current is zero (after [101]).

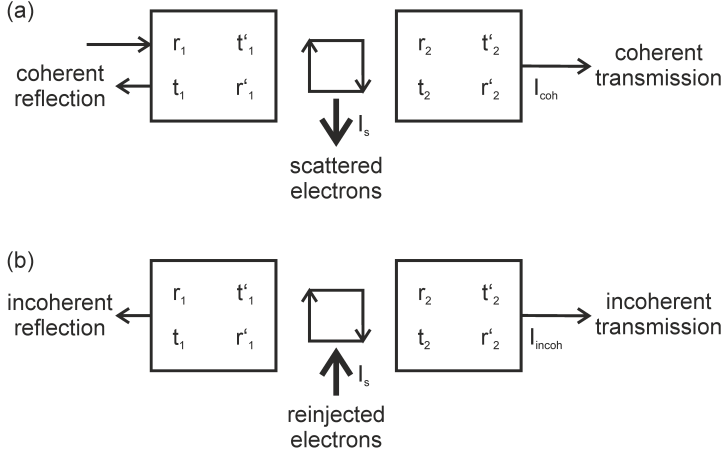


Figure 3.6: Double barrier with scattering events. Barrier '1' and '2' with scattering matrices. (a) Some of the electrons pass the barrier coherently, some are scattered. (b) The scattered electrons are reinjected, some of the reinjected electrons pass through barrier '2'. This is the incoherent current (after [101]).

### 3.4 Molecular vibrations

Due to thermal excitation molecules are vibrating. When an electron and a molecular vibration interact the conductance is typically increased in the tunneling junction [108, 109]. This interaction is measured by inelastic electron tunneling spectroscopy (IETS) [108]. The signal measured by IETS can help to gain further knowledge about the molecules adsorption site, orientation and changes in bonding upon adsorption [109, 110].

The first time molecular vibrations in tunneling junctions were observed by Jaklevic *et al.* [111]. In their experiment a molecular monolayer was deposited on the oxide layer of an metal-oxide-metal junction. A bias voltage was swept up to 1 V and the tunneling current was measured. In the bias range 0.05 V to 0.5 V they observed that the differential conductance  $dI/dV$  is increasing stepwise at certain voltages and thus peaks are observed in the second derivative of the tunneling current  $d^2I/dV^2$  at those voltages. These voltages were then identified to be resulting from vibrational modes of the molecules in the junction, namely C-H and O-H bending and stretching modes.

The observed conductance increase is described as follows [68]. When a electron has sufficient energy it can excite a vibrational mode of the molecule. Depending on the energy level alignment and the applied bias voltage non-resonant or resonant electron-vibration coupling may be observed. In the non-resonant case the highest occupied molecular orbital (HOMO) and the lowest unoccupied molecular orbital (LUMO) are far away from the applied bias voltage. The molecular vibrations are triggered by inelastic scattering of the tunneling electrons at the molecule. The electrons loose energy and by this a new transport channel opens which is observed as a step in the differential conductance  $dI/dV$ . This scattering effect is very weak, which makes the observation of the conductance increase difficult. This picture changes as the molecule has a state very close to the Fermi level. If the molecular junction is now probed near the Fermi level, resonant electron tunneling is observed. The electron-vibration coupling opens a resonant transmission channel. This leads to the observation of peaks in the  $dI/dV$  spectra. The condition for the observation of vibrational modes is given by  $eV = \hbar\Omega$ , with  $\Omega$  the frequency of the vibrational mode,  $\hbar$  Planck's constant and  $eV$  the energy of the electron.

### 3.5 The Kondo effect

The resistance of metals is limited by defects, vacancies and impurities on one side and the nuclei motion on the other. As a metal is cooled down the motion of the nuclei gets smaller until it almost disappears at some temperature  $T$ . One would expect the resistance to be constant when cooling further down the metal as defects, vacancies and impurities are not temperature dependent.

In 1934 however de Haas, de Boer and van den Berg from the Kamerling Onnes Laboratory in Leiden discovered that gold had a resistance minimum at 3.7 K [112]. That implies that there is another scattering mechanism which gets dominant at low temperatures. It was not until 1964 that Sarachik *et al.* [113] made a relation between this newly discovered resistance at low temperatures and localized magnetic moments due to impurities in metals. In the same year Jun Kondo [114] published a theoretical description of this effect, which involved a scattering effect between the localized magnetic moment and the delocalized electron cloud of the metal.

The prerequisite for the observation of Kondo physics is the quantization of charge and energy. This can be achieved by the confinement of electrons in space. Therefore the Kondo effect can be observed on various systems, as long as the electrons are confined, such as in single atoms, single electron transistors and molecules. The Kondo effect was found in many different systems, e.g. Ce adatoms on a Ag(111) surface [115], single electron transistors (SET) [116], a Co ion connected by organic linkers to metal electrodes [24], single-molecule transistors [25] or C<sub>60</sub> molecules contacted by Au electrodes in a mechanical break junction (MBJ) [117]. The Kondo effect was also observed as the coexistence of local and non-local Kondo screening in a so-called Kondo lattice formed by O<sub>2</sub> molecules adsorbed along chains on a [Au(111)-1x2] surface [118].

The increase of the resistivity at low temperatures results from the interaction between a localized unpaired electron, e.g. in a molecule, with the delocalized electron cloud in metal electrodes. This means the Kondo effect results from an interaction between a single particle with many particles. The unpaired electron is characterized by a spin, this spin is screened by the delocalized electron cloud, i.e. a spin singlet state is formed ( $S = 0$ ). To screen the localized electron spin the delocalized electrons behave as a single quantum-mechanical object.

In Fig. 3.7 a double-barrier structure is depicted as it is observed in a metal-molecule-metal junction [116]. The charging or Coulomb energy  $U$  is the energy needed to add or

### 3 Theory of transport

remove one electron in a molecule.  $\Delta\epsilon$  is the energy difference between two molecular orbitals. This energy  $\Delta\epsilon$  increases the smaller the molecule is.  $\Gamma$  is the coupling strength of the molecular orbital in the barrier to the electrodes. This strength of the coupling is given by the width of the orbitals electronic state. The larger  $\Gamma$  is, the stronger the coupling between the orbital and the electrodes. When  $\Gamma \gg \Delta\epsilon$  the energy and charge quantization is lost as electrons can fluctuate between the molecule and the metal electrodes.

To observe the Kondo effect the energy  $k_B T_K$  must be smaller than the coupling  $\Gamma$ , with  $k_B$  the Boltzmann's constant and  $T_K$  the Kondo temperature. In order to measure the Kondo effect the energy difference  $\Delta\epsilon$  between two orbitals has to be large, as found e.g. in the  $\pi$ -conjugated molecules probed in the context of this thesis. In this way the coupling  $\Gamma$  can be large and thus the temperature at which the measurement takes place is accessible with a LT-STM. Later it will be shown that by lifting the molecule from the metal substrate the coupling  $\Gamma$  of the electronic state to the electrodes can be tuned. Further the energy of the lowest unoccupied molecular orbital (LUMO) can be tuned such, that the orbital is singly occupied at an energy  $\epsilon_0 = 0$  mV.

The electrons in a molecule occupy orbitals, with an occupancy of two electrons of opposite spin per orbital. In consequence the inner energy spacing of an orbital is given by the charging energy  $U$ . The energy spacing between two orbitals is given by the inner energy spacing and the energy difference between two orbitals  $U + \Delta\epsilon$ . When a molecular orbital at the Fermi energy is singly occupied, then an increase of the zero-bias differential conductance can be observed at low temperatures. This conductance increase results from the Kondo effect. The localized unpaired electron in the orbital is screened by the conducting electrons in the electrodes to form a spin singlet. This increases the density of states at the Fermi energy and thus the conductance. Hence the energies have to fulfill following criteria so that Kondo physics can be observed:

$$\frac{U}{\Gamma} \gg \epsilon_0 \quad (3.42)$$

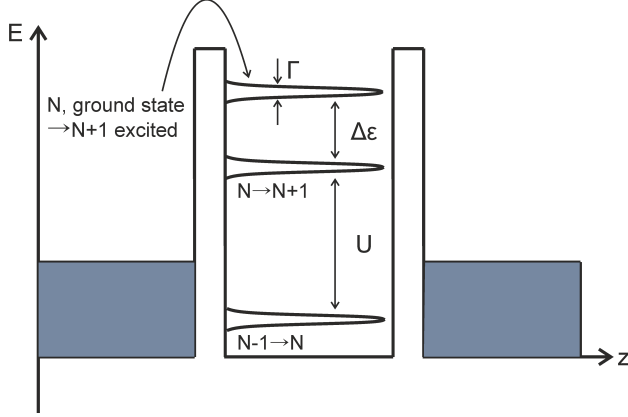


Figure 3.7: Energy diagram of a double tunneling barrier with a molecule in between the barriers. The bias voltage between the electrodes is zero. The Fermi energy is in the conductance minimum between two states of the same molecular orbital. The charging energy  $U$  is needed to add or remove one electron in a molecular orbital. To add an electron in the lowest excited state the energy  $U + \Delta\epsilon$  is needed. The width of a state  $\Gamma$  gives the coupling strength of the state to the electrodes. To observe the Kondo effect at low temperatures the following energy relation has to be given:  $U/\Gamma \gg \Delta\epsilon$  (after [116]).

### 3.6 Conclusions

In this chapter an overview about the theoretical concepts of charge transport through metal-molecule-metal junction was given. The discussion was started by introducing the Landauer formalism to describe ballistic transport. It was shown that the current is discrete and depends on the number of transverse modes. Then double-barrier tunneling, which is the transport observed in metal-molecule-metal junction, was described. Thereby the differences between coherent and incoherent tunneling in the resonant and non-resonant condition were worked out. The transport through the  $\pi$ -conjugated molecules studied in this thesis seems to be off-resonant coherent tunneling. Finally some physical observations of a molecule in a vacuum junction were introduced, such as the interaction between molecular vibrations and tunneling electrons and the Kondo effect.



## 4 Electronic structure of $\pi$ -conjugated molecules

### 4.1 Introduction

To obtain an understanding of the charge transport through a molecule it is of great importance to know its electronic structure. As soon as a molecule gets into contact with a metal surface, its electronic structure changes [32,35,36]. Therefore it is important to probe the density of states of each molecule-metal system before performing transport experiments. The density of states and the coupling strength (see chapter 3) between the molecule and the electrodes define the charge transport through the junction tip-molecule-substrate.

Four different molecules were probed on two different metals in this thesis, namely the four planar  $\pi$ -conjugated molecules NTCD (1,4,5,8-naphthalene-tetracarboxylic-dianhydride), PTCD, TTCD and QTCD (see Fig. 4.1) on Ag(111) and Au(111). These molecules were chosen as they represent a family of wires which allow a systematic study of the transport as a function of length, the end groups being identical (see chapter 1). It was not possible to prepare clean QTCD islands on Au(111) since the molecules were deposited unintentionally together with another, unknown type of particle which could not be separated from the QTCD molecules on Au(111). Hence the electronic structure of QTCD on Au(111) could not be probed (for more details see chapter 6). The electronic structure of the other seven systems are presented in this chapter. While making this investigation, a Kondo resonance was discovered for NTCD on Ag(111). This system was then studied in more depth, and the results of this study are discussed in the second part of this chapter.

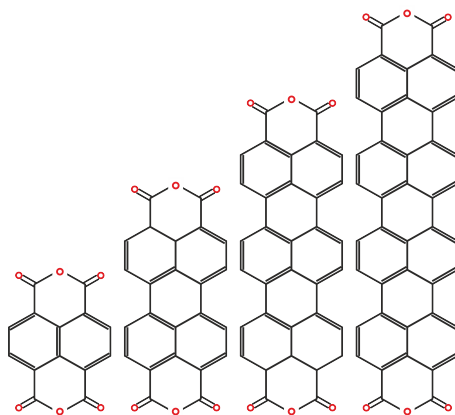


Figure 4.1: The structure models of the four planar  $\pi$ -conjugated molecules investigated. From left to right: NTCD (1,4,5,8-naphthalene-tetracarboxylic-dianhydride), PTCD, TTCD and QTCD. The molecules have a carbon backbone consisting of naphthalene units. On each short side the molecules are terminated by two carboxylic oxygen atoms and one anhydrate oxygen atom (red dots). The long sides are terminated by hydrogen atoms (not shown here).

## 4.2 Electronic structure of the seven systems

To measure the electronic structure the molecules were deposited on metal surfaces and then probed by scanning tunneling spectroscopy (STS). To be able to probe molecules inside a molecular island and at the same time have areas of clean metal to prepare the tip a submonolayer coverage was chosen. This is important as the tip should have no tip states when it is used to measure the differential conductance spectrum of a molecule (see section 2.3.2). This is realized by recording a scanning tunneling spectrum of the bare metal surface with the tip. If this spectrum exhibits the Shockley surface state as its most prominent feature, the tip is considered as suitable, because the measured electronic structure of the surface is barely influenced by tip states (see Fig. 2.7). If this is not the case, the tip has to be cleaned by dipping it slightly into the bare metal substrate and then check its electronic structure again (see chapter 2.2.5).

### 4.2.1 Electronic structure of the Ag(111) systems

In Fig. 4.2 the spectra measured for the four molecules on Ag(111) are shown. Each spectrum was taken with the tip placed above a molecule within a molecular island. The peaks in the range  $-500$  mV to  $0$  mV are the former lowest unoccupied molecular orbitals (LUMO) of the free molecules (see arrows in Fig. 4.2). Upon adsorption charge is transferred from the metallic substrate into the LUMO, this shifts the LUMO below the Fermi energy [66, 119, 120]. This is known for PTCDA and NTCDA, and we assume this to be true for TTCDA and QTCDA as well. The second feature, the onset of a sharp step in the bias voltage range  $300$  mV to  $700$  mV, is the signature of the mixing of the LUMO+1/LUMO+2 molecular orbitals with the depopulated Ag(111) surface state [66, 120].

In the case of NTCDA on Ag(111) two distinct types of molecules are observed within the molecular layer. Type A is characterized by a bright contrast in the STM image and has a sharp resonance at the Fermi level (shown in Fig. 4.2). Type B is characterized by a darker contrast in the STM image and has its LUMO at  $-30$  mV (no sharp feature at the Fermi level). This will be investigated in more detail later in this chapter.

PTCDA on Ag(111) is characterized by two types of molecules (A+B) in the submonolayer herringbone phase [39, 66, 67, 119–121]. This is the consequence of the different alignment of the two types with the Ag(111) substrate [121]. Type A molecules are

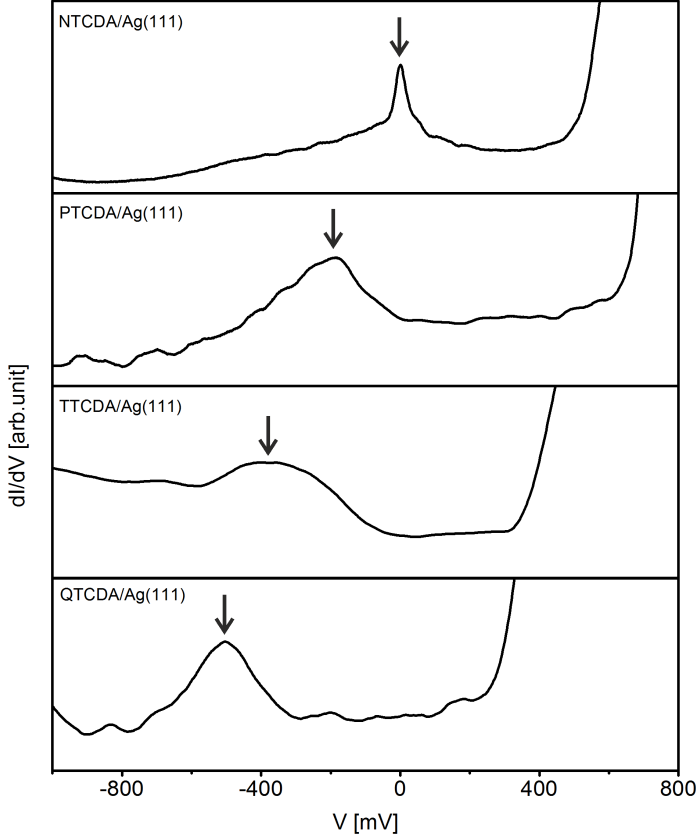


Figure 4.2: Scanning tunneling spectra (STS) of the four molecules investigated on Ag(111). The spectra were taken on molecules within the molecular island on a substrate with submonolayer coverage. In the range  $-500$  mV to  $0$  mV the former lowest unoccupied molecular orbitals (LUMO) are visible. The orbitals shift to negative values upon adsorption of the molecules with the metal surface. Due to the overlap of the wave functions a charge redistribution occurs [119]. The steps in the range  $300$  mV to  $700$  mV are signatures of the mixing of the LUMO+1/LUMO+2 molecular orbitals with the depopulated Ag(111) surface state [66, 120]. In the case of NTCDA the electronic structure of the bright molecule (type A) is shown. It is characterized by a sharp peak at the Fermi energy. This is the signature of a new transport channel opening (more details in section 4.4.1). For PTCDA on Ag(111) the electronic structure of type A is shown [39, 66, 67, 119–121].

perfectly aligned with the  $[10\bar{1}]$  Ag lattice direction and type B molecules are rotated by  $18 \pm 2^\circ$  within respect of the  $[0\bar{1}1]$  direction [121]. Both molecules have slightly different LUMO positions. In Fig. 4.2 the electronic structure of a type A molecule with its LUMO at  $-190$  mV is shown.

For a better representation the position of the LUMO was plotted against the length of the molecule (see Fig. 4.3). The longer a molecule is, the more its LUMO is shifted to larger binding energies. A linear relation between the LUMO position and the molecule length is observable, with a regression coefficient of  $\beta_{\text{Ag}(111)} = -41 \text{ mV}/\text{\AA}$ .

The behavior can be explained by the influence of the electron affinity ( $E_{\text{EA}}$ ) on the level alignment. To zero order, the level alignment at the molecule-metal interface can be predicted by vacuum level alignment. The larger the  $E_{\text{EA}}$  of the molecule, the larger the binding energy of this orbital after interface formation and charge transfer. The results of Fig. 4.3 therefore imply that  $E_{\text{EA}}$  rises in the sequence NTCDA to QTCDA. This is to be expected, since the smaller a molecule is the larger is the energy gap between the orbitals. In consequence the electron affinity  $E_{\text{EA}}$  of the filled lowest unoccupied molecular orbital increases the longer the molecule is. The same tendency is found when discussing the delocalization of the electrons. The longer the molecule is the smaller is the electron confinement. Hence the electron affinity  $E_{\text{EA}}$  is increasing the longer the molecule is.

Of course adsorption changes the work function  $\Phi_0$  of the surface, and this will additionally influence the energy level alignment. It is known that the work function  $\Phi_0$  of the bare Ag(111) surface is increased upon adsorption of PTCDA [122]. Two contributions influence the work function change  $\Delta\Phi$ :

**bend dipole  $D_{\text{bend}}$**  As the PTCDA is adsorbed on the Ag(111) surface its carboxylic oxygen bend towards the surface [123]. This creates a dipole moment which decreases the work function.

**bond dipole  $D_{\text{bond}}$**  Charge is redistributed between the Ag surface and PTCDA upon adsorption. In consequence a bond dipole  $D_{\text{bond}}$  is formed which increases the work function [122].

As the bond dipole is the more prominent contribution, a net work function increase is observed for the system PTCDA/Ag(111) [122]. We assume here that a similar situation prevails for the other molecules. Moreover it is known that the adsorption height of PTCDA is smaller than the one of NTCDA on Ag(111) [124]. Again, we extrapolate this

tendency to the adsorption height of TTCDA and QTCDA, i.e. the longer the molecule, the smaller is the adsorption height. This could be explained by a superlinear increase of the van der Waals interaction with the molecule size [125, 126]. As a consequence of a smaller adsorption height, a smaller bond dipole is formed (assuming the same charge transfer), and thus the work function increase is smaller the longer the molecule is. This is depicted in Fig. 4.4 (note that the energy scales are largely exaggerated for a better representation). The vacuum level  $E_{\text{vac}}$  and the work function  $\Phi_0$  refer to the bare Ag(111) surface, with the Fermi energy  $E_F$ . Upon adsorption of the molecules the work function is changed, resulting in the new work functions  $\Phi_N$ ,  $\Phi_P$ ,  $\Phi_T$  and  $\Phi_Q$ .

We can thus conclude that both the electron affinity and the adsorption induced work function change work in the same direction and together can explain the observed energy level alignments for NTCDA, PTCDA, TTCDA and QTCDA on Ag(111).

#### 4.2.2 Electronic structure of the Au(111) systems

In Fig. 4.5 the spectra measured for three molecules on Au(111) are presented. As for the spectra taken on Ag(111), these spectra were taken on molecules within a molecular island on a substrate with submonolayer coverage. The preparation of clean molecular islands of QTCDA on Au(111) was not possible, therefore no spectrum was measured for this system. The peaks in the bias voltage range 900 mV to 1500 mV stem from the LUMO of the molecules (see arrows in Fig. 4.5). In contrast to the case of Ag(111) the LUMO is not filled upon adsorption of the molecules on Au(111). This means that no charge transfer occurs as the molecule adsorbs on Au(111). It is a physisorption process, i.e. the molecules are bonding to the surface by van der Waals interaction only [43].

The LUMO is plotted against the length of the molecule in Fig. 4.6. Also here a linear dependence between the molecule length and the LUMO position is observable, with a regression coefficient of  $\beta_{\text{Au(111)}} = -79 \text{ mV}/\text{\AA}$ . As on Ag(111) the LUMO position moves to larger binding energies with increasing molecule length.

Since there is no charge transfer, there is no bond dipole. Also, no bending of the molecule is expected. Nevertheless, combination of energy affinities and work function changes can also explain the energy level alignments of NTCDA, PTCDA, TTCDA and QTCDA on Au(111). The argument based on  $E_{\text{EA}}$  applies in precisely the same way as on Ag(111). Regarding the work function change, it is known that even without the

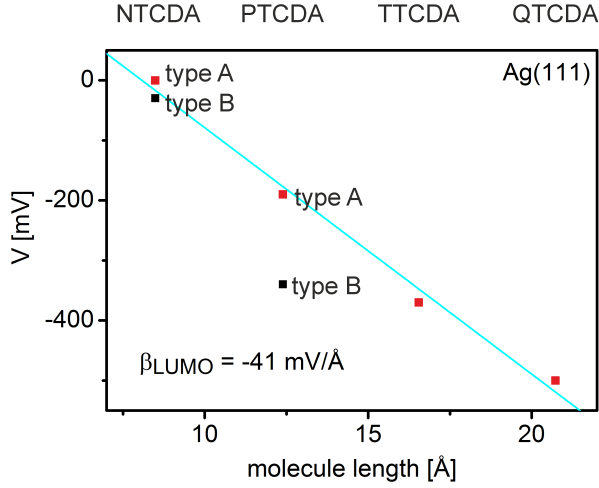


Figure 4.3: Position of the former lowest unoccupied molecular orbital (LUMO) plotted versus the length of the molecule in the case of Ag(111). For NTCDA and PTCDA both observed LUMO positions, as discussed in section 4.2.1, are plotted. With increasing molecule size the LUMO position shifts to larger binding energies. Considering only the LUMO positions marked in red a linear dependency between the LUMO position and the molecule length is observed. This trend can be explained by the work function increase upon deposition of the molecules on Ag(111) and the different electron affinities (see Fig. 4.4).

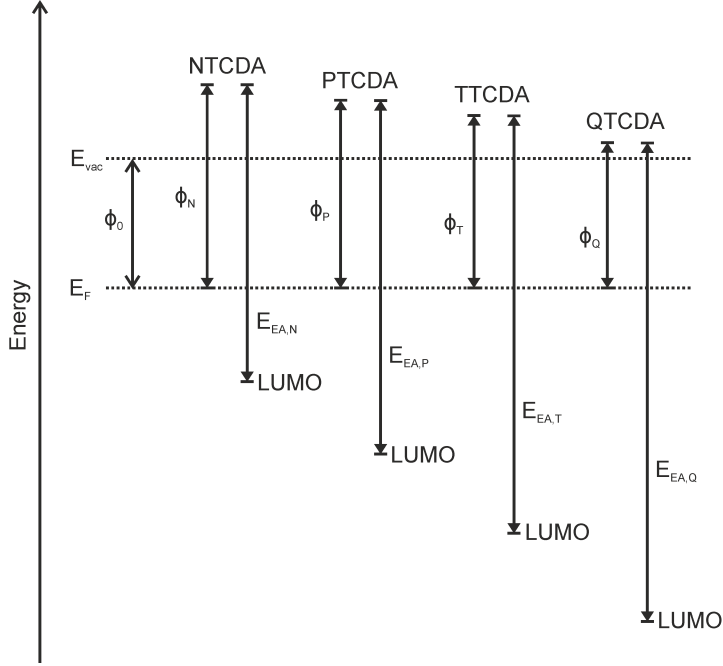


Figure 4.4: Sketch of the energy level shifts upon adsorption of molecules on Ag(111). For a better representation the energy scales are largely exaggerated. The vacuum level  $E_{vac}$  and the work function  $\Phi_0$  refer to the bare metal surface. As the molecules are adsorbed, the work function is changed, resulting in the new work functions  $\Phi_N$ ,  $\Phi_P$ ,  $\Phi_T$  and  $\Phi_Q$ . The new work functions decrease the longer the molecule is. This is a consequence of the smaller adsorption height the longer the molecules is. This in return results in a smaller bond dipole formation, which is responsible for the work function change. Additionally the electron affinity  $E_{EA}$  is increasing the longer the molecule is. These two effects together result in the observed LUMO position behavior.



presence of charge transfer the push-back effect influences the work function [127]. This push-back effect decreases the electron density at the surface and thus reduces the work function. This decrease of the electron density is larger the longer and hence closer to the surface the molecule is because for larger molecules physisorption interaction will be larger.

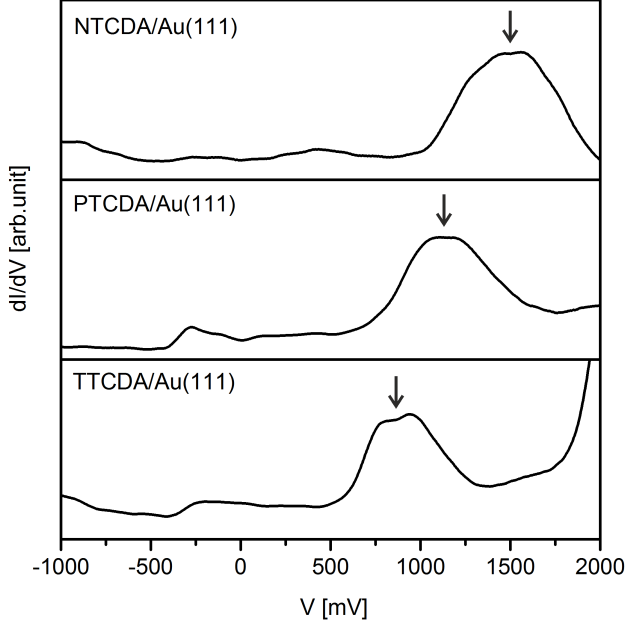


Figure 4.5: Scanning tunneling spectra (STS) of the three molecules investigated on Au(111). The spectra were taken on molecules within the molecular island. A clean preparation of QTCDA on Au(111) was not possible, therefore no spectrum was taken for this system. The peaks in the bias range 900 mV to 1500 mV are signatures of the LUMO of the molecules. In contrast to the case of Ag(111) the LUMO is at positive values, i.e. upon deposition the molecules physisorb on the metal, no charge transfer occurs.

In this section it was shown that the electronic structures of the molecules are significantly different depending on which metal they are deposited. On Ag(111) the LUMO is below the Fermi energy, i.e. charge is transferred from the metal to the molecular orbital, it

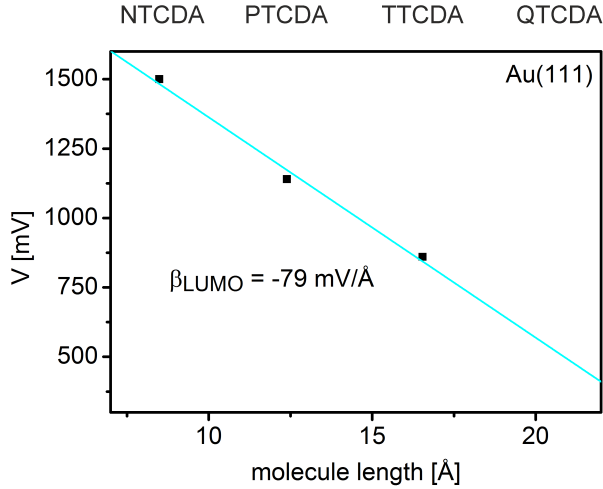


Figure 4.6: Position of the lowest unoccupied molecular orbital (LUMO) plotted versus the length of the molecule in the case of Au(111). For QTCDA no measurement was performed. As in the case of Ag(111) the LUMO is at larger binding energies the longer the molecule is. A linear dependency between the LUMO position and the molecule length is observed, with a regression coefficient twice as high as in the case of Ag(111). The decrease of the LUMO with increasing molecule length can be explained by the work function decrease upon deposition of the molecules on Au(111) due to the push-back effect and the increase of the electron affinity as was explained for Ag(111) (see Fig. 4.4).

is a chemisorption process. In the case of Au(111) the LUMO stays at positive values, i.e. the molecules physisorb, no charge transfer is observed. For both metals a linear dependency between the LUMO position and the size of the molecule was found. This was explained by the change of the work function upon adsorption of the molecules on the dependence of the electron affinity on the molecule size. In table 4.1 the positions of the LUMO for all systems are summarized.

substrate	molecule	$V_{LUMO}[\text{mV}]$
Ag(111)	NTCDA	0 -30
	PTCDA	-190 -340
	TTCDA	-370
	QTCDA	-500
Au(111)	NTCDA	1500
	PTCDA	1140
	TTCDA	860

Table 4.1: Position of the LUMO, obtained by scanning tunneling spectroscopy (STS), of the adsorbed molecules within the molecular layer. For NTCDA and PTCDA on Ag(111) the first value refers to the type A molecule, the second value to the type B molecule (see section 4.4.1) [39, 66, 67, 119–121].

### 4.3 Investigation of NTCDA on Ag(111)

The case of NTCDA adsorbed on Ag(111) is particular interesting as the spectrum shows a sharp peak at the Fermi energy. To get a better understanding of its origin the geometric and electronic properties of this system were investigated in more detail. By STM in UHV at low temperatures the system was imaged and by STS the electronic structure was probed.

In earlier investigations on the system PTCDA/Ag(111) in our group, it was found that a Kondo-like transport behavior is observable when the PTCDA is lifted up from the surface [39, 66]. This can be explained by a reversed chemisorption as the molecule is lifted. As the molecule-surface bond is reduced, the coupling  $\Gamma_s$  of the molecule to the surface is lowered. At the same time, as the molecule is lifted the energy of the molecular bonding orbital  $\epsilon_0$  is shifted towards the Fermi energy  $E_F$  (in accordance with

the tendency discussed in 4.2.1). The correlation energy  $U$ , i.e. the Coulomb repulsion between two electrons in one orbital (here: the LUMO), will also increase during the lifting process, because as the molecule is removed from the metal surface, the screening of the electron-electron interaction by the latter decreases. However with  $\approx 0.5$  eV to 1 eV this change is smaller than the change in  $\Gamma$ , such that the condition for the Kondo effect,

$$\frac{U}{\Gamma} \gg \epsilon_0 \quad (4.1)$$

is increasingly fulfilled. With the total coupling  $\Gamma = \Gamma_t + \Gamma_s$  of the molecule to the two electrodes tip and surface.

The physics of NTCDA on Ag(111) make the observation of the Kondo effect even more likely. Because of its smaller size the correlation energy  $U$  of NTCDA is larger than the correlation energy of PTCDA, also the coupling  $\Gamma$  to the metal electrodes is smaller as the molecule is adsorbed at a larger adsorption distance [124]. Considering this, the equation 4.1 is more likely to be fulfilled, even in the adsorbed state without lifting by the tip. From this we can expect to observe a Kondo resonance at the Fermi level in the spectrum of NTCDA on Ag(111).

Another motivation to investigate this system is the still ongoing debate about the geometric structure of NTCDA/Ag(111). Stahl *et al.* [92] proposed two superstructures based on their low-energy electron diffraction (LEED) and STM experiments. The so called “relaxed monolayer” is found at a low coverage of about 0.8 monolayers. The molecules are arranged in a slightly twisted brick-wall structure with two NTCDA molecules per unit cell. The “compressed monolayer” is found at a coverage of 0.9 monolayers. In this case the unit cell consists of four molecules which are arranged in a herringbone structure. In 2008 Kilian *et al.* [128] investigated the system with high-resolution spot profile analysis low-energy electron diffraction (SPA-LEED). In contrast to earlier results, they found three different superstructures named  $\alpha$ ,  $\alpha_2$  and  $\beta$ .  $\alpha$  and  $\beta$  are the structures introduced by Stahl *et al.* [92], but in contrast to them Kilian *et al.* [128] suggested  $\beta$  to be incommensurate, while the new structure  $\alpha_2$  was found to be uniaxially incommensurate. The forming of the three structures depends on the coverage (0.9 to 1.0 monolayers) and is reversible by variation of the coverage.

## 4.4 Geometric and electronic structure of NTCDA on Ag(111)

In this section details about the geometric and electronic structures of NTCDA on Ag(111) are discussed. The technical details of the sample preparation, i.e. the sputtering and annealing cycles and the deposition of the molecules are discussed in chapter 2.

Three different geometric structures were found when imaging NTCDA on Ag(111) (see Fig. 4.7). The different structures were obtained by variation of the sample temperature  $T_{\text{sample}}$  during the molecule deposition, the coverage of the sample and by variation of the annealing procedure after the deposition of molecules.

### 4.4.1 The commensurate phase

The most commonly observed structure was the commensurate phase, also known as the  $\alpha$  structure or relaxed monolayer in previous publications [92, 128]. This phase (see Fig. 4.7a) is obtained when a submonolayer is deposited with the sample at room temperature  $T_{\text{sample}} \approx 293$  K. The molecules form a brick-wall-like structure. The unit cell of this phase consists of two NTCDA molecules. By STM the following lattice parameters were derived for the unit cell:  $a = 15.1$  Å,  $b = 12.1$  Å and  $\alpha = 91^\circ$ . In comparison, Stahl *et al.* [92] found very similar parameters with LEED and STM:  $a = 15$  Å,  $b = 11.6$  Å and  $\alpha = 90^\circ$ . The STM image shows different brightnesses for the two molecules in the unit cell. This can be explained by different electronic structures of the two NTCDA molecules. Different electronic structures can be the result of different adsorption sites and in-plane arrangements and thus the consequence of different molecule-substrate and/or molecule-molecule interactions [120, 121].

To probe the electronic structure of the two different molecules, called type A and B as introduced earlier, STS measurements (see section 2.3) were performed. The electronic structure was probed on both types of molecules inside molecular islands, i.e. on molecules with four neighboring molecules. To probe the dependence of the electronic structure on molecule-substrate and molecule-molecule interactions, additionally NTCDA molecules with less than four neighbors were probed. For this purpose molecules were removed from an islands by vertical manipulation with the STM tip. By this a vacancy in the island was created (see Fig. 4.8), in which molecules in various different

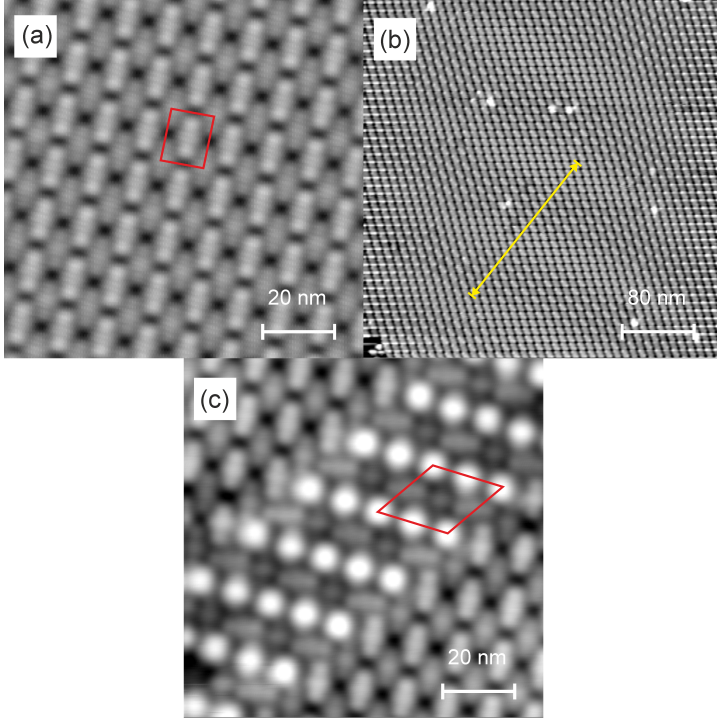


Figure 4.7: Constant current images of the three different phases observed for NTCDA on Ag(111). By the red parallelograms the unit cells as discussed in this section are depicted. (a) Commensurate phase with the unit cell containing two molecules. The lattice parameters are  $a = 15.1 \text{ \AA}$ ,  $b = 12.1 \text{ \AA}$  and  $\alpha = 91^\circ$ .  $100 \text{ \AA} \times 100 \text{ \AA}$ ,  $0.1 \text{ nA}$ ,  $50 \text{ mV}$ . (b) Incommensurate phase with a unit cell which is 2% smaller than the commensurate unit cell ( $a = 15.3 \text{ \AA}$ ,  $b = 11.8 \text{ \AA}$  and  $\alpha = 91^\circ$ ). The yellow line indicates the periodic length of the superimposed moiré-pattern of about 17 molecules.  $400 \text{ \AA} \times 400 \text{ \AA}$ ,  $50 \text{ pA}$ ,  $200 \text{ mV}$ . (c) Compressed phase, which has an unit cell of four molecules ( $a = 21.4 \text{ \AA}$ ,  $b = 21 \text{ \AA}$  and  $\alpha = 121^\circ$ ). Two molecules in this unit cell have the same electronic structure, i.e. three different electronic structures are observed in the unit cell. The compressed phase is observed in stripes which are incorporated into the commensurate phase.  $100 \text{ \AA} \times 100 \text{ \AA}$ ,  $0.1 \text{ nA}$ ,  $50 \text{ mV}$ .

configurations within respect of the neighboring molecules and the substrate were investigated.

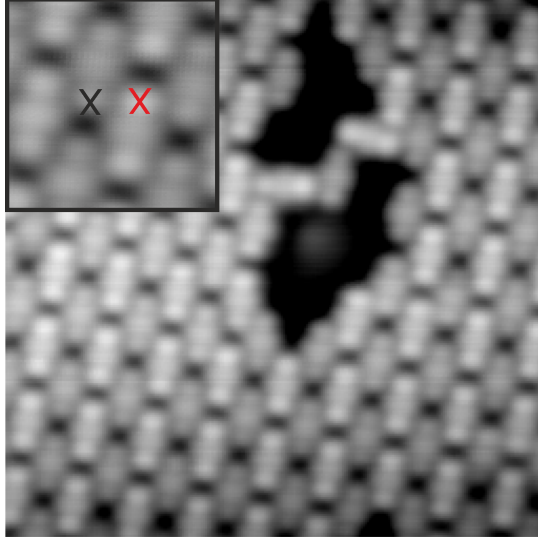


Figure 4.8: Constant current image of a commensurate phase of NTCDA on Ag(111) ( $100 \text{ \AA} \times 100 \text{ \AA}$ ,  $0.1 \text{ nA}$ ,  $50 \text{ mV}$ ). The STM tip was used to remove molecules from the molecular island to create a vacancy. In the inset the NTCDA layer is blown up ( $25 \text{ \AA} \times 25 \text{ \AA}$ ,  $0.1 \text{ nA}$ ,  $50 \text{ mV}$ ). By the crosses the position are indicated where the spectra of Fig. 4.9 were measured. The red cross shows the position where the STS on the type A molecule (showing a bright contrast) and the black cross where the STS on the type B molecule (dark contrast) was recorded.

In the inset of Fig. 4.8 the black and red cross indicate where the STS spectra were recorded. The bias voltage of the STM measurement in Fig. 4.8 was chosen such that the LUMO of NTCDA is imaged [129]. The STS spectra shown in Fig. 4.9 were taken on the outer lobe of the imaged molecule, i.e. in the region of the hydrogen atoms. The red spectrum shows the measurement with the tip above the type A molecule, the black spectrum the measurement above the type B molecule. For a better comparison of the two spectra the red spectrum was normalized such that the broad peaks associated to the LUMO in both spectra coincide. A remarkable difference between the two spectra is the peak at  $V = 0 \text{ mV}$  in the red spectrum (marked by K). This could be the signature of a Kondo resonance, as NTCDA likely fulfills the criteria for the observation of Kondo

physics, similar to the case of PTCA on Ag(111) [39]. The other features are present in both spectra. The peak of width 400 mV at  $V = -30$  mV is attributed to the LUMO of NTCDA. The large step at  $V = 500$  mV is the signature of the LUMO+1/LUMO+2, mixing with the depopulated Ag(111) surface state [66,120]. In the inset of Fig. 4.9 small side-peak pairs marked by S, which are symmetrical within respect of the Fermi energy, are visible. These side-peak pairs are signatures of molecular vibrations (see section 3.4) which will be discussed in more details in section 4.5.

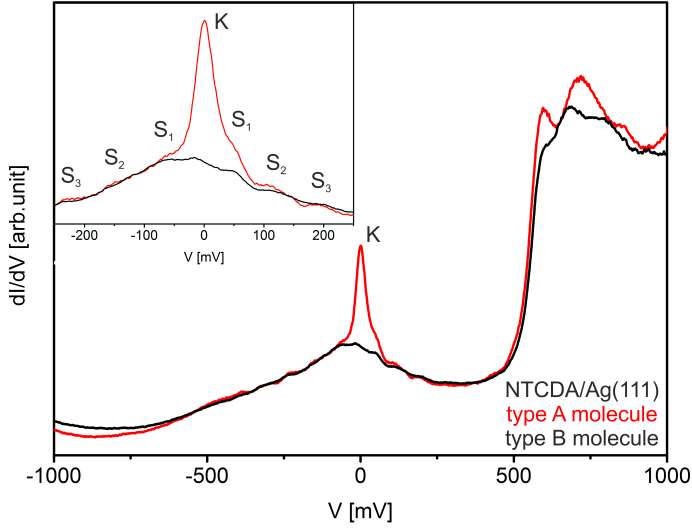


Figure 4.9: Scanning tunneling spectra recorded with the tip above the type A and B molecules. For a better comparison the red spectrum was normalized. A remarkable difference of the spectra is the peak at  $V = 0$  mV (marked by K). The peak of width 400 mV at  $V = -30$  mV is a feature of both spectra and can be associated to the LUMO of NTCDA. The step at  $V = 500$  mV is attributed to the LUMO+1/LUMO+2 and the depopulated surface state [66,120]. The side-peak pairs in the inset (marked by S) are signatures of molecular vibrations (see section 4.5).

All molecules of type A show the peak at  $V = 0$  mV. However, these molecules are not found everywhere. It seems that the appearance of a type A molecule depends crucially on its environment. In Fig. 4.8 three molecules form a bridge in the vacancy which was made



by removing single molecules with the STM tip. The two outer molecules in the bridge are rotated by  $90^\circ$  compared to the molecules in the layer, i.e. they have a different orientation within respect of the substrate. Yet, they show the peak at  $V = 0$  mV, characteristic for type A molecules. The molecule in the middle of the bridge is shifted from its row and shows no peak at  $V = 0$  mV, i.e. it is a molecule of type B discernible also from its dark appearance. The molecule left of the bridge is of type A showing the peak at  $V = 0$  mV, breaking the symmetry of alternating type A and B rows.

Next to this vacancy other structures were probed. It was found that all single isolated molecules observed so far, i.e. molecules with no neighbors, were of type B. The smallest molecular cluster containing both types of molecules was a diamond structure of four molecules (see Fig. 4.10). The occurrence of one of the two different electronic structure can be the result of three different mechanism:

- (1) The number of neighboring molecules and their position within respect of the probed molecule determine the electronic structure, i.e. the molecule-molecule interaction.
- (2) The adsorption site determines the electronic structure, i.e. the molecule-substrate interaction.
- (3) The electronic structure is defined by an interplay of the adsorption site and the orientation within respect of neighboring molecules, i.e. the molecule-molecule and molecule-substrate interaction.

From the observation made on the system NTCDA on Ag(111) it seems as the electronic structure of a molecule is determined by the adsorption site. This is in contrast to the observations made by Kilian *et al.* [130] on the system PTCDA on Ag(111) and Willenbockel *et al.* [131] for the system PTCDA on Ag(110), where the authors showed that the different electronic structures observed were the result of the intermolecular interaction.

#### 4.4.2 The incommensurate phase

The incommensurate phase (see Fig. 4.7b) is obtained when the molecules are deposited at submonolayer coverage. The unit cell of the incommensurate phase is about 2% smaller than the commensurate unit cell:  $a = 15.3 \text{ \AA}$ ,  $b = 11.8 \text{ \AA}$  and  $\alpha = 91^\circ$ . The molecules form a brick-wall-like structure, but with a superimposed moiré-pattern. In their study on NTCDA/Ag(111) with SPA-LEED, Kilian *et al.* [128] found an incommensurate phase  $\alpha_2$  which had a slightly smaller unit cell than the commensurate phase

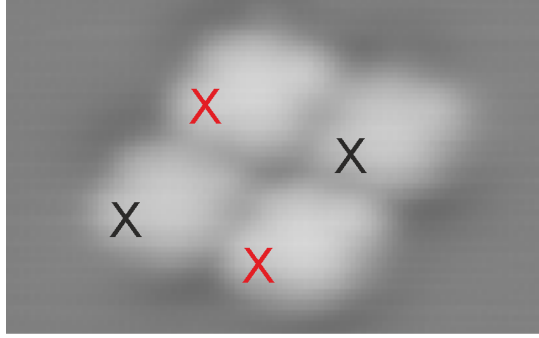


Figure 4.10: Constant current image of four NTCDA molecules forming a diamond. The upper and lower molecules are of type A, the left and right are of type B. This was confirmed by probing the molecules by STS, the red and black crosses indicate where the spectra were taken. The type A molecules show the characteristic peak at the Fermi energy, the type B molecules do not. This is the smallest molecule cluster found which shows both types of NTCDA molecules.  $40 \text{ \AA} \times 25 \text{ \AA}$ ,  $0.1 \text{ nA}$ ,  $600 \text{ mV}$ .

$\alpha$ . It is therefore assumed that the incommensurate phase observed here is the  $\alpha_2$  phase observed by Kilian *et al.* [128].

The periodic length of the superimposed moiré-pattern is about  $17 \pm 2$  molecules, indicated by the yellow line in Fig. 4.7b. There was no indication found that the formation of the commensurate or incommensurate structure depends on the exact submonolayer coverage, i.e. at similar coverages of about 0.2 monolayers both structures were observed. But it seems that the formation of an incommensurate or commensurate phase depends on the thermal energy given to the molecules. The formation of the incommensurate phase was observed for a deposition at  $T_{\text{sample}} \approx 273 \text{ K}$  and also after heating up a sample with a commensurate phase to  $T_{\text{sample}} \approx 350 \text{ K}$ . This seems contradictory as on the one hand the incommensurate phase is observed as the system gets less energy than in the case of the commensurate phase. On the other hand the commensurate phase transforms into an incommensurate phase by giving the system additional energy. Thus the question remains open which mechanism is responsible for the phase transformation.

As for the commensurate phase a distinction between type A and B molecules can be made for each molecule in the incommensurate phase. This was verified by taking a spectrum of each third molecule along a molecular row (see Fig. 4.11). Every spectrum

can be associated either to a type A (red spectra) or type B (black spectra) molecule. No intermediate types of molecules were found, either they show the Kondo resonance at  $V = 0$  mV or not. From this one can conclude that very subtle changes in the geometrical configuration lead to the formation of the Kondo resonance.

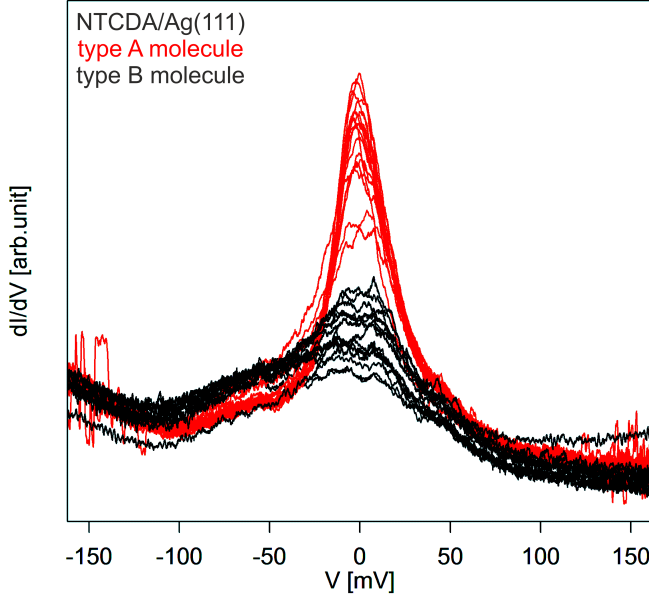


Figure 4.11: On every third molecule along a molecular row in the incommensurate phase a spectrum was taken. Every spectrum can be associated either to type A (red spectra) or type B (black spectra), i.e. no intermediate type of molecule is observed.

#### 4.4.3 The compressed phase

The compressed phase (see Fig. 4.7c) was observed after a deposition at  $T_{\text{sample}} \approx 273$  K and a coverage close to a full monolayer. This phase is incorporated into the commensurate brick-wall structure and forms stripes. It consists of an unit cell of four molecules. The observed stripes have a width of about  $40 \text{ \AA}$  and are not forming a regular pattern

inside the commensurate phase, but are randomly distributed. Two of the four molecules inside the compressed phase unit cell have the same electronic structure, i.e. three different electronic structures are found in the unit cell. The unit cell has the following dimensions:  $a = 21.4 \text{ \AA}$ ,  $b = 21 \text{ \AA}$  and  $\alpha = 121^\circ$ . A single NTCDA molecule in the unit cell of the compressed phase occupies in average an area of  $96 \text{ \AA}^2$ , in comparison in the commensurate unit cell a single molecule occupies in average an area of  $92 \text{ \AA}^2$ , i.e. a single NTCDA molecule has in average about 5% more space in the compressed phase compared to the commensurate phase.

The coordinates of the three different geometric phases found for NTCDA on Ag(111) are summarized in table 4.2. The commensurate and incommensurate phases were reported earlier by Kilian *et al.* [128] with very similar lattice parameters. It was shown that the molecules in these two phases can be separated into the two types A and B by their electronic structures. The striking feature of the type A molecules is a peak around the Fermi energy observed in STS. The origin of this peak is a Kondo resonance at the Fermi energy  $E_F$ . The nature of this resonance is studied further in section 4.5 to 4.7. The compressed phase with four molecules in the unit cell was found to show three different electronic structures, revealed by their different appearance in STM images.

Phase	a [ $\text{\AA}$ ]	b [ $\text{\AA}$ ]	$\alpha$ [ $^\circ$ ]	Area [ $\text{\AA}^2$ ]	No. of mol.	$\frac{\text{Area}}{\text{Molecule}}$ [ $\text{\AA}^2/\text{mol.}$ ]
commensurate	15.1	12.1	91	183	2	92
incommensurate	15.3	11.8	91	180	2	90
compressed	21.4	21	121	384	4	96

Table 4.2: The coordinates of the unit cells of the three NTCDA phases observed by STM on Ag(111).

## 4.5 Mapping the electronic structure within a molecule

In the previous section the differences in the scanning tunneling spectra of the two types of molecules were discussed. It was found that the type A molecule shows a peak at the Fermi energy, while the type B does not. The appearance of the resonance at the Fermi energy was related to the Kondo effect. However, only spectra taken with the tip at the position of the highest local density of states, i.e. in the region of the the hydrogen atoms, were considered. In this section spectra taken on various spots within one molecule are

discussed. By this the electronic structure of the molecule is mapped. Again, a distinction between type A and B molecules is found.

#### 4.5.1 Electronic structure within a type A molecule

In Fig. 4.12 four spectra recorded on a type A molecule are shown. Each spectrum was measured at another position of the tip above the molecule. The arrow in the inset of Fig. 4.12 indicates at which spatial position these spectra were taken. The first one (black spectrum) was recorded with the tip above the region of the hydrogen atoms of a type A molecule, i.e. at the position at which the spectra discussed in section 4.4 were measured. The last spectrum (red) was measured with the tip above the center of the molecule. The closer to the center of the molecule the spectra were taken, the smaller the central peak  $K$  at the Fermi energy becomes. But even the spectrum taken in the center of the type A molecule shows a small peak at  $K = 0$  mV. While the central peak  $K$  is attenuated, the side-peak pair  $S_1$  (and to a lesser extent also  $S_2$ ) gets more and more pronounced. The inner side-peak pair is found at  $S_1 = \pm 53 \pm 3$  mV, the outer at  $S_2 = \pm 118 \pm 6$  mV.

To determine the origin of the side-peaks in the spectra of NTCDA/Ag(111) and their dependence on the spatial position of the tip above the molecule, density functional theory (DFT) calculations were performed in collaboration with Prof. Dr. Michael Rohlfing from the University of Osnabrück for NTCDA. In Fig. 4.13a the local density of states (LDOS) of the LUMO of NTCDA is shown at two positions above the molecule. A few Å above the molecule center, the LUMO has no amplitude. This is the result of the annihilation of the positive and negative contributions to the LUMO in the region of the center. This can be seen in Fig. 4.14b in the cutting plane perpendicular to the molecular plane (solid line:  $\Psi(r) > 0$ , dashed line:  $\Psi(r) < 0$ ). This cutting plane is indicated by a line in Fig. 4.14a. In consequence of this annihilation elastic tunneling through the LUMO is only visible when the tip is placed above the region of the hydrogen atoms (Fig. 4.14a).

This picture stays the same for most of the molecular vibrations except of one. The displacement pattern of this particular vibration, with the phonon energy  $50 \pm 5$  meV, is depicted in Fig. 4.14d. The particularity of this mode is the different vertical displacement direction of the atoms in the regions where the LUMO is positive respectively negative (see Fig. 4.14c). This results in a considerable change of the LUMO LDOS above the molecule (see Fig. 4.13b), since the earlier described annihilation process of positive and

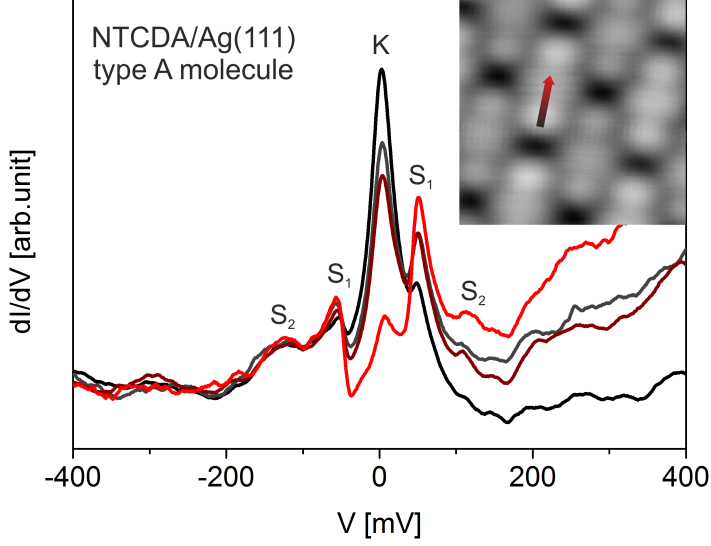


Figure 4.12: Scanning tunneling spectra of a type A molecule. The spectra were measured along a line above the molecule. The black spectrum was taken with the tip in the region of the hydrogen atoms, this corresponds to the red spectrum shown in Fig. 4.9. The red spectrum was measured with the tip above the center, the two other in between (see the arrow in inset with  $21 \text{ \AA} \times 21 \text{ \AA}$ ,  $0.1 \text{ nA}$ ,  $50 \text{ mV}$ ). The closer to the center the spectrum was recorded, the smaller the peak  $K$  at the Fermi energy gets. Contrary to that the side-peak pairs, which were introduced in the inset of Fig. 4.9, at  $S_1 = \pm 53 \pm 3 \text{ mV}$  and  $S_2 = \pm 118 \pm 6 \text{ mV}$  get more and more pronounced. The source of these side-peaks are replicas of the central Kondo peak by inelastic tunneling due to electron-vibration coupling [109, 132, 133].

negative LUMO contributions gets weaker. This can also be seen in Fig. 4.14b and c, whereas in Fig. 4.14b the positive and negative contributions are at same height, the positive contributions in Fig. 4.14c are enhanced in a direction perpendicular to the molecular plane.

The influence of the electron-vibration coupling on the differential conductance  $dI/dV$  was introduced in section 2.3.3. It was shown that the electron-vibration coupling changes the local density of state (LDOS)  $\rho(\vec{r}_0, \epsilon)$  and thus the differential conductance. This change of the LDOS  $\delta\rho$  has a discontinuous part  $\Delta\rho$ , which could be separated in an inelastic contribution  $\Delta\rho_{\text{inel}}$  and an elastic contribution  $\Delta\rho_{\text{el}}$ . The inelastic contribution was found to be responsible for a step-like increase of the differential conductance at the vibrational threshold  $\epsilon = \hbar\Omega$ , with the reduced Planck constant  $\hbar$  and the frequency of the vibrational mode  $\Omega$ .

In the present case the quasistatic limit has to be considered, as the energy of the vibrational mode is approaching zero ( $\hbar\Omega \rightarrow 0$ ). In this case the inelastic term of the LDOS change (see equation 2.14) can be written as [78]:

$$\Delta\rho_{\text{inel}}(\vec{r}_0) = \delta Q^2 \sum_{\mu} \left| \left\langle \frac{\delta\mu}{\delta Q} | \vec{r}_0 \right\rangle \right|^2 \delta(\epsilon_F - \epsilon_{\mu}) \quad (4.2)$$

where  $\Delta\rho_{\text{inel}}$  denotes the inelastic part of the discontinuity of the change of the local density of states  $\delta\rho(\vec{r}_0, \epsilon)$  at the vibrational threshold caused by the electron-vibration coupling.  $\delta Q^2 = \hbar/(2M\Omega)$  is the mean-square of the vibrational displacement  $Q$  with the mass  $M$  and the vibrations frequency  $\Omega$ .  $\epsilon_{\mu}$  is the energy of the one-electron state  $|\mu\rangle$  in the sample and  $\epsilon_F$  the Fermi energy, i.e. the energy of the electron in the tip.  $\left| \left\langle \frac{\delta\mu}{\delta Q} | \vec{r}_0 \right\rangle \right|^2$  is the change of the wavefunction at  $\vec{r}_0$ ,  $|\delta\Psi_{\mu}(\vec{r}_0)|^2$ , due to the excitation of a vibrational mode.

This equation explains why side peaks are strong in the center while the peak  $K$  is weak. However, in the spectra of NTCDA/Ag(111) (see Fig. 4.12) peaks are observed. These peaks can be explained by a replica of the Kondo peak at the vibrational threshold due to the opening of an inelastic channel. In Fig. 4.15 and 4.16 this scenario is depicted. The energy diagram in Fig. 4.15a shows the situation with no bias voltage applied ( $V = 0$  mV). Around the Fermi energy at the sample a Kondo state of width  $\Delta^K$  is shown which is half populated. This Kondo state increases the LDOS of the sample from  $n_s^0$  to  $n_s^K$ . The LDOS of the tip  $n_t$  is constant in the relevant energy interval. The tunneling current

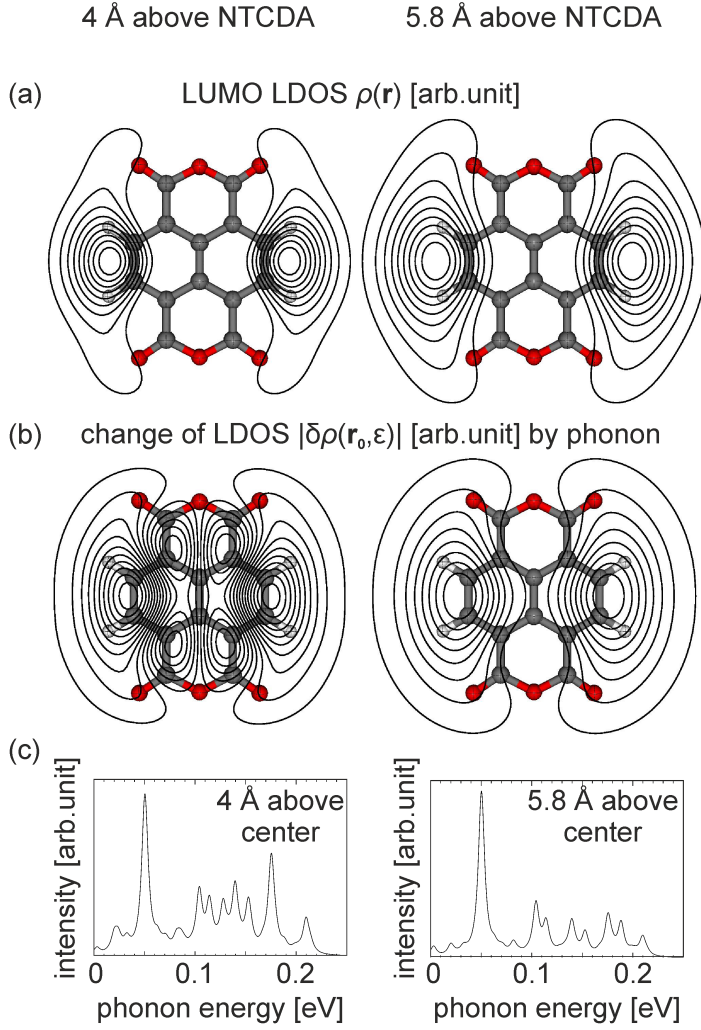


Figure 4.13: DFT calculation on a free NTCDA molecule. (a) Local density of states (LDOS)  $\rho(\vec{r})$  of the LUMO. No density is found at the center of the molecule. (b) Change of the density of states  $\delta\rho(\vec{r}_0, \epsilon)$  induced by the phonon of energy  $50 \pm 5$  meV. An enhancement of the LDOS at the center of the molecule is visible. (c) Inelastic tunneling intensity in dependence of the phonon energy above the center of the molecule.



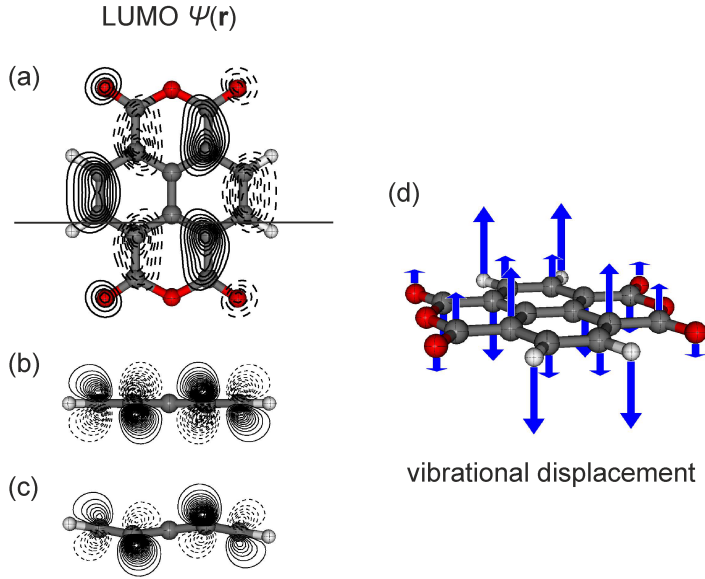


Figure 4.14: DFT calculation on a free NTCDA molecule. (a) The LUMO of the free NTCDA, with positive (solid line:  $\Psi(r) > 0$ ) and negative (dashed line:  $\Psi(r) < 0$ ) contributions. (b) Cutting plane through the molecular plane at the position indicated by the line in (a). (c) The same cutting plane as in (b) but for the molecule displaced by the phonon of energy  $50 \pm 5$  meV. (d) Vibrational displacement of the NTCDA molecule due to the phonon.

can than be calculated with  $I = n_t n_s eV$ , i.e. it only depends on the LDOS in the range of the applied bias.

When a bias voltage  $V$  is applied, the energy diagram looks as shown in Fig. 4.15b. To calculate the tunneling current the energy interval has to be split into two parts and the tunneling current has to be calculated for each parts separately. The two parts are depicted by the blue and red colors. For a bias voltage which is below half the width of the Kondo state ( $eV < \frac{\Delta^K}{2}$ ) the tunneling current is given by:

$$I = n_t n_s^K eV \quad (4.3)$$

As the voltage is increased above half the width of the Kondo state ( $eV \geq \frac{\Delta^K}{2}$ ) the tunneling current has to be separated into two cases. This can be expressed as follows:

$$I = \begin{cases} n_t n_s^K eV & \text{for } eV < \frac{\Delta^K}{2} \\ n_t n_s^0 (eV - \frac{\Delta^K}{2}) + n_t n_s^K \frac{\Delta^K}{2} & \text{for } eV \geq \frac{\Delta^K}{2} \end{cases} \quad (4.4)$$

with the LDOS of the sample at the Kondo state  $n_s^K$  and elsewhere  $n_s^0$ . This results in the current  $I$  and differential conductance  $dI/dV$  behavior as shown in Fig. 4.15c. With the tunneling junction symmetric with respect to the direction of the applied bias the peak around the Fermi energy in the differential conductance can be understood. This process is determined by elastic tunneling only. The change of the LDOS  $\delta\rho(\vec{r}_0, \epsilon)$  due to the vibrational displacement is proportional to the contribution of a phonon to the inelastic tunneling. This can be seen in Fig. 4.13b where the phonon with energy  $50 \pm 5$  meV changes the LDOS in the center of the molecule. The inelastic tunneling intensity as a function of the phonon energy with the tip placed above the center of the molecule is shown in Fig. 4.13c, with the peak at 50 meV of the vibration denoted earlier. Assuming that the energy of the phonon does not change significantly as the molecule is adsorbed on Ag(111) we can explain the behavior of the Kondo peak  $K$  and the side-peak pairs  $S_1$  and  $S_2$ . If the tip is placed above the region of the hydrogen atoms,  $K$  is the most prominent feature in the measured spectra. This is a result of the density of states of the LUMO being maximum in this region. The more the tip is moved to the center of the molecule, the more the intensity of  $K$  is attenuating as a consequence of the LUMO LDOS decreasing.

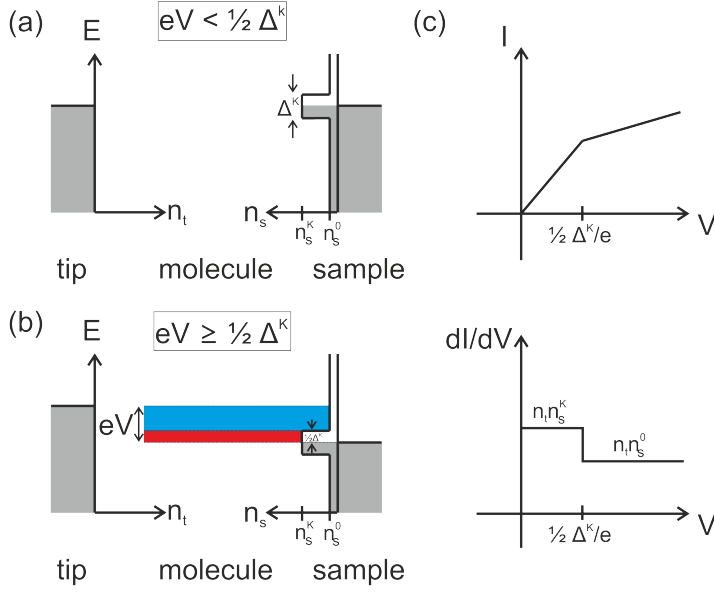


Figure 4.15: Elastic tunneling spectra of a sample with a sharp resonance of width  $\Delta^K$  at the Fermi level. (a) Energy diagram of the tunneling junction with a Kondo state of width  $\Delta^K$  at the Fermi level. For simplicity, the Kondo peak is represented by a square function. By  $n_t$  and  $n_s$  the LDOS of the tip and sample are denoted. (b) Energy diagram of the tunneling junction with an applied bias voltage  $V$ . The blue and red colors denote the different contributions to the tunneling current. (c) The resulting tunneling current  $I$  and differential conductance  $dI/dV$ .

The energy diagram shown in Fig. 4.16 depicts the situation where the bias voltage is equal and above the vibrational threshold ( $eV \geq \hbar\Omega$ ). As the bias voltage is equal with the vibrational threshold  $\hbar\Omega$ , the tunneling current can be separated into an elastic and inelastic contribution. The elastic contribution, i.e. when the electron loses no energy in the vacuum junction, is depicted by the dashed arrow in Fig. 4.16a (this corresponds to the energy diagram shown in Fig. 4.15b). Next to elastic tunneling inelastic tunneling is observed, i.e. the electron loses energy by emitting a vibron. This is depicted by the solid line arrow in Fig. 4.16a. In Fig. 4.16b the bias voltage is above the vibrational threshold. In this case the tunneling current is composed by several elastic and inelastic contributions. In the following the tunneling current above the threshold  $\hbar\Omega$  is described.

For  $\hbar\Omega \leq eV \leq \hbar\Omega + \frac{\Delta^k}{2}$  the total current  $I = I_{\text{el}} + I_{\text{inel}}$  is given as:

$$I = n_t n_s^k \frac{\Delta^k}{2} + n_t n_s^0 (eV - \frac{\Delta^k}{2}) + n_t n_s^k \eta eV \quad (4.5)$$

with the elastic current  $I_{\text{el}} = n_t n_s^k \frac{\Delta^k}{2} + n_t n_s^0 (eV - \frac{\Delta^k}{2})$  and the inelastic current  $I_{\text{inel}} = n_t n_s^k \eta eV$ . The resulting differential conductance is given as:

$$\frac{dI}{dV} = n_t n_s^0 e + n_t n_s^k \eta e = n_t e (n_s^0 + n_s^k \eta) \quad (4.6)$$

For  $\hbar\Omega + \frac{\Delta^k}{2} \leq eV$  the total current  $I = I_{\text{el}} + I_{\text{inel}}$  is given as:

$$I = n_t n_s^k \frac{\Delta^k}{2} + n_t n_s^0 (eV - \frac{\Delta^k}{2}) + n_t n_s^k \eta \frac{\Delta^k}{2} + n_t n_s^0 \eta (eV - \frac{\Delta^k}{2}) \quad (4.7)$$

with the elastic current  $I_{\text{el}} = n_t n_s^k \frac{\Delta^k}{2} + n_t n_s^0 (eV - \frac{\Delta^k}{2})$  and the inelastic current  $I_{\text{inel}} = n_t n_s^k \eta \frac{\Delta^k}{2} + n_t n_s^0 \eta (eV - \frac{\Delta^k}{2})$ . The resulting differential conductance is given as:

$$\frac{dI}{dV} = n_t n_s^0 e + n_t n_s^0 \eta e = n_t n_s^0 (1 + \eta) e \quad (4.8)$$

with the cross-section of the vibrational excitation  $\eta$ . In Fig. 4.16c the different tunneling current contributions and the differential conductance are represented schematically. With the symmetry with respect of the direction of the tunneling electrons given, the side-peaks at the vibrational threshold  $\hbar\Omega$  for negative and positive bias can be explained.

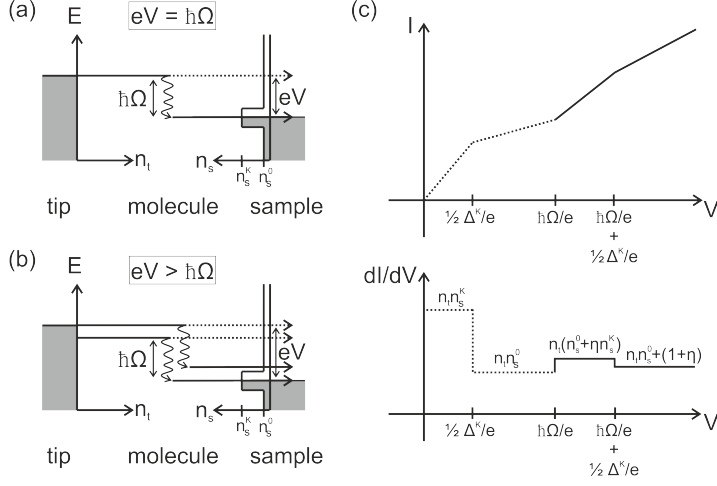


Figure 4.16: Kondo peak replica. (a) Energy diagram of the tunneling junction with a Kondo state of width  $\Delta^K$  which is half populated. The applied bias voltage is equal with the vibrational threshold ( $eV = \hbar\Omega$ ). Elastic and inelastic contributions to the tunneling current have to be considered. (b) Energy diagram in the case that the bias voltage is above the vibrational threshold ( $eV > \hbar\Omega + 0.5\Delta^K$ ). (c) The different contributions to the tunneling current and the corresponding differential conductance. As a result the Kondo peak around the Fermi energy and the side-peak at the vibrational threshold are visible.

Symmetrical peaks or steps in the differential conductance or its derivative were observed by various groups before [68, 109, 110, 132–135]. Fernandez-Torrente *et al.* [133] describe the observation of a Kondo resonance on TCNQ in a TTF-TCNQ (TTF: tetrathiafulvalene and TCNQ: tetracyanoquinodimethane) monolayer deposited on Au(111). The LUMO of TCNQ is singly occupied, thus an unpaired electron which interacts very weakly with the underlying metal substrate leads to an Kondo resonance. As for NTCDA on Ag(111) they observe side-peaks next to the Kondo resonance. They assign the side-peaks to the strong coupling of the unpaired electron with molecular vibrations.

#### 4.5.2 Electronic structure within a type B molecule

In Fig. 4.17 five STS spectra are shown that have been measured on different positions on a type B molecule. The position where the spectrum has been recorded is shown by the arrow in the inset of Fig. 4.17, starting with the tip above the region of the hydrogen atoms (black spectrum) moving to the center of the molecule (red spectrum). The spectra are characterized by a broad peak with a width of 400 mV with its center around  $-30$  mV. Within this broad peak a fine structure is observed. As for the type A molecule a central peak  $K$  at the Fermi energy and side-peak pairs around  $S_1 = \pm 52 \pm 2$  mV and  $S_2 = \pm 114 \pm 5$  mV are visible. Similar to the observation described before for the type A molecule, the ratio between central peak and side-peaks  $K/S$  is changing. Again the center peak  $K$  is attenuating while the side-peak pairs get more pronounced. Further an asymmetry is observed between the two side-peaks of pair  $S_1$ . While the side-peak at positive bias gets more and more pronounced as the tip is moved to the center of the molecule, the peak at negative bias shows a step-like behavior. This step-like evolution was not observed for the type A molecule or at least not as prominent as for the type B molecule.

The same description used before to understand the side-peaks in the case of type A molecules is valid for the type B molecule. The mechanism which leads to the formation of a step at  $-52$  mV is not yet understood. Interestingly the side-peaks are found at the same energies for both molecular types. This suggests that the different electronic structure of the two types of NTCDA molecule is not the consequence of different molecular mechanics.

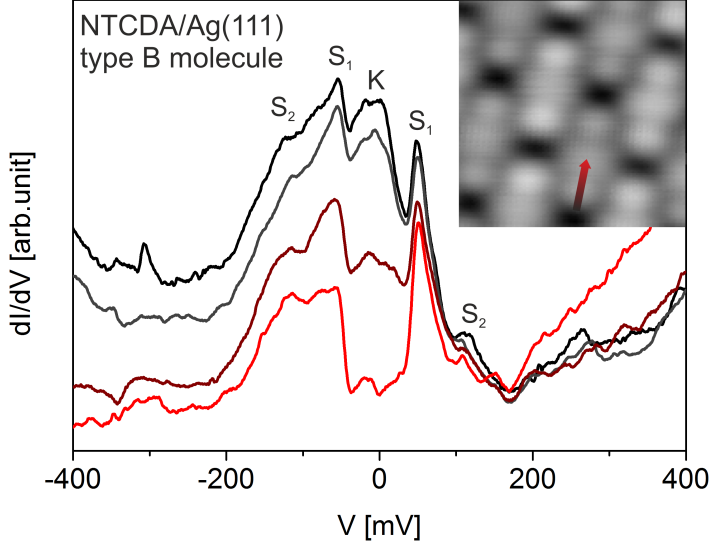


Figure 4.17: Scanning tunneling spectra on a type B molecule. The spectra were measured along a line above the molecule. The black spectrum was taken with the tip in the region of the hydrogen atoms, this corresponds to the black spectrum shown in Fig. 4.9. The side-peaks introduced in the inset of Fig. 4.9 are again visible. The red spectrum was measured with the tip above the center of the molecule, the two other in between (see arrow in the inset with  $21 \text{ \AA} \times 21 \text{ \AA}$ ,  $0.1 \text{ nA}$ ,  $50 \text{ mV}$ ). The closer to the center the spectrum was measured, the smaller the peak  $K$  at the Fermi energy gets. Contrary to that the side-peaks at  $S_1 = \pm 52 \pm 2 \text{ mV}$  and  $S_2 = \pm 114 \pm 5 \text{ mV}$  get more and more pronounced. The side-peaks are at the same position as for the type A molecule, i.e. that the molecular mechanics are the same and thus not responsible for the different electronic structure.

## 4.6 Temperature dependence of the Kondo resonance

As shown in section 4.4, the type A NTCDA molecule on Ag(111) is characterized by a prominent peak  $K$  at 0 mV in the scanning tunneling spectrum. Based on the knowledge of the system PTCDA/Ag(111) it was assumed that this peak is a signature of the Kondo effect [39]. To prove that the peak is really originating from the Kondo effect further analysis are done. A well known feature of the Kondo effect is that the peak at the Fermi energy, i.e. the Kondo resonance, is temperature dependent [25, 133, 134, 136–139]. Two different correlations are observed, first the dependence of the peak height  $K_{\text{height}}$  on the temperature and second the dependence of the peak full width at half maximum  $K_{\text{FWHM}}$  on the temperature. In principle it is possible to recover the Kondo temperature  $T_K$  from these physical quantities. This Kondo temperature  $T_K$  is the binding energy of the spin singlet formed between the localized, unpaired electron in the molecule and the delocalized electron cloud in the sample [137].

To probe these two correlations a series of temperature dependent STS measurements was performed in the temperature range  $T_{\text{sample}} = 12.5 \text{ K}$  to  $78 \text{ K}$ . Therefore the sample was heated up to a specific temperature and than given time to find its thermal equilibrium. After some time spectra were recorded with the tip placed above the region of the hydrogen atoms of a type A molecule, i.e. the region where the Kondo resonance was found to be most prominent (see section 4.5). To derive the temperature dependent correlations, i.e. peak height  $K_{\text{height}}$  and peak full width at half maximum  $K_{\text{FWHM}}$ , the raw data is fitted [133, 140, 141]. As the central Kondo peak  $K$  is accompanied by side-peak pairs  $S$  and underlay by a broad LUMO peak the fit is rather complex. Following terms are included in the fit:

- Lorentzian fit of the Kondo resonance  $K$
- Lorentzian fit of the side-peak pair  $S_1$
- steps at the position of the side-peak pair  $S_1$
- Gaussian fits of the LUMO and LUMO+1

It is assumed that the width of all three peaks (Kondo peak  $K$  and the two side-peaks  $S_1$ ) is the same. Next, the temperature broadening of the steps at the position of the side-peak pair is included into the fit. The further observed side-peak pairs  $S_2$  and  $S_3$  (see Fig. 4.9) are not included, as they were not always prominent enough in the raw data.



#### 4.6.1 Temperature dependence of the peak height

It was observed earlier that the peak height of the Kondo resonance is decreasing with increasing temperature [133, 139]. To probe this dependence 34 individual spectra were measured at different temperatures. In Fig. 4.18a one spectrum for each temperature measured is shown. To analyze the peak height dependence the individual spectra are normalized to the off-resonant background. In Fig. 4.18b the fits corresponding to the raw spectra are shown. In the insets the temperature dependence of the peak heights is shown. As can be seen the predicted temperature dependence of the peak height is not observed, i.e. the peak height is not decreasing with increasing sample temperature.

All reasons for not observing the predicted dependence are not fully clear. One reason is certainly that temperature dependent measurements with STM are characterized by large drifts between tip and sample and tip instabilities, making it difficult to record series of spectra under constant conditions.

#### 4.6.2 Temperature dependence of the peak width

It was found earlier that the full width at half maximum (FWHM) of the Kondo resonance is increasing with increasing sample temperature, i.e. the peak is broadening as the temperature goes up [24, 133, 137, 139, 142, 143]. In Fig. 4.19 the peak width is plotted versus the sample temperature. For each temperature several spectra were measured and then summarized. As can be seen the standard deviation is increasing with increasing temperature. This is a result of the measurement difficulties as discussed earlier. To determine the Kondo temperature  $T_K$  from the peak width a fitting function was derived from the Anderson impurity model [144, 145] by Nagaoka *et al.* [142]:

$$K_{\text{FWHM}} = \sqrt{(2\pi k_B T_{\text{sample}})^2 + 8(k_B T_K)^2} \quad (4.9)$$

with the Kondo temperature  $T_K$  and the Boltzmann constant  $k_B$ . In another publication by Ternes *et al.* [143] a similar function with slightly different pre-factors is given:

$$K_{\text{FWHM}} = \sqrt{(5.4k_B T_{\text{sample}})^2 + 4(k_B T_K)^2} \quad (4.10)$$

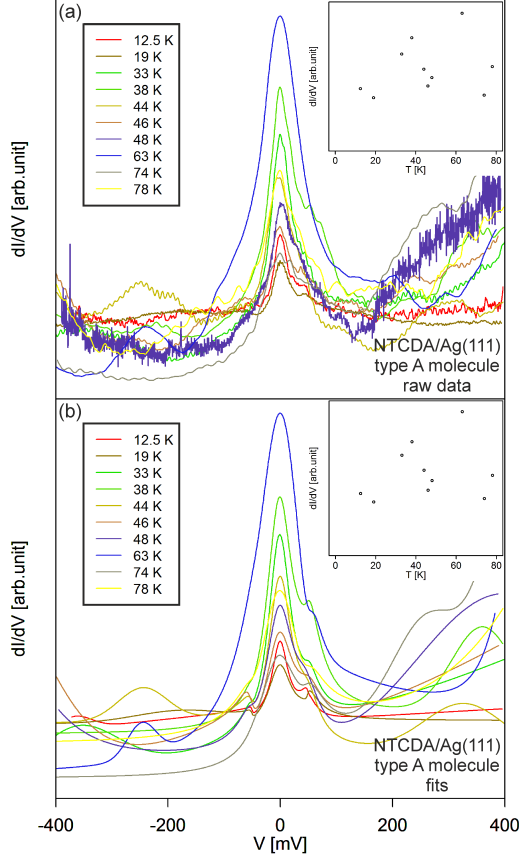


Figure 4.18: Temperature dependent STS on NTCDA on Ag(111). (a) The measured spectra, normalized to the off-resonant background to compare the peak heights. In the inset the peak height is plotted versus the sample temperature. (b) The corresponding fitted spectra. The predicted temperature dependence of the peak height as discussed in literature is not observed [139]. It is believed that the large drift and the tip changes during the measurements due to thermal instability and the fact that the measurements were performed on a new STM under construction, not running at optimum conditions, made it impossible to observe the predicted dependence.

Because of these different functions the function is again determined in our group by Taner Esat [146] based on the publication by Costi *et al.* [145]. Once more different pre-factors are obtained. This new function is much closer to the originally proposed function by Nagaoka *et al.* [142] compared to the one proposed by Ternes *et al.* [143]:

$$K_{\text{FWHM}} = \sqrt{(2\pi k_{\text{B}} T_{\text{sample}})^2 + 7.2(k_{\text{B}} T_{\text{K}})^2} \quad (4.11)$$

This new fit function is now applied to the full width at half maximum data derived from the 34 fits as shown in Fig. 4.18b, plus additional four spectra obtained at an even lower sample temperature ( $T_{\text{sample}} = 5$  K) on a different LT-STM/AFM. In Fig. 4.19 the full width at half maximum of the Kondo peak  $K_{\text{FWHM}}$  is plotted versus the sample temperature  $T_{\text{sample}}$ . The red line shows the fit with the resulting Kondo temperatures  $T_{\text{K}} = 236$  K. As predicted the full width half maximum of the peak is increasing with increasing sample temperature. Nevertheless the fitting function 4.11 does not fit the raw data satisfactorily. The same explanation as given earlier for the peak width can be used here to account for the bad fit, i.e. the difficulties to measure spectra at constant conditions when operating a STM at high temperature. Note that also the two other functions by Nagaoka *et al.* [142] and Ternes *et al.* [143] did not result in a satisfying fit.

It was found that the Kondo temperature of a system dramatically depends on the geometrical configuration of the magnetic impurity with respect to the electrode [147]. Most of the studies probe system with metal atoms as magnetic impurities [24, 25, 148–150]. The temperature found for NTCDA on Ag(111) can be compared to studies on organic molecules. An organic molecule which is probed by several groups is the fullerene. Scheer *et al.* [139] contacted  $C_{60}$  by aluminum electrodes and found Kondo temperatures in the range 35 K to 160 K, Yu *et al.* [134] probed the same molecule contacted by Ti/Au electrodes and reported about Kondo temperatures  $T_{\text{K}} > 100$  K. The earlier mentioned study from Fernandez-Torrente *et al.* [133] found a Kondo temperature of 26 K for the organic molecules TCNQ/TTF on Au(111).

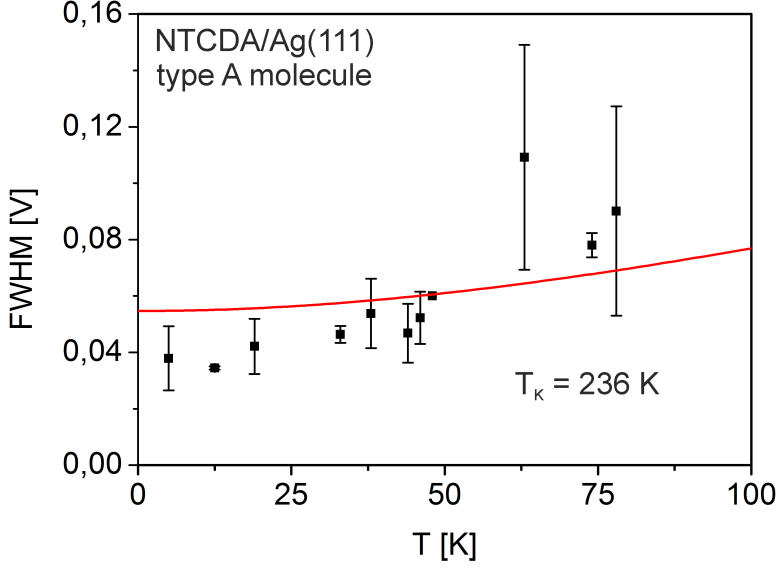


Figure 4.19: Full width at half maximum  $K_{\text{FWHM}}$  of the Kondo resonance versus the sample temperature  $T_{\text{sample}}$ .  $K_{\text{FWHM}}$  was determined by fitting the 34 measured scanning tunneling spectra as shown in Fig. 4.18, plus four additional spectra obtained at  $T_{\text{sample}} = 5 \text{ K}$ . The red line shows the fitting with function 4.11, with the corresponding Kondo temperatures  $T_K = 236 \text{ K}$ . The fit is not satisfying which might be a consequence of the experimental difficulties discussed earlier.

## 4.7 Differential conductance map of NTCDA on Ag(111)

In section 4.4 and 4.5 it was shown that NTCDA exists on Ag(111) in two configuration, distinguished by a brighter or darker contrast in the STM image. The type A molecule (brighter contrast) is characterized by a Kondo resonance in the STS while the spectrum of the type B molecule (darker contrast) shows only a small Kondo resonance signature. In PTCDA it was possible to induce the Kondo effect by pulling the molecule, i.e. by decreasing the coupling to the substrate. It can now be speculated that also the coupling of the type B NTCDA molecule can be tuned such, that the Kondo effect is observed. Therefore it is now of interest to know how the transport depends on the geometrical molecule-substrate configuration. Therefore differential conductance maps as described by Toher *et al.* [40] were recorded.

A molecule at the edge of a molecular island was contacted by the STM tip at one of the carboxylic oxygen and lifted up and lowered down 50 times. Each manipulation cycle was performed with another fixed bias voltage. The probed bias range was  $-100$  mV to  $100$  mV, i.e. the first manipulation was performed with a bias voltage of  $-100$  mV, the second with  $-96$  mV et cetera. The molecule-substrate bond was not ruptured completely during the lifting. This made it possible to have a very stable and reproducible junction geometry for each of the 50 lifting. The differential conductance  $dI/dV$  was measured with a lock-in amplifier with a modulation amplitude of  $V = 4$  mV and a frequency of  $f = 1333$  Hz.

The pattern of type A and B molecules as described in section 4.4 continues throughout the whole molecular island in the commensurate phase. Even the molecules at the edge show the alternating contrast. This made it possible to contact both types of molecules, lift them and measure the transport through them. Only molecules at the edge of an island could be manipulated in the way just described. When such an experiment is performed on a molecule in the layer then typically more than one molecule was contacted during the manipulation. Single molecules could not be probed, as they show no distinction between type A and type B molecules.

To compare the conductance map with the electronic structure of the NTCDA molecule in the equilibrium position it is of importance to know the absolute tip height during the manipulation. In general it is difficult to estimate the absolute tip-sample distance. From the exponential decay of the tunneling current  $I$  with respect to the tip-surface distance  $z$  in principle one could calculate the absolute distance. The tunneling current is given by:

$$I = I_0 \exp(-2kz) \quad (4.12)$$

with the decay constant  $k$ :

$$k = \frac{\sqrt{2m\phi}}{\hbar} \quad (4.13)$$

which depends on the work function of the tip and the sample:

$$\phi = \frac{\phi_{\text{tip}} + \phi_{\text{sample}}}{2} \quad (4.14)$$

As we do not know the work function of the tip, the absolute tip-surface distance has to be derived from geometrical assumptions.

Toher *et al.* [40] calibrated the absolute tip height by stabilizing the tip above the center of a PTCDA at a setpoint of  $V = 340$  mV and  $I = 0.1$  nA. Then the tip was moved towards the molecule until contact which was observed by a deviation from the exponential approach curve. No jump into contact was observed as the tip was approached above the carbon backbone. The height was then calculated using the following equation:

$$z_{\text{setpoint}} = h_{\text{PTCDA}} + r_{\text{vdW}}^{\text{carbon}} + r_{\text{vdW}}^{\text{silver}} + \Delta z \quad (4.15)$$

where  $h_{\text{PTCDA}}$  is the height of PTCDA plane within respect of the outermost lattice plane of Ag(111),  $r_{\text{vdW}}^{\text{carbon}}$  and  $r_{\text{vdW}}^{\text{silver}}$  are the van der Waals radii of the carbon and silver atoms and  $\Delta z$  is the distance between the setpoint and the PTCDA plane as measured by moving the tip into the molecule. This approach could not be realized for the NTCDA experiments, as no measurement of the distance  $\Delta z$  was performed. Therefore another approach is used. With the following equation the absolute tip-surface distance at which the tip and the molecule are in contact, i.e. where the molecule is in an equilibrium position when contacted by the tip can be determined:

$$z_{\text{setpoint}} = h_{\text{ox}} + d_{\text{t-ox}} \quad (4.16)$$

with the distance between the outermost Ag(111) lattice plane and the carboxylic oxygen  $h_{\text{ox}}$  of NTCDa in the equilibrium position and  $d_{\text{t-ox}}$ , the bonding distance between the tip apex atom and the carboxylic oxygen. The former value ( $h_{\text{ox}} = 2.747 \text{ \AA}$ ) was measured by Stadler *et al.* [124] by normal incidence x-ray standing wave (NIXSW), the latter ( $d_{\text{t-ox}} = 2.16 \text{ \AA}$ ) was calculated by Toher *et al.* [40] with DFT for PTCDa. With this a tip-surface distance of  $z_{\text{setpoint}} \approx 5 \text{ \AA}$  is determined (see Fig. 4.20c). To compare this with the tip-surface distances recorded during the manipulation, the height of the tip in the stabilization point ( $I = 1 \times 10^{-10} \text{ A}$  and  $U = 0.05 \text{ V}$ ) has to be known. This height was measured by crashing the tip into the bare Ag(111) surface, the contact between tip and surface was identified by a jump in the measured tunneling current. It was found that the tip is about  $9 \text{ \AA}$  above the surface in the stabilization point (see Fig. 4.20a). With this assumption the relative tip-surface distance of  $4 \text{ \AA}$  is identified as the equilibrium position of the molecule. This distance is sketched by a red line in Fig. 4.21 and 4.22.

In Fig. 4.21 the differential conductance map of a type A molecule is shown. The z-scale is plotted relative to the stabilization point ( $z = 0 \text{ \AA}$ ), which was defined with  $I = 1 \times 10^{-10} \text{ A}$  and  $V = 50 \text{ mV}$  above the clean Ag(111) substrate. The tip is moved down from this stabilization point, making contact to the molecule and then lifting the molecule up and lowering it down in the z-interval  $[5 \text{ \AA}, 1 \text{ \AA}]$ , with  $z = 5 \text{ \AA}$  being the closest the tip approaches to the substrate. The gray scale represents the differential conductance with white being the largest conductance. As there are no discontinuities in the map it must be assumed that the tip made contact during the first cycle and kept the contact until the end of the manipulation.

When looking at cuts through the map at constant height one can see the following evolution: When the tip is at  $z = 5 \text{ \AA}$  there is a broad peak in the differential conductance at negative voltages, this peak can be attributed to the filled LUMO. The further the molecule is lifted by the tip the more this peak shifts towards the Fermi energy ( $V = 0 \text{ mV}$ ), i.e. the LUMO gets depopulated. The peak gets sharper until it gets pinned at the Fermi energy at around  $4 \text{ \AA}$ . At this z-scale the molecule is in its equilibrium position, i.e. to the left of the red line in Fig. 4.21 the molecule is pushed towards the surface and to the right of the red line the molecule is lifted relative to the equilibrium position. This resonance at the Fermi energy is the signature of the Kondo effect as discussed earlier. As the molecule is lifted further away from the substrate, the peak attenuates until it vanishes completely. This happens as the molecular orbital at the Fermi energy gets depopulated and thus the localized electron forming the spin singlet with the delocalized

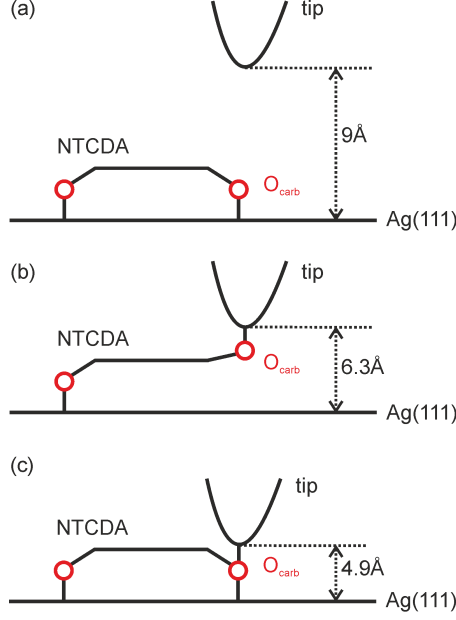


Figure 4.20: Absolute tip height derived from geometrical assumptions. (a) The tip is about 9 Å above the sample surface in the stabilization point, as was measured by crashing the tip into the surface. (b) When tip and molecule are in contact the tip is about 6.3 Å above the sample surface. This can be derived from the measurement of the distance between carboxylic oxygen and sample surface ( $h_{ox} = 2.747$  Å [124]), the distance the oxygen atom flips up when the tip-molecule contact is formed ( $d_{flip} = 1.36$  Å [40]) and the bonding distance between the tip apex atom and the carboxylic oxygen ( $d_{t-ox} = 2.16$  Å [40]). (c) By pushing the oxygen atom further down until the molecule is in an equilibrium position the tip is about  $z_{setpoint} \approx 4.9$  Å above the sample surface ( $h_{ox} + d_{t-ox}$ ). With this a relative tip-surface distance of 4 Å is given at which the molecule is in an equilibrium position (see red line in Fig. 4.21 and 4.22).



electron cloud of the sample disappears.

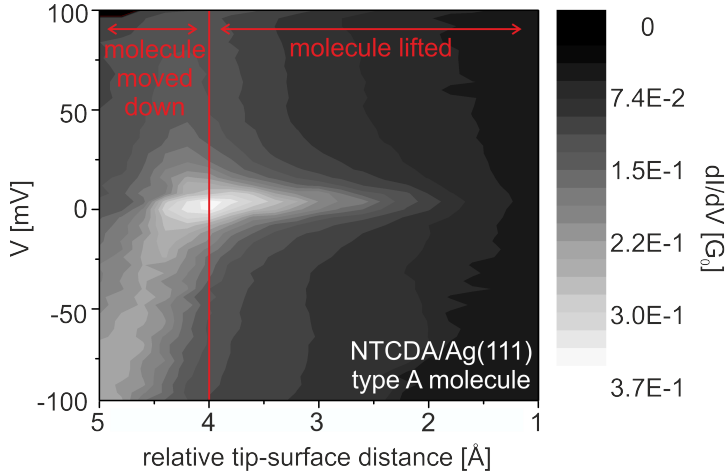


Figure 4.21: Differential conductance map of a type A molecule. The z-scale is relative to the stabilization point above Ag(111) with 5 Å the closest position towards the surface. As the molecule is lifted up, a peak in the differential conductance shifts from negative voltages to the Fermi energy. This peak is the filled LUMO which gets depopulated. At the same time the LUMO gets sharper until it gets pinned to the Fermi energy in the molecules equilibrium position at  $z = 4$  Å. This resonance at the Fermi energy is a signature of the Kondo effect. As the molecule is lifted further, the peak vanishes.

Fig. 4.22 shows the differential conductance map of a type B NTCD molecule. This measurement was done immediately after the differential conductance map of the type A NTCD molecule shown in Fig. 4.21 was recorded. No tip preparation was done in between the manipulations and the STM image has not changed, thus it can be assumed that both manipulations were done with tips of exactly the same geometry. The stabilization point was chosen in the same manner as for the conductance map of the type A molecule, i.e. the same z-scale was used for both maps.

Both maps show a very similar conductance behavior. In contrast, the features in the differential conductance map of the type B molecule are shifted by 1 Å with respect to the differential conductance map of the type A molecule. For the tip position  $z = 5$  Å the peak is at a more negative voltage in the case of the type B molecule compared to the type A molecule. At the molecules equilibrium position at  $z = 4$  Å the peak is still at negative voltage and only gets pinned at 3 Å to the Fermi energy ( $V = 0$  mV). After

this the peak vanishes as the molecule is lifted further away from the substrate, as seen for the type A molecule.

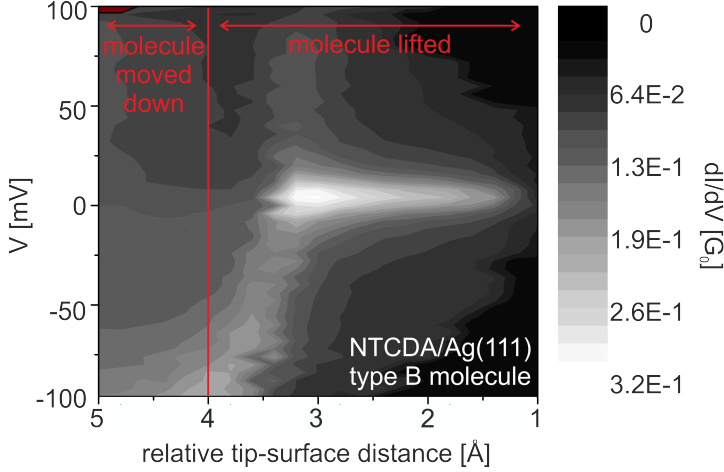


Figure 4.22: Differential conductance map of a type B molecule. The conductance map shows the same features as the conductance map of the type A molecule, but shifted by 1 Å. This means that in the molecules equilibrium position (red line) no peak at the Fermi energy ( $V = 0$  mV) is observed. Only as the molecule is lifted up to  $z \approx 3$  Å a peak in the differential conductance pinned to the Fermi energy appears.

To get a better understanding of the mechanism responsible for the different behavior of the type A and B molecule, the maps can be further analyzed by comparing them to scanning tunneling spectra. In Fig. 4.23 the spectra shown previously in Fig. 4.9 are plotted together with the spectra taken from the conductance maps at the molecules equilibrium position at the relative tip-surface distance  $z = 4$  Å. Note that this represents two different scenarios. While measuring the scanning tunneling spectra, the tip is not in contact with the molecule, the spectra from the conductance maps were measured with the tip contacting the molecule via one of the carboxylic oxygen atoms. Further the scanning tunneling spectra were measured on molecules inside the layer and the conductance maps on molecules at the border of an island.

While in the case of the type A molecule both spectra are very similar, the type B spectra show a significant difference. In both cases the conductance of the contact tunneling ( $dI/dV$  map) is about four magnitudes higher than the conductance of the vacuum tunneling (STS). In the case of type A molecules both spectra show the Kondo peak

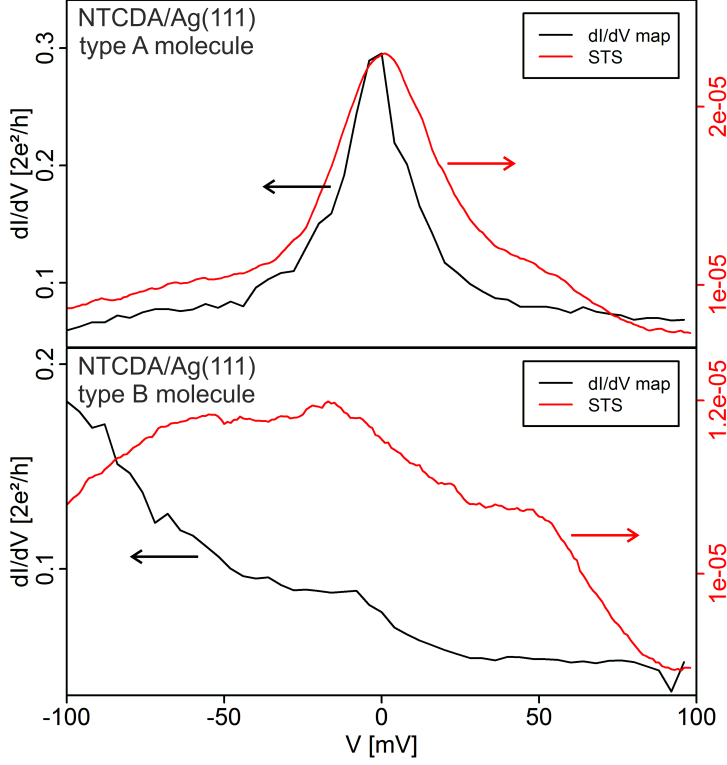


Figure 4.23: Scanning tunneling spectra shown in Fig. 4.9 versus the spectra taken from the conductance maps at the molecules equilibrium position at  $z = 4 \text{ \AA}$ . The conductance of the vacuum tunneling measurement (STS) is about four orders of magnitude lower than the conductance of the contact tunneling measurement ( $dI/dV$  map). The spectra of the type A molecule show both the peak at the Fermi level. The STS peak is broader, i.e. the lifetime of the electron is shorter in the vacuum tunneling case. The LUMO peak of the type B molecule is at higher binding energies in the spectrum taken from the conductance map, i.e. the LUMO gets more populated as the molecule is contacted by the tip. The same tendency was observed earlier for the system PTCDA/Ag(111) [67].

at the Fermi level. The peak width measured by STS is larger than the peak width measured while contacting the molecule. In the case of type B molecules, the LUMO as measured by STS is closer to the Fermi energy than the LUMO measured when contacting the molecule, i.e. the LUMO is at higher binding energies  $\epsilon_0$  when the molecule is contacted. This increase of  $\epsilon_0$  results in a decrease of the Kondo temperature  $T_K$  which is proportional to the width the Kondo resonance. This is in consistency with the observations made in Fig. 4.23 for both types of molecules.

The contact of the tip to one of the carboxylic oxygen of the molecule shifts the LUMO to higher binding energies, i.e. the LUMO gets more populated. In consequence the NTCDA type B molecule has to be lifted from the surface to depopulate the LUMO and subsequently create a Kondo state. As the lower measuring limit of the  $dI/dV$  map was at  $-100$  mV the shift of the LUMO can only be estimated to about 100 mV. This result can be compared to studies of the system PTCDA/Ag(111) [67] where a similar comparison of spectra was performed. Also there a shift of about 100 mV of the LUMO was observed as the molecule is contacted by the tip of a STM.

## 4.8 Conclusions

In the first part of this chapter the electronic structure of seven systems presented in this thesis were probed. It was found that in the case of Ag(111) the LUMO shifts to negative values upon adsorption of the molecule on the metal. Furthermore it was found that the position of the LUMO and the size of the molecules show a linear dependence. This was explained by a work function increase upon molecule adsorption. This increase is found to be larger the smaller the molecule is, as a consequence of the bond dipole being larger the smaller the molecules is. Further it was argued that the electron affinity is increasing the longer the molecule is. These two effects create the observed dependency of the LUMO position on the molecules length. In the case of Au(111) the LUMO is not filled upon adsorption of the molecules, i.e. no charge transfer is observed. The molecules are physisorbed on Au(111), only van der Waals interaction is observed between the molecules and the Au(111) substrate. Also here a linear dependence between LUMO position and molecule size was found. This can be explained in a similar picture as for the Ag(111) case by the change of the work function and the electron affinity upon adsorption.

The system NTCDA on Ag(111) was investigated more profoundly as a particular elec-

#### 4 Electronic structure of $\pi$ -conjugated molecules

tronic structure was observed. Three different geometric phases were found during the study, two of which were introduced in earlier publications. Their appearance upon the deposition parameters was discussed and the unit cells were measured. It was found that the molecular layer is composed of two different types of NTCDA molecules. Every second molecule shows an electronic signature which was attributed to the Kondo effect. A peak in the differential conductance at the Fermi energy and vibrational signatures were found in the spectroscopic data. By measuring spectra at different positions above the molecule and by performing DFT calculation the spatial variance of the electronic structure and the influence of vibrations on the inelastic tunneling was explained. Measuring temperature dependent STS the Kondo temperature of the Kondo resonance at the Fermi energy was determined to  $T_K = 236\text{ K}$  by fitting the FWHM of the Kondo resonance. However, due to experimental difficulties this fit was not satisfying. The requirement for the appearance of the Kondo resonance was investigated and it was found that it critically depends on the adsorption site. Finally differential conductance maps were measured by lifting NTCDA molecules from the island borders. It was found that both types of molecules form the Kondo resonance. While the type A molecule shows a peak in the differential conductance in the equilibrium position, the type B molecule has to be lifted by  $1\text{ \AA}$  to show a peak.



## 5 Highly reproducible lifting of $\pi$ -conjugated molecules

In this chapter a new method is introduced, which was used to probe single molecules. The main idea of this method is to simultaneously measure the frequency shift and the zero-bias differential conductance through a molecular junction while manipulating the molecule with a combined LT-STM/AFM. The frequency shift is used to monitor the geometry in the junction, by comparing the experimental frequency shift measurement to simulations of the frequency shift based on force-field calculations. The features observed in the zero-bias differential conductance can then be assigned to specific junction geometries. This new method is introduced by presenting two published letters [42, 43].

In the first letter “Force-controlled lifting of molecular wires” by Fournier *et al.* [42] the new method was first introduced. In contrast to the vertical manipulations discussed in chapter 6 the tip was moved on a customized trajectory which was chosen to reduce the lateral force on the tip during the manipulation. It was shown exemplary on the system PTCDA on Ag(111) that while manipulating single isolated molecules reproducibly, the frequency shift and the zero-bias differential conductance can be measured. Further it was shown that the frequency shift data measured is in very good agreement with the simulations based on force-field calculations. Finally the features A and B in the frequency shift were introduced and the conductance of the molecule in the wire configuration was determined.

In the second letter “Measurement of the Binding Energies of the Organic-Metal Perylene-Tetracarboxylic-Dianhydride/Au(111) Bonds by Molecular Manipulation Using an Atomic Force Microscope” by Wagner *et al.* [43] the new method was applied to the two molecules NTCD and PTCDA on Au(111). The focus of this paper was on the measured frequency shift. This measured frequency shift was used to identify the individual binding energy contributions to the total molecule-metal bond. Therefore many simulations were

generated with a Monte Carlo algorithm. From these simulations the best one was chosen by comparing the simulated frequency shift to the experimental frequency shift by determining the reduced  $\chi_2$ . From this best simulation the energy contributions were extracted. It was found that the molecule-metal bond is mostly the result of van der Waals interaction.





## Force-controlled lifting of molecular wires

N. Fournier, C. Wagner, C. Weiss, R. Temirov,<sup>\*</sup> and F. S. Tautz

*Peter Grünberg Institut (PGL-3), Forschungszentrum Jülich, 52425 Jülich, Germany and*

*JARA-Fundamentals of Future Information Technology, 52425 Jülich, Germany*

(Received 12 May 2011; published 25 July 2011)

Lifting a single molecular wire off the surface with a combined frequency-modulated atomic force and tunneling microscope it is possible to monitor the evolution of both the wire configuration and the contacts simultaneously with the transport conductance experiment. In particular, critical points where individual bonds to the surface are broken and instabilities where the wire is prone to change its contact configuration can be identified in the force gradient and dissipation responses of the junction. This additional mechanical information can be used to unambiguously determine the conductance of a true molecular wire, that is, of a molecule that is contacted via a pointlike “crocodile clip” to each of the electrodes but is otherwise free.

DOI: [10.1103/PhysRevB.84.035435](https://doi.org/10.1103/PhysRevB.84.035435)

PACS number(s): 82.37.Gk, 73.63.-b, 81.07.-b

Recently it has been demonstrated that the application of scanning tunneling microscopy (STM) to single-molecule transport studies increases the degree of experimental control considerably, because the conformation and the local environment of the molecule before and after the transport measurement can be determined.<sup>1–6</sup> In those instances when the molecule can be contacted in a point-contact-like manner, essentially like an atom, this degree of control is sufficient to make transport measurements fully reproducible; examples are conductance measurements of  $C_{60}$ .<sup>1,3,5,6</sup> In the more general cases of ribbonlike or platelet molecules, however, the molecule must be manipulated into a free-standing configuration in which it remains connected to the junction electrodes (i.e., substrate surface and STM tip) via the two pointlike contacts. As no direct methods exist to control and monitor the molecule during this manipulation, its configuration in the junction is typically deduced from the transport data itself or from theoretical simulations.<sup>7–9</sup> This approach, however, often leads to ambiguities with respect to the molecular conformation and thus cannot yield detailed and reliable characterizations of molecular junctions.

In this work we propose a new approach to single-molecule transport measurements based on, first, contacting a surface-adsorbed molecule with the tip of a combined atomic force and tunneling microscope (AFM/STM), second, lifting up the molecule into the free-standing wire configuration on a trajectory that has been optimized before in a simulation, and third, verifying the proper execution of the lifting by monitoring online the AFM signal that measures the junction’s stiffness. We show that molecular wire junctions formed in this way can be characterized reproducibly. For our proof-of-principle experiment we have chosen the well-studied system of 3,4,9,10-perylene-tetracarboxylicacid-dianhydride (PTCDA).<sup>10</sup> The structure of PTCDA, shown in Fig. 1, can be understood as a graphene nanoribbon<sup>11</sup> with functional groups attached at both ends. Therefore, PTCDA represents a wider class of molecular wires which consist of two separated parts: first, a conducting  $\pi$ -conjugated core and, second, clamps at its ends which provide a mechanically stable electronic coupling of the wire’s conducting body to the electrodes.<sup>2,12</sup>

For our experiments we prepared an atomically clean Ag(111) surface in UHV by successive cycles of  $Ar^+$

sputtering and annealing at 550 °C. A submonolayer coverage of PTCDA molecules was evaporated onto the Ag(111) surface kept at RT from a home-built Knudsen cell at a temperature of 300 °C. Finally, isolated PTCDA molecules on Ag(111) were produced by detaching them with the STM tip from the edge of a PTCDA island.<sup>2</sup>

In detail, we contact the single, isolated PTCDA molecule, which initially is adsorbed flat on a single-crystal Ag(111) surface, with the atomically sharp Ag-covered tungsten tip of a low temperature CREATEC STM/AFM (based on the qPlus tuning fork design<sup>13</sup>). Moving the tip into contact with the molecule and then retracting it away from the surface, we bring the molecule into the free-standing wire geometry, in which the molecule is bound to the surface on one side and to the tip on the other, each via a carboxylic oxygen atom (Fig. 1). To gain full control over the lifting process, we retract the tip along a trajectory that minimizes lateral forces in the junction. Lateral forces can lead to abrupt sliding of the molecule on the surface and undermine external control of the junction structure.<sup>2,14</sup> The trajectory with vanishing lateral forces is shown in Fig. 1<sup>14</sup> and was obtained from force-field simulations that take into account both the chemical bonding and the van der Waals interaction between the molecule and the electrodes.

Force-field calculations have been carried out for the tip/PTCDA/Ag(111) junction. The tip was modeled by a single Ag atom. The Ag(111) surface was modeled by one atomic layer. The interaction between the atoms within the PTCDA molecule was described by the AMBER<sup>15</sup> parameter set. The tip-molecule interaction is modeled by a Morse potential (depth 1 eV) acting between the tip atom and one of the carboxylic oxygens of PTCDA.<sup>12</sup> The molecule-substrate interaction is modeled by interaction potentials between individual atoms constituting the molecule and the surface as a whole. The interaction potential for each species in the molecule (C, H, carboxylic O, anhydride O) with Ag is represented by a one-dimensional  $z$ -dependent Morse potential; for each of these potentials, the position of the energy minimum and the depth has been chosen separately to reproduce the available experimental data, namely the adsorption height of PTCDA on Ag(111),<sup>16–18</sup> its deformation,<sup>16–18</sup> and the adsorption energy for PTCDA/Au(111),<sup>19</sup> which is taken as a lower boundary

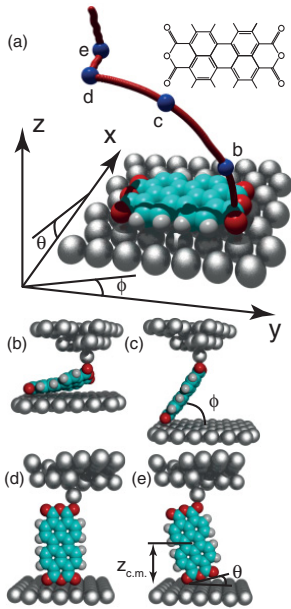


FIG. 1. (Color) Simulated junction geometries during tip retraction. (a) PTCDA adsorbed on Ag(111). The molecule is shown in the adsorption site that is used in the simulation. The tip trajectory employed in experiment and simulation is shown in red (its projection into the  $xy$  plane is shown as a shadow). An animation of this tip trajectory is provided in the supplemental material (Ref. 14). Tip positions corresponding to the four junction geometries in panels (b) to (e) are marked in blue. The two angles  $\phi$  and  $\theta$  describe the orientation of the molecule in the junction. (b) The second carboxylic oxygen is detached from the surface. (c) The almost planar molecule is lifted into the upright configuration. (d) Upright molecule ( $\phi = 90^\circ, \theta = 0^\circ$ ) bound to Ag(111) via two carboxylic oxygen atoms. (e) Molecular wire configuration, that is,  $\phi = 90^\circ, \theta = 15^\circ$ . The coordinate  $z_{c.m.}$  describes the motion of the molecule after it is detached from the surface.

for the adsorption energy for PTCDA/Ag(111). Finally, the potentials have been fine-tuned to optimize the fit to the experimental  $\frac{dF}{dz}(z)$  data. The corrugation of the interaction potential between the carboxylic O atoms and the surface has been set to 40 meV, according to the activation energy of PTCDA diffusion that was measured on Ag(100).<sup>20</sup> The force-field simulations have been carried out for a PTCDA molecule that is aligned along the high symmetry direction of Ag(111).<sup>21</sup> In the simulations the tip is retracted in steps of 0.25 pm. After each step the junction geometry is relaxed. To define the tip trajectory of Fig. 1(a), the lateral position of the tip apex atom is adjusted at each tip height  $z_{tip}$  such that all lateral forces on the tip vanish. The thus-obtained tip trajectory has also been used in the experiments.

To measure the junction stiffness experimentally during tip retraction, we record the frequency shift  $\Delta f$  of the tuning fork oscillations. In our experiments we have used qPlus sensors from Createc Fischer GmbH. They consist of a tungsten tip

that is glued to the quartz tuning fork. The tip was etched electrochemically. Then it was prepared *in situ* by crashing into the clean Ag(111) surface at a bias voltage of  $V = 100$  V with the current limited to 1 mA. The qPlus sensor ( $k_0 = 1800$  N/m) oscillates with its resonance frequency  $f_0 \approx 20.9$  kHz and an amplitude of  $A_0 \approx 0.1$ – $0.2$  Å. The  $\Delta f$  signal can be directly related to the stiffness (or force gradient)  $k = \frac{dF}{dz} \approx -\frac{2k_0}{f_0} \Delta f$  of the molecular wire junction, where  $F$  is the force acting on the apex of the tip.<sup>22,23</sup> The inset of Fig. 2(a) displays  $\Delta f$  data of a single cycle of tip approach toward the not-yet-contacted molecule (black) and tip retraction after contacting the molecule (red). The black curve shows a decreasing stiffness due to the increasing attraction between the tip and the substrate (the latter consisting of both the PTCDA

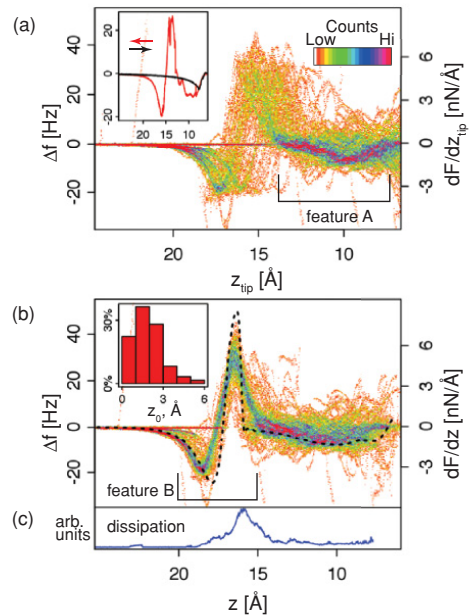


FIG. 2. (Color) Stiffness of the tip/PTCDA/Ag(111) junction. (a) Two-dimensional histogram of 121  $\Delta f(z)$  curves recorded while lifting up single isolated PTCDA molecules. After each manipulation cycle the molecule remained at the tip. In 65% of the cases it was possible to redeposit the molecule back onto the surface by having the tip approach the surface and applying a voltage of +0.6 V to the sample. The inset shows  $\Delta f(z)$  for a single approach/retraction cycle: Approach is shown in black, retraction in red. For all curves in the histogram, the  $\Delta f$  signal during tip approach was subtracted from the  $\Delta f$  data taken during retraction. (b) Same dataset as in panel (a), but each curve is shifted on the horizontal axis by individual values  $z_0$  such that the peak belonging to feature B is aligned with the corresponding peak in the simulated  $\Delta f$  curve (dashed line) (Ref. 24). The inset shows a histogram of shift distances  $z_0$ . (c) Averaged dissipation signal for all 121 retractions of panel (b). Before averaging, each curve was shifted by the same  $z_0$  as the corresponding  $\Delta f$  curve in panel (b). The dissipation is a measure of the energy needed to sustain a constant oscillation amplitude of the tuning fork sensor.

molecule and the metal surface). At the end of the approach, the jump-into-contact of the PTCDA molecule to the tip apex can be discerned as a sharp kink in the stiffness curve. To exclude long-range forces that are not related to the lifting of the molecule from our analysis, we subtract the approach curves (background) from the retraction curves. The resulting background-subtracted retraction curves of all 121 approach cycles that we have performed are shown as a two-dimensional color-coded histogram in Fig. 2(a).

In the range  $z_{\text{tip}} = 5$  to  $14 \text{ \AA}$ ,<sup>25</sup> Fig. 2(a) exhibits a shallow dip in the junction stiffness  $\frac{dF}{dz}$ , which we label as feature A. When the tip is retracted beyond  $z_{\text{tip}} \approx 14 \text{ \AA}$ , the stiffness curves in Fig. 2(a) scatter more strongly. Nevertheless, it is evident that most of the curves show a characteristic peak/dip structure, to which we refer as feature B from now on. In Fig. 2(b), we have aligned all individual stiffness curves at feature B, with the result that in the range  $z = 16$  to  $24 \text{ \AA}$ , the experimental curves collapse onto one. Apparently, the macroscopically measured  $z_{\text{tip}}$  does not characterize the configuration of the molecule in the junction unambiguously. This ambiguity may, for example, arise due to different bonding positions of the carboxylic oxygen atom of PTCDA on the tip. In the remainder of the paper, we exclusively discuss the aligned stiffness curves of Fig. 2(b), because feature B defines a reference point for the microscopic  $z$  coordinate, as will become clear below. This coordinate  $z$  is related to  $z_{\text{tip}}$  by  $z = z_{\text{tip}} + z_0$ , where  $z_0$  is an offset that varies from experiment to experiment [inset, Fig. 2(b)].

Before discussing Fig. 2 in detail, it is necessary to analyze which part of the junction the measured stiffness signal  $\frac{dF}{dz}$  is related to. Because we have never observed structural changes of either the tip or the Ag(111) surface in our experiments, we conclude that the Ag(111) surface and the tip apex are so stiff that their small deformations occur within the harmonic limit ( $\frac{dF}{dz} = \text{const}$ ). Consequently, any influence of these deformations on the curves in Fig. 2 can be ruled out. The three remaining elements which could in principle affect the  $\frac{dF}{dz}$  curves in Fig. 2 are the molecule itself and its bonds to the surface and to the tip. According to *ab initio* calculations<sup>12</sup> and our experimental data, which show that at the end of the approach-retraction cycle the PTCDA molecule nearly always remains connected to the tip, we conclude that the tip-molecule bond is the stiffest. Hence, it should deform much less than the molecule and its bond to the surface. We can therefore conclude that the measured  $\frac{dF}{dz}$  curves are a property of the PTCDA molecule itself and of the PTCDA/Ag(111) surface contact, revealing their response to the chosen tip trajectory. This illustrates the benefits of using stiff sensors for force spectroscopy: If the sensor is much stiffer than the probed object, its properties do not affect the measurement.<sup>26</sup> In particular, unlike traditional force spectroscopy techniques, which work only until bond ruptures occur,<sup>27,28</sup> stiff sensors like the qPlus offer the possibility to coerce the molecular junction smoothly through bond rupture processes. This is vital in the present context, because it allows the stabilization of the molecular junction in any desired configuration along the chosen trajectory.

With this knowledge, we are able to interpret the experimental stiffness curves  $\frac{dF}{dz}(z)$  in Fig. 2(b) by comparing them

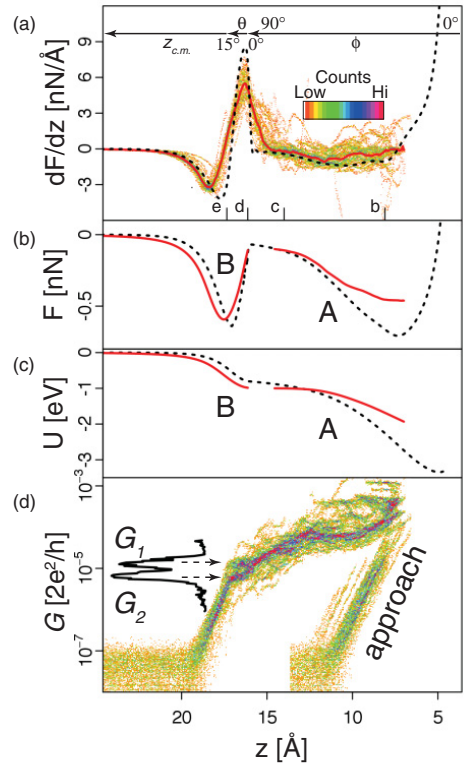


FIG. 3. (Color) Force, potential energy, and conductance of the molecular wire. (a) Histogram of the 35 integrable  $\frac{dF}{dz}$  curves (i.e., no abrupt jumps for  $z > 15 \text{ \AA}$ ) from the dataset in Fig. 2(b). The solid red line displays the averaged experimental data. The black dashed line shows the simulated  $\Delta f$  curve (Ref. 24). The tip heights that correspond to the junction geometries in Fig. 1 are indicated and labeled as b, c, d, and e. The upper horizontal axis ( $\phi, \theta, z_{c.m.}$ ) indicates the coordinates of molecular motion, enforced by the tip trajectory shown in Fig. 1(a). (b) Black dashed line, force on the tip as calculated in the force-field simulation; red solid lines, force on the tip as calculated by integrating the averaged experimental  $\frac{dF}{dz}$  in panel (a) [red solid line in panel (a)] for  $z > 16 \text{ \AA}$  and for  $z < 15 \text{ \AA}$ . The branch for  $z < 15 \text{ \AA}$  was shifted along the vertical axis such that it starts at the value where the left section of the curve ended. (c) Black dashed line, potential energy of PTCDA in the junction as calculated in the force-field simulation; red solid lines, potential energy of PTCDA in the junction as calculated by integrating the experimental  $F(z)$  curves in panel (b) [red solid line in panel (b)]. The integration constant for  $z < 15 \text{ \AA}$  was again chosen to match the value where the left section of the curve ended. (d) Histogram of the junction conductance  $\frac{dI}{dV}(z)$  at a bias voltage of  $V = -0.5 \text{ mV}$  for the same dataset as in panels (a)–(c). At  $z \approx 17 \text{ \AA}$  the last molecule-substrate bond breaks and the junction enters the tunneling regime. The inset is a line profile through the histogram parallel to the vertical axis in the corridor between  $z = 16.25 \text{ \AA}$  and  $z = 17.0 \text{ \AA}$ .

to a simulated  $\frac{dF}{dz}(z)$  curve [black dashed lines in Figs. 2(b) and 3(a)], which is obtained from the same force-field model

that was used to extract the tip retraction trajectory.<sup>24</sup> For this comparison, we remove all curves from the experimental dataset in which the lifting of the molecule ends prematurely, for example, because the molecule instantaneously snaps to the tip. The remaining histogram in Fig. 3(a) is in very good agreement with the simulation, particularly for  $z > 16$  Å, indicating that the lifting process in the corresponding experiments proceeds as predicted by the simulation. This conclusion is confirmed by the more detailed analysis in the next paragraph.

Because it is more intuitive to discuss the junction in terms of its total energy  $U(z)$  and the force  $F(z) = \frac{dU}{dz}$  than in terms of its stiffness  $\frac{dF}{dz} = \frac{d^2U}{dz^2}$ , we turn to the simulated  $F(z)$  [dashed line in Fig. 3(b)] and  $U(z)$  [dashed line in Fig. 3(c)] with the aim to understand the origin of features A and B in the measured stiffness curves. The simulated  $F(z)$  and  $U(z)$  reveal that feature A is associated with the molecule being lifted out of a shallow attractive potential as the tip moves away from the surface. Considering the corresponding configurations in Fig. 1, it becomes clear that this attractive potential A is due to the delocalized  $\pi$  bond between PTCDA and Ag(111), which is broken gradually as the tip is retracted from 7 to 15 Å. According to Fig. 1 and animation 2 in the supplemental material,<sup>14</sup> in this range the retracting tip essentially changes the angle  $\phi$  between the molecule and the surface plane. At  $z \approx 16$  Å (point d), the tip trajectory changes [cf. Fig. 1(a)], and the motion of the molecule is from there on constrained to a different coordinate when the tip is retracted further. From Fig. 1 and animation 2 in the supplemental material<sup>14</sup> it is clear that the relevant new coordinates are the angle  $\theta$  until point e ( $z \approx 17$  Å), and the  $z$  position of the center of mass of the PTCDA molecule,  $z_{c.m.}$ , beyond point e ( $z > 17$  Å). The simulated  $F(z)$  and  $U(z)$  in Figs. 3(b) and 3(c) show that immediately after the coordinate change  $\phi \rightarrow (\theta, z_{c.m.})$  the molecule is again lifted out of an attractive potential (potential B). Therefore, we can conclude that feature B in the experimental stiffness curves originates from the interaction of the lower end of the vertically upright molecule with the surface. Outside this potential well the molecule is completely removed from the surface and both  $F$  and  $U$  approach zero (at  $z \approx 24$  Å).

Summarizing up to this point, we have seen that the shape of the experimental stiffness curves verifies that the target trajectory is executed in the experiments as predicted by the simulation. In other words, starting from the surface-adsorbed molecule that has been contacted with the STM tip, a free-standing molecular wire of controlled geometry is created in a systematic and reproducible manner. Unlike in the simulation, however, the real junction passes through an instability at  $z \approx 16$  Å, as evidenced by the sharp peak in the dissipation signal of Fig. 2(c). In dynamic AFM, energy dissipation arises whenever the work  $\int F ds$  in the downward and upward half cycles of the tip oscillation is not the same. In the present case, this indicates that the configuration of the molecule in the junction changes within one cycle. We have seen in the previous paragraph that at  $z \approx 16$  Å, where the maximum in the dissipation signal appears, the molecule stands upright in the junction and the change in coordinate  $\phi \rightarrow \theta$  takes place. It is clear that in this configuration the oscillations of the tip

(which, incidentally, are not contained in the simulation) may lead to particularly large compressive or tensile stress in the junction. This, in turn, makes the molecule prone to change its configuration in the junction. The presence of the sharp dissipation maximum at  $z \approx 16$  Å therefore confirms that at this distance the molecule in the junction stands indeed upright, and thereby it also confirms our interpretation of features A and B to either side of the dissipation maximum.

To compare experiment and simulation quantitatively, we have integrated the averaged experimental stiffness of Fig. 3(a) (red line), once to yield the force  $F$  [Fig. 3(b), red line] and twice to yield the potential energy  $U$  [Fig. 3(c), red line]. It is clear that this integration cannot be extended meaningfully across the dissipative region because here the molecule traverses different trajectories with different forces in the upward and downward half cycles of the tip oscillation, and hence the measured frequency shift  $\Delta f$  is not any more related to a unique stiffness in a well-defined configuration. The sharp dissipation maximum at the instability therefore divides the lifting process into two regimes, both of which must be integrated separately. Starting from  $z = 24$  Å, where the force and the potential energy can be set to zero to fix the integration constants, we have integrated the average experimental curve of Fig. 3(a) up to  $z = 16$  Å. The results for both  $F$  and  $U$  agree very well with their simulated counterparts [cf. dashed lines in Figs. 3(b) and 3(c)]. We can therefore conclude that the maximal force that has to be overcome to remove the upright molecule from the surface is 0.6 nN. This force corresponds to a binding energy in this configuration of 1 eV. This binding energy includes contributions both from the short-range (chemical) interaction between the carboxylic oxygen atoms and the surface as well as long-range van der Waals interaction between the whole of the molecule and the surface. For the integration from  $z = 5$  Å to  $z = 14$  Å, there is no experimentally accessible limiting case which can be used to fix the integration constant. We have therefore adjusted the integration constant such that the integrated curve starts at the value where its left section ended. According to this integration, the maximal force during cleaving of the delocalized  $\pi$  bond between PTCDA and Ag(111) is 0.5 nN.

Finally, we turn to the electrical conductance measurements through the PTCDA wire. Figure 3(d) shows the two-dimensional color-coded conductance histogram for the data set of Fig. 3(a), made with logarithmic bins. For  $6 \text{ Å} < z < 10 \text{ Å}$  the conductance behavior of the PTCDA wire has been reported and discussed before.<sup>2,12</sup> Here we concentrate on the range  $z > 16$  Å. At  $z \approx 17$  Å, we observe a sharp turning point at which the conduction through the molecular wire abruptly gives way to tunneling, the latter revealed by the characteristic exponential dependence of the conductance on the distance. This shows that precisely at the point of largest force across the wire junction a vacuum gap opens between the molecular wire and the surface. Through the last angstrom before the transition to tunneling, we observe a plateau in the conductance, which should correspond to the conductance of a PTCDA wire that is contacted by its carboxylic oxygens at one end to the tip and at the other end to the Ag(111) surface [Fig. 1(e)]. Interestingly, on this plateau the distribution of wire conductances exhibits two well-defined peak values,  $G_1 = (1.3 \pm 0.3) \times 10^{-5} G_0$

and  $G_2 = (0.6 \pm 0.1) \times 10^{-5} G_0$ , where  $G_0$  is the quantum of conductance  $(12.9 k\Omega)^{-1}$ . This indicates that there exist two stable configurations of the molecular wire junction. Note that the two conductances vary by nearly a factor of 2, that is,  $\frac{G_1}{G_2} \approx 2.1$ . One may speculate that these configurations have one or two (carboxylic) oxygen atoms, respectively, in contact with the tip electrode.

The method used here for the characterization of a prototypical molecular wire provides independent force-based control over the conformation of the molecule in the junction. The large stiffness and the low oscillation amplitudes of the qPlus sensor make it a unique tool for single-molecule transport studies. The experimental strategy described here is directly applicable to the broad class of molecules that are composed of the nanometer-sized graphene ribbons or flakes and functionalized with carboxylic or other groups of sufficient reactivity as contacts to the tip. Since this

type of molecular wire is of practical importance,<sup>11</sup> their systematic study is highly desirable. Furthermore, the case of PTCDA analyzed here inspires optimism since it demonstrates that molecular wires can sustain stable electrical contacts between two macroscopic electrodes even if one of the leads is subjected to mechanical oscillations with amplitudes of about 10% of the total length of the wire. At the same time, the rather low conductance of the present wire should improve as the size of the conducting nanoribbon and/or the number of carboxylic clamps per contact increases.

We gratefully acknowledge fruitful discussions with M. Rohlfling (Universität Osnabrück) and C. Toher (TU Dresden), as well as the financial support from the Deutsche Forschungsgemeinschaft (DFG SPP 1243). R.T. acknowledges support by the Helmholtz-Gemeinschaft.

\*Corresponding author: r.temirov@fz-juelich.de

<sup>1</sup>N. Néel, J. Kröger, L. Limot, T. Frederiksen, M. Brandbyge, and R. Berndt, *Phys. Rev. Lett.* **98**, 065502 (2007).

<sup>2</sup>R. Temirov, A. Lassise, F. B. Anders, and F. S. Tautz, *Nanotechnology* **19**, 065401 (2008).

<sup>3</sup>N. Néel, J. Kröger, L. Limot, and R. Berndt, *Nano Lett.* **8**, 1291 (2008).

<sup>4</sup>L. Lafferentz, F. Ample, H. Yu, S. Hecht, C. Joachim, and L. Grill, *Science* **323**, 1193 (2009).

<sup>5</sup>Y. F. Wang, J. Kröger, R. Berndt, H. Vazquez, M. Brandbyge, and M. Paulsson, *Phys. Rev. Lett.* **104**, 176802 (2010).

<sup>6</sup>G. Schull, T. Frederiksen, A. Arnau, D. Sanchez-Portal, and R. Berndt, *Nat. Nanotechnol.* **6**, 23 (2011).

<sup>7</sup>A. Nitzan and M. A. Ratner, *Science* **300**, 1384 (2003).

<sup>8</sup>N. J. Tao, *Nat. Nanotechnol.* **1**, 173 (2006).

<sup>9</sup>F. Chen, J. Hihath, Z. F. Huang, X. L. Li, and N. J. Tao, *Annu. Rev. Phys. Chem.* **58**, 535 (2007).

<sup>10</sup>F. S. Tautz, *Prog. Surf. Sci.* **82**, 479 (2007).

<sup>11</sup>F. Munoz-Rojas, J. Fernandez-Rossier, and J. J. Palacios, *Phys. Rev. Lett.* **102**, 136810 (2009).

<sup>12</sup>C. Toher, R. Temirov, A. Greuling, F. Pump, M. Kaczmarek, M. Rohlfling, G. Cuniberti, and F. S. Tautz, *Phys. Rev. B* **83**, 155402 (2011).

<sup>13</sup>F. J. Giessibl, *Rev. Mod. Phys.* **75**, 949 (2003).

<sup>14</sup>See Supplemental Material at <http://link.aps.org/supplemental/10.1103/PhysRevB.84.035435> for animation1.avi and animation2.avi.

<sup>15</sup>W. D. Cornell, P. Cieplak, C. I. Bayly, I. R. Gould, K. M. Merz, D. M. Ferguson, D. C. Spellmeyer, T. Fox, J. W. Caldwell, and P. A. Kollman, *J. Am. Chem. Soc.* **117**, 5179 (1995).

<sup>16</sup>A. Hauschild, K. Karki, B. C. C. Cowie, M. Rohlfling, F. S. Tautz, and M. Sokolowski, *Phys. Rev. Lett.* **94**, 036106 (2005).

<sup>17</sup>A. Hauschild, K. Karki, B. C. C. Cowie, M. Rohlfling, F. S. Tautz, and M. Sokolowski, *Phys. Rev. Lett.* **95**, 209602 (2005).

<sup>18</sup>R. Rurali, N. Lorente, and P. Ordejón, *Phys. Rev. Lett.* **95**, 209601 (2005).

<sup>19</sup>P. Fenter, F. Schreiber, L. Zhou, P. Eisenberger, and S. R. Forrest, *Phys. Rev. B* **56**, 3046 (1997).

<sup>20</sup>J. Ikononov, P. Bach, R. Merkel, and M. Sokolowski, *Phys. Rev. B* **81**, 161412 (2010).

<sup>21</sup>A. Kraft, R. Temirov, S. K. M. Henze, S. Soubatch, M. Rohlfling, and F. S. Tautz, *Phys. Rev. B* **74**, 041402(R) (2006).

<sup>22</sup>M. Ternes, C. P. Lutz, C. F. Hirjibehedin, F. J. Giessibl, and A. J. Heinrich, *Science* **319**, 1066 (2008).

<sup>23</sup>M. Ternes, C. Gonzalez, C. P. Lutz, P. Hapala, F. J. Giessibl, P. Jelinek, and A. J. Heinrich, *Phys. Rev. Lett.* **106**, 016802 (2011).

<sup>24</sup>The simulated  $\Delta f(z)$  curve was obtained as  $\Delta f = \frac{d^2 V_{\text{total}}}{dz^2} \times \frac{f_0}{2k_0}$ . The resultant curve was smoothed to remove numerical noise.

<sup>25</sup>The determination of the absolute  $z_{\text{tip}}$  scale in the experiment was done as reported in Ref. 12.

<sup>26</sup>A. Noy, *Surf. Interface Anal.* **38**, 1429 (2006).

<sup>27</sup>M. Rief, F. Oesterhelmt, B. Heymann, and H. E. Gaub, *Science* **275**, 1295 (1997).

<sup>28</sup>T. Hugel and M. Seitz, *Macromol. Rapid Commun.* **22**, 989 (2001).



**Erratum: Force-controlled lifting of molecular wires [Phys. Rev. B **84**, 035435 (2011)]**

N. Fournier, C. Wagner, C. Weiss, R. Temirov, and F. S. Tautz  
(Received 25 November 2011; published 16 December 2011)

DOI: [10.1103/PhysRevB.84.239906](https://doi.org/10.1103/PhysRevB.84.239906)

PACS number(s): 82.37.Gk, 73.63.-b, 81.07.-b, 99.10.Cd

In Figs. 2(a), 2(b), and 3(a) the units of  $dF/dz$  scale should be nN/nm. In Fig. 3(d) the  $G$  scale is incorrect. The corrected Fig. 3(d) is shown here. The conductance values  $G_1$  and  $G_2$  are changed accordingly:  $G_1 = (1.3 \pm 0.3) \times 10^{-2} G_0$ ,  $G_2 = (0.6 \pm 0.1) \times 10^{-2} G_0$ . None of the claims of the paper are affected.

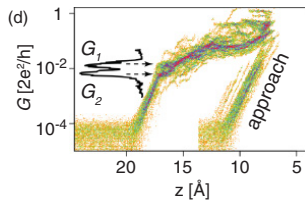


FIG. 3. (Color online) (d) Histogram of the junction conductance  $dI/dV(z)$  at a bias voltage of  $V = -0.5$  mV for the same data set as in panels (a)–(c). At  $z \approx 17$  Å the last molecule-substrate bond breaks, and the junction enters the tunneling regime. The inset is a line profile through the histogram parallel to the vertical axis in the corridor between  $z = 16.25$  Å and  $z = 17.0$  Å.

# Measurement of the Binding Energies of the Organic-Metal Perylene-Tetracarboxylic-Dianhydride/Au(111) Bonds by Molecular Manipulation Using an Atomic Force Microscope

C. Wagner,<sup>1,2,\*</sup> N. Fournier,<sup>1,2</sup> F. S. Tautz,<sup>1,2</sup> and R. Temirov<sup>1,2</sup>

<sup>1</sup>*Peter Grünberg Institut (PGI-3), Forschungszentrum Jülich, 52425 Jülich, Germany*

<sup>2</sup>*Jülich Aachen Research Alliance (JARA), Fundamentals of Future Information Technology, 52425 Jülich, Germany*  
(Received 14 March 2012; published 16 August 2012)

Based on single molecule manipulation experiments in a combined scanning tunneling microscope/frequency modulated atomic force microscope, we quantify the individual binding energy contributions to an organic-metal bond experimentally. The method allows the determination of contributions from, e.g., local chemical bonds, metal-molecule hybridization, and van der Waals interactions, as well as the total adsorption energy.

DOI: [10.1103/PhysRevLett.109.076102](https://doi.org/10.1103/PhysRevLett.109.076102)

PACS numbers: 68.37.Ef, 68.37.Ps, 82.37.Gk

The bonding of large organic adsorbates to metal surfaces is subject of an intense research effort [1–6]. If the molecule has functional groups, one may expect different bonding channels to contribute to the overall bonding of the molecule to the surface. An example for such a multifunctional bond is that of the well-studied model molecule 3,4,9,10-perylene-tetracarboxylic-dianhydride (PTCDA) to noble metal (111)-surfaces. According to the established picture, derived mainly from structural and electronic structure data, the PTCDA-metal bond consists of three attractive components [4,7–13]: firstly, local bonds of the reactive carboxylic oxygen atoms ( $O_{\text{carb}}$ ) to metal atoms in the surface; secondly, weak chemisorption of the perylene core due to hybridization of delocalized molecular and metal states; and thirdly, the van der Waals interaction. The theoretical description of such multifunctional bonds presents a challenge because individual contributions may compete against or reinforce each other depending on the situation at hand. Moreover, the van der Waals interaction is only now being included into density functional theory (DFT) [12,14–17], and there is still some uncertainty regarding the reliability of the various approaches [18]. In this situation, it would be helpful if the various contributions to the total energy of a multifunctional bond could be determined experimentally.

In this Letter, we present an experimental method which allows the partitioning of the overall bonding energy between different bonding channels and apply it to PTCDA/Au(111). The approach is based on molecular manipulation in a combined scanning tunneling microscope/frequency modulated atomic force microscope (STM/FM-AFM) with a qPlus sensor (cf. Fig. 1) [19]. STM is used for high resolution imaging and location of the functional group at which to dock the tip to the molecule, and FM-AFM is used to measure the junction stiffness  $dF_z/dz$  [20] while manipulating the molecule off the surface by tip retraction ( $z$  = vertical tip coordinate) [21–23]. Because the stiffness of the surface-molecule-tip junction is measured throughout the complete removal process, the

strength of all interaction potentials constituting the PTCDA-Au(111) bond is probed, albeit in a tangled manner. To disentangle the various contributions, we use a procedure which is based on the hypothesis that the  $(dF_z/dz)(z)$  curve contains enough information to retrieve the quantitative shape of all relevant interaction potentials. This hypothesis is fully borne out by our results. The retrieval, discussed in detail below, proceeds by firstly, parameterizing the various bonding channels of the molecule-substrate interaction with generic potentials of sufficient generality, secondly, simulating the junction stiffness  $dF_z/dz$  based on these generic potentials throughout the whole manipulation process, and thirdly, fitting the simulated junction stiffness to the experiment, thereby extracting the correct potential parameters, from which the desired partitioning can finally be calculated.

The experiments are performed with a commercial STM/FM-AFM (CREATEC) operated at 5 K in ultrahigh

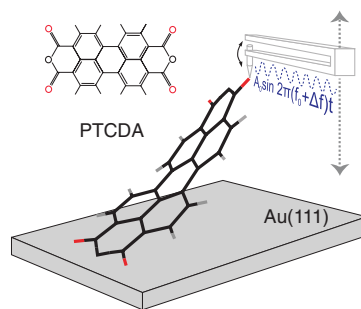


FIG. 1 (color). Scheme of the experimental setup. A single PTCDA molecule on Au(111) is contacted by a tip attached to a qPlus sensor. The oscillating sensor is retracted from and approached to the surface [28]. In this way, the molecule is repeatedly detached from the surface and brought back. Changes in the resonance frequency of the sensor reflect changes in the stiffness of the junction.

vacuum. The 15  $\mu\text{m}$  diameter PtIr tip wire of the qPlus sensor was cut and sharpened using a focused ion beam. The tip was finally prepared at 5 K by indentation into the clean Au(111) surface. The frequency of the qPlus sensor was  $f_0 = 30311$  Hz, its spring constant  $k = 1800$  N m $^{-1}$  [19]. The surface was prepared using Ar $^+$  sputtering and annealing in ultrahigh vacuum. The molecules were deposited from a home-built Knudsen cell. Single molecules were prepared by detaching them from the molecular islands with the STM/FM-AFM tip in STM mode. The contact between the tip and one of the O $_{\text{carb}}$  atoms of PTCDA was established according to the procedure described earlier [20–22]. Note that during contacting and throughout the experiment the tip is vibrating with an amplitude of  $\approx 0.2$  Å [24].

Having established the contact, the tip is retracted vertically from the surface by 27 Å, lifting the molecule and fully breaking the molecule-surface bond. Then, the tip is approached back to the surface, restoring the bond between PTCDA and Au(111). In each of the experiments, the retraction-approach cycle is repeated 10 times while  $dF_z/dz(z) = -(2k_0/f_0)\Delta f(z)$  [19] is recorded. As Fig. 2(a) shows, the gradual breaking of the molecule-surface bond is reversible and reproducible. The dramatic improvement in reproducibility over previous work [20] is attributed to the low corrugation of the adsorption potential of PTCDA on Au(111). Hence, during tip retraction the lower end of the molecule slides smoothly over the surface, while on Ag(111) its motion is more abrupt and thus less controlled [20].

In order to extract the desired information from the histogram in Fig. 2(a), we model the PTCDA-metal bond by generic potentials for the following four molecule-surface interaction channels that are qualitatively well established for PTCDA on noble metal surfaces [4]: (1) the local chemical bonds between the O $_{\text{carb}}$  atoms and the surface, (2) the chemical interaction due to hybridization of the delocalized molecular orbitals with substrate states, (3) the dispersion attraction, and finally (4) the Pauli repulsion. The delocalized chemical and dispersion interactions are split into interactions of individual atoms in the molecule with the surface. In this way, three atom-surface interaction potentials are defined for each atom in PTCDA (Table I). These potentials are parametrized by a set  $P$  of nine parameters [25]. There is no surface corrugation in our model, which is a good approximation for PTCDA/Au(111) [26].

The internal mechanical properties of the molecule itself are described by a standard molecular-mechanics model including covalent bonds, valence and dihedral angles, and van der Waals and electrostatic interactions. Because the molecule is strongly distorted during the lift-off [23] and because the distortion determines the precise way in which the molecule-surface interaction potentials are sampled in the experiment, the correct description of the internal

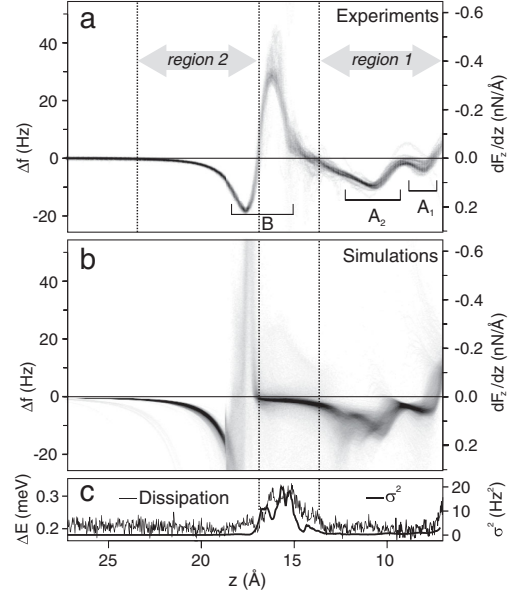


FIG. 2. (a) Histogram ( $\sqrt{N}$ ) of 226  $\Delta f$  traces acquired during lifting and lowering of PTCDA. All curves have been aligned at feature B. The  $\Delta f$  signal during tip approach was subtracted [20]. The  $z$  axis is shifted to match the simulated curves in panel (b). Dotted lines mark regions 1 and 2 within which the correspondence between experiment and simulation is calculated (reduced  $\chi^2$ ). Distinct features of the histogram are labeled A $_1$ , A $_2$ , and B. (b) Histogram ( $\sqrt{N}$ ) of 4166  $\Delta f$  traces simulated with different parameter sets  $P$  that have passed the preselection criteria (see text). (c) The energy dissipation of the qPlus sensor as well as the experimental variance  $\sigma^2$  show a peak around  $z = 16$  Å (see text).

mechanics of PTCDA is essential. We have therefore optimized the set  $Q$  of 34 force field parameters for the internal mechanics of PTCDA by fitting them to DFT calculations [BLYP/6–31(d)] [27] of molecular geometries that correspond to the 108 vibrational modes of a free PTCDA molecule. The DFT energies for the different geometries are reproduced with an average deviation of 18% by our

TABLE I. Atom-surface potentials used to describe the PTCDA-Au(111) interaction.  $z$  denotes the atom height above the surface. Superscript  $C$  refers to all atoms except O $_{\text{carb}}$ , O to O $_{\text{carb}}$ .

Potential	Parameters (set $P$ )
$V_{\text{Pauli}} = D_p \exp(-A_p z)$	$D_p^C, D_p^O, A_p^C, A_p^O$
$V_{\text{chem}} = -D_c \exp(-A_c z)$	$D_c^C, D_c^O, A_c^C, A_c^O$
$V_{\text{vdW}} = -D_{\text{vdW}} z^{-3}$	$D_{\text{vdW}}$



force field. Details of the fitting procedure are given in the Supplemental Material [28].

The thus specified potentials allow the calculation of the total energy of the system

$$E_t(P, z) = E_{\text{mol-sub}}(P, z) + E_{\text{intra}}(z) \quad (1)$$

as a function of the tip coordinate  $z$  that parametrizes the equilibrium junction geometry, including the molecular distortion. The equilibrium geometry for each  $z$  is determined by retracting the tip vertically (as in experiment) in steps of  $\Delta z = 0.25$  nm and relaxing the molecular geometry with a force tolerance of  $5 \times 10^{-4}$  eV/Å. For each  $z$ ,  $E_{\text{mol-sub}}(P, z)$  is obtained by summing the potentials of Table I for each atom in the molecule.  $E_{\text{intra}}(z)$  is the energy of the distorted molecule in the junction, calculated with force field parameters  $Q$  and the molecule-tip bond [29]. The frequency shift of the qPlus sensor is calculated as described in Ref. [30]:

$$\Delta f(P, z) = \frac{f_0}{\pi k_0 A^2} \int_{-A}^A \frac{d^2 E_t(P, z - q)}{dz^2} \sqrt{A^2 - q^2} dq. \quad (2)$$

The convolution with a semicircle simulates the experimental tip oscillation amplitude of  $A = 0.2$  Å.

The task is to find the parameter set  $P$  which, if inserted into Eqs. (1) and (2), reproduces the experimental  $\Delta f$  curve in Fig. 2(a). Since each set  $P$  requires a separate simulation of the complete manipulation process (which is costly in terms of CPU time), a fast preselection routine is employed which identifies promising parameter sets  $P$  and discards the rest [28]. From a total of  $10^8$  parameter sets that were randomly generated by a Monte Carlo algorithm [28], we have selected 4166 sets  $P$  for which full simulations were carried out.

A histogram of the simulated  $\Delta f(P, z)$  curves [Eq. (2)] for the 4166 sets  $P$  is shown in Fig. 2(b). Evidently, our generic potentials simulate the experiment very well. The features  $A_1$ ,  $A_2$ , and  $B$  are reproduced with remarkable accuracy [31]. There is, however, a small  $z$  shift of  $\approx 1$  Å between experiment and simulation for  $z > 15$  Å. Moreover, the experimental  $\Delta f$  peak  $B$  at  $z = 16$  Å is much wider than its simulated counterpart. We suggest that both the  $z$  shift and the broadening of the experimental  $\Delta f$  peak are due to the finite stiffness of the Au covered PtIr tip resulting in measurable relaxations that occur while lifting the molecule. Additionally, the spurious vertical forces that occur when the lower end of the molecule moves laterally on a corrugated surface also contribute to the broadening of the  $\Delta f$  peak. The occurrence of such motion is indicated by an increase in dissipation around 16 Å [Fig. 2(c)]. Both of the described effects can, in principle, be simulated by including a tip of finite stiffness that oscillates in the direction perpendicular to the surface in the simulation of the molecule lifting process. The results of such simulations will be discussed in the forthcoming publication. Here we account for both effects

( $z$  shift and  $B$  broadening) by neglecting the experimental data between 13.7 and 16.9 Å when quantifying the correspondence between individual simulations and the averaged experiment by calculating a reduced  $\chi^2$ . Because of the discontinuity in the experimental  $z$  scale, regions 1 and 2 [as marked in Fig. 2(a)] are aligned separately with each simulated curve to calculate  $\chi^2$ .

We now examine the best parameter sets  $P$  with the lowest  $\chi^2$  values. In Fig. 3(a),  $\chi^2$  is plotted versus the total binding energy of PTCDA for all sets  $P$  with  $\chi^2 < 3$ . While the best fit to the experiment is found for a parameter set  $P^*$  with  $E_{\text{bind}}^* = 2.6$  eV, the distribution of points in Fig. 3(a) yields a binding energy of  $E_{\text{bind}} = (2.5 \pm 0.1)$  eV for PTCDA on Au(111). The  $\Delta f(z)$  curve that was simulated using set  $P^*$  is shown in Fig. 4(a) [28]. We note the excellent fit between the experimental  $\Delta f(z)$  and the calculated  $\Delta f(P^*, z)$  (apart from the issue of the peak width discussed above).

To identify the nature of the PTCDA-Au(111) bond, we plot the contributions of the different potentials in Figs. 3(b) and 3(c). Here, each set  $P$  is represented by six points with identical  $\chi^2$ . From the plots a clear picture emerges. While the van der Waals attraction is in the range

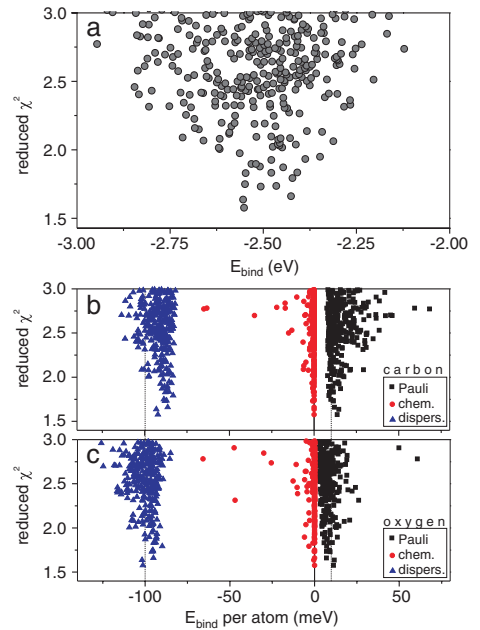


FIG. 3 (color). (a) Plot of the correspondence between individual simulations and experiment (reduced  $\chi^2$ ) versus the adsorption energy of PTCDA for all sets  $P$  with  $\chi^2 < 3$ . (b) and (c) Plots of  $\chi^2$  versus the energy contributions of the different potentials (and different types of atoms). “Carbon” stands for all atoms except  $\text{O}_{\text{carb}}$ . Dotted lines are a guide for the eye.

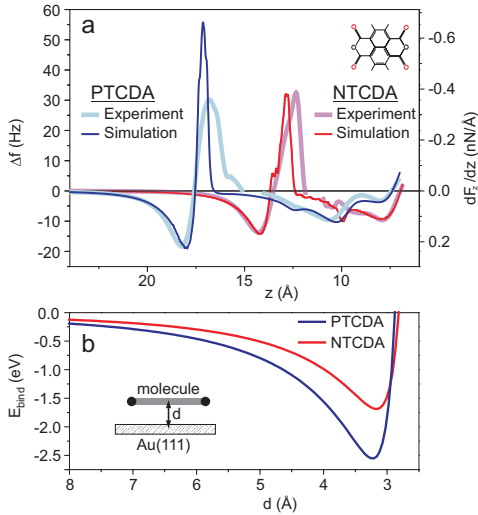


FIG. 4 (color). (a) Comparison between simulated and experimental  $\Delta f$  curve for PTCDA and NTCDA on Au(111). Parameter set  $P^*$ , derived for PTCDA (see text), was used for both simulations. The experimental curves are cut in the region of an unstable junction (Fig. 2), and both parts are separately aligned with the simulation. (b) Binding potential as a function of molecule-substrate separation calculated with set  $P^*$  for PTCDA and NTCDA. The molecule is relaxed on the surface and subsequently moved to different heights without further relaxation.

of 100 meV for C as well as  $O_{\text{carb}}$  atoms, neither of the two species has any chemical interactions with the Au(111) surface. The fact that  $O_{\text{carb}}$  atoms tend to bind slightly stronger is due to their smaller distance ( $\approx 0.1$  Å less) to the surface in the equilibrium geometry. To get the net adsorption energy, the (positive) Pauli repulsion of  $\approx 10$  meV has to be added. Comparing our result to theory, we find a good correspondence insofar as also *ab initio* calculations, as well as other spectroscopic methods (ultraviolet photoelectron spectroscopy, x-ray standing wave, etc.), suggest pure physisorption of PTCDA on Au(111) [4,10,32]. However, our experiment yields a significantly higher adsorption energy than predicted from calculations ( $\approx 2.0$  eV [18,26]). This indicates an underestimation of dispersion interaction in the (semiempirically corrected) DFT method(s) used. Parameter sets  $P$  which yield total binding energies in the range of 2.0 eV are clearly inconsistent with our experimental result [Fig. 3(a)] and, hence, can be discarded. Recent DFT calculations which include dielectric screening within the substrate yield an energy of 2.4 eV, which is close to our experimental result [33].

To validate our method further and to check whether the parameters obtained are meaningful beyond the fitted example of PTCDA on Au(111), we use the parameter sets  $P^*$  and  $Q$  to calculate the frequency shift of the smaller

NTCDA (1,4,5,8-naphthalene-tetracarboxylic-dianhydride) molecule during lift-off from Au(111) [also NTCDA is known to physisorb on Au(111) [32]]. The comparison between simulation and experiment is shown in Fig. 4(a), showing an excellent agreement. Note that this agreement for NTCDA is not the result of any fitting but just a consequence of the universal character of our potentials. The potentials, once fitted properly to yield the correct parameter set  $P^*$ , hence have predictive power for systems which exhibit similar physics. The bonding energy of NTCDA turns out to be 1.7 eV (compared to 1.3 eV from DFT calculations [26]).

In conclusion, in this Letter we have reported the—to our knowledge—first analysis which allows the quantitative identification of different bonding channels of large organic adsorbates on the basis of experimental data alone. As a result of this analysis, the precise shape of the total binding potential can be determined. As an example, we show the van der Waals-like potential that results if the distance between a flat and fully relaxed PTCDA molecule and the Au(111) surface is varied [Fig. 4(b)]. The resulting curves can be compared to *ab initio* calculations. Moreover, the method reported in this Letter represents a novel way to measure the adsorption energy of molecular adsorbates on a single-molecule level. Note that this method is also applicable in cases where the determination of the adsorption energy by thermal desorption spectroscopy is impossible because molecules decompose before desorbing. In the present Letter, we have carried out the experiments and the corresponding analysis for an adsorbate-substrate combination which exhibits a small lateral corrugation potential to demonstrate the principle. However, we anticipate that our approach is also applicable to more strongly corrugated substrates, if combined with a customized tip retraction trajectory [20] which minimizes sliding as much as possible.

We gratefully acknowledge T. Lippert, N. Attig, O. Büchner, and W. Homberg (Forschungszentrum Jülich) who have supported us with CPU time on JUDGE. We thank D. Park and J. Mayer from RWTH Aachen for help with the focused ion beam. R. T. thanks the Helmholtz-Gemeinschaft for financial support for his Young Investigator Research Group. This work has been supported by the Deutsche Forschungsgemeinschaft under projects TA244/5-1 and TA244/5-2.

\*Corresponding author: c.wagner@fz-juelich.de

- [1] F. Rosei, M. Schunack, Y. Naitoh, P. Jiang, A. Gourdon, E. Laegsgaard, I. Stensgaard, C. Joachim, and F. Besenbacher, *Prog. Surf. Sci.* **71**, 95 (2003).
- [2] G. Witte and C. Wöll, *J. Mater. Res.* **19**, 1889 (2004).
- [3] J. V. Barth, *Annu. Rev. Phys. Chem.* **58**, 375 (2007).
- [4] F. S. Tautz, *Prog. Surf. Sci.* **82**, 479 (2007).

- [5] J. Hwang, A. Wan, and A. Kahn, *Mater. Sci. Eng.* **64**, 1 (2009).
- [6] R. Otero, J.M. Gallego, A.L. Vázquez de Parga, N. Martín, and R. Miranda, *Adv. Mater.* **23**, 5148 (2011).
- [7] A. Hauschild, K. Karki, B.C.C. Cowie, M. Rohlfing, F.S. Tautz, and M. Sokolowski, *Phys. Rev. Lett.* **94**, 036106 (2005).
- [8] R. Rurali, N. Lorente, and P. Ordejón, *Phys. Rev. Lett.* **95**, 209601 (2005).
- [9] A. Hauschild, K. Karki, B.C.C. Cowie, M. Rohlfing, F.S. Tautz, and M. Sokolowski, *Phys. Rev. Lett.* **95**, 209602 (2005).
- [10] S. Henze, O. Bauer, T.-L. Lee, M. Sokolowski, and F.S. Tautz, *Surf. Sci.* **601**, 1566 (2007).
- [11] L. Kilian, A. Hauschild, R. Temirov, S. Soubatch, A. Schöll, A. Bendounan, F. Reinert, T.-L. Lee, F.S. Tautz, M. Sokolowski *et al.*, *Phys. Rev. Lett.* **100**, 136103 (2008).
- [12] M. Rohlfing and T. Bredow, *Phys. Rev. Lett.* **101**, 266106 (2008).
- [13] A. Abbasi and R. Scholz, *J. Phys. Chem. C* **113**, 19897 (2009).
- [14] M. Dion, H. Rydberg, E. Schröder, D.C. Langreth, and B.I. Lundqvist, *Phys. Rev. Lett.* **92**, 246401 (2004).
- [15] S. Grimme, *J. Comput. Chem.* **27**, 1787 (2006).
- [16] A. Tkatchenko, L. Romaner, O.T. Hofmann, E. Zojer, C. Ambrosch-Draxl, and M. Scheffler, *MRS Bull.* **35**, 435 (2010).
- [17] S. Grimme, *WIREs Comput. Mol. Sci.* **1**, 211 (2011).
- [18] L. Romaner, D. Nabok, P. Puschnig, E. Zojer, and C. Ambrosch-Draxl, *New J. Phys.* **11**, 053010 (2009).
- [19] F.J. Giessibl, *Rev. Mod. Phys.* **75**, 949 (2003).
- [20] N. Fournier, C. Wagner, C. Weiss, R. Temirov, and F.S. Tautz, *Phys. Rev. B* **84**, 035435 (2011).
- [21] R. Temirov, A. Lassise, F.B. Anders, and F.S. Tautz, *Nanotechnology* **19**, 065401 (2008).
- [22] C. Toher, R. Temirov, A. Greuling, F. Pump, M. Kaczmarzski, M. Rohlfing, G. Cuniberti, and F.S. Tautz, *Phys. Rev. B* **83**, 155402 (2011).
- [23] A. Greuling, M. Rohlfing, R. Temirov, F.S. Tautz, and F.B. Anders, *Phys. Rev. B* **84**, 125413 (2011).
- [24] G.H. Simon, M. Heyde, and H.-P. Rust, *Nanotechnology* **18**, 255503 (2007).
- [25] Since PTCDA is neutral, electrostatic image forces are neglected.
- [26] M. Mura, A. Gulans, T. Thonhauser, and L. Kantorovich, *Phys. Chem. Chem. Phys.* **12**, 4759 (2010).
- [27] M.J. Frisch *et al.* *Gaussian 03* (Gaussian Inc., Wallingford CT, 2004).
- [28] See Supplemental Material at <http://link.aps.org/supplemental/10.1103/PhysRevLett.109.076102> for a detailed description of the method that was used to generate and assess the parameter sets  $Q$  and  $P$  for the intramolecular and the molecule-substrate interactions and an animation of the lifting process.
- [29] The molecule-tip bond is a Morse potential ( $D = 1$  eV,  $r_0 = 2.2$  Å,  $a = 2.0$  Å<sup>-1</sup>) between one O<sub>carb</sub> atom and the tip apex atom. The potential depths  $D$  has barely any influence on the simulation as long as the bond is strong enough to lift the molecule.
- [30] F.J. Giessibl, *Appl. Phys. Lett.* **78**, 123 (2001).
- [31] The physical origin of  $A_1$ ,  $A_2$ , and  $B$  is discussed in Ref. [20]. Our simulations show that the splitting of  $A$  into  $A_1$  and  $A_2$  that is observable in the present experiments arises from the lifting of the first and second naphthalene unit of PTCDA.
- [32] J. Ziroff, P. Gold, A. Bendounan, F. Forster, and F. Reinert, *Surf. Sci.* **603**, 354 (2009).
- [33] V.G. Ruiz, W. Liu, E. Zojer, M. Scheffler, and A. Tkatchenko, *Phys. Rev. Lett.* **108**, 146103 (2012).



## 6 Systematic study of transport through a homologous series of $\pi$ -conjugated molecules

### 6.1 Introduction

In this chapter the transport through single molecules is investigated. Therefore a systematic study on the four molecules NTCDA, PTCDA, TTCDA and QTCDA on Ag(111) and Au(111) was performed. In the previous chapters important preliminary investigation were performed. In chapter 4 the electronic structures of the four different molecules adsorbed on the two different electrodes material were investigated. It was found that the adsorption differs significantly, with physisorption on Au(111) and chemisorption on Ag(111). In chapter 5 a method was introduced to control the configuration of the wire in the junction. It was shown that by comparing the frequency shift of the qPlus sensor with simulations the geometry of the junction can be verified.

In the first part of the present chapter the measurement routine is discussed. In the second part of the chapter the data processing procedure will be explained. Since a large number of manipulations were performed, a statistical analysis has to be done. Therefore the single differential conductance and frequency shift curves had to be sorted into different classes. Two main behaviors were observed, one is characterized by a hysteresis between lifting and lowering curves of the molecule. The second one is characterized by a stable junction configuration, which allowed very reproducible measurements.

The sorted data was then visualized in 2D histograms. From these histograms generic behaviors were extracted by calculating arithmetic means or determining the correlation between each measured curve. With the help of these generic behaviors two different transport regimes were identified, which were found for all four molecules on both metal

substrates. The last and main part of the chapter is dedicated to the analysis and interpretation of the generic behaviors. Next to the already mentioned two different classes of manipulations, the data is analyzed with respect to dependencies of the transport on the molecule length and the electrodes material.

## 6.2 Transport measurements on single molecules

In this section the measurement routine is explained. To illustrate the quantities measured simultaneously, a single data set recorded in one manipulation cycle is shown. The data set presented is a highly reproducible measurement of QTCDA on Ag(111).

### 6.2.1 Measurement routine

After a sample preparation (see section 2.5) the STM was given time to find its thermal equilibrium. This was important to reduce the drift, as the feedback loop of the STM was open up to 40 min during a measurement. Then the transport measurement could be performed. The measurements presented in this chapter are performed in a similar way as described in chapter 5.

First, a molecule had to be isolated from the molecular island. This was done by dragging it by a lateral manipulation with the tip a few nm away from the island border (see section 2.2.6). Then the isolated molecule was contacted with atomic precision with the Pt/Ir tip of the LT-STM/AFM. The molecule was then lifted up and lowered down many times in a triangle wave-like manner by the tip. Next to the frequency shift  $\Delta f$ , the zero-bias differential conductance  $dI/dV$  and the second derivative of the differential conductance  $d^2I/dV^2$  were measured, the latter two by the lock-in technique. For the measurement of  $\Delta f$  the tip had to oscillate during the whole manipulation. To remove the molecule from the tip after the manipulation was over, a voltage pulse was applied. It was not always possible to detach the intact molecule from the tip. In fact most of the time the molecule did not stay intact when it was removed. In those cases a new molecule had to be isolated to perform the next measurement.

In contrast to the experiments reported in chapter 5, one manipulation cycle consisted of 47 lifting and lowerings (see 6.1 for the definition of the expressions manipulation cycle, approach, lifting curve and lowering curve). The advantage of having more up and down cycles in one manipulation cycle comes at the price of a larger distance of

about 0.05 Å between two data points. This is the consequence of the employed digital signal processor (DSP) being only able to store 100 000 data points in one manipulation cycle.

As more lifting and lowering cycles require more time, the total drift in one manipulation would have increased. Therefore, to minimize the drift, the manipulation time had to be reduced. To do this, the moving speed of the tip was increased up to  $v_{\text{tip}} \approx 2.7 \text{ Å/s}$ . The consequence of the faster moving tip was a hysteresis caused by the propagation delay of the electronics. It was thus essential to find a good balance between this propagation delay and the drift.

### 6.2.2 Highly reproducible measurement

More than 600 manipulation cycles (see Fig. 6.1) were performed on the eight systems, with about 23 500 lifting and lowering curves recorded. Here a particularly reproducible manipulation will be presented to illustrate the main features of the experiment. It was found that the most reproducible experiments were performed with QTCDA on Ag(111).

Fig. 6.2 shows a data set acquired by lifting and lowering a single QTCDA molecule from Ag(111) 47 times in one manipulation cycle. The differential conductance  $dI/dV$  is plotted logarithmically, in this way the features are better visualized. The conversion of the conductance into units of  $G_0 = 2e^2/h$  was done by the conversion factor  $\alpha$ , which was introduced in section 2.3.5.

The data trace recorded while the tip approaches the first time the molecule to make contact is removed. Also the data of the first lifting and of the last lifting and lowering, when the molecule is detached, is removed (this corresponds to the green and red lines in Fig. 6.1). This is done as this data always differs from the rest as will be discussed in section 6.3.1.

The data in Fig. 6.2 shows a hysteresis, splitting the curves into two groups. One group is composed of curves recorded while lifting the molecule up with the tip, the other while lowering the molecule down. This hysteresis is more pronounced for the frequency shift  $\Delta f$  measurement than for the differential conductance  $dI/dV$  measurement. The hysteresis is a consequence of the propagation delay, i.e. the delay between the physical action

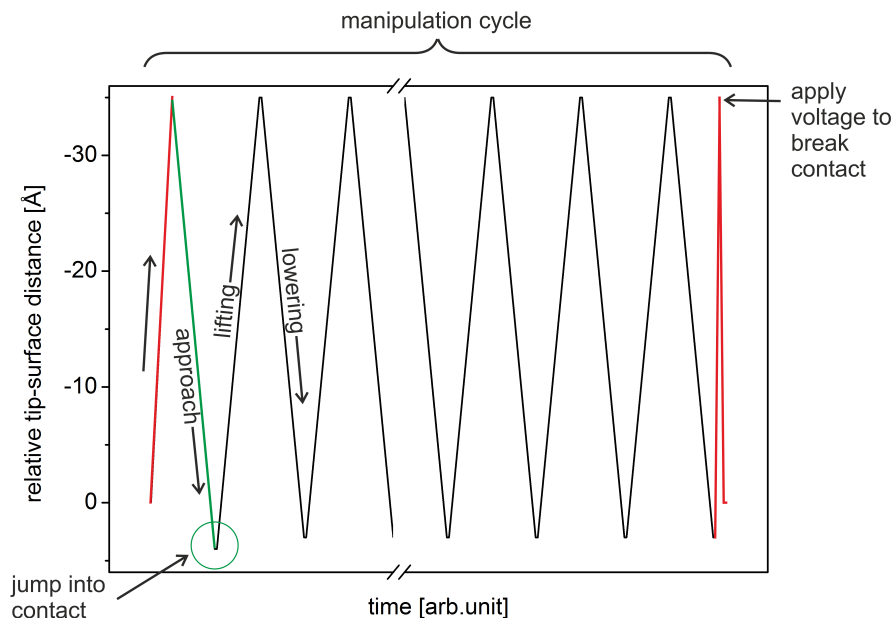


Figure 6.1: Tip manipulation procedure depicted by the movement of the STM tip relative to the surface versus the time. A manipulation starts with the tip in the setpoint (relative tip-surface distance = 0 Å). The tip is moved up to the maximum distance relative to the surface (red line). Then the tip is moved towards the molecule until a predefined position, this movement is called the approach (green line). Around the minimum distance to the surface, tip and molecule make contact by the jump into contact of the carboxylic oxygen atom (green circle). After the contact is established the tip is moved 47 times up and down (black lines). An up movement is called lifting, with the corresponding data called lifting curve. A down movement is called lowering, with the corresponding data called lowering curve. At the end of the manipulation the tip is lifted up a last time and a voltage is applied to break the tip-molecule contact at the maximum tip-surface distance (red lines). A whole manipulation experiment is referred to as manipulation cycle. For the analysis of the frequency shift and conductance data only the so-called lifting and lowering curves are used, i.e. the maximum number of curves from one manipulation cycle is 94.



and the reaction of the measuring electronics. This means that this hysteresis is dependent on the moving speed of the tip  $v_{\text{tip}}$ . To eliminate the unphysical hysteresis in the data the two groups of curves are moved towards each other.

All four physical quantities measured show a very high reproducibility in this data set. This is especially remarkable, considering that the tip was oscillating with an amplitude of about  $0.4 \text{ \AA}$  during the whole measurement to measure the frequency shift. However, this high reproducibility is not always observed. The reason is that there are parameters, such as the exact adsorption geometry of the molecule, the contact point between tip and molecule and the geometry of the tip, which we do not control. These parameters together with the unavoidable residual drift between the tip and the substrate affect the reproducibility.

Many features are visible in Fig. 6.2. The interpretation of the physics in the junction tip-molecule-substrate will be based upon the measurement of the frequency shift  $\Delta f$  and the zero-bias differential conductance  $dI/dV$ . Most of the features visible in those are found in every manipulation cycle. However, the uncontrolled parameters, drifts and mechanical instabilities of the setup let to variation of the position and magnitude of certain features. Therefore a statistical analysis is needed. This was realized by performing many manipulation cycles for each system. Thereby a total number of about 2000 to 6000 lifting and lowering curves were measured per system. The procedure applied to process this data is described in the next section.

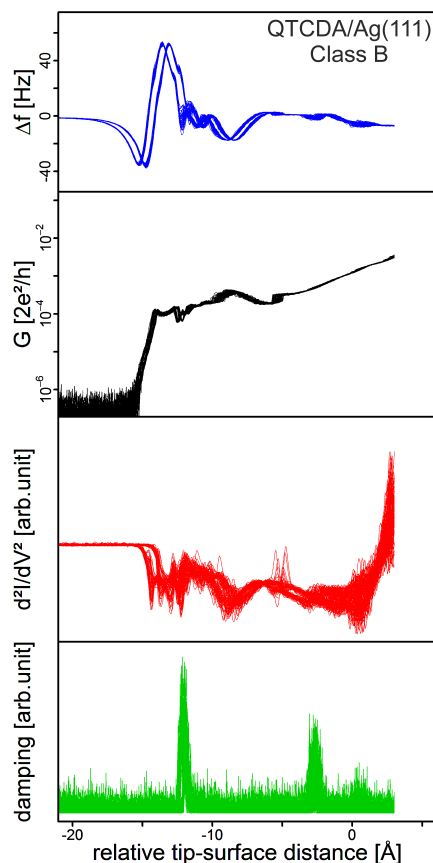


Figure 6.2: Lifting and lowering a single QTCDA molecule from Ag(111) 47 times. The frequency shift  $\Delta f$  and the damping were measured by the deflection of the qPlus sensor. The differential conductance  $dI/dV$  and its derivative  $d^2I/dV^2$  were measured by lock-in technique from the tunneling current. The data shows a very high reproducibility, which is remarkable as the tip was oscillated by the qPlus sensor at about  $0.4 \text{ \AA}$  during the whole manipulation to measure the frequency shift. A hysteresis splits the data into two groups, this results from a propagation delay in the electronics. By shifting the two groups the hysteresis effect can be almost eliminated.

### 6.3 Processing the data

The large data volume obtained for each system has to be processed before physical information can be extracted. The first step of this procedure is to assign each lowering and lifting curve to a certain class. Then a shifting procedure is applied to each curve. By this the effects of some of the uncontrolled parameters, such as, for example, the vertical drift, are reduced. The resulting curves of a system, assigned to a certain class, are then plotted in a 2D histogram. This 2D histogram is already a good representation of the general physical behavior of the quantities measured during the manipulation. But to make further analysis possible, two different procedures are applied to find a curve which represented best the whole set of lifting and lowering curves of one system molecule-substrate of each class.

These data processing procedures are described in this section. As an example the data sets measured by manipulation of QTCDA on Ag(111) are used. The best representing or generic curves of the other systems will be shown, but their processing will not be discussed. They were obtained in the same way as shown here for QTCDA/Ag(111). In Figs. A.1 to A.8 and A.10 to A.48 in chapter A the 2D histograms of all eight systems are shown.

#### 6.3.1 Sorting the data by classes

It is found that the lifting and lowering curves can be separated into four different classes (see Fig. 6.3). To the class app are assigned the curves measured while the tip initially approaches the surface to contact the molecule by the jump into contact (see green line in Fig. 6.1). Class A is characterized by a strong hysteresis between lifting and lowering curves especially in the region of the global frequency shift minimum. This hysteresis is not the earlier mentioned hysteresis due to the propagation delay which is observed for all classes. The origin of the distinctive class A hysteresis will be discussed later. Class B is characterized by a smooth peak-dip feature in the frequency shift. This class of curves is the one of which was reported in the publications by Fournier *et al.* [42] and Wagner *et al.* [43]. The peak-dip feature was labeled feature B as introduced earlier [42, 43]. To class C, which will not be considered in the analysis, are assigned all lifting or lowering curves which could not be assigned to class app, A or B. In the following the four classes are listed, in brackets is given percentage of occurrence of classes A, B and C:

- app: the initial approach of the tip towards the molecule before contact
- A: curves characterized by a hysteresis, especially in the region of the global frequency shift minimum, between lifting and lowering (17 %)
- B: curves characterized by a smooth peak-dip feature (feature B) in the frequency shift [42, 43] (72 %)
- C: all remaining lifting and lowering curves (11 %)

All manipulation cycles with at least two curves are used for the statistical analysis. The first curve of a manipulation cycle is always tagged as app, the second one either A, B or C. This means that in such a manipulation cycle tip and molecule made contact and the molecule was at least lifted once from the metal surface. Interestingly, this first lifting of the molecule usually showed at the beginning features of class A and then during the first lifting most of the time switched to a class B behavior. It seems that the mechanical tension which is build up at the beginning of the lifting process leads to a conformational change in the junction. The switch from class A to class B also happened in the first lifting of the manipulation cycle shown in Fig. 6.2, for a better representation this first lifting curve is removed from the data set used for this figure. These first lifting curves which showed features of class A and class B are all assigned to class C. The opposite switching from class B to A is never observed.

Also the last lowering curve always differed from the other curves as a voltage pulse of 1 V was applied to the molecule to remove it from the tip. This voltage pulse together with an increased manipulation speed made the last lowering curve differ and thus all last lowering curves were assigned to class C. This last lowering curve was removed as well from the data set used for Fig. 6.2.

Another observation made was that often after the first lifting of the molecule the lowering curve looked similar to the class app curves. This happened when the molecule had jumped up to the tip as soon as the molecule-substrate interaction was zero. These manipulations had to be interrupted and the tip had to be cleaned from the molecule to perform a new manipulation with another molecule.

In Fig. 6.4 all 4112 lifting and lowering curves measured for the system QTCDA on Ag(111) are plotted in a 2D histogram with the counts, i.e. the density of measurement points, on a logarithmic scale. To generate a 2D histogram the number of bins and subsequently the bin size has to be defined. As the data range varied the number of bins for

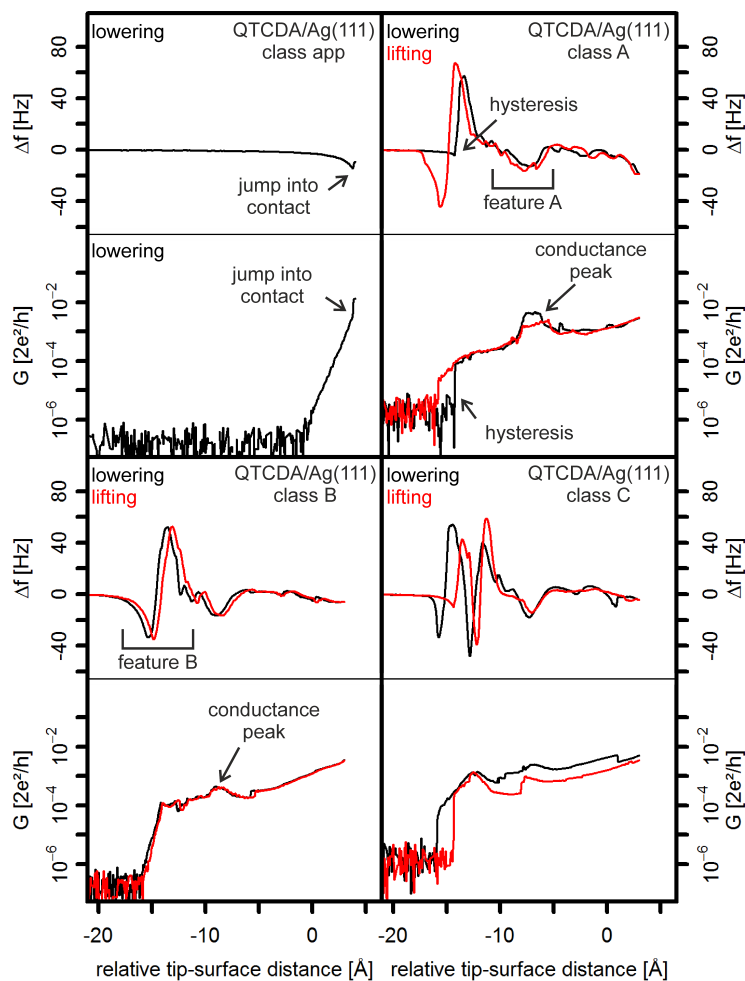


Figure 6.3: The four different classes which were found in all systems investigated, shown here exemplary for QTCDA on Ag(111). The first approach of the bare metal tip towards the molecule of each manipulation is assigned to class app. Class A is characterized by a hysteresis between the lifting and lowering curves. Class B is characterized by a smooth feature B (see chapter 5). To the class C all remaining lifting and lowering curves are assigned.

each 2D histogram has to be determined separately. Therefore the following equation is used:

$$\text{number of bins} = \text{round}((\max(z) - \min(z)) * 10) \quad (6.1)$$

where  $\max(z)$  is the maximum relative tip-surface distance and  $\min(z)$  the minimum relative tip-surface distance of the data used in this particular 2D histogram. From this number of bins the bin size can be calculated as follows:

$$\text{bin size} = \frac{\max(z) - \min(z)}{\text{number of bins}} \quad (6.2)$$

This is done for the frequency shift and the conductance data of each 2D histogram. As the frequency shift is plotted on a linear scale one bin size is given for the z-axis (relative tip-surface distance [ $\text{\AA}$ ]) and one bin size is given for the y-axis ( $\Delta f$  [Hz]). The conductance is plotted on a semi-logarithmic scale. As for the frequency shift one bin size is given for the z-axis (relative tip-surface distance [ $\text{\AA}$ ]). Because of the logarithmic conductance scale the bin size of the y-axis is varying. Therefore the smallest and largest bin size is given for the y-axis ( $G$  [ $2e^2/h$ ]). These two bin sizes are determined using a different approach. To get the smallest bin size the difference between the lower and upper limit of the smallest bin is calculated, to get the largest bin size the difference between the lower and upper limit of the largest bin is calculated. The bin size is given at the end of the caption of every 2D histogram in the form: bin size of z-axis of  $\Delta f$  [ $\text{\AA}$ ], bin size of y-axis of  $\Delta f$  [Hz], bin size of z-axis of  $G$  [ $\text{\AA}$ ], minimum bin size of y-axis of  $G$  [ $2e^2/h$ ] and maximum bin size of y-axis of  $G$  [ $2e^2/h$ ].

The further processing is done by assigning every single one of the lifting or lowering curves of one system substrate-molecule to a certain class. By this the whole statistics of one system is split into the different types of behavior. In table 6.1 the total number of all lifting and lowering curves and the number of lifting and lowering curves assigned to each class are listed. From this table one can see that curves assigned to class B are much more often observed than class A curves, which only represent 16% of the total number of curves.

It is found that the most reproducible data sets were of class B (see Figs. A.11, A.16, A.21, A.26, A.31, A.36, A.41 and A.46 in chapter A). This high reproducibility is the result of a stable junction geometry. Apparently, one stable junction geometry leads to manipulations where the molecule is lifted and lowered over a whole manipulation cycle.

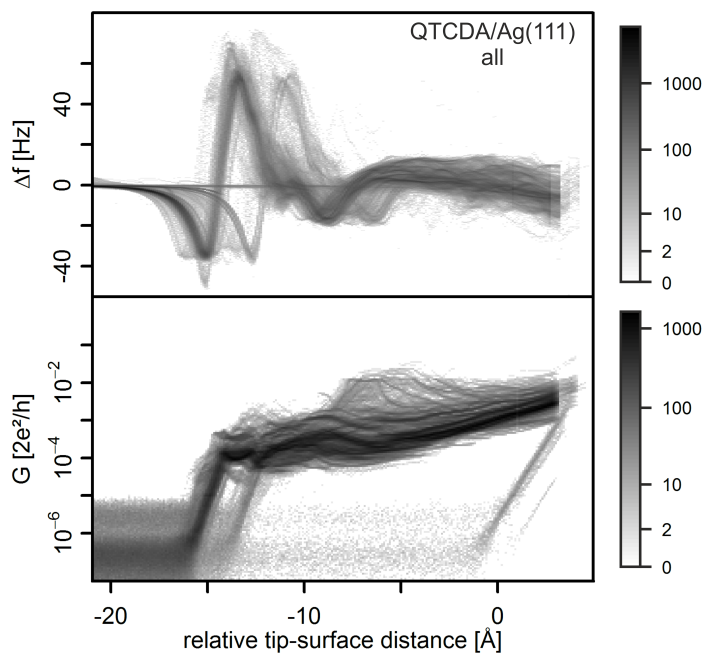


Figure 6.4: 2D histogram of all 4112 curves measured while manipulating QTCDA on Ag(111). The counts are plotted on a logarithmic scale, as can be seen in the legend. In this 2D histogram lifting and lowering curves of all four classes app, A, B and C are represented. To gain physical information from these curves they have to be processed. This is done by splitting them into different classes of behavior. Then shifting each individual curve and finally finding the best representing curve for each class of curves. Bin size of  $\Delta f$ :  $z = 0.1 \text{ Å}$ ,  $y = 0.4 \text{ Hz}$ ; bin size of  $G$ :  $z = 0.1 \text{ Å}$ ,  $\min(y) = 2.8 \times 10^{-21} 2e^2/h$ ,  $\max(y) = 5.2 \times 10^{-3} 2e^2/h$ .

Substrate	Molecule	all	class app	class A	class B	class C
Ag(111)	NTCDA	1748	26	135 (8 %)	1334 (77 %)	253 (15 %)
	PTCDA	3706	54	305 (8 %)	3207 (88 %)	140 (4 %)
	TTCDA	6121	123	1354 (23 %)	4138 (69 %)	506 (8 %)
	QTCDA	4111	74	393 (10 %)	3441 (85 %)	203 (5 %)
Au(111)	NTCDA	2362	51	41 (2 %)	1912 (81 %)	358 (15 %)
	PTCDA	2156	81	404 (19 %)	1504 (72 %)	167 (8 %)
	TTCDA	2384	53	1035 (44 %)	796 (34 %)	500 (21 %)
	QTCDA	793	32	116 (15 %)	184 (24 %)	461 (61 %)

Table 6.1: Total number of lifting and lowering curves and number of lifting and lowering curves assigned to each class. In brackets is denoted the percentage of lifting and lowering curves of each class from the total number of curves.

The molecule does not jump to the tip before the end of these manipulation cycles. At the end of these manipulations it was typically possible to detach the molecule from the tip by a voltage pulse. The tip neither changed its geometry upon contact with the molecule, nor when the contact to the molecule was broken by applying a voltage. The identical molecule then could be contacted again and probed once more. This made it sometimes possible to probe the identical molecule over several days.

In Fig. 6.5 only the curves of the system QTCDA/Ag(111) assigned to class B are shown. The data set is reduced to 3441 curves. As can be seen the individual curves are scattered with respect to the relative tip-surface distance. This is a result of the uncontrolled parameters of the setup, such as the drift, and the hysteresis due to the propagation delay. To get a better representation of the data the curves have to be aligned. This aligning eliminates the fluctuations originating from the parameters just mentioned to some extent.

Next to the class B lifting and lowering curves the curves assigned to class A will be discussed in this chapter. In Fig. 6.6 the 394 curves of class A of QTCDA on Ag(111) are plotted in a 2D histogram. The junction configuration leading to this class of manipulations has a bistable tip-molecule-substrate geometry. The consequence is a hysteresis in the frequency shift and the differential conductance in the region of the global minimum of the frequency shift.

The characteristic of the lifting or lowering curves can change in one manipulation cycle. Sometimes a switching from one class to another is observed. This switching behavior between the different classes is depicted in Fig. 6.7. The segments represent individual



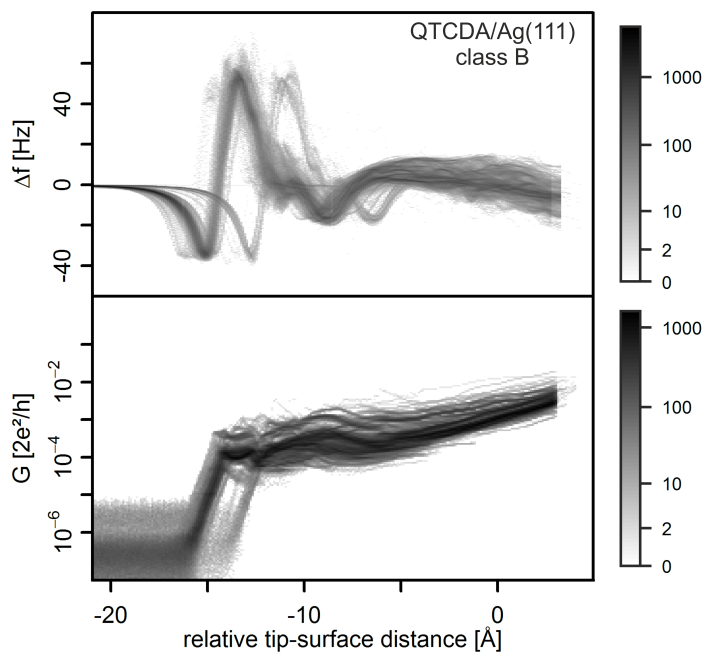


Figure 6.5: 2D histogram of the 3441 curves measured while manipulating QTCDA on Ag(111) assigned to class B. The curves are scattered with respect to the relative tip-surface distance. This happens because some parameters, such as the drift for example, are uncontrolled. By aligning the data the fluctuations due to these parameters can be reduced. Bin size of  $\Delta f$ :  $z = 0.1 \text{ \AA}$ ,  $y = 0.3 \text{ Hz}$ ; bin size of  $G$ :  $z = 0.1 \text{ \AA}$ ,  $\min(y) = 2.8 \times 10^{-21} 2e^2/h$ ,  $\max(y) = 1.9 \times 10^{-3} 2e^2/h$ .

liftings or lowerings. By the up arrow a lifting of the tip is symbolized, by the down arrow a lowering of the tip. In Fig. 6.7a the most often observed scenario is shown. After the initial approach of the tip towards the molecule and the jump into contact the molecule is lifted up. In the first lifting always a switching from a less stable molecule-tip configuration to class B is observed. This switching is characterized by a decrease of the conductance, which suggests that at the beginning of the first lifting always class A is observed. Most of the time a switch to class B is observed during this first lifting. In the following liftings and lowerings only class B characteristic is observed. The first lifting of such a manipulation cycle, which shows class A and class B characteristic, is then assigned to class C. The switching behavior shown in Fig. 6.7b is characterized by the preservation of class A over several liftings and lowerings before switching to class B behavior. In general those class A phases are much less stable and therefore shorter than the class B phases. In Fig. 6.7c a switching from class B to class A is depicted. This switching order was never observed. From these observation it can therefore be concluded that the geometry leading to class A is less stable than the geometry leading to class B. More details will be discussed in section 6.4.2.

### 6.3.2 Aligning the individual curves within class B

In the following the aligning procedure is described. This procedure was only applicable to the curves tagged with class B. Curves of class A were not shifted, as the alignment would screen out the effects of the hysteresis.

The aligning is done by determining a point  $(Z_{\text{shift}}, Y_{\text{shift}})$  which defines where to shift each single lifting and lowering curve  $i$  of a particular system (see Fig. 6.8). This is done by first choosing a value  $Y_{\text{shift}}$  which is global for all liftings or lowerings of one system molecule-substrate. Then the value on the z-scale at which a lifting or lowering curve  $i$  cuts this value  $z_{\text{old},i}$  is determined for each curve. By taking the arithmetic mean of all the z-values determined as just described the value  $Z_{\text{shift}}$  is defined:

$$Z_{\text{shift}} = \frac{1}{N} \sum_{i=1}^n z_{\text{old},i} \quad (6.3)$$

with  $N$  the total number of lifting and lowering curves of one system assigned to class B.

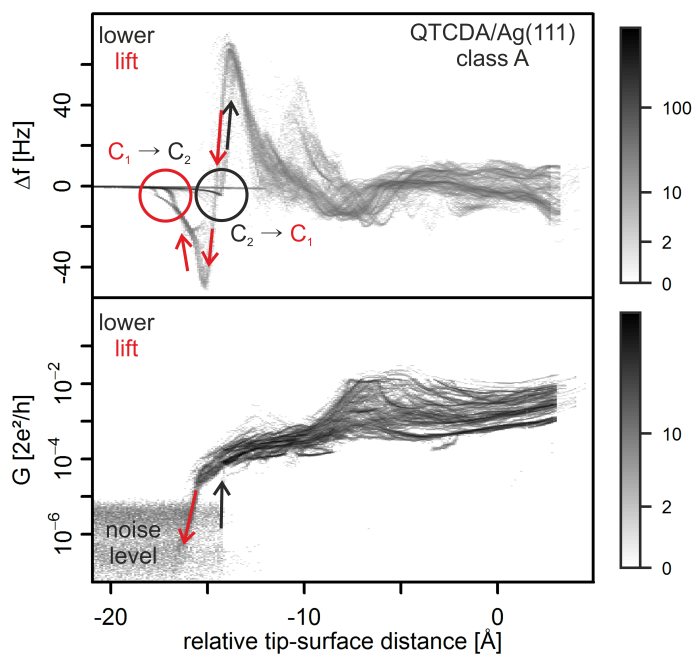


Figure 6.6: 2D histogram of the 394 curves measured while manipulating QTCDA on Ag(111) assigned to class A. This class is observed for bistable junction configuration. This leads to a hysteresis in the frequency shift and differential conductance data. More details will be discussed in section 6.4.2. Bin size of  $\Delta f$ :  $z = 0.1$  Å,  $y = 0.4$  Hz; bin size of  $G$ :  $z = 0.1$  Å,  $\min(y) = 1.6 \times 10^{-12} 2e^2/h$ ,  $\max(y) = 1.6 \times 10^{-3} 2e^2/h$ .

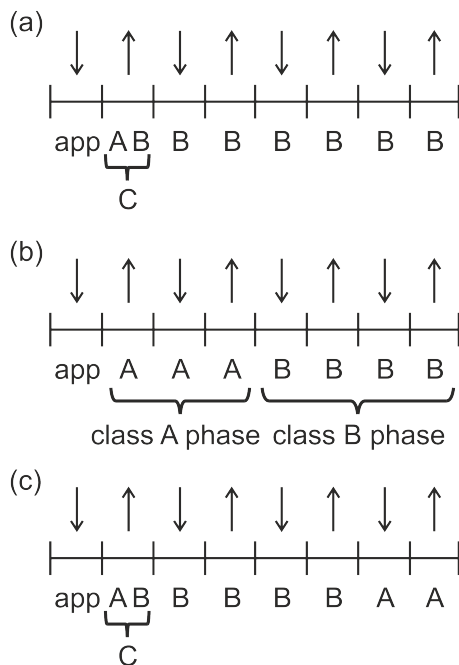


Figure 6.7: Different manipulation scenarios. The segments represent individual liftings (arrow up) or lowerings (arrow down) of the tip. (a) The most common scenario observed: After the initial approach and the jump into contact the molecule is lifted up showing class A characteristic, but switching to class B characteristic during the first lifting (a lifting or lowering which shows the characteristic of two classes is defined as class C and will thus not be used in the further analysis). In the following liftings and lowerings only class B characteristic is observed. (b) Sometimes it is observed that the class A characteristic is stable over several liftings and lowerings. But in most of the cases this class A phases are short compared to the class B phases. (c) It was never observed that once the liftings and lowerings show class B characteristic a switch to class A occurs.

## 6 Systematic study of transport through a homologous series of $\pi$ -conjugated molecules

Then each individual lifting and lowering curve  $i$  is shifted along the  $z$ -scale by  $z_{\text{shift},i}$  such that the following relation is fulfilled:

$$z_{\text{new},i} = z_{\text{old},i} - z_{\text{shift},i} \quad (6.4)$$

After this all curves of one system cross the point  $(Z_{\text{shift}}, Y_{\text{shift}})$  and are thus aligned. This is done for the frequency shift  $\Delta f$  curves of all liftings and lowerings assigned to class B. Each corresponding differential conductance  $dI/dV$  curves  $j$  are then shifted in the same way as the frequency shift  $\Delta f$  curve by  $z_{\text{shift},j}$  with:

$$z_{\text{shift},j} \equiv z_{\text{shift},i} \quad (6.5)$$

From this an average shifting value  $z_{\text{shift,ave}}$  can be determined for each system:

$$z_{\text{shift,ave}} = \frac{1}{N} \sum_{i=1}^N z_{\text{shift},i} \quad (6.6)$$

which gives a value for the scattering of the frequency shift data of a system molecule-substrate at the point where the shifting is performed. Except for the system QTCDA/Au(111) all systems have a very similar average shifting value. The average shifting value of QTCDA/Au(111)  $z_{\text{shift,ave}} = 0.80 \text{ \AA}$  is much higher than the average shifting value of the other systems. This indicates that this measurement was not consistent as will be discussed later in this chapter. In table 6.2 the values  $Z_{\text{shift}}$  and  $Y_{\text{shift}}$  for the alignment of the lifting and lowering curves of each system and the average shifting value  $z_{\text{shift,ave}}$  are listed.

In Fig. 6.8 the 3441 curves, assigned to class B and shifted according to the procedure just introduced, are shown. The red line indicates the chosen value  $Y_{\text{shift}}$  and the red arrow indicates the calculated value  $Z_{\text{shift}}$ . To the intersection of the red line and the arrow each individual frequency shift  $\Delta f$  curve is shifted. The corresponding differential conductance  $dI/dV$  curves are shifted by the same values.

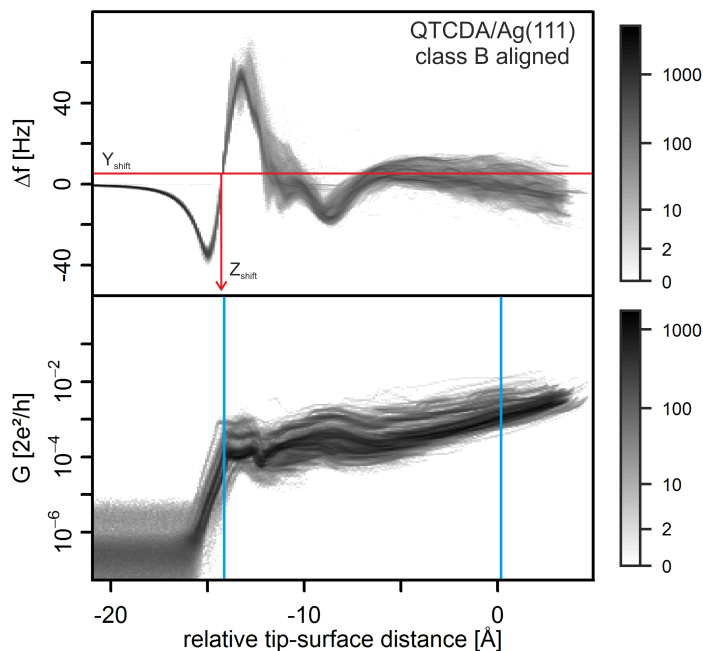


Figure 6.8: 2D histogram of the 3441 curves assigned to class B and shifted according to the procedure described in section 6.3.2. The red line indicates the value  $Y_{\text{shift}}$  chosen to determine the value  $Z_{\text{shift}}$ . Where both lines cross each individual frequency shift  $\Delta f$  curve is shifted. The corresponding differential conductance  $dI/dV$  curves are shifted by the same values. The blue lines indicate in which range the correlation, discussed in section 6.3.3.2, is determined. Bin size of  $\Delta f$ :  $z = 0.1 \text{ \AA}$ ,  $y = 0.3 \text{ Hz}$ ; bin size of  $G$ :  $z = 0.1 \text{ \AA}$ ,  $\min(y) = 2.6 \times 10^{-21} 2e^2/h$ ,  $\max(y) = 1.8 \times 10^{-3} 2e^2/h$ .

Substrate	Molecule	$Z_{\text{shift}}$ [Å]	$Y_{\text{shift}}$ [Hz]	$z_{\text{shift,ave}}$ [Å]
Ag(111)	NTCDA	-1.42	5	0.22
	PTCDA	-5.58	5	0.36
	TTCDA	-9.92	5	0.36
	QTCDA	-14.26	5	0.37
Au(111)	NTCDA	-2.66	5	0.30
	PTCDA	-7.66	5	0.34
	TTCDA	-11.97	5	0.22
	QTCDA	-13.26	5	0.80

Table 6.2: The parameters  $Z_{\text{shift}}$  and  $Y_{\text{shift}}$  determine the point to which each individual curve was shifted.  $Y_{\text{shift}}$  was chosen global to determine the arithmetic mean  $Z_{\text{shift}}$ . The value  $z_{\text{shift,ave}}$  is the average value a lifting or lowering curve is shifted.

### 6.3.3 Finding a curve which represents an individual system best

#### 6.3.3.1 Class A: Determine a generic curve

After assigning each lifting and lowering curve to a class, one generic curve is extracted for all curves of a system assigned to class A. This generic curves of class A are extracted from the unaligned curves, as an alignment would screen out the effects of the hysteresis.

The generic behavior is extracted by calculating the arithmetic mean of the 2D histogram. This was done for the frequency shift and the differential conductance data. In Fig. 6.9 the same 2D histogram as shown in Fig. 6.6 is plotted together with the generic curve (blue curve) of the lifting and lowering curves of QTCDA on Ag(111) assigned to class A. This procedure to obtain a generic curve was applied to all systems investigated. As there were eight systems, there are in total 8 pairs (frequency shift and differential conductance) of generic curves which were extracted from the raw data sets.

In Figs. A.10, A.15, A.20, A.25, A.30, A.35, A.40 and A.45 in chapter A all the 2D histograms together with the generic curves determined as described here are shown. In section 6.4 and 6.5 these generic behaviors of the frequency shift and differential conductance data of the curves assigned to class A will be used to gain physical information. As by taking the arithmetic mean information about the individual curves can get lost, another procedure is applied to find the curve which represents the best the class B lifting and lowering curves.

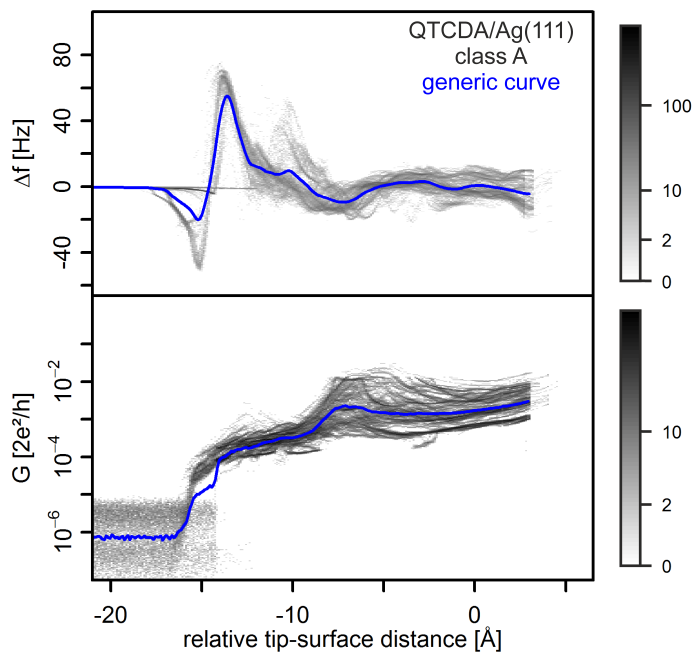


Figure 6.9: 2D histogram of the 393 curves assigned to class A. The blue line is the generic curve obtained by calculating the arithmetic mean of the 2D histogram as described in section 6.3.3.1. Bin size of  $\Delta f$ :  $z = 0.1 \text{ \AA}$ ,  $y = 0.4 \text{ Hz}$ ; bin size of  $G$ :  $z = 0.1 \text{ \AA}$ ,  $\min(y) = 1.6 \times 10^{-12} 2e^2/h$ ,  $\max(y) = 1.6 \times 10^{-3} 2e^2/h$ .



### 6.3.3.2 Class B: Determine the measured curve with the largest correlation with all other curves

The procedure to find the curve which represents the best the lifting and lowering curves assigned to class B is based on determining the correlation between every lifting and lowering curve measured. In principle this correlation can be determined for the frequency shift or the differential conductance data or for a combination of both. For this thesis the correlation is determined upon the differential conductance curves, as the differential conductance is the main quantity we are interested in the further analysis.

The whole procedure to find the best representing curve is a four step process:

**step 1** Align the data set as described in section 6.3.2.

**step 2** Determine the correlation between each differential conductance curve in the data set. The result of this first correlation determination can be plotted in a  $N * N$  matrix (see Fig. 6.10), where  $N$  is the number of curves in the data set. Identify the curve with the best correlation  $L_{best,1}$  with all the other curves of the data set.

**step 3** Shift every differential conductance curve, i.e. multiply, of the data set such that the correlation with the best curve  $L_{best,1}$  is maximized.

**step 4** Repeat step 2 with the shifted differential conductance, i.e. determine again the correlation between each curve in the shifted data set (see Fig. 6.15). From this second correlation determination find the curve with the best correlation  $L_{best,2}$  with all the other curves of the data set.

In step 1 the shifting is performed as described in section 6.3.2, i.e in the example discussed here the data set of QTCDA/Ag(111) class B shown in Fig. 6.8 is used. In step 2 the first correlation is determined. There are several possibilities to determine the correlation between each curve. One possibility is to determine the correlation  $c_{jk}$  between two curves  $j$  and  $k$  by calculating the absolute difference of every differential conductance data point pair  $n$  and then sum up these absolute differences:

$$c_{jk} = \frac{1}{n} \sum_{i=1}^n \frac{2|G_j(i) - G_k(i)|}{G_j(i) + G_k(i)} \quad (6.7)$$

where  $G_j(i)$  is the differential conductance of curve  $j$  at point  $i$ . With the factor  $(G_j(i) + G_k(i))/2$  the correlation  $c_{jk}$  is normalized to the mean value of the differential conductance at point  $n$ . This has to be done as not to weight the correlation on higher conductance values. By the factor  $\frac{1}{n}$  the correlation  $c_{jk}$  is normalized to the number of points  $n$ , which depends on the range used for the correlation determination. In this way correlations of different systems and therefore different lengths and thus different number of points  $n$  can be compared. The number of points are calculated in the following way:

$$n = \frac{|min(z)| + |max(z)|}{20} \quad (6.8)$$

where  $min(z)$  is a value chosen next to the noise level of the measured conductance. This is done to exclude the noise level in the determination of the correlation between two curves (see blue lines Fig. 6.8).  $max(z)$  is the closest distance to the substrate of the curve which is the farthest away from the substrate. This is necessary since a correlation can only be determined if both curves have data points in the investigated range. The factor 20 results from calculating the absolute difference every 0.05 Å. In table 6.3 the three parameters just discussed are listed for all eight systems.

Substrate	Molecule	$min(z)$ [Å]	$max(z)$ [Å]	$n$
Ag(111)	NTCDA	-1.62	3.14	95
	PTCDA	-5.17	0.82	120
	TTCDA	-9.28	0.48	195
	QTCDA	-13.9	0.19	282
Au(111)	NTCDA	-2.76	1.76	90
	PTCDA	-5.29	0.02	106
	TTCDA	-8.29	0.75	181
	QTCDA	-13.02	1.49	290

Table 6.3: By the parameter  $min(z)$  and  $max(z)$  the range used to determine the correlation between two curves is given. With equation 6.8 the number of points  $n$  can be calculated from this range.

Another possibility to determine the correlation  $c_{jk}$  between two curves  $j$  and  $k$  is to calculate the absolute differences of the logarithmic conductance values at every point  $n$  and sum them up:

$$c_{jk} = \frac{1}{n} \sum_{i=1}^n \left| \log_{10} \frac{G_j(i)}{G_k(i)} \right| \quad (6.9)$$

again a factor  $\frac{1}{n}$  is used to normalize the correlation for a better comparison between different systems. The absolute differences of the logarithmic conductance values was chosen to be used for the correlation determination in this thesis. This was done as it was found that most of the dependencies observed in the further analysis show an exponential behavior and are thus represented the best on a logarithmic scale. In fact both ways to determine the correlation, i.e. taking the absolute differences of the conductance values or taking the absolute differences of the logarithmic conductance values, result in twelve out of 16 performed correlation determination in the same curve with the best correlation.

The correlations between each curve, calculated using equation 6.9, are represented in a  $N * N$  matrix (see Fig. 6.10), i.e. each matrix element  $c_{jk}$  gives the correlation between the curves  $j$  and  $k$ . The correlations are plotted on a gray scale, with white the smallest value ( $c_{jk} = 0$ , largest correlation) and black the highest  $c_{jk}$  (smallest correlation). For the  $N * N$  matrix this means that the diagonal line is white, as in the diagonal line the correlation between the same curve is given, which is always zero. Further each correlation is represented two times in the matrix as the correlation between curve  $j$  and  $k$  is the same as the correlation between curve  $k$  and  $j$ . Therefore the matrix elements are mirrored at the diagonal line.

From the correlation matrix the curve with the best correlation  $L_{\text{best},1}$  within respect of all other curves can be determined. This is done by summing up every row of the  $N * N$  matrix. This results in a total correlation  $C_{i,1}$  for every curve  $i$  (see Fig. 6.11). The curve  $L_{\text{best},1}$  with the minimum  $C_{i,1}$  is then considered to be the curve which represents the best the data set investigated, as the smaller the correlation value the higher the correlation between two curves. In Fig. 6.12 this best representing curve, called generic curve 1, is plotted together with the data set QTCD/Ag(111) of class B investigated here. See Figs. A.12, A.17, A.22, A.32, A.37, A.42 and A.47 in chapter A for the generic curves of the other seven systems investigated.

This best representing curve  $L_{\text{best},1}$  could already be used for the further analysis. But it is believed that an additional step gives an even better representing curve for each system. In Fig. 6.8 in the region 12 Å to 15 Å three different conductance branches can be identified. As they all show the same behavior it is assumed that the difference in

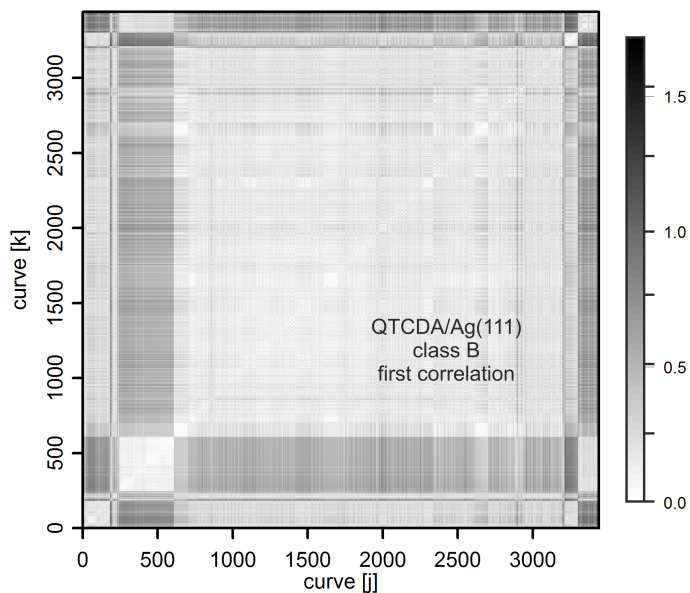


Figure 6.10: First correlation matrix of the aligned QTCDA/Ag(111) curves of class B. Every matrix element represents one correlation value, i.e. the matrix element  $c_{jk}$  gives the correlation between the curves  $j$  and  $k$ . The darker the matrix element the smaller the correlation between the two curves. The correlation value determined between a curve and itself is zero, therefore the diagonal line is white. Also every correlation value is represented two times, as the correlation between curve  $j$  and  $k$  is the same as the correlation between curve  $k$  and  $j$ . This results in the mirroring of the matrix elements at the diagonal.

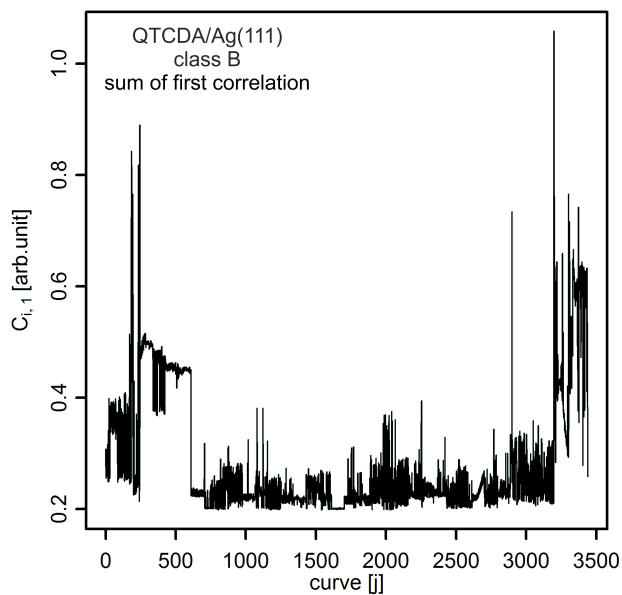


Figure 6.11: Sum of the first correlation matrix of the aligned QTCDA/Ag(111) curves of class B. This sum was calculated summing up the matrix elements of every column of the  $N * N$  matrix shown in Fig. 6.10. The curve with the smallest sum is then considered to be the best representing curve  $L_{\text{best},1}$  of the aligned data set.

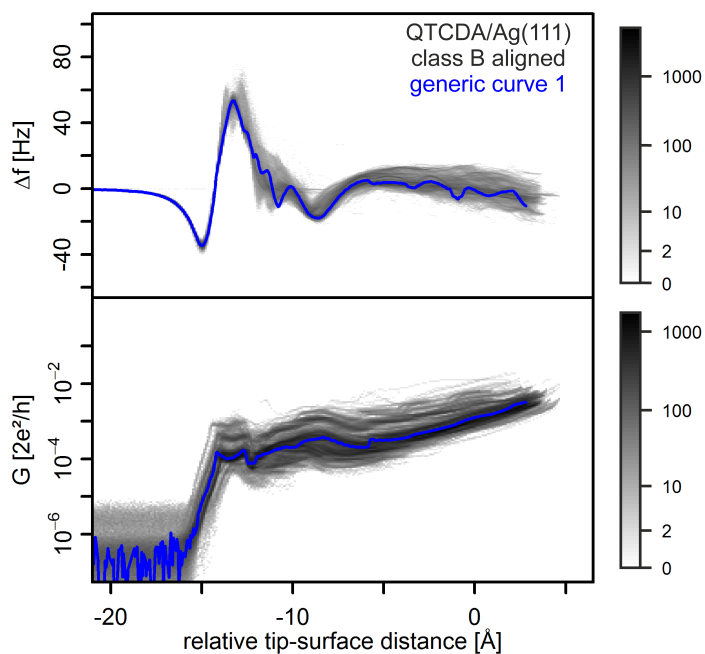


Figure 6.12: The blue curve is the best representing curve  $L_{\text{best},1}$ , called generic curve, of the aligned QTCDA/Ag(111) of class B. This curve is plotted together with the whole data set used for the correlation determination. It is the same histogram as shown in Fig. 6.8. Bin size of  $\Delta f$ :  $z = 0.1 \text{ \AA}$ ,  $y = 0.3 \text{ Hz}$ ; bin size of  $G$ :  $z = 0.1 \text{ \AA}$ ,  $\min(y) = 2.6 \times 10^{-21} 2e^2/h$ ,  $\max(y) = 1.8 \times 10^{-3} 2e^2/h$ .

the conductance magnitude is not an intrinsic feature of the junction only. It is rather believed that other parameters, e.g. the geometry of the contacts, affect the conductance magnitude as well. Therefore, to eliminate the influence of these parameters, we multiply the conductance values by a normalization factor. In the logarithmic plot  $\log \frac{dI}{dV}$  vs.  $z$ , this multiplication corresponds to vertical shifts of the curves. In this way the correlation with the best correlating curve can be maximized for each differential conductance curve. This new set of conductance curves, determined by multiplication, is shown in the 2D histogram in Fig. 6.18.

The multiplication factors used to shift each individual curve can be plotted in a histogram (see Figs. 6.13 and 6.14). By calculating the normal distribution of each histogram the full width at half maximum (FWHM) of each system can be determined. It is found that the average FWHM determined from the manipulations on Ag(111) is 0.079 and thus substantially higher than the average FWHM found for the manipulations on Au(111) (0.051). This could be a consequence of the larger coupling between the molecule and the silver tip compared to the coupling between the molecule and the gold tip. The larger coupling could allow more transport path and thus a larger spectrum of conductance in the case of silver.

With this new set of conductance curves step 2 can be repeated. Again a  $N*N$  correlation matrix can be determined (see Fig. 6.15). In this second correlation matrix every matrix element has a smaller value as every curve was multiplied such that the correlation to the best representing curve  $L_{\text{best},1}$  is maximized. The smaller correlation values can be shown by looking at the histogram of all correlation values. This is shown in Fig. 6.16 where the red line denotes the histogram of the correlation values calculated for the unshifted differential conductance and the green line denotes the shifted differential conductance data correlation values histogram. It can be seen that after the shifting the correlation values are smaller, i.e. the correlation between each pair of curves is higher. See Figs. A.49 to A.56 in chapter A for the histograms of the correlation values of all eight systems probed.

From this second correlation matrix the sum of every column can now be calculated, resulting in the total correlation  $C_{i,2}$  of every curve with all other curves shown in Fig. 6.17. Finally by choosing the curve with the smallest total correlation value  $C_{i,2}$  the best representing curve  $L_{\text{best},2}$  of the aligned and shifted QTCDA/Ag(111) curves of class B is determined. In Fig. 6.18 this best representing curve  $L_{\text{best},2}$ , called generic curve 2, is shown together with the 2D histogram of the aligned and shifted QTCDA/Ag(111) curves of class B. See Figs. 6.19 to 6.25 for the generic curves 2 of the other seven

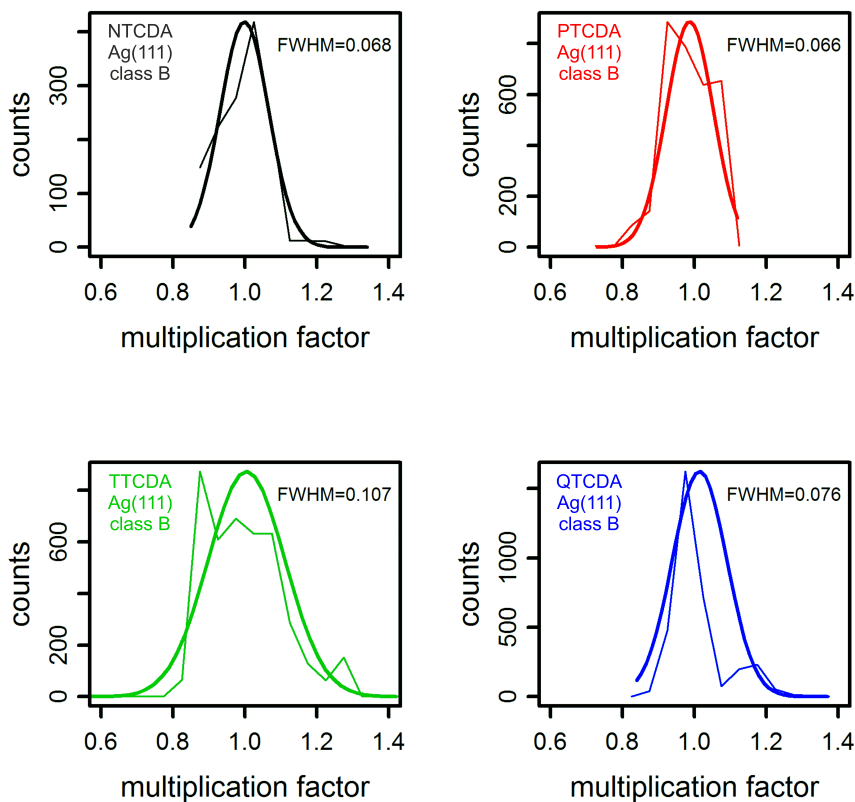


Figure 6.13: Histogram of multiplication factors used to shift each individual curve to maximize the correlation to the generic curve 1 for class B lifting and lowering curves on Ag(111). By fitting this histogram with a normal distribution the full width at half maximum (FWHM) is determined. An average FWHM of 0.079 is found for Ag(111).



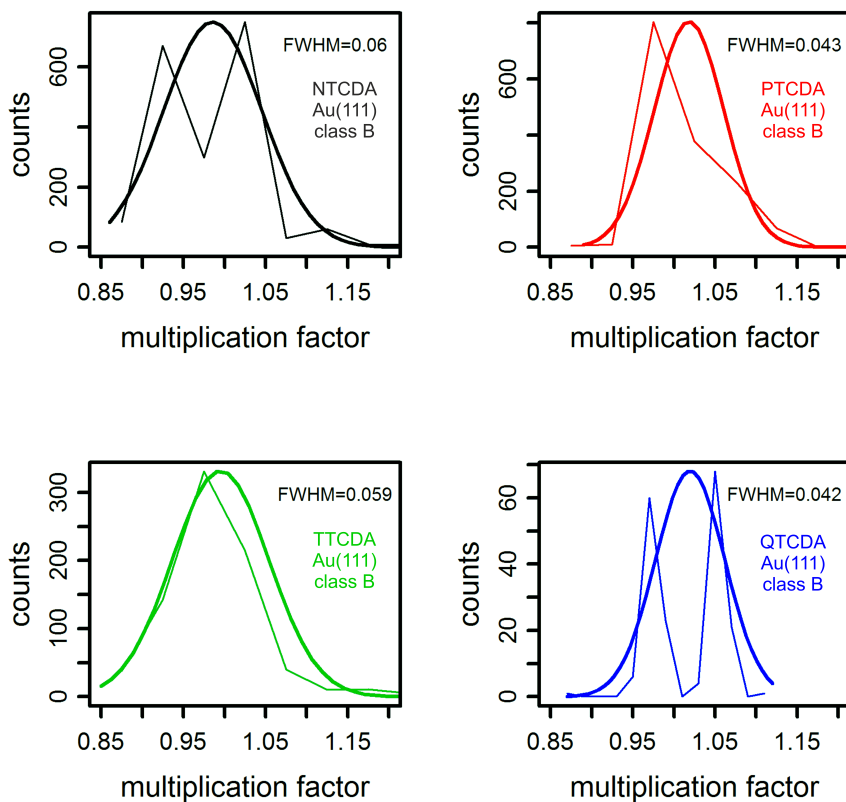


Figure 6.14: Histogram of multiplication factors used to shift each individual curve to maximize the correlation to the generic curve 1 for class B lifting and lowering curves on Au(111). By fitting this histogram with a normal distribution the full width at half maximum (FWHM) is determined. An average FWHM of 0.051 is found for Au(111).

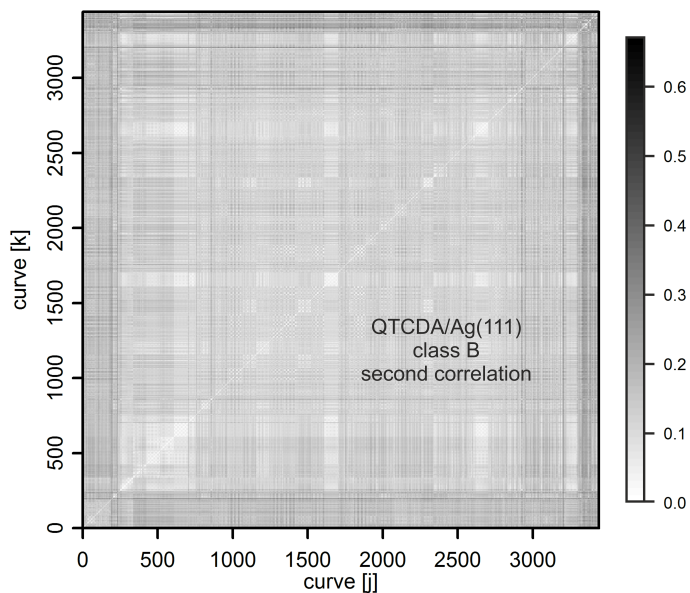


Figure 6.15: Second correlation matrix of the aligned and shifted QTCDA/Ag(111) curves of class B. Every matrix element is smaller than the corresponding matrix element of the first correlation matrix (see Fig. 6.10). This is a result of the shifting of the conductance curves.

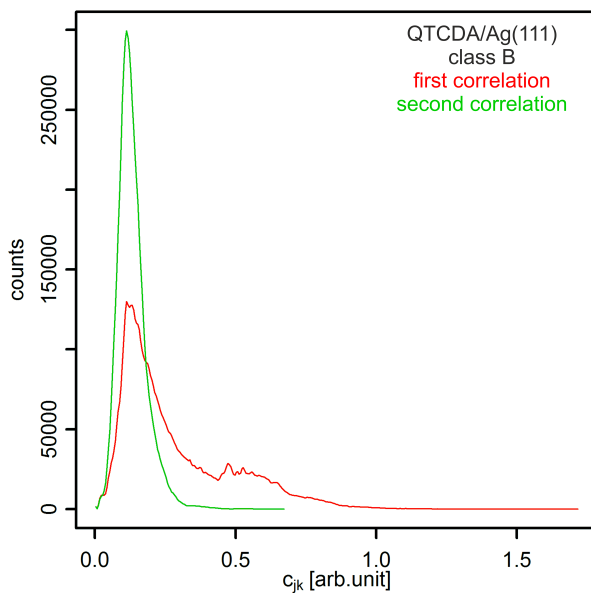


Figure 6.16: Comparing the first and second correlation values of QTCDA/Ag(111) (class B). The second correlation values (green) are smaller than the first correlation values (red) as every conductance curve was shifted such, that the correlation with the best representing curve  $L_{\text{best},1}$  is maximized.

systems investigated. Note that the generic curves of the systems NTCDA/Au(111) and PTCDA/Au(111) are significantly shorter than the ones for the other six systems. These two curves are the result of an attempt to get more reproducible manipulations by not lifting the molecule up completely from the substrate. This procedure was later not continued as it was found that it had no influence on the reproducibility of the manipulations.

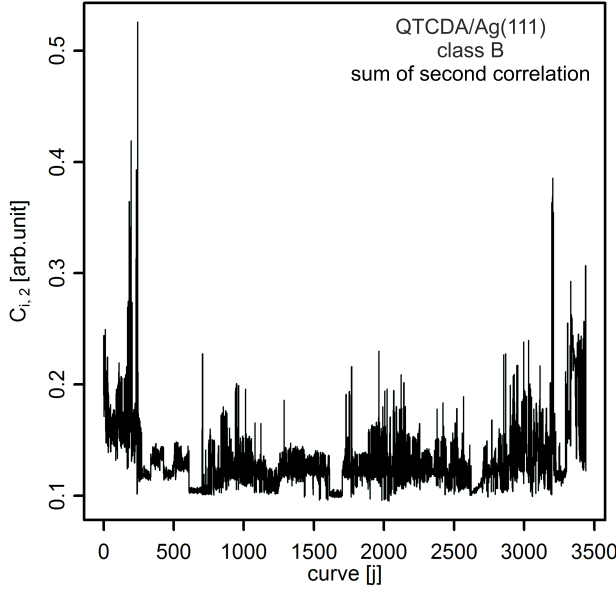


Figure 6.17: Sum of the second correlation matrix of the aligned QTCDA/Ag(111) curves of class B. This sum was calculated summing up the matrix elements of every column of the  $N \times N$  matrix shown in Fig. 6.15. The curve with the smallest sum is then considered to be the best representing curve  $L_{\text{best},2}$  of the aligned and shifted data set.

### 6.3.4 Exponential decay in the tunneling barrier

After having explained the procedure to extract the best representing curve for class A (arithmetic mean) and class B (largest correlation), in the following these curves will be used for the further analysis. As shown in chapter 3 the current decays exponentially

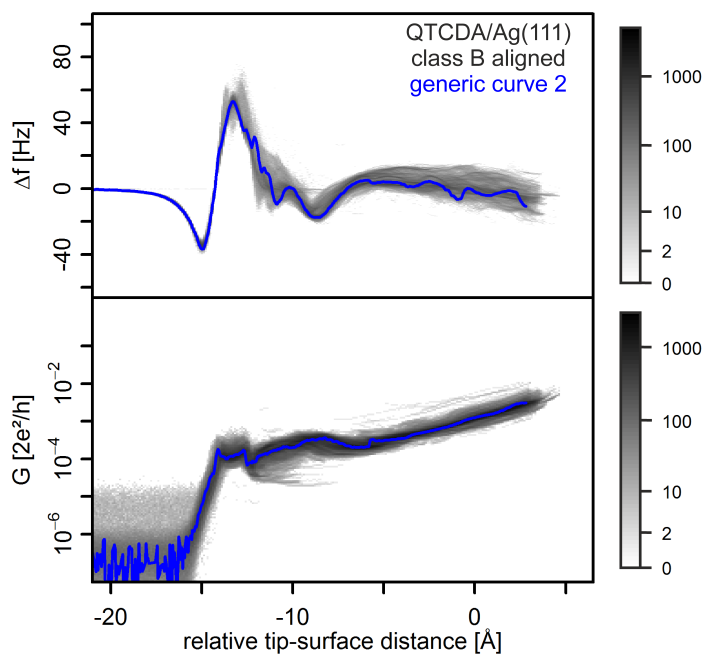


Figure 6.18: The blue curve is the best representing curve  $L_{\text{best},2}$  of the aligned and shifted QTCDA/Ag(111) of class B. This curve is plotted together with the whole data set used for the correlation determination. In contrast to the data set shown in Fig. 6.8, the conductance curves are shifted by multiplication as described in section 6.3.3.2. Bin size of  $\Delta f$ :  $z = 0.1 \text{ \AA}$ ,  $y = 0.3 \text{ Hz}$ ; bin size of  $G$ :  $z = 0.1 \text{ \AA}$ ,  $\min(y) = 1.6 \times 10^{-21} 2e^2/h$ ,  $\max(y) = 1.0 \times 10^{-3} 2e^2/h$ .

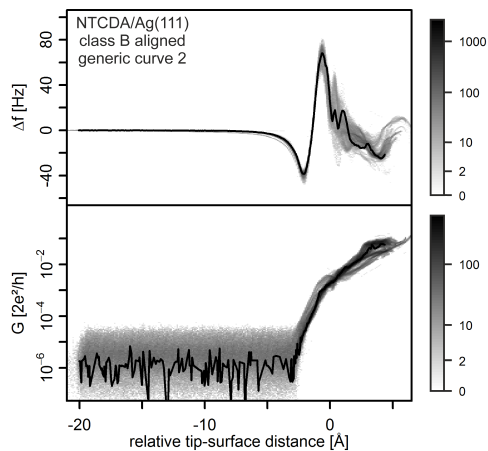


Figure 6.19: NTCDA/Ag(111) lifting and lowering curves of class B aligned with the generic curve 2. Bin size of  $\Delta f$ :  $z = 0.1 \text{ \AA}$ ,  $y = 0.5 \text{ Hz}$ ; bin size of  $G$ :  $z = 0.1 \text{ \AA}$ ,  $\min(y) = 2.6 \times 10^{-12} 2e^2/h$ ,  $\max(y) = 1.2 \times 10^{-2} 2e^2/h$ .

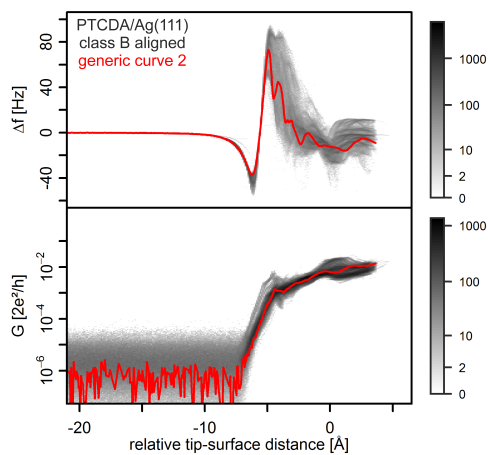


Figure 6.20: PTCDA/Ag(111) lifting and lowering curves of class B aligned with the generic curve 2. Bin size of  $\Delta f$ :  $z = 0.1 \text{ \AA}$ ,  $y = 0.4 \text{ Hz}$ ; bin size of  $G$ :  $z = 0.1 \text{ \AA}$ ,  $\min(y) = 1.7 \times 10^{-13} 2e^2/h$ ,  $\max(y) = 1.8 \times 10^{-3} 2e^2/h$ .

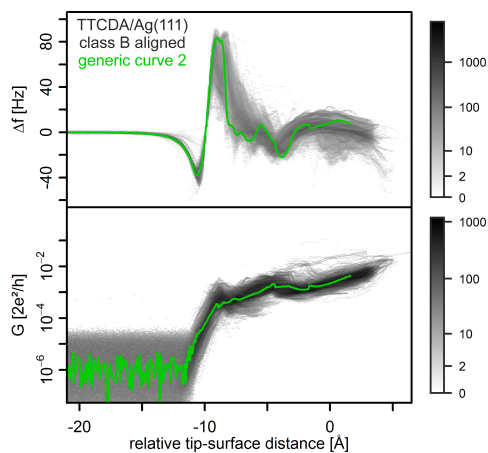


Figure 6.21: TTCTDA/Ag(111) lifting and lowering curves of class B aligned with the generic curve 2. Bin size of  $\Delta f$ :  $z = 0.1 \text{ \AA}$ ,  $y = 0.4 \text{ Hz}$ ; bin size of  $G$ :  $z = 0.1 \text{ \AA}$ ,  $\min(y) = 5.7 \times 10^{-15} 2e^2/h$ ,  $\max(y) = 7.0 \times 10^{-3} 2e^2/h$ .

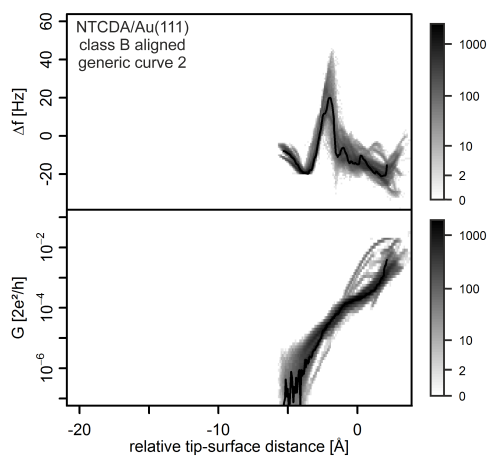


Figure 6.22: NTCTDA/Au(111) lifting and lowering curves of class B aligned with the generic curve 2. Bin size of  $\Delta f$ :  $z = 0.1 \text{ \AA}$ ,  $y = 0.9 \text{ Hz}$ ; bin size of  $G$ :  $z = 0.1 \text{ \AA}$ ,  $\min(y) = 3.4 \times 10^{-12} 2e^2/h$ ,  $\max(y) = 6.9 \times 10^{-3} 2e^2/h$ .

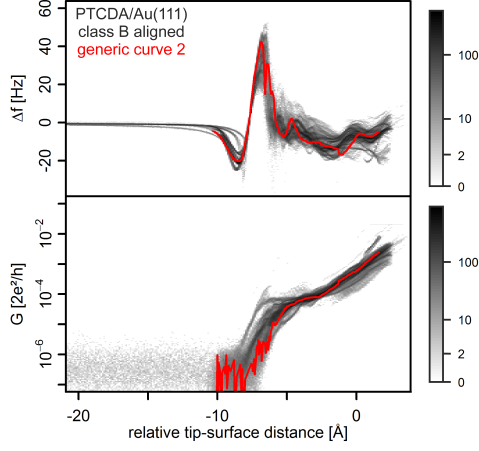


Figure 6.23: PTCDA/Au(111) lifting and lowering curves of class B aligned with the generic curve 2. Bin size of  $\Delta f$ :  $z = 0.1 \text{ \AA}$ ,  $y = 0.3 \text{ Hz}$ ; bin size of  $G$ :  $z = 0.1 \text{ \AA}$ ,  $\min(y) = 4.1 \times 10^{-14} 2e^2/h$ ,  $\max(y) = 1.7 \times 10^{-3} 2e^2/h$ .

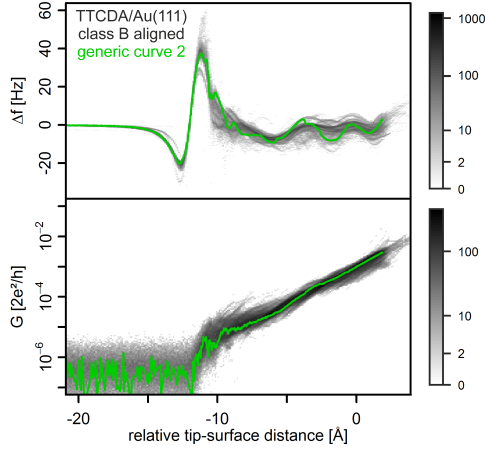


Figure 6.24: TTCDA/Au(111) lifting and lowering curves of class B aligned with the generic curve 2. Bin size of  $\Delta f$ :  $z = 0.1 \text{ \AA}$ ,  $y = 0.3 \text{ Hz}$ ; bin size of  $G$ :  $z = 0.1 \text{ \AA}$ ,  $\min(y) = 1.7 \times 10^{-21} 2e^2/h$ ,  $\max(y) = 1.8 \times 10^{-3} 2e^2/h$ .



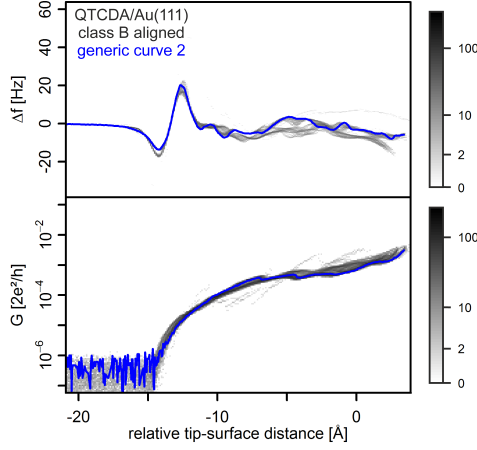


Figure 6.25: QTCDA/Au(111) lifting and lowering curves of class B aligned with the generic curve 2. Bin size of  $\Delta f$ :  $z = 0.1 \text{ \AA}$ ,  $y = 0.2 \text{ Hz}$ ; bin size of  $G$ :  $z = 0.1 \text{ \AA}$ ,  $\min(y) = 1.8 \times 10^{-22} 2e^2/h$ ,  $\max(y) = 1.5 \times 10^{-3} 2e^2/h$ .

with the barrier width  $z$  in a tunneling barrier (see equation 3.19). The conductance  $G$  is the ratio between the current and the voltage ( $G = I/V$ ). Therefore a characteristic decay constant  $\beta$  for the conductance  $G$  can be defined as:

$$G \propto e^{-\beta z} \quad (6.10)$$

In the study presented in this chapter this exponential decay constant is analyzed. This decay constant is defined for different scenarios. In Fig. 6.26 all investigated exponential decay constant  $\beta$  are depicted. The exponential decay constants in Fig. 6.26a-c are measured for every type of molecule separately. The bare metal tip tunneling decay constant ( $\beta_{\text{silver tip}}$  and  $\beta_{\text{gold tip}}$ ) is measured by approaching the bare metal (silver or gold) tip towards the molecule and record the zero-bias differential conductance. The contact tunneling decay constant  $\beta_{\text{contact}}$  is measured by approaching the tip, with the molecule in contact to the tip and the substrate, towards the surface and record the zero-bias differential conductance. And finally the vacuum tunneling decay constant  $\beta_{\text{vacuum}}$  is measured by approaching the tip, with the molecule bonded to the tip, towards the surface, while the molecule has no contact to the surface.

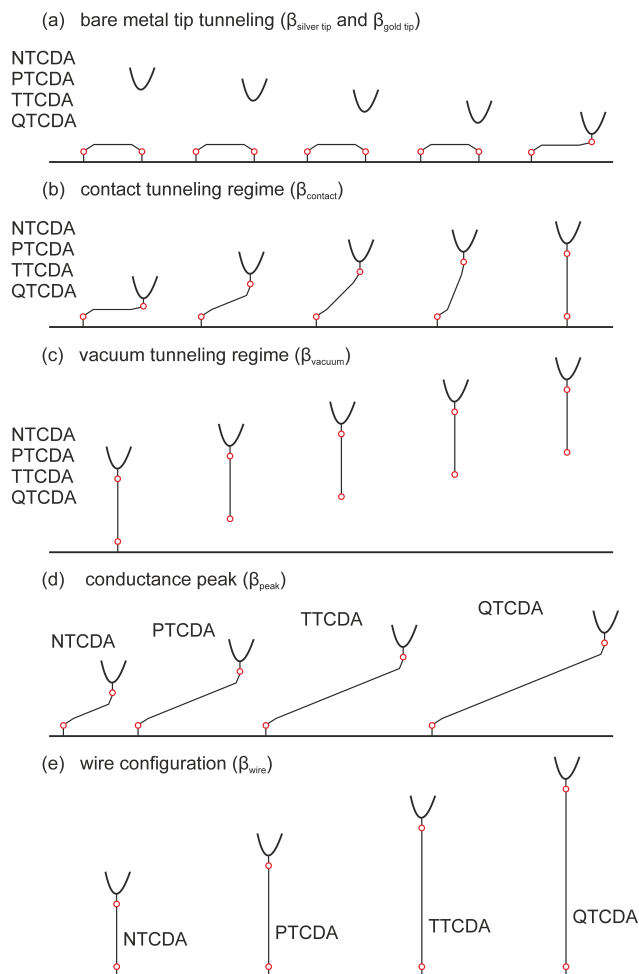


Figure 6.26: Different types of decay constants that are determined in the following. (a)-(c) These decay constants are determined separately for each molecule. (d)-(e) These decay constants are determined by measuring the conductance for each molecule at a specific geometrical junction configuration and plotting the conductance values versus the molecule length.

The decay constants in Fig. 6.26d-e are determined by measuring a single zero-bias differential conductance value for each molecule and then plot it versus the molecule length. The conductance peak decay constant  $\beta_{\text{peak}}$  is determined by measuring the differential conductance of the molecule at the position where a peak is observed. The wire configuration decay constant  $\beta_{\text{wire}}$  is determined by measuring the conductance for each molecule as the molecule is standing upright in the junction.

## 6.4 Results: Molecular wires on Ag(111)

In the first part of this section the manipulations with silver electrodes assigned to class B are presented. Based on the generic curve 2 of QTCDA on Ag(111) (see section 6.3.3.2) it is explained how features are identified and quantified. These quantified features are then used to interpret the generic curves. It will be shown that the transport through molecules on Ag(111) can be split into two regimes. Then the observation of a conductance peak will be discussed. Finally the conductance through the molecular wire, i.e. through the upright standing molecule, will be determined from the data. In the second part of the section the findings regarding manipulations of class A are presented, based on the generic curves as introduced in section 6.3.3.1. First the origin of the hysteresis will be discussed. Then the even stronger conductance peak observed in class A will be discussed. All these discussions will be focused on the comparison of class A and class B.

The procedure to class, align, calculate the correlations and determine the generic curve as described in section 6.3.3.2 was applied to the data sets of all four molecules on Ag(111) assigned to class B. For each of the four molecules all lifting and lowering curves assigned to class B were used for the determination of the generic curve. The procedure to class, align, and determine the generic curve as described in section 6.3.3.1 was applied to the data sets of all four molecules on Ag(111) assigned to class A. For each of the four molecules all lifting and lowering curves tagged as class A were used for the determination of the generic curve. In table 6.4 the total number of lifting and lowering curves used are listed.

### 6.4.1 Manipulations of class B on Ag(111)

The generic curves 2 for all manipulations of molecules on Ag(111) assigned to class B are shown in Fig. 6.27. The generic curve 2 determined from the NTCDA on Ag(111) lifting

Molecule	class A	class B
NTCDA	135	1334
PTCDA	305	3207
TTCDA	1354	4138
QTCDA	393	3441

Table 6.4: Number of lifting and lowering curves of the Ag(111) manipulations used for the statistical analysis.

and lowering curves reaches to much higher positive  $z$ -values. The reason is a slightly different way to manipulate NTCDA on silver. The tip was moved much closer to the substrate after the tip-molecule contact was established by the jump into contact. This was done to observe the dip in the frequency shift and the peak in the conductance close to the substrate ( $z \approx 4 \text{ \AA}$ ). The disadvantage of this procedure was a higher instability in the region close to the substrate, as the forces in the junction increase significantly in that region. As no features were observed for the other molecules in that region, the manipulations of them were not carried out so close to the metal. In Fig. 6.28 the generic curve 2 of QTCDA on Ag(111) of class B is shown, with the differential conductance plotted on a linear scale. In Figs. A.61 to A.64 in chapter A the generic behaviors with the differential conductance on a linear scale of all eight systems are shown for comparison. In the following of this chapter the logarithmic representation of the differential conductance will be used to interpret the generic behaviors.

The interpretation of the physics in the junction during the manipulation will be done by the observation of features in the generic curves and their quantitative analysis. Remember that the frequency shift can be directly related to the stiffness  $k = \frac{dF}{dz}$  of the tip-molecule-substrate junction, where  $F$  is the force acting on the tip and  $z$  is the relative tip-surface distance [42, 43] (for more details see chapter 5). In the upper panel of Fig. 6.29 the generic frequency shift of QTCDA/Ag(111) of class B is shown. In the lower panel the integrated frequency shift, i.e. the force  $F$ , is shown. By the arrows is shown that a peak or a dip in the frequency shift corresponds to an inflexion point in the force. Note that the force is positive, i.e. repulsive, at the beginning of the lifting process. This positive force is spurious and stems from the combined effects of the surface corrugation, the elasticity of the tip material and the finite oscillation of the tip [151].

In Fig. 6.30 the two generic curves of QTCDA on Ag(111) assigned to class B are shown. The points and arrow indicate some features that were identified and will be used in the

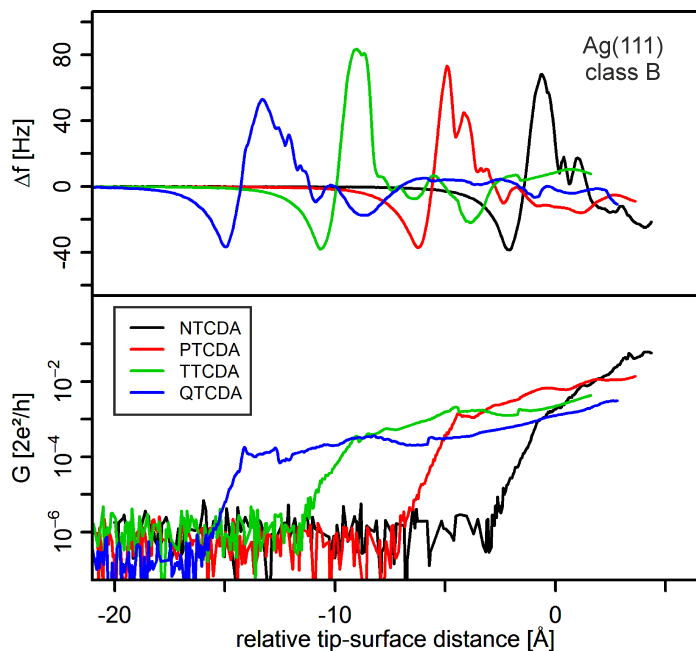


Figure 6.27: The generic curves 2 of all four molecules on Ag(111) of class B. The upper panel shows the generic behavior of the frequency shift, the lower panel shows the zero-bias differential conductance behaviors. In section 6.3 the procedure to calculate these generic curves was described.

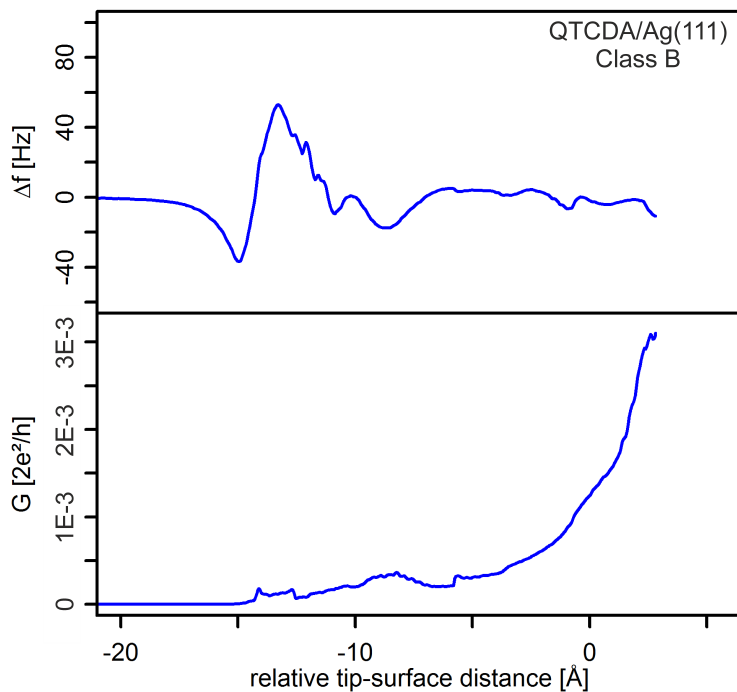


Figure 6.28: The generic behavior of QTCDA on Ag(111) of class B. The same data as in Fig. 6.27 is shown, but with the differential conductance plotted on a linear scale.

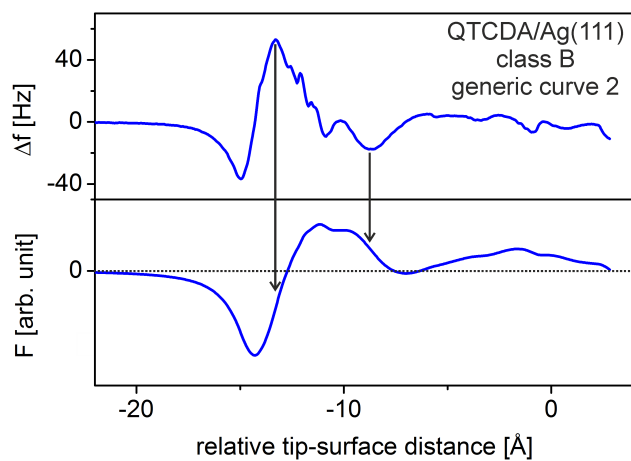


Figure 6.29: The upper panel shows the generic frequency shift of QTCDA/Ag(111) and the lower the force acting on the tip determined by integrating the frequency shift. By the arrows is shown that a peak or a dip in the frequency shift corresponds to a inflexion point in the force.

following. The point  $P_2$  indicates a peak in the conductance data and is at the position of the last dip in the frequency shift before feature B as shown by the arrow. With the points  $P_1$ ,  $P_3$ ,  $P_4$  and  $P_5$  two different slopes are identified in the differential conductance data. By making two separate linear regressions (purple lines) these two different slopes are quantified. The point  $P_4$  further marks the transition between the two slopes and is in the region of the global peak of the frequency shift data.

In the following the discussed points are summarized:

$P_1$  Conductance  $G_{\text{start}}$  at the closest z-position relative to the substrate.

$P_2$  The conductance peak  $G_{\text{peak}}$ . This peak matches with a dip in the frequency shift, as indicated by the arrow.

$P_3$  Conductance selected to determine the first slope by making a linear regression.

$P_4$  The knee  $G_{\text{wire}}$  in the conductance data. This knee is in the region of the global peak in the frequency shift.

$P_5$  Conductance  $G_{\text{end}}$  at the transition of the conductance data to the noise level.

In Figs. A.57 to A.60 in chapter A all generic curves and the corresponding points, linear regressions and the arrow are shown. In table 6.5 the coordinates of the points are listed.

Molecule	$P_1$ [ $\text{\AA}$ , $2e^2/h$ ]	$P_2$ [ $\text{\AA}$ , $2e^2/h$ ]	$P_3$ [ $\text{\AA}$ , $2e^2/h$ ]
NTCDA	$(4.36, 5.80 \times 10^{-2})$	$(4.08, 6.01 \times 10^{-2})$	$(-0.86, 9.01 \times 10^{-4})$
PTCDA	$(3.62, 1.38 \times 10^{-2})$	$(1.22, 8.81 \times 10^{-3})$	$(-3.64, 1.10 \times 10^{-3})$
TTCDA	$(1.60, 4.33 \times 10^{-3})$	$(-3.87, 1.69 \times 10^{-3})$	$(-8.90, 2.60 \times 10^{-4})$
QTCDA	$(2.81, 3.10 \times 10^{-3})$	$(-8.66, 3.28 \times 10^{-4})$	$(-12.47, 7.21 \times 10^{-5})$
Molecule	$P_4$ [ $\text{\AA}$ , $2e^2/h$ ]	$P_5$ [ $\text{\AA}$ , $2e^2/h$ ]	
NTCDA	$(-0.86, 8.65 \times 10^{-4})$	$(-2.51, 7.58 \times 10^{-6})$	
PTCDA	$(-4.43, 1.38 \times 10^{-3})$	$(-6.51, 3.91 \times 10^{-6})$	
TTCDA	$(-9.02, 3.53 \times 10^{-4})$	$(-11.04, 5.87 \times 10^{-6})$	
QTCDA	$(-14.09, 1.77 \times 10^{-4})$	$(-15.36, 1.21 \times 10^{-6})$	

Table 6.5: The coordinates of the points  $P_1$ ,  $P_2$ ,  $P_3$ ,  $P_4$  and  $P_5$  as defined above for the class B manipulations of all four molecules on Ag(111).



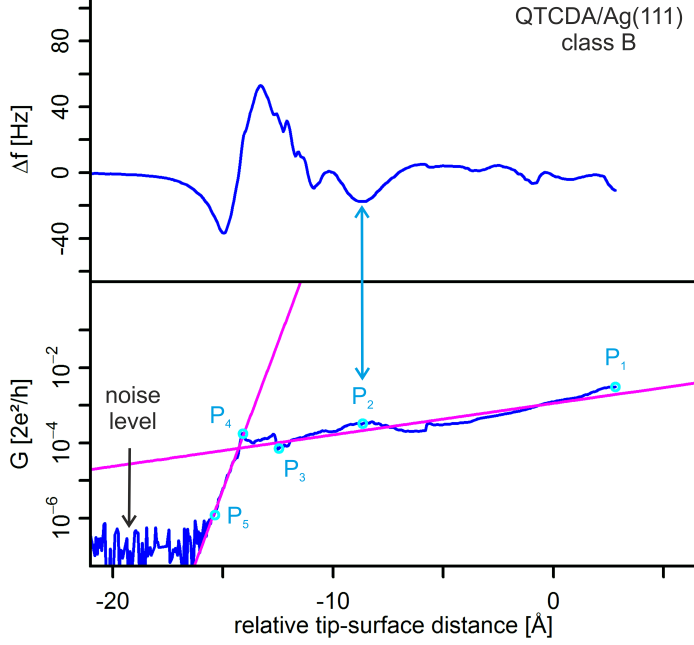


Figure 6.30: The generic behavior of QTCDA on Ag(111) lifting and lowering curves assigned to class B. Five points were chosen, which will be used to discuss the transport through the molecules.  $P_1$  indicates the conductance measured the closest to the substrate.  $P_5$  indicates the point of the transition of the conductance data to the noise level.  $P_2$  is at the position of a peak  $G_{\text{peak}}$  in the conductance. This conductance peak matches with a dip in the frequency shift, which is indicated by a blue arrow.  $P_4$  is at the position of a knee in the conductance. This knee is in the region of the global peak in the frequency shift. By making two linear regressions (purple lines) between the points  $P_1$  and  $P_3$  and  $P_4$  and  $P_5$  the two slopes of the conductance data are quantified. For all eight systems investigated (NTCDA, PTCDA, TTCDA and QTCDA on Ag(111) and Au(111)) the points  $P_1$  to  $P_5$  can be found in chapter A.

**6.4.1.1 Two transport regimes**

Having defined the points  $P_1$  to  $P_5$  in the previous section, we can discuss general trends. The conductance in the beginning of the manipulation is larger the smaller the molecule is (see  $P_1$  in table 6.5). This difference in the conductance is a result of the position of the LUMO at the beginning of the manipulation. In Fig. 4.3 in section 4.2.1 it was shown that the smaller the molecule is, the closer the LUMO is to the Fermi level. The larger density of states at the Fermi level for smaller molecules results in a larger conductance.

Further the generic conductance curve has two distinct branches,  $P_1$  to  $P_3$  and  $P_4$  to  $P_5$ . We call these two branches two transport regimes. Both show an exponential drop of the conductance which suggests tunneling. Note however that exponential behavior of tunneling follows from exponential drop of wave function tails. Overlap of wave function tails is the relevant quantity here.

The first transport regime takes place as long as the molecule is in contact or overlapping with the substrate, i.e. as long as the molecule or at least some of its parts are chemically interacting with the metal. We call it contact tunneling regime. During this regime the LUMO is sharpened and shifted towards the Fermi level. Wave function overlap remaining the same, this should increase the conductance at zero bias. However, in the present case not only the energetic position of the LUMO changes, but also the overlap with relevant states in the metal. Apparently, this wave function overlap is reduced exponentially, such that exponential behavior results.

The second transport regime is observed after the contact of the molecule to the substrate is broken (from  $P_4$  to  $P_5$ ). It is obvious that in this regime wave function overlap between bottom of the molecule and metal surface is reduced exponentially as the tip is retracted. Therefore it is not surprising to observe tunneling here. We name the second transport regime vacuum tunneling regime.

These findings are summarized in Fig. 6.31. The pictogram show the simplified geometry of the junction required for the two transport regimes. Note that in the contact tunneling regime small deviations from strictly exponential behavior are observed. These will be discussed in section 6.4.1.2. Moreover, in the transition region between the two transport regimes a more complex behavior is observed. It is found that the conductance increases shortly before the contact is broken. From force-field simulations (see chapter 5) we know that the molecule is stretched shortly before the breaking of the contact,

it was found that the molecular diagonal of PTCDA is stretched by 0.5% on Au(111). As the interaction between Ag(111) and the molecules is stronger a larger stretching is assumed for the manipulations on silver. This could in principle lead to modifications in the electronic structure of the molecule (at unchanged overlap) with the possible outcome that the conductance could increase. For example, Bruot *et al.* [152] observed that the conductance through a 1,4'-benzenedithiol molecule contacted by gold electrodes increases up to an order of magnitude as the molecule is stretched. They explain this by a shift of the highest occupied molecular orbital (HOMO) towards the Fermi level of the gold electrode and thus an enhancement of resonant transport. Further experiments and/or calculations would be necessary to decide whether a similar mechanism also applies here.

When one looks carefully at the histogram of QTCDA on Ag(111) assigned to class B one can see that the conductance increase just before the contact rupture is composed of two peaks in the conductance (see e.g. Fig. 6.8). These two peaks could be signatures of the removal of the last two oxygen atoms. With this it can be assumed that these two peaks in the conductance are originating from a stretching of the molecule just before the last and last but one oxygen atom are detached from the substrate.

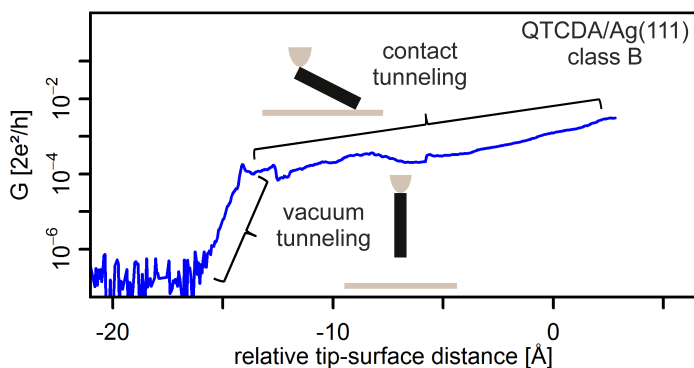


Figure 6.31: The two transport regimes as discussed in section 6.4.1.1. The first transport regime takes place as long as the molecule is still in contact with the substrate. Because of its exponential decay it is assumed that tunneling is observed. The second transport regime takes place after the molecule-substrate contact is broken, again tunneling is observed.

After identifying the two transport regimes it is now of interest to investigate how these

two transport regimes depend on the length of the molecule. Therefore the decay constant  $\beta$  of the conductance is determined (see chapter 3). The decay constant is defined as the change of the conductance  $G$  upon electrode separation  $z$  by the following relation  $G \sim \exp(-\beta z)$ . This decay constant can be determined by making a linear regression through the points defined earlier. The decay constant of the contact tunneling transport regime  $\beta_{\text{contact}}$  is determined by the points  $P_1$  and  $P_3$ . The decay constant of the vacuum tunneling transport regime  $\beta_{\text{vacuum}}$  by the points  $P_4$  and  $P_5$ . In order to calculate the decay constants the points  $P_1$  to  $P_5$  were measured for all four generic behaviors measured on silver. In Fig. 6.30 the generic behavior of QTCDA/Ag(111) for class B is shown together with the points  $P_1$  to  $P_5$ . The other three generic behaviors and the corresponding points for manipulations on silver assigned to class B are shown in Fig. A.58 in chapter A.

In Fig. 6.32a the  $\beta_{\text{contact}}$  is plotted as a function of molecule length. The length of the molecules was calculated on the basis of the DFT calculations used for the simulation of the molecules in the publication of Wagner *et al.* [43]. By the length of the molecule the diagonal through the molecule from one carboxylic oxygen to the other is meant. The diagonal is taken in view of the geometry of the molecule in the junction just before rupture of the contact, as we know from force-field simulations (see chapter 5). It is found that the decay constant is decreasing with the length of the molecule. To analyze the behavior of  $\beta_{\text{contact}}$  as a function of molecular length  $l_m$  further, we rescale the  $z$ -axis in Fig. 6.30 from  $z$  to  $\frac{z}{l_m}$ . This renormalizes  $\beta_{\text{contact}}$  to  $\beta_{\text{contact}} l_m$ . Plotting  $\beta_{\text{contact}} l_m$  as a function of molecule length (see Fig. 6.32b), we find a reduced dependence of the decay constant on molecules. However, the decay constant still decreases systematically as we go from NTCDA to TTCDA, with the decay constant for QTCDA increasing slightly. Assuming similar transport orbitals, and assuming that orbital overlap determines the decay, this indicates that geometrically the lifting process proceeds differently. Specifically a smaller decay constant indicates that the molecule bends more strongly.

To probe the geometry of the molecule during the lifting process the force-field simulations introduced earlier [42, 126] are analyzed (see Fig. 6.33). This analysis is done with the geometric configurations of the molecule during the lifting process. By averaging the position of each atom in the molecule relative to the surface, the average atom position is determined. This average atom position is determined for different molecular configurations during the lifting process from Au(111) for the four molecules NTCDA, PTCDA, TTCDA and QTCDA. This average atom position is then plotted versus the top atom

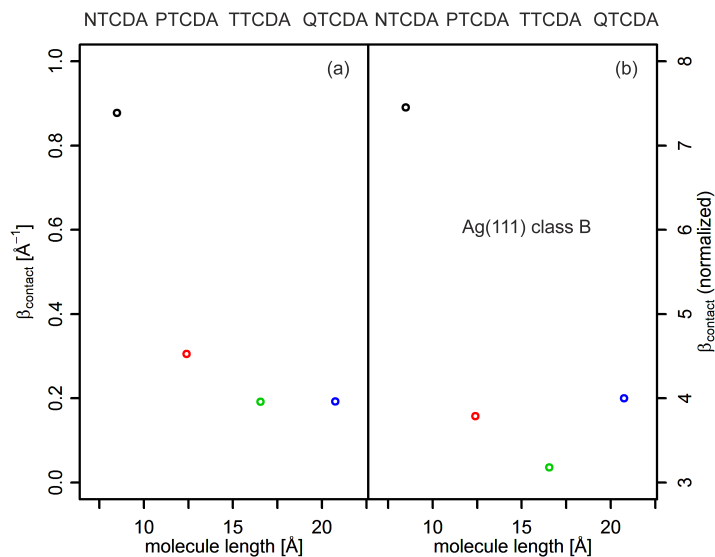


Figure 6.32: Decay constant of the contact tunneling transport regime  $\beta_{\text{contact}}$ . It is determined by measuring a linear regression between the points  $P_1$  and  $P_3$ . (a) The decay constant plotted versus the molecule length shows a decreasing of the decay constant with increasing molecule length. (b) The decay constant normalized to the molecular length plotted versus the molecule length also shows a decreasing of the decay constant with increasing molecule length.

position of this molecular configuration, i.e. versus the position of the carboxylic oxygen making contact to the tip. The comparison of the results for the four molecules in Fig. 6.33 shows that the longer the molecule is, the more it is bent towards the surface. This is consistent with our expectations. The longer molecule is more flexible, bends more and thus its transport orbital keeps contact (overlap) with the metal for longer. The bending visualized for Au(111) in Fig. 6.33 should be even more pronounced on Ag(111), as the interaction between the molecules and the surface is larger on Ag(111) than Au(111).

The exponential dependence of the conductance upon the electrode separation was observed in several metal-molecule-metal junctions before [153–155]. This exponential dependence of the conductance was explained by coherent electron tunneling through the molecule [153, 154]. Not surprisingly the decay constant found varied a lot depending on the investigated system. Lafferentz *et al.* [153] found  $\beta = 0.38 \text{ \AA}^{-1}$  for polyfluorene probed with Au(111) electrodes. Koch *et al.* [155] studied graphene nanoribbons on gold and found that the decay constant varied upon the bias voltage applied to the junction. In the low bias regime ( $\sim 1.6 \text{ V}$ ) they found  $\beta = 0.45 \text{ \AA}^{-1}$  and in the high bias regime (1.8 V to 2.4 V) a smaller  $\beta = 0.18 \text{ \AA}^{-1}$ , at negative bias they measured  $\beta = 0.1 \text{ \AA}^{-1}$ .

In Fig. 6.34 the decay constant of the conductance in the vacuum tunneling regime  $\beta_{\text{vacuum}}$  is plotted versus the molecule length. In contrast to the observation made for the decay constants in the contact tunneling transport regime  $\beta_{\text{contact}}$  no systematic dependence between the molecule length and the decay constant is observed. This seems to be a consequence of the correlation approach used to determine the generic curves. The part of the curve which shows the vacuum tunneling regime is not included in the correlation determination (see Fig. 6.8), therefore in these curves this part is not represented generic. The decay constants of the vacuum tunneling regime  $\beta_{\text{vacuum}}$  are independent of the molecule length, with an average  $\beta_{\text{vacuum}} = 2.8 \text{ \AA}^{-1}$ . This means that the length of the molecule bound to the tip is not influencing the tunneling behavior. This indicates that tunneling indeed occurs from the bottom end of the molecule, i.e. the molecule is contacted to the tip well enough for efficient charge transfer.

The decay constant measured for the bare silver tip, i.e. the decay constant measured before tip and molecule get into contact (class app), is in average  $\beta_{\text{silver tip}} = 1.93 \text{ \AA}^{-1}$  (see Fig. 6.35). This means the tunneling current is decaying faster when the tip is decorated with a molecule with an average  $\beta_{\text{vacuum}} = 2.8 \text{ \AA}^{-1}$ . This indicates that the tail of the wave function decays faster into the vacuum for the molecules than for the

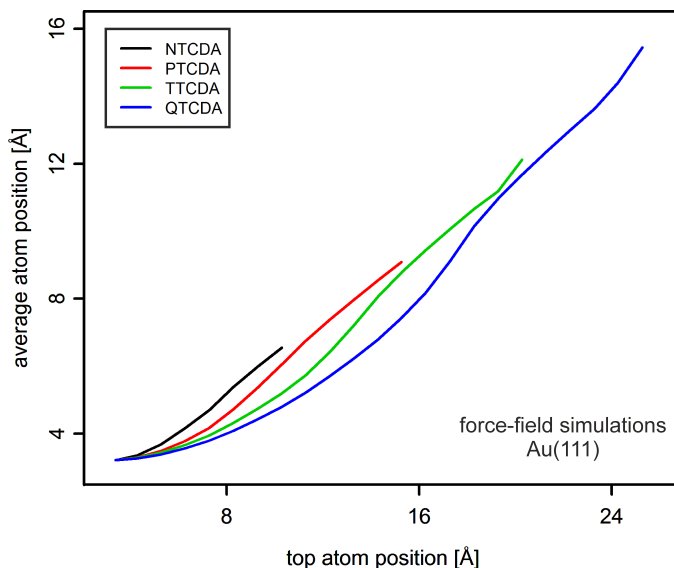


Figure 6.33: From the force-field simulations introduced earlier [42, 126] the geometric configuration of the molecule during the lifting process is known. With this information the average atom position relative to the surface can be determined for the molecule and plotted versus the top atom, i.e. the carboxylic oxygen atom making contact to the tip, position. This is shown here for the four molecules on Au(111). The comparison of the four molecules shows that the longer the molecule is, the more it bends towards the surface during the lifting process. In consequence its transport orbital keeps contact with the metal for longer. This explains the different slopes of the contact transport regime as seen in Fig. 6.32. On Ag(111) this effect is expected to be even more pronounced as a consequence of the larger interaction.

tip. This could have geometric or electronic reasons (geometric: sharper tip, electronic: higher barrier due to vacuum levels). In table 6.6 the decay constants of both transport regimes observed in the silver junction are listed together with the decay constant of the bare silver tip and bare gold tip approaching the surface, but without having made contact to the molecule.

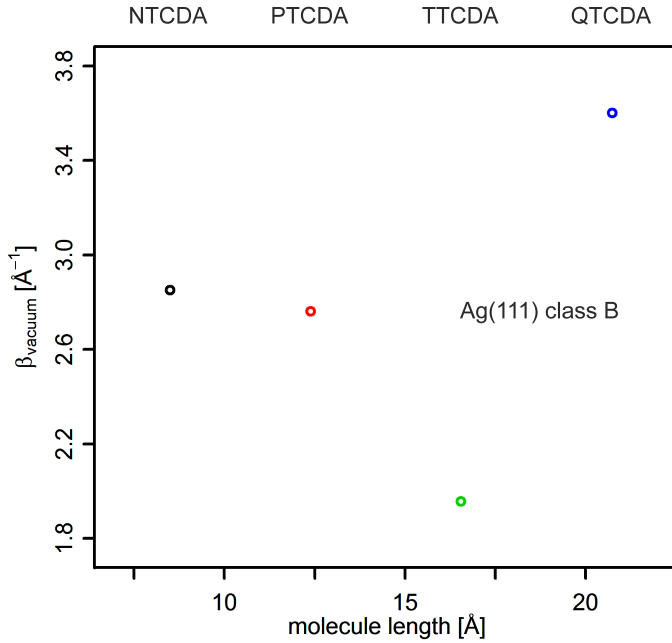


Figure 6.34: Decay constant of the vacuum tunneling regime  $\beta_{\text{vacuum}}$  versus the molecule length. It is determined by measuring a linear regression between the points  $P_4$  and  $P_5$ . No systematic dependence of the decay constant on the molecule length is observed. This is a result of the approach used to determine the generic behavior. An average  $\beta_{\text{vacuum}} = 2.8 \text{\AA}^{-1}$  is found. The decay constant of the bare silver tip, i.e. before the tip makes contact to the molecule, is smaller ( $\beta_{\text{silver tip}} = 1.93 \text{\AA}^{-1}$ ), which could have geometric or electronic reasons.



Molecule	$\beta_{\text{contact}}$ [ $\text{\AA}^{-1}$ ]	$\beta_{\text{vacuum}}$ [ $\text{\AA}^{-1}$ ]	$\beta_{\text{silver tip}}$ [ $\text{\AA}^{-1}$ ]	$\beta_{\text{gold tip}}$ [ $\text{\AA}^{-1}$ ]
NTCDA	0.88	2.87	2.02	2.12
PTCDA	0.31	2.74	1.94	2.07
TTCDA	0.19	1.96	1.86	2.11
QTCDA	0.19	3.62	1.89	2.03

Table 6.6: Decay constants of the two tunneling transport regimes for class B manipulations on Ag(111) and decay constant of the bare silver tip and bare gold tip approaching the surface before making contact to the tip.

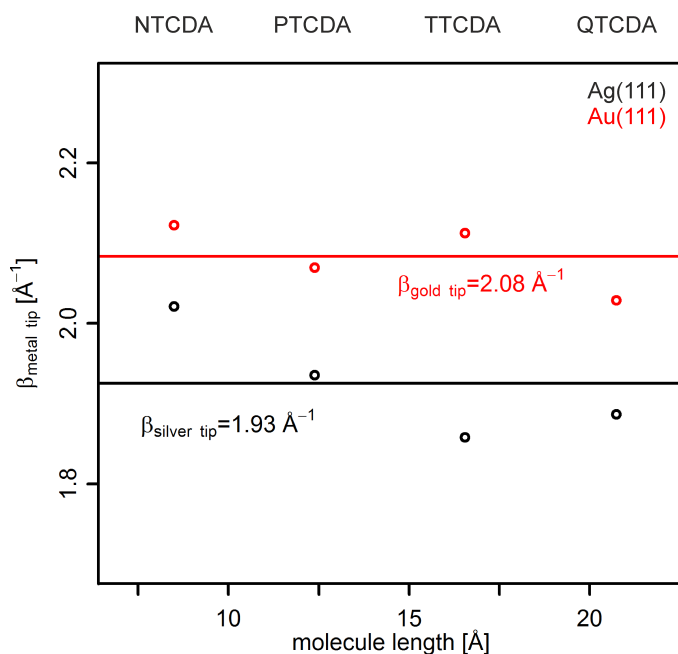


Figure 6.35: Decay constant of the tunneling current through the bare metal tip before making contact to the molecule for the two surfaces Ag(111) and Au(111). The average decay constant for silver is  $\beta_{\text{silver tip}} = 1.93 \text{ \AA}^{-1}$  and for gold  $\beta_{\text{gold tip}} = 2.08 \text{ \AA}^{-1}$ . These values were obtained from the class app histograms (see Figs. A.1 to A.8 in chapter A).

### 6.4.1.2 The conductance peak

We now turn to the discussions of deviations from strictly exponential behavior in the contact regime, see e.g. Fig. 6.28. Most notably, a peak in the conductance is clearly visible in the zero bias conductance. This peak coincides with a dip in the frequency shift. The occurrence of a peak in the conductance upon reverse chemisorption was observed in earlier experiments when a PTCDA molecule was lifted from Ag(111) (see section 4.3) [39, 40]. A Kondo resonance was identified, which led to an increase of the conductance. In those experiments no frequency shift was measured, hence it was unclear up to this point in which exact geometry the molecule is as the Kondo resonance is observed.

In Fig. 6.30 the blue arrow at  $P_2$  indicates that the conductance peak is observed where a dip in the frequency shift occurs. By the force-field simulation we can attribute this dip to the lifting of the last naphthalene unit of the molecule from the substrate. This means that the condition for a conductance peak is given for a junction geometry in which the molecule is contacted at one side by one carboxylic oxygen to the tip, and on the other side the molecule is in contact with the substrate with one naphthalene unit and the carboxylic functional group. For all four molecules this observation is valid (see Fig. A.58 in chapter A).

To check the origin of the conductance peak observed in the class B manipulations another type of experiments was performed. A molecule, isolated from the molecular island, was contacted at one of the carboxylic oxygen atoms and then lifted up stepwise by 0.2 Å. At each step the manipulation was stopped and a differential conductance spectrum was measured with lock-in technique by sweeping the bias voltage in the range  $-50$  mV to  $50$  mV. The results are exemplary discussed on a single measurement of TTCDA manipulated on silver in Fig. 6.36. In Fig. 6.36a the frequency shift and the zero-bias differential conductance measured while stepwise manipulating TTCDA are shown. Every 0.2 Å a spectrum was recorded, a signature of these spectra are the vertical lines in the zero-bias differential conductance curve. The arrows indicate the position of the three spectra displayed in Fig. 6.36b. The red spectrum was taken at the beginning of the manipulation, the green at the conductance peak and the blue at the transition between the two transport regimes discussed earlier. The spectra were all shifted to a uniform base and normalized for a better comparison. In absolute scales the red spectrum is at higher conductance than the green one, and the green one at higher conductance than the blue one as can be seen by the three axis.

In the beginning of the manipulation, the minimum in the density of states is at the Fermi level (red spectrum). As the molecule is lifted up from the surface the zero-bias differential conductance decreases. At a relative tip-surface distance of about 6 Å the zero-bias differential conductance shows a peak (see Fig. 6.36a). The corresponding green spectrum is not changing a lot relative to the earlier measured red spectrum. In the last spectrum measured before the junction is ruptured a small peak at the Fermi level is observable (blue spectrum). The behavior observed here is the same for QTCDA manipulated on Ag(111) (see Fig. A.70 in chapter A). NTCDA (see Fig. A.65 in chapter A) and PTCDA (see Fig. A.67 in chapter A) on the other side show a peak at the Fermi level in the spectra recorded when a peak in the differential conductance is observed. This means that the origin of the peak in the zero-bias differential conductance is a Kondo resonance for NTCDA and PTCDA, but not for TTCDA and QTCDA of class B. Later it will be shown that in manipulations of class A the Kondo resonance is at the origin of the conductance peak for all molecules measured.

From the simulations we know that the molecules snaps into a linear geometry with the removal of the last naphthalene unit. This implies that the distortion of the molecule is maximized just before the snapping, when the molecule is in the geometry in which the conductance peak appears. It is clear that such snapping events will lead to deviations from strictly exponential behavior. However, while such discontinuities in the structural evolution can explain non-uniform rates of decay, they cannot explain the increase of conductance with  $z$ . However, discontinuities in the structural evolution necessarily imply the build-up of strain. This can modify the electronic structure of the molecule, resulting in different conductance behavior. Whether this can explain the behavior observed here needs calculations. It was found earlier that a distortion of the molecule could trigger an increase of the conductance by Bilic *et al.* [156]. They investigated the charge transport through p-phenylene-vinylene molecules contacted by gold electrodes with DFT. Their results showed that the charge transport through the molecule is enhanced when the molecule is tilted by a contraction. This was explained by a better band alignment at the cost of the coupling strength. Also Lafferentz *et al.* [153] observed a conductance increase in their investigation of polyfluorene on Au(111). This conductance increase was observed as the molecule was lifted from the Au(111) substrate with the tip of a STM. They related this conductance increase to the flat adsorption of a monomer unit on the substrate.

To investigate the conductance peak in the zero bias differential conductance as a function of  $z$  further, its dependency upon the molecule length is analyzed. In Fig. 6.37 the

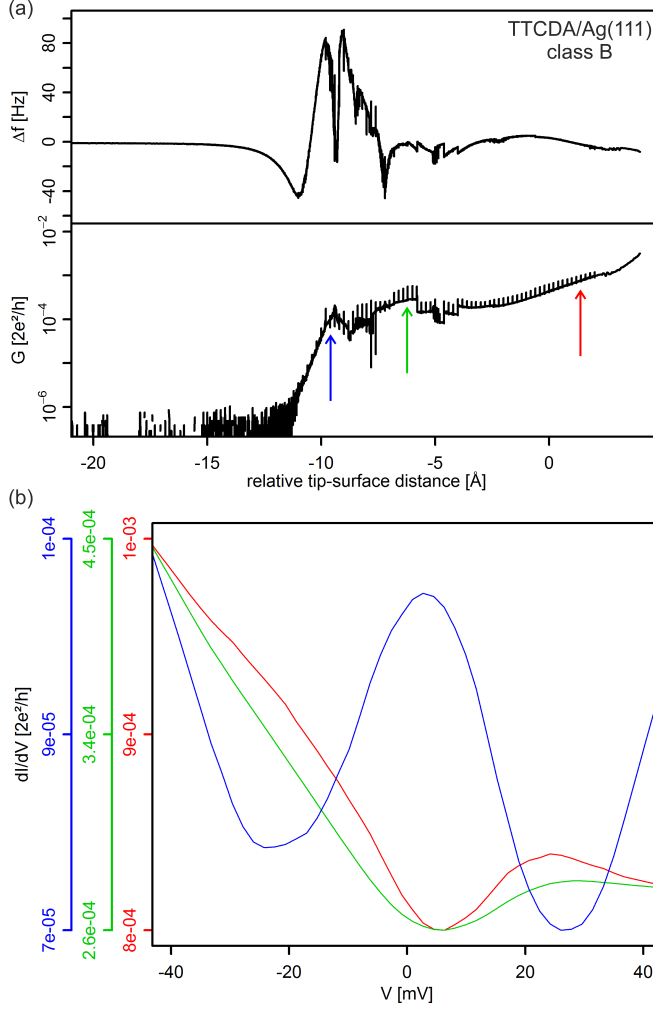


Figure 6.36: Spectra taken while lifting a TTCDA molecule from Ag(111). (a) The frequency shift and the differential conductance of the lifting process. (b) Every  $0.2 \text{ Å}$  the manipulation was interrupted and a spectrum in the bias voltage range  $-50 \text{ mV}$  to  $50 \text{ mV}$  was taken. By the arrows in (a) the position of the three spectra presented is shown. The spectra show, that the Kondo resonance, as described earlier for PTCD/Ag(111) [39], is not the origin of the conductance peak in TTCDA/Ag(111) of class B.

conductance of the conductance peak is plotted versus the molecule length. The longer a molecule is, the smaller is the conductance peak, as a consequence of the overall lower conductance for longer molecules. Similar to the decay constants of the two tunneling transport regimes (see section 6.4.1.1) an exponential decay is observed. The decay constant of this exponential decay is found to be  $\beta_{\text{peak}} = 0.43 \text{ \AA}^{-1}$ . Further it can be noted that the distance between the positions of the conductance peaks relative to the tip-surface distance show a linear relation, with an average distance of  $4.25 \text{ \AA}$  between two conductance peaks. This is a consequence of the conductance peak always being observed when the molecules are in the same geometric configuration within the junction, i.e. in contact to the substrate with the last naphthalene unit.

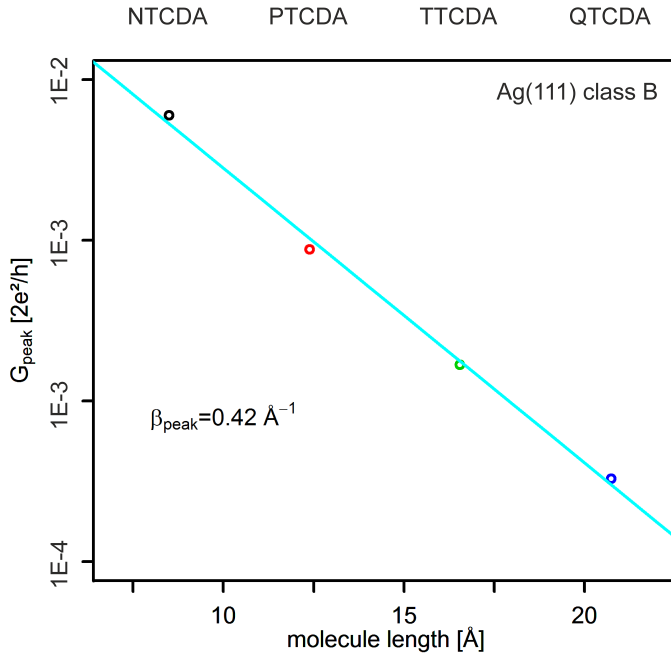


Figure 6.37: Conductance of the conductance peaks in class B manipulations with silver electrodes for all four molecules. The conductance of the peaks show an exponential decay with the length of the molecule. The decay constant of is found to be  $\beta_{\text{peak}} = 0.42 \text{ \AA}^{-1}$ .

### 6.4.1.3 Molecules in wire configuration on Ag(111) of class B

When the frequency shift shows its global peak the molecules are standing upright in the junction as we know from force field simulations [42, 43]. We call this geometry the wire configuration. Also in the conductance data this position was identified as the transition between the two transport regimes. The molecule is only contacted by the carboxylic oxygen to the silver electrodes tip and surface. The electrons are passing through the whole molecular backbone. It is now of interest how high the conductance through the molecules is at this state.

The position of the wire configuration is marked by point  $P_4$  in Fig. 6.30. The conductance measured for the molecules in this junction configuration contacted by silver electrodes range between  $10^{-4} G_0$  to  $10^{-3} G_0$  (see table 6.5). The conductance is very low compared to the conductance found in atomic point contacts for example, where conductance values in the range of the conductance quantum  $G_0$  are found [157]. This is the consequence of the low transmission probability  $T$  through the molecule (see chapter 3). By plotting the conductance of the molecular wires versus the molecule length we find an exponential decay for the wire conductance (see Fig. 6.38). We find a decay constant of  $\beta_{\text{wire}} = 0.15 \text{ \AA}^{-1}$  assuming the following dependency  $G \sim \exp(-\beta L)$  between the conductance  $G$  and the molecule length  $L$ .

Note that this  $\beta_{\text{wire}}$  is the intrinsic decay constant of the molecular wire, as here the contacts are the same for all four molecules, unlike the decay constants  $\beta_{\text{contact}}$  and  $\beta_{\text{vacuum}}$  introduced earlier. The decay constant in the wire configuration  $\beta_{\text{wire}} = 0.15 \text{ \AA}^{-1}$  is smaller than the ones observed for the contact tunneling and vacuum tunneling regime. This is a result of the superimposition of two contributions to the conductance. First the decay of the molecular length and second the reduction of the contact. Using this one can split the decay constant change in Fig. 6.32 and Fig. 6.34 into the two superimposed contributions.

The exponential decay of the conductance upon molecule length was observed in several metal-molecule-metal junctions before [22, 31, 158–167]. This observation of an exponential decay suggests that tunneling is observed. For molecules of the size investigated here off-resonant coherent tunneling (see section 3.3) is often proposed as the underlying transport mechanism [161, 168]. Therefore it is believed that in the systems studied here also off-resonant coherent tunneling is observed. Incoherent hopping mechanism is only observed for molecules longer than  $\approx 3 \text{ nm}$  [168, 169].

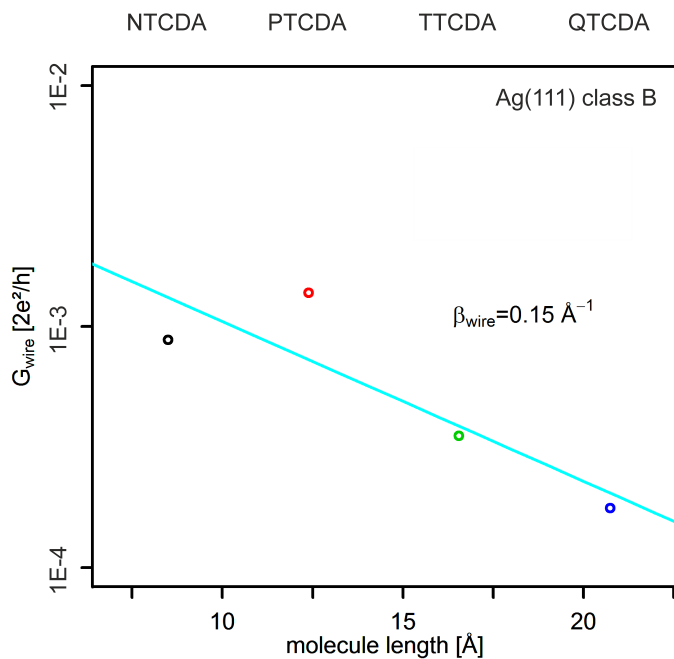


Figure 6.38: Conductance of the molecule in the wire configuration, i.e. conductance of the junction tip-molecule-substrate, with the molecule standing upright between the silver electrodes in class B. The conductance  $G$  is plotted versus the length of the molecules  $L$ . We find the exponential dependence  $G \sim \exp(-\beta L)$  with the decay constant  $\beta_{\text{wire}} = 0.15 \text{ \AA}^{-1}$ .

Most of the systems investigated up to now are thiolated molecules on gold surfaces, which form a strong Au-S bond [160]. The decay constant found for alkanedithiols and peptides on gold range from  $0.8 \text{ \AA}^{-1}$  to  $0.9 \text{ \AA}^{-1}$  [22]. The transport mechanism is believed to be coherent electron tunneling [22,31,159]. Comparable small decay constant ( $\beta = 0.16 \text{ \AA}^{-1}$ ) as in our system were found by Peng *et al.* [162] for amine-terminated thiophene on gold at zero-bias voltage in density functional calculations. With  $\beta = 0.06 \text{ \AA}^{-1}$  almost no dependence of the conductance on the molecule length was observed for oligoynes molecules contacted by gold electrodes [163].

The absolute conductance values vary a lot depending on the system investigated. As most of the systems investigated are on thiol-terminated molecules and on gold electrodes it is difficult to find comparable experimental results to our study. Peng *et al.* [166] probed the conductance through single alkanedicarboxylic acids of different length contacted by silver electrodes. They measured conductance values in the range  $2.6 \times 10^{-5} G_0$  to  $4.1 \times 10^{-4} G_0$ . In their study on amine-terminated oligophenyl and alkane molecules of different length contacted by silver electrodes Kim *et al.* [167] measured conductance values in the range  $10^{-5} G_0$  to  $10^{-3} G_0$ . Compared to these two studies it can be seen that the  $\pi$ -conjugated molecules we are probing contacted to silver electrodes are good conductors.

#### 6.4.2 Manipulations of class A on Ag(111)

In this section the lifting and lowering curves assigned to class A are discussed. The statistics acquired for this class of manipulations have a much higher variance (see Figs. A.10, A.15, A.20 and A.25 in chapter A). This is the result of the junction being less stable than the one assigned to class B. As mentioned earlier, the class A manipulations are characterized by a hysteresis between the lifting and the lowering of a molecule in the frequency shift and differential conductance data. This is caused by a bistable tip-molecule-substrate junction configuration. Bistability in conductance measurements on molecules were reported in earlier experiments [170–174]. The two states observed in these experiments were attributed to either conformational changes of the molecule or changes of the contact geometry between the electrodes and the molecule.

In contrast to the analysis done for the class B manipulations on Ag(111), only three characteristic points  $P_1$  to  $P_3$  were defined. This had to be done as no statement can be done about the vacuum tunneling regime for the class A manipulations. This is the consequence of the hysteresis in the region of the vacuum tunneling regime, therefore



making it impossible to define a slope for the vacuum tunneling regime (see Fig. A.57 in chapter A). As for the class B manipulations two points  $P_1$  and  $P_3$  are defined to determine the slope of the contact tunneling regime by making a linear regression. The point  $P_1$  denotes the conductance value the closest to the substrate and  $P_3$  defines the position at which the transition between the two transport regimes (see section 6.4.1), i.e. where the molecule is standing upright, is observed. It is determined using features in the conductance, i.e. where a change of the slope of the generic behavior is observed. As for the class B manipulations this transition is found in the region of the global peak in the frequency shift data. This point  $P_3$  is then also used to determine the conductance of the junction in the wire configuration. The point  $P_2$  is the conductance corresponding to the last dip before feature B in the frequency shift. In table 6.7 the points are listed which were used for the further analysis. In Fig. A.57 in chapter A these points are shown together with the generic curves.

In the following the discussed points are summarized:

- $P_1$  Conductance  $G_{\text{start}}$  at the closest z-position relative to the substrate.
- $P_2$  The conductance peak  $G_{\text{peak}}$ . This peak matches with a dip in the frequency shift, as indicated by the arrow.
- $P_3$  The knee  $G_{\text{wire}}$  in the conductance data. This knee is in the region of the global peak in the frequency shift.

Molecule	$P_1$ [ $\text{\AA}, 2e^2/h$ ]	$P_2$ [ $\text{\AA}, 2e^2/h$ ]	$P_3$ [ $\text{\AA}, 2e^2/h$ ]
NTCDA	$(4.93, 6.49 \times 10^{-2})$	$(3.73, 9.13 \times 10^{-2})$	$(-0.42, 9.82 \times 10^{-4})$
PTCDA	$(2.84, 2.19 \times 10^{-2})$	$(1.24, 2.50 \times 10^{-2})$	$(-4.88, 2.87 \times 10^{-4})$
TTCDA	$(1.84, 5.19 \times 10^{-3})$	$(-2.95, 3.74 \times 10^{-3})$	$(-8.55, 2.64 \times 10^{-4})$
QTCDA	$(2.93, 3.00 \times 10^{-3})$	$(-7.16, 2.25 \times 10^{-3})$	$(-13.76, 9.87 \times 10^{-5})$

Table 6.7: The coordinates of the points  $P_1$ ,  $P_2$  and  $P_3$  as defined above for the class A manipulations of all four molecules on Ag(111).

#### 6.4.2.1 The hysteresis in class A manipulations

In Fig. 6.39 the 2D histogram of all class A manipulations of QTCDA on Ag(111) is shown. By the red arrow the group of curves measured while the molecule was lifted from the surface is indicated. The black arrow indicates the group of curves measured while the molecule was lowered towards the surface. By the red and black circle the

signature of the switching from one configuration to the other is highlighted. As the molecule is lifted, the switching from junction configuration  $C_1$  to another configuration  $C_2$  occurs when the molecule-substrate interaction is almost zero (red circle). When the molecule is lowered the switching back from junction configuration  $C_2$  to  $C_1$  happens at a higher molecule-surface interaction, i.e. when the tip is closer to the surface (black circle). This characteristic of the hysteresis is the same for all four molecules probed and can be found in the same way for the experiments performed on Ag(111), as discussed here, and the experiments performed on Au(111) (see Figs. A.10, A.15, A.20, A.25, A.30, A.35, A.40 and A.45 in chapter A).

Another difference between class A and B manipulations can be seen in Fig. 6.40, where the unshifted curves assigned to class A and class B manipulations of QTCDA on Ag(111) are shown. The red lines indicate the distance at which the transition from one transport regime to the other is observed. For class A manipulations this transition occurs at a larger tip-surface distance than in the case of class B manipulations. The transport regime transition in the case of class B occurs at the same relative tip-surface distance at which the junction switches from configuration  $C_2$  to  $C_1$  in the case of class A (see Fig. 6.39). A distance of about 1.4 Å is found between the transport regime transitions for class A and class B. The comparison of the frequency shift and the conductance of both classes for QTCDA on Ag(111) (see Fig. 6.18 and Fig. 6.39) shows that for class A the transport regime transition happens at the position of the negative dip in  $\Delta f$ , while for class B the transport regime transition occurs on the steep slope before the dip. Further class A has a larger negative dip in the frequency shift than class B. This indicates a stronger attraction. Also the negative dip is sharper, which indicates extension and contraction.

From these observations the following can be concluded. Three different junction configurations are observed in the manipulations assigned to class A and class B (see Fig. 6.41). The configuration  $C_3$  is the origin of the conductance behavior observed in the manipulations of class B. The two other configurations  $C_1$  and  $C_2$  are observed for the lifting and lowering curves in the manipulations of class A. The two configurations of class A have to differ from the configuration of class B as the conductance peak observed in class A is at a different distance and has a different magnitude than the conductance peak in class B manipulations. The class A tip deforms elastically, shown schematically by the spring in Fig. 6.41, this results in an extension of the tip in the  $C_1$  configuration until the switching to the  $C_2$  configuration. Eventually the  $C_1$  configuration deforms plastically and switches to the  $C_3$  configuration observed for class B. This  $C_3$  is stable

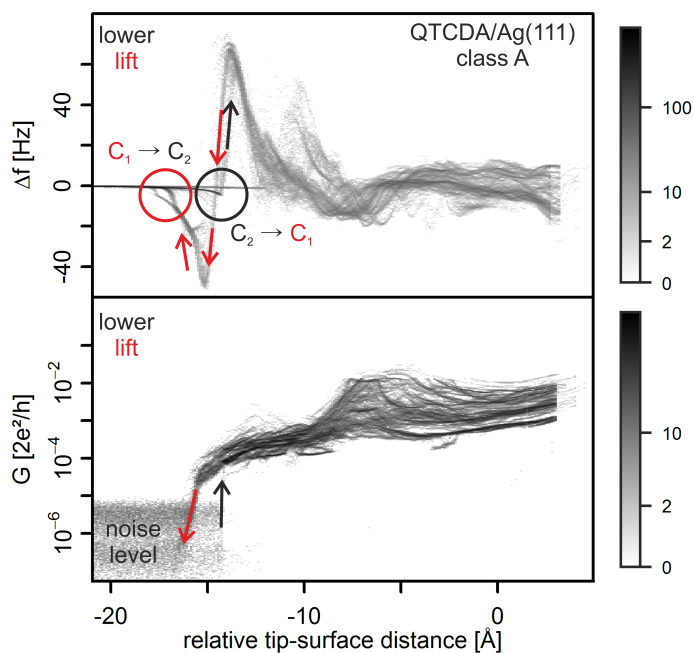


Figure 6.39: Hysteresis in class A manipulations for QTCDA on Ag(111). As the molecule is lifted, one junction configuration  $C_1$  is switching to another configuration  $C_2$ , when the molecule-surface interaction is almost zero (red circle). As the molecule is lowered the configuration  $C_2$  switches back into the first configuration  $C_1$  at a higher molecule-surface interaction (black circle). The two levels in the noise result from different amplifier gains used for the experiments. The same behavior is observed for all four molecules on both metal surfaces Ag(111) and Au(111) investigated. Bin size of  $\Delta f$ :  $z = 0.1 \text{ \AA}$ ,  $y = 0.4 \text{ Hz}$ ; bin size of  $G$ :  $z = 0.1 \text{ \AA}$ ,  $\min(y) = 1.6 \times 10^{-12} 2e^2/h$ ,  $\max(y) = 1.6 \times 10^{-3} 2e^2/h$ .

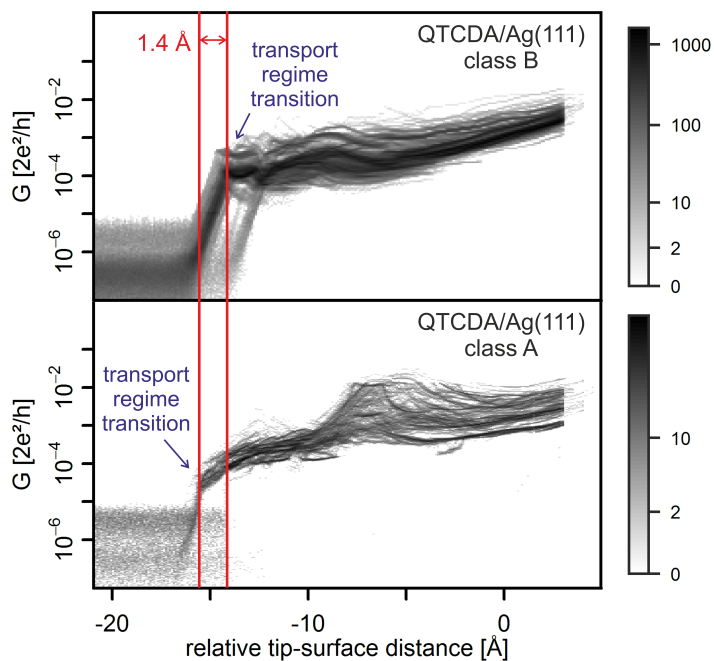


Figure 6.40: The red lines indicate the transition from the contact tunneling to the vacuum tunneling regime for both classes A and B. The transition in class B is observed at the same tip-surface distance as the switching from configuration  $C_2$  to configuration  $C_1$  in class A (see Fig. 6.39). A distance of 1.4 Å is found between the two transitions, which indicates that the configuration change is related to different atomic arrangements on the tip apex.

and does not switch back to  $C_1$  or  $C_2$ .

A possible explanation for the different junction configuration could be the tip apex being decorated either by an silver atom (class B) or an platinum or iridium atom (class A). A silver atom at the tip apex would lead to an s-orbital. As an s-orbital is spherically symmetric in space the bonding to the oxygen atom of the molecule would not be under stress. On the other side a platinum or iridium tip apex would lead to an d-orbital. The d-orbital is not spherically symmetric in space, as a consequence a force is acting on the molecule which results in a switching between two different junction configurations  $C_1$  and  $C_2$ . This force leads to a conformational change at the tip-molecule bond as soon as the interaction between molecule and substrate undercuts a certain threshold.

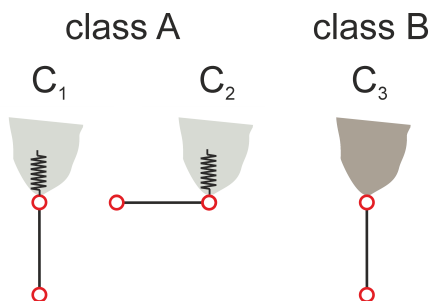


Figure 6.41: Schematic representation of the different junction configurations. Class A is characterized by a hysteresis in the conductance and frequency shift data. This suggests that two different junction configuration exist. These two junction configurations  $C_1$  and  $C_2$  could be the consequence of a platinum or iridium atom on the tip apex. The resulting unsymmetrical d-orbital on the tip apex creates a force acting on the molecule which produces a switching between both configurations in dependence of the molecule-substrate interaction. This switching process is accompanied by an elastic deformation, represented schematically by the spring. Eventually the tip deforms plastically and switches to the stable junction configuration  $C_3$  of class B. This stable configuration suggests a symmetric s-orbital on the tip apex and therefore a silver atom making the bond to the molecule.

The influence of the exact molecule-metal contact configuration on the conductance was observed by several groups before [175–178]. Dulic *et al.* [177] probed terphenylene molecules contacted in a mechanical break junction (MCBJ) experiment by Au electrodes. They observed a switching between two conductance. This was explained by a thermally activated switching between two different molecule-metal contact geome-

tries.

The influence of the binding geometry on the conductance was the subject of many investigations [163, 164, 179–184]. Binding geometries influence the charge distributions, the spin population, the ionization energy and the electron affinity of the molecule in the junction [179]. In consequence the transport behavior is very sensitive to the contact configuration. Kameneteska *et al.* [164] investigated pyridine-terminated molecules elongated by gold electrodes. In their conductance histogram two peaks were observed, which they attributed to two different pyridine-gold binding geometries. Also they measured different conductance values, the decay constant  $\beta = 0.5 \text{ \AA}^{-1}$  was not changing upon the different binding geometries. In their study, Wang *et al.* [163], investigated the influence of the binding geometry of a pyridyl group on the conductance. They found that the conductance of the molecule could differ by 150 % whether the pyridyl group is bound to a flat electrode or to a step or a similar high coordination site.

#### 6.4.2.2 Transport in class A manipulations

In Fig. 6.42 the generic behaviors (as defined in section 6.3.3.1) of all class A manipulations are shown. The manipulations on Ag(111) of class A are more scattered than the manipulations of class B. This is a consequence of the bistable junction configuration and the resulting hysteresis from the switching events. But nevertheless the generic curves obtained by calculating the arithmetic mean (see section 6.3.3.1) of the 2D histograms show a smooth behavior.

Two different transport regimes as introduced earlier are occurring while lifting and lowering the molecules. By making a linear regression through the points  $P_1$  and  $P_3$  the decay constants of the contact tunneling transport regime  $\beta_{\text{contact}}$ , as defined in section 6.4.1.1, were calculated for each molecule. A decay constant for the vacuum tunneling regime  $\beta_{\text{vacuum}}$  cannot be defined as a consequence of the hysteresis in that region.

In Fig. 6.43 the decay constants of class A (black dots) are plotted versus the molecule length together with the decay constants of the molecules of the class B statistics (red dots) which were already shown in Fig. 6.32. As for the manipulations of class B the decay constants of the contact tunneling regime of class A is decreasing with the molecule length. In fact the calculated values are very similar, which indicates similar junction configurations for class A and B. For both classes the decay constant is decreasing with molecule length and a saturation of the decay constant is observed for longer molecules.

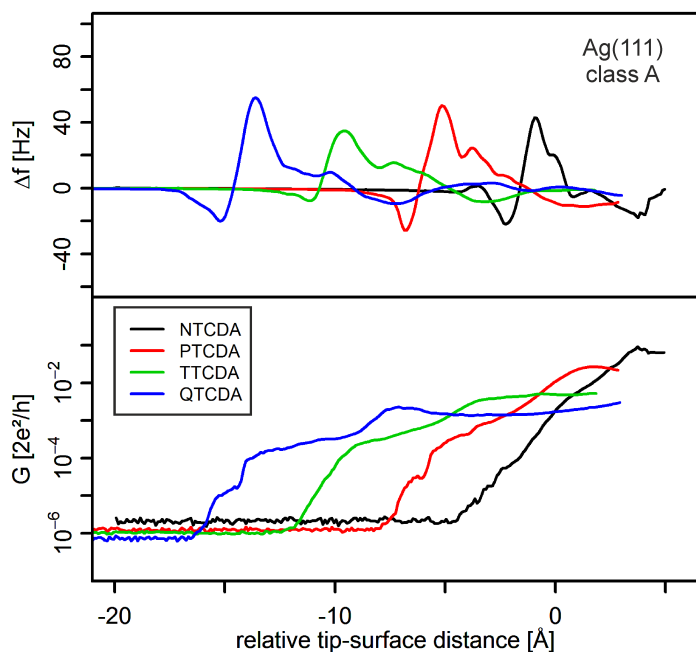


Figure 6.42: Generic curves of the four molecules probed on Ag(111) assigned to class A. The differential conductance and frequency shift data of class A manipulations is more scattered than the data from class B manipulations as a consequence of the bistable junction. Nevertheless the generic curves obtained by calculating the arithmetic mean show a smooth behavior.

For the manipulations of PTCDA and TTCTDA the decay constants assigned to class A are larger than the ones assigned to class B, the decay constant of NTCDA and QTCDA are the same for both classes. To compare the classes, the decay constants  $\beta_{\text{contact}}$  of class A and class B and their difference class A – class B are listed in table 6.8.

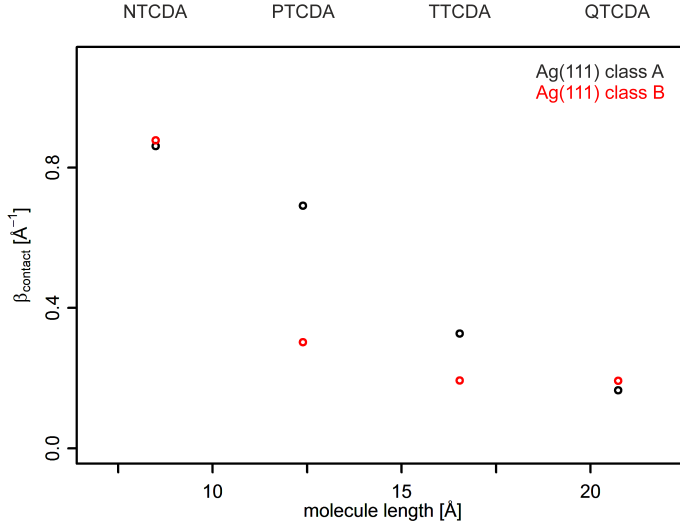


Figure 6.43: Decay constants of the contact tunneling transport regime  $\beta_{\text{contact}}$  of class A and class B manipulations on Ag(111). The decay constants are calculated by measuring a linear regression through the points P<sub>1</sub> and P<sub>3</sub>. In both classes the decay constant is decreasing with molecule length. A saturation is observed for both classes.

### 6.4.2.3 The conductance peak

As for class B manipulations a peak is observed in the generic conductance curves of class A on Ag(111). To investigate its physical origin measurements were performed as introduced earlier (see section 6.4.1.2). A molecule is isolated from the molecular island. This isolated molecule is then contacted at one of the carboxylic oxygen atoms and lifted up. Every 0.2 Å the manipulation is stopped and a differential conductance spectrum is measured in the bias voltage range –50 mV to 50 mV. In this way the electronic structure



Molecule	$\beta_{\text{contact}} [\text{\AA}^{-1}]$		
	class A	class B	class A – class B
NTCDA	0.86	0.88	−0.02
PTCDA	0.69	0.31	0.38
TTCDA	0.32	0.19	0.13
QTCDA	0.17	0.19	−0.02

Table 6.8: Decay constants of the contact tunneling regime of class A and class B and the differences between the decay constants of both classes on Ag(111).

of the junction is probed for different geometries and can be compared to the electron transport through the molecule. In Fig 6.44 the findings are exemplary shown for the lifting of a single TTCDA molecule from Ag(111). In the inset of the figure the frequency shift and the zero-bias differential conductance measured for the whole manipulation is shown. By the four arrows the points are indicated at which the spectra shown were measured. As before, the spectra are shifted to an uniform base and normalized for a better representation.

The interpretation of the class A manipulation differs from the interpretation of the class B manipulations discussed earlier. Just before the onset of the conductance peak the spectrum shows a dip at the Fermi level (red spectrum). As the zero-bias differential conductance goes trough a peak, the LUMO shifts to the Fermi level and sharpens (green spectrum). The level stays pinned at the Fermi level (blue spectrum) and thus increases the conductance, resulting in the Kondo peak. At the end of the manipulation no more signature at the Fermi level is observable (light blue spectrum). This behavior observed here is the same as was reported of earlier by Temirov *et al.* [39]. By the mechanical gating of the molecule the LUMO shifts to positive values, the LUMO gets depopulated. At the same time the coupling to the electrodes  $\Gamma$  is getting weaker. At some point the LUMO is occupied by one electron which acts as a magnetic impurity. As the energy gap  $\epsilon_0$  between the LUMO and the Fermi level is reduced to zero, the prerequisite for the observation of a Kondo resonance  $U/\Gamma \gg \epsilon_0$  is given.

The same observation was also made for PTCDA/Ag(111) of class A (see Fig. A.66 in chapter A). For NTCDA and QTCDA it was not possible to perform this measurement. To sum up the results of this measurements the findings are summarized in table 6.9. As PTCDA/Ag(111) shows Kondo behavior in both classes A and B it is unclear which class of liftings were performed earlier by Temirov *et al.* [39]. The fact that no hysteresis was observed in this former publication stems from the simple reason that no manipula-

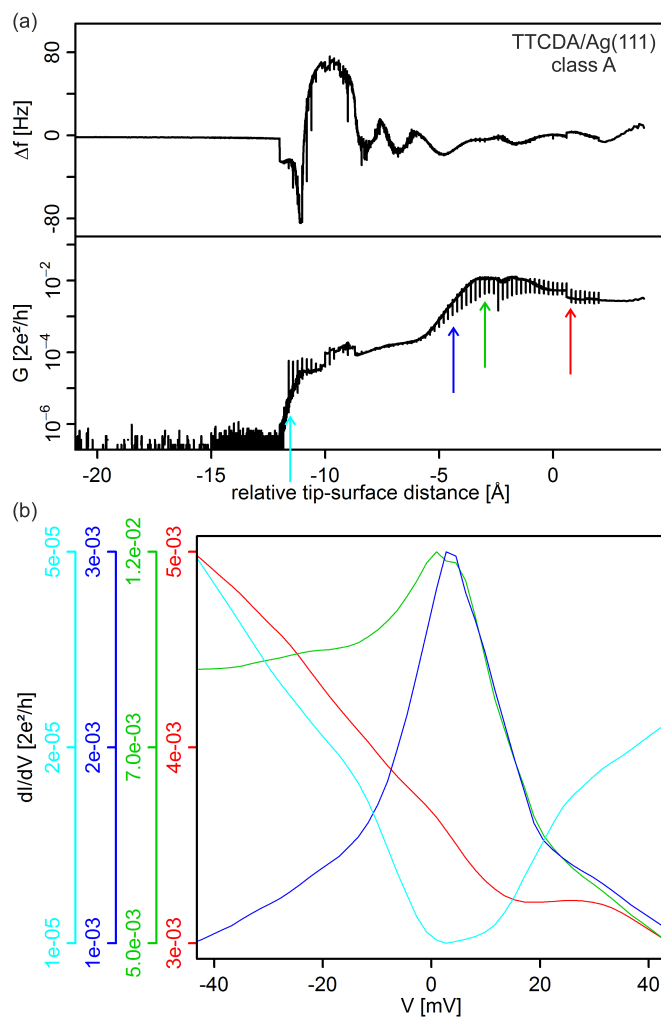


Figure 6.44: Spectra taken while lifting a TTCDA molecule from Ag(111). (a) The frequency shift and the differential conductance of the lifting process. (b) Every  $0.2 \text{ \AA}$  the manipulation was interrupted and a spectrum in the bias voltage range  $-50 \text{ mV}$  to  $50 \text{ mV}$  was taken. By the arrows in (a) the position of the four spectra presented is shown. The spectra show, that the Kondo resonance, as described earlier [39], is the origin of the conductance peak.

tion was performed where the molecule was lowered. Also note that no frequency shift measurement were performed at that time.

Molecule	class A	class B
NTCDA	no measurement	Kondo
PTCDA	Kondo	Kondo
TTCDA	Kondo	no Kondo
QTCDA	no measurement	no Kondo

Table 6.9: Observation of Kondo physics in class A and class B manipulations on Ag(111).

The position of the conductance peaks relative to the tip-surface distance is different for class A compared to class B manipulations. The distance between the conductance peak position relative to the surface for different molecules is in average about  $3.63 \text{ \AA}$  in the case of class A manipulations. For the manipulations of class B an average distance of about  $4.25 \text{ \AA}$  (see table 6.10) is found, i.e. the peaks are further apart in the case of class B compared to class A. The position at which the conductance peak is found in the case of NTCDA is about the same in class A and class B. The longer the molecule is the more the positions differ between both classes. This means that in the case of class A the molecule is closer to the surface than in class B when the peak is observed. This suggests that the formation of the conductance peak in both classes is not exactly the same.

It is found that also the conductance of the peak differs between both classes. In Fig. 6.45 the conductance values are plotted versus the molecule length. For both classes an exponential decay is observed. The decay constant of the peak conductance in class A is found to be  $\beta_{\text{peak}} = 0.32 \text{ \AA}^{-1}$ , i.e. the conductance peak is decreasing slower than in the case of the class B ( $\beta_{\text{peak}} = 0.42 \text{ \AA}^{-1}$ ). For all molecules the conductance of the peak is higher for class A than for class B. The longer the molecule is, the more the conductance difference increases. This is a consequence of the increasing coupling strength difference between both classes the longer the molecule is.

In table 6.10 the coordinates of the conductance peaks for both classes are listed. Note that they correspond to P<sub>2</sub> of table 6.5 and 6.7.

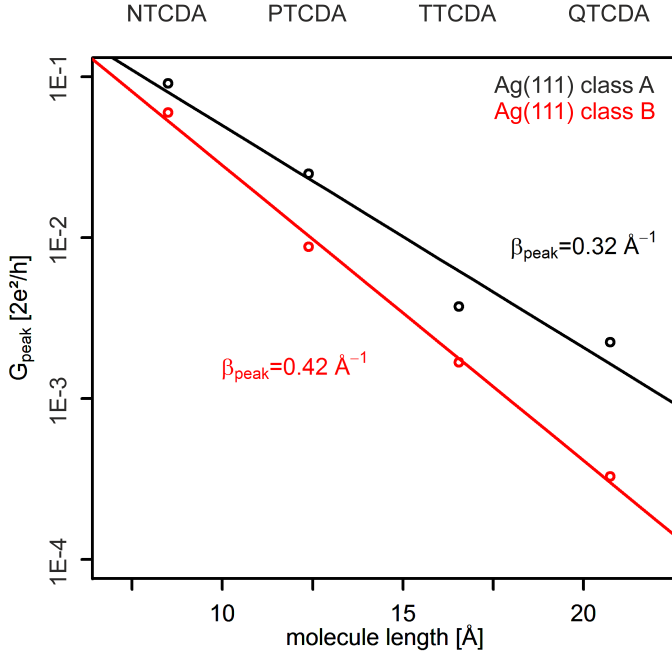


Figure 6.45: Conductance of the peak in class A and class B manipulations on Ag(111). The conductance of the peak shows an exponential decay upon the length of the molecule for both classes. The decay constant of class A with  $\beta_{\text{peak}} = 0.32 \text{ Å}^{-1}$  is smaller than the one found for class B ( $\beta_{\text{peak}} = 0.42 \text{ Å}^{-1}$ ).

Molecule	class A		class B	
	$z(\text{P}_2)$ [Å]	$G(\text{P}_2)$ [ $2e^2/h$ ]	$z(\text{P}_2)$ [Å]	$G(\text{P}_2)$ [ $2e^2/h$ ]
NTCDA	3.73	$9.13 \times 10^{-2}$	4.08	$6.01 \times 10^{-2}$
PTCDA	1.24	$2.50 \times 10^{-2}$	1.22	$8.88 \times 10^{-3}$
TTCDA	-2.95	$3.74 \times 10^{-3}$	-3.87	$1.69 \times 10^{-3}$
QTCDA	-7.16	$2.25 \times 10^{-3}$	-8.66	$3.28 \times 10^{-4}$

Table 6.10: Coordinates of the conductance peaks  $K$  in class A and class B on Ag(111). This are the coordinates of point  $\text{P}_2$  of table 6.5 and 6.7. The positions of the conductance peaks  $K_z$  refer to the relative tip-surface distance.

## 6.4.2.4 Molecules in wire configuration on Ag(111) of class A

As for class B the conductance of the molecular wire in the wire configuration was determined for class A. As in class B the position where the molecule is in the upright standing geometry was determined by a knee in the conductance data, indicating a transition between two transport regimes. This knee in the conductance data was always found in the region of the global peak of the frequency shift data. Not surprisingly the position of the molecule in the wire configuration relative to the tip-surface distance are for both classes very similar (see table 6.11). An average distance of 4.45 Å between two molecules is found for the class A manipulations and of 4.41 Å for class B manipulations.

In Fig. 6.46 the conductance values of the wires for the four different molecules contacted by silver electrodes of both classes are shown. The conductance values for both classes are very similar. For PTCDA, TTCDA and QTCDA the conductance in the wire configuration is smaller than the conductance found for class B. This could be the result of a weaker tip-molecule coupling in the case of class A, which could also explain the less stable junction configuration of class A compared to class B. For both classes an exponential dependence between the conductance and the length of the molecule is found. In fact the corresponding decay constants are very similar with  $\beta_{\text{wire}} = 0.17 \text{ \AA}^{-1}$  for class A and  $\beta_{\text{wire}} = 0.15 \text{ \AA}^{-1}$  for class B.

In table 6.11 the coordinates of the conductance of the molecule in the wire configuration for both classes are listed. Note that they correspond to  $P_3$  of table 6.7 and  $P_4$  of 6.5.

Molecule	class A		class B	
	$z(P_3) [\text{\AA}]$	$G(P_3) [2e^2/h]$	$z(P_4) [\text{\AA}]$	$G(P_4) [2e^2/h]$
NTCDA	-0.42	$9.82 \times 10^{-4}$	-0.86	$8.65 \times 10^{-4}$
PTCDA	-4.88	$2.87 \times 10^{-4}$	-4.43	$1.38 \times 10^{-3}$
TTCDA	-8.55	$2.64 \times 10^{-4}$	-9.02	$3.53 \times 10^{-4}$
QTCDA	-13.76	$9.87 \times 10^{-5}$	-14.09	$1.77 \times 10^{-4}$

Table 6.11: Coordinates of the conductance in the wire configuration in class A and class B on Ag(111). This are the coordinates of point  $P_3$  of table 6.7 and  $P_4$  of 6.5. The positions of the conductance refer to the relative tip-surface distance.

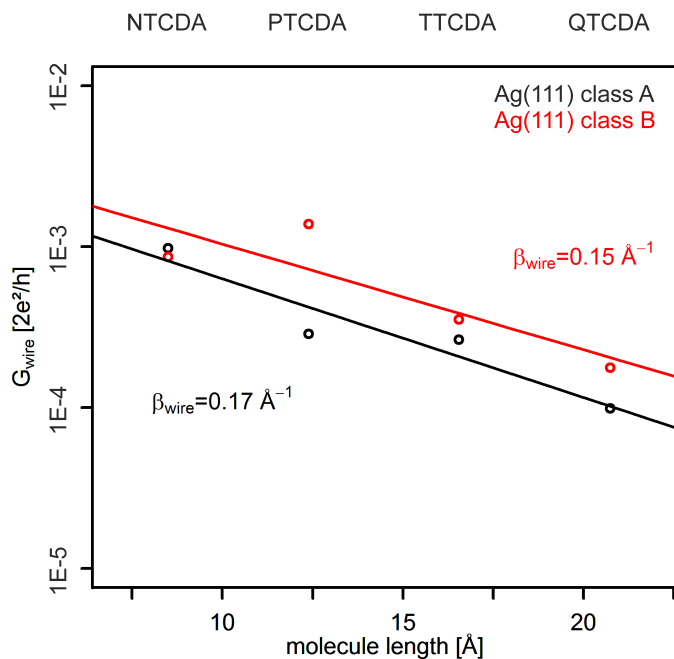


Figure 6.46: Conductance of the molecule in the wire configuration for class A (black dots) and class B (red dots) on Ag(111). The conductance  $G$  is plotted versus the length of the molecules  $L$ . The conductance values for class A and class B are very similar. While for class A an exponential dependence with the decay constant  $\beta_{\text{wire}} = 0.17 \text{ Å}^{-1}$  is found, for class B the decay constant is  $\beta_{\text{wire}} = 0.15 \text{ Å}^{-1}$ .

#### 6.4.2.5 Differences between class A and B on Ag(111)

The differences between class A and B are a result of the different geometric junction configurations (see Fig. 6.41). It was suggested that for class A the molecule is changing its configuration relative to the tip when the molecule is far away from the surface, as a consequence of a force induced by a spherically unsymmetrical d-orbital at the tip apex. This change of configuration is not observed for class B and thus it can be speculated that a spherically symmetric s-orbital is on the tip apex. These different orbitals at the tip apex could be the result of either a platinum or iridium atom at the tip in case of class A or a silver atom at the tip in case of class B. The configurations of the tip-molecule contact in the case of class A are less stable than the one in class B, therefore the configuration evolves most of the time from class A to class B. The opposite evolution from class B to class A was not observed.

The different junction configurations lead to different electronic properties. Only the electronic properties of class A show always Kondo physics when the conductance peak is observed. The influence of the junction configuration on the conductance of the molecule in the wire configuration is small.

### 6.5 Results: Molecular wires on Au(111)

After discussing the results of the molecule manipulations with silver electrodes, in the following sections will be discussed the manipulations of molecules with gold electrodes. The sample preparation and the measurement routines were introduced in section 2.5 and 6.2. In principle the experiments were performed in the same way as the ones discussed earlier for the silver electrodes.

Compared to Ag(111) the adsorption height of the molecules is higher on Au(111) [43, 122, 124, 185]. In Fig. 6.47 the average distance at which the jump into contact, i.e. the relative tip-surface distance at which the carboxylic oxygen of the molecule formed a bond with the tip, is plotted versus the molecule length. In the case of the Ag(111) surface (black dots) this jump into contact occurred on average for  $z_{\text{jump}}$  values 1.3 Å smaller than on Au(111) (red dots).

The z-axis used for the molecule manipulation data is relative to a stabilization point. The absolute distance of this stabilization point to the surface is not known and can be different for Ag(111) and Au(111). Therefore a smaller value of  $z_{\text{jump}}$  for Ag(111) does

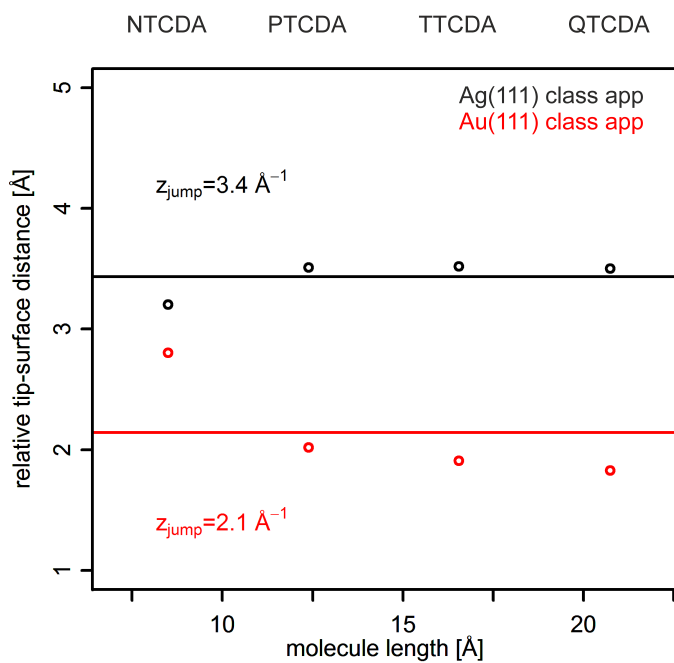


Figure 6.47: Average distance at which the carboxylic oxygen of the molecule and the tip formed a bond. This jump into contact occurred 1.3 Å closer to the surface in the case of manipulations on Ag(111) compared to manipulations on Au(111).



not necessarily imply that the jump occurs closer to the surface. But it is known from literature that in fact the gold tip has to be moved closer to the surface to make contact by about 0.4 Å, although the molecule-substrate bonding is weaker on Au(111) than on Ag(111) [40].

The carboxylic oxygen-tip bond in the case of Au(111) is not as strong as the carboxylic oxygen-tip bond in the case of Ag(111). Two difficulties arose from this: First, it was more difficult to isolate a molecule from the molecular islands on Au(111) than on Ag(111). Second, the probability to lift the molecule, after the contact was made, was smaller. As a consequence the total number of experiments is smaller on Au(111) than on Ag(111).

QTCDA was deposited together with another type of particles on Au(111). In contrast to the deposition on Ag(111) it was not possible to separate the two types of particles by annealing (see Fig 2.14 in section 2.5). This made it very difficult to isolate single QTCDA molecules on Au(111). The small data set obtained for QTCDA/Au(111) furthermore deviates substantially from the statistics of the other systems. It is therefore assumed that the manipulations measured on QTCDA/Au(111) are of defect QTCDA molecules, or QTCDA molecules together with the smaller particles.

In table 6.12 the total number of lifting and lowering curves used for the further analysis are listed. Again the manipulations were separated into class A and class B and will be discussed separately in the following. All histograms of manipulations on Au(111) are shown in Figs. A.29 to A.48 in chapter A. The total number of lifting and lowering is about the same for every molecule. But as the probability to observe manipulations of class A is increasing the longer the molecule is, the probability to observe manipulations of class B is decreasing. Such a relation was not observed for the manipulations on Ag(111).

Molecule	class A	class B
NTCDA	41	1912
PTCDA	404	1504
TTCDA	1035	796
QTCDA	116	184

Table 6.12: Number of lifting and lowering curves of the manipulations on Au(111) used for the statistical analysis.

### 6.5.1 Manipulations of class B on Au(111)

As for the manipulations with silver electrodes generic behaviors are extracted from the histograms of the manipulations with gold electrodes. The data is shifted and assigned to the different classes as it is described in section 6.3. For the class B manipulations the generic curves are determined by calculating the correlation between each curve as described in section 6.3.3.2. These generic behaviors are then used for the further analysis. In Fig. 6.48 the generic curves 2 for the three molecules NTCDA, PTCDA and TTCDA probed on Au(111) and assigned to class B are shown. The manipulations of NTCDA and PTCDA on Au(111) were done in a slightly different way than the manipulations of the other molecules. The molecules were not lifted up until the molecule-substrate bond was completely broken, but only until the peak-dip feature (feature B) was measured. By this a higher control of the junction was gained, the molecule was less likely to jump on the tip. This procedure was not applied to TTCDA and QTCDA as the junction is more stable for larger molecules. As the manipulations of QTCDA differ due to the contamination of the sample, they are not shown here.

Comparing the generic curves of class B on Ag(111) (see Fig. 6.27) to the ones on Au(111) (see Fig. 6.48) some differences can be observed. First of all no peak in the conductance is observed at the position of the last dip before feature B in the frequency shift. Further the transition between the two transport regimes as introduced in section 6.4.1.1 is much smoother.

As on Ag(111) the conductance in the contact tunneling regime is steeper for shorter molecules. This means that the bending mechanism observed and discussed for Ag(111) (see Fig. 6.33) is also valid on Au(111). The knee in the conductance data appears always before the main peak-dip feature. The main-peak dip feature still must correspond to the final removal of the molecule from the substrate [43]. The transition from the contact tunneling regime to the vacuum tunneling regime occurs after the removal of the last naphthalene unit, i.e. at a different junction configuration than on Ag(111). This would be a good indication for the absence of any electric interaction between oxygen atoms and the Au(111) substrate. This observation results in two different wire geometries as shown in Fig. 6.49.

The vacuum tunneling regime is not so clearly distinguishable as in the case of Ag(111). Therefore, to investigate the influence of the electrode material on the conductance of the molecules only point  $P_1$  and  $P_3$  are defined for Au(111) manipulations. With these two points the contact tunneling regime decay constant can be determined by making

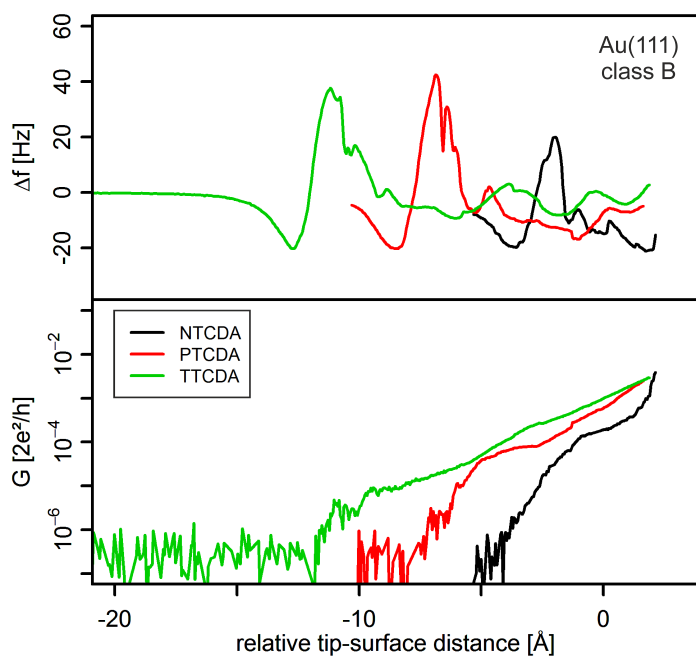


Figure 6.48: The generic curves 2 of three molecules manipulated on Au(111) assigned to class B. The upper panel shows the generic curves of the frequency shift, the lower panel shows the zero-bias differential conductance. In section 6.3 the procedure to determine these generic curves is described. The NTCDA and PTCDA curves are shorter because of a different manipulation routine (see section 6.5.1).

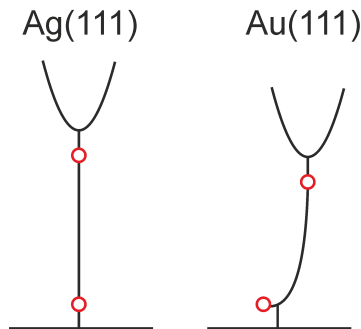


Figure 6.49: The wire configuration, i.e. the transition between the two transport regimes, for molecules contacted by silver electrodes is observed when the last oxygen atom is removed from the substrate. For molecules contacted by gold electrodes the wire configuration is observed after the removal of the last naphthalene unit, i.e. before the last oxygen atom is removed from the gold substrate.

a linear regression. The conductance of the molecule in the wire configuration can be calculated by  $P_3$  as was done earlier for the manipulations on Ag(111). In Fig. A.60 of chapter A these points and the linear regression are depicted together with the generic curves.

The two points  $P_1$  and  $P_3$  were defined by the following criteria:

$P_1$  Conductance  $G_{\text{start}}$  at the closest z-position relative to the substrate.

$P_3$  The conductance  $G_{\text{wire}}$  at the knee in the conductance data in the region of the global frequency shift peak.

Molecule	$P_1$ [ $\text{\AA}, 2e^2/h$ ]	$P_3$ [ $\text{\AA}, 2e^2/h$ ]
NTCDA	$(2.13, 3.89 \times 10^{-3})$	$(0.30, 2.00 \times 10^{-4})$
PTCDA	$(1.63, 2.45 \times 10^{-3})$	$(-4.92, 4.33 \times 10^{-5})$
TTCDA	$(1.87, 2.93 \times 10^{-3})$	$(-5.42, 3.33 \times 10^{-5})$
QTCDA	$(3.44, 3.07 \times 10^{-3})$	$(-10.15, 9.79 \times 10^{-5})$

Table 6.13: The coordinates of the points  $P_1$  and  $P_3$  for the analysis of the class B manipulations on Au(111).

The most striking feature in the frequency shift data, next to the earlier discussed peak-dip feature (feature B), are dips in the beginning of the lifting process (see chapter 5),

called feature A. In Fig. 6.50 these dips are highlighted by arrows. The number of dips is equal to the number of naphthalene units the molecule has. To clarify this the dips are grouped together by the ellipses 1 to 4. The dips in the first ellipse correspond to the removal of the first naphthalene units when the molecule is lifted from the substrate, the dips in the second ellipse correspond to the removal of the second naphthalene units and so on. If all molecules would be at the same adsorption site, the dips in every ellipse should be at the same position relative to the tip-surface distance.

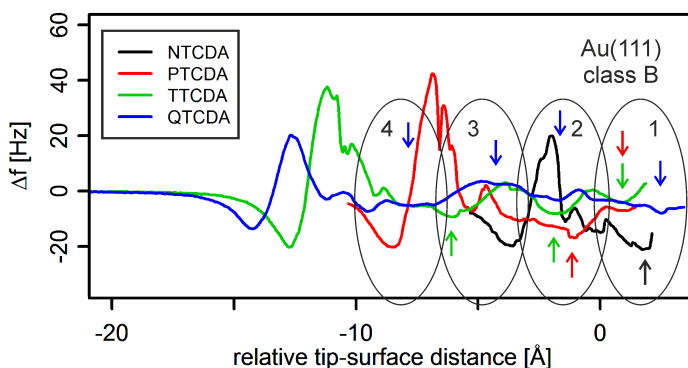


Figure 6.50: The dips in the generic curves of the frequency shift are assigned to the removal of a naphthalene unit. By the arrows the position of the dips is shown. The first ellipses shows which naphthalene unit is removed first from the substrate when lifting up the molecule, the second ellipse shows which naphthalene unit is removed second and so on.

In the manipulations on Ag(111) these dips are not observed that clearly. Nevertheless in some of the single individual lifting or lowering curves dips are visible, but much less pronounced than on Au(111) and at less regular distances and less regular shapes. The reason that the dips are less pronounced on Ag(111) is the higher corrugation of Ag(111) compared to Au(111) [186]. This leads to jumps of the molecule as the molecule slides above the surface when being manipulated by the tip. As a consequence the frequency shift measured is more scattered than on Au(111). Further in the case of Ag(111) the molecule is charged in contrast to Au(111). This charging of the molecule creates additional forces in the junction. These forces are also measured by the qPlus sensor and thus influence the frequency shift observed. These two effects could lead to the less reproducible observation of the dips in the case of Ag(111) compared to

Au(111).

To probe the electronic structure within the junction the molecule was manipulated and differential conductance spectra were measured by lock-in technique as introduced earlier. The molecule was lifted up in steps of 0.5 Å, at every step the manipulation was stopped and a differential conductance spectrum was measured. This spectrum was recorded in a bias voltage range from -50 mV to 50 mV. In Fig. 6.51 three spectra are shown measured on a PTCDA molecule manipulated by gold electrodes. In the inset the frequency shift and the zero-bias differential conductance measured for the whole lifting process are displayed. The arrows indicate at which positions the spectra were measured. For a better representation the spectra are brought to a uniform base and are normalized such that all three spectra have the same maximum value. In absolute values the red spectrum shows the highest differential conductance and the blue spectrum the lowest.

The spectra show a dip around the Fermi level. As the molecule is lifted up and the zero-bias differential conductance is decreasing no change in the spectra is observed. There is no orbital moving across the Fermi level. As no states are at the Fermi level the electrons are tunneling off-resonant in contrast to the observation made on Ag(111). In consequence the conductance through the junction is much lower in comparison to the molecule junctions with silver electrodes.

#### 6.5.1.1 Influence of the electrodes material on the conductance of the junction

In section 6.4.1.1 it was shown that we can distinguish between two transport regimes in the manipulations on Ag(111). This is not the case for the manipulations on Au(111). There we see a much smoother transition from one regime to the other in comparison to Ag(111) (compare Fig. 6.27 to Fig. 6.48). As a consequence the position at which the junction is ruptured is not as clearly visible in the case of gold electrodes. The reason for the smooth transition is that the molecules are physisorbed on Au(111) and not chemisorbed as on Ag(111). In the case of Ag(111) the molecule hybridizes with the substrate, this hybridization is ruptured at the moment of the transport regime transition. In the case of Au(111) no hybridization occurs and therefore the electronic structure is not changing so dramatically as the molecule is ruptured from the surface.

As done in section 6.4.1.1 from the two points  $P_1$  and  $P_3$  defined earlier the decay constants of the contact tunneling regime is determined. Note that the decay constant

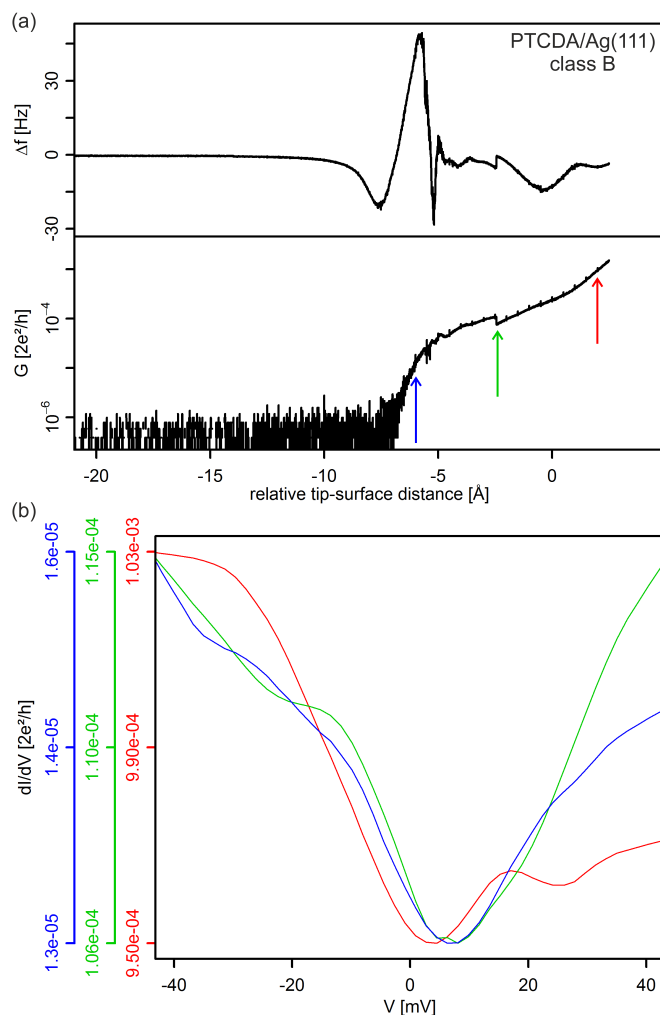


Figure 6.51: Spectra taken while lifting a PTCDA molecule from Au(111). In the inset is shown the frequency shift and the zero-bias differential conductance measured during the lifting process. Every  $0.5 \text{ \AA}$  the manipulation was interrupted and a spectrum in the bias voltage range  $-50 \text{ mV}$  was recorded. By the arrows in the inset the position of the three spectra presented is shown. The spectra show no changes upon the lifting of the molecule. No states are at the Fermi level, in contrast to the observation made on Ag(111).

determined for QTCDA on Au(111) will not be considered in the following discussion, due to the preparation difficulties mentioned earlier. The decay constants of molecules on Au(111) are shown in Fig. 6.52 (red dots) together with the decay constants found for the manipulations on Ag(111) assigned to class B (black dots). The latter decay constants correspond to the ones shown in Fig. 6.32. For both metals the decay constants are decreasing with increasing molecule length. The decay constants determined for the manipulations on Au(111) exceed the ones found on Ag(111) in average by  $0.4 \text{ \AA}^{-1}$ . Further it can be seen that the decay constants of both metals show a similar behavior. A saturation with increasing molecule length is observed.

A larger decay constant results from a lower transmission probability for the tunneling electrons. In section 6.4.1.1 it was argued that the work function is increased as a molecule gets in contact with the tip, in consequence the transmission probability was decreased. The dependence of the decay constants upon the electrode material can be explained by the different work function of Ag(111) and Au(111). Romaner *et al.* [122] calculated the work function of coinage metals with DFT and found that the work function of Au(111) ( $\phi = 5.56 \text{ eV}$ ) is larger than the work function of Ag(111) ( $\phi = 4.91 \text{ eV}$ ). This observation is consistent with the decay constants measured for the molecules on the two metals.

The conductance of the molecule standing upright in the junction, i.e. in the wire configuration is shown in Fig. 6.53. Next to the conductance of the molecular wire contacted by gold electrodes (red dots), the conductance of the molecular wire contacted by silver electrodes, as shown in Fig. 6.38, is presented (black dots). Again the conductance of QTCDA on Au(111) is neglected in the discussion. As for the wire contacted by silver electrodes an exponential dependence is observed between the wire conductance and the molecule length. A decay constant of  $0.22 \text{ \AA}^{-1}$  is determined for gold, in contrast to  $0.15 \text{ \AA}^{-1}$  for class B manipulations on Ag(111). This means in both junctions the decay constant is similar. The absolute conductance of the molecule in the wire configuration is about one magnitude higher in the case of silver electrodes. This is a consequence of the stronger coupling of the silver electrodes with the carboxylic oxygen of the molecule and the non-existence of a orbital crossing the Fermi level in the Au(111) case. Therefore the transport mechanism observed here is believed to be off-resonant coherent tunneling. In table 6.14 the wire conductance values for both metals for manipulations of class B are shown.

The influence of the electrodes material on the conductance through molecules was investigated by several groups [158,166,167,187–190]. Most groups found higher conductance



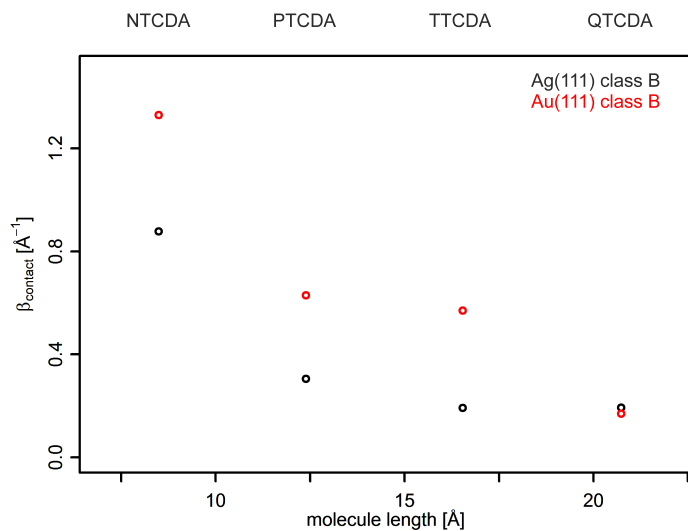


Figure 6.52: Decay constants of the contact tunneling transport regime of the manipulations on Au(111) (red dots) and Ag(111) (black dots) assigned to class B. Both decay constants are decreasing with increasing molecule length in a similar way. The decay constants determined on Au(111) are in average about  $0.4 \text{ \AA}^{-1}$  larger than on Ag(111).

Molecule	$G_{\text{wire}} [2e^2/h]$	
	Au(111)	Ag(111)
NTCDA	2.00e-4	8.65e-4
PTCDA	4.33e-5	1.38e-3
TTCDA	3.33e-5	3.53e-4
QTCDA	9.79e-5	1.77e-4

Table 6.14: Conductance of the molecular wire  $G_{\text{wire}}$  for both metal electrodes of manipulations assigned to class B.

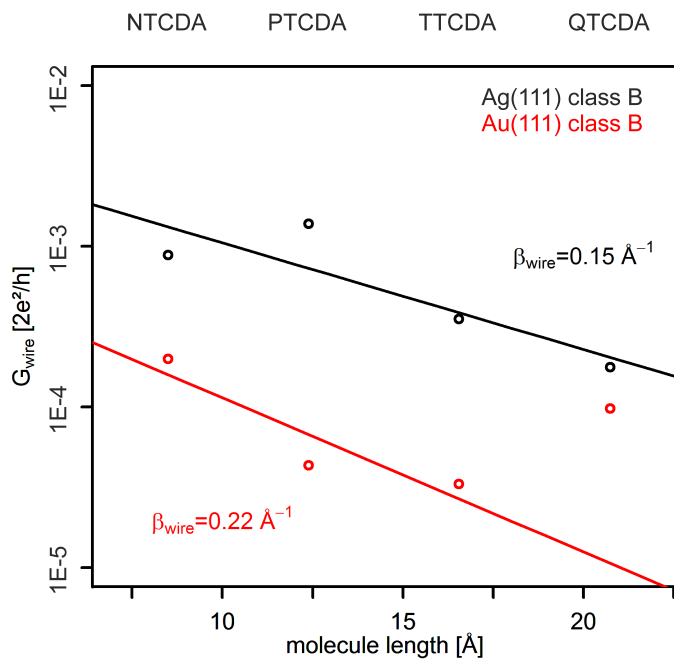


Figure 6.53: Conductance of the molecular wires for manipulations of class B on Au(111) (red dots) and Ag(111) (black dots). On both metals an exponential dependence is observed (neglecting QTCDA/Au(111)). The conductance values measured with molecular wires contacted by silver electrodes are about one magnitude higher than the ones measured with gold electrodes.

in the case of gold electrodes contacting the molecules [167,187–189]. Yaliraki *et al.* [187] state in their study on dithiols that the Au(111)-thiol bond is weaker than the Ag(111)-thiol, but in consequence the C-S bond is weaker when the molecule is bond to the silver electrode. Thus in result the conductance is higher in the case of gold electrodes. Kim *et al.* [167] measured the conductance through a 1,4-benzenediamine molecule by scanning tunneling microscope based break-junction technique. They found a three times higher conductance when the molecule is contacted by gold electrodes ( $G = 6.4 \times 10^{-3} G_0$ ) compared to silver electrodes ( $G = 2.1 \times 10^{-3} G_0$ ). This was explained by the work function difference between the two electrodes. Engelkes *et al.* [158] investigated self assembled monolayers of alkanethiol contacted by electrodes of different materials. They found that the contact transmission is higher for chemisorbed contacts than physisorbed contacts.

### 6.5.2 Manipulations of class A on Au(111)

As in the case of manipulations with silver electrodes on gold two different classes of generic behaviors were observed. The hysteresis that was observed for class A manipulations on Au(111) showed the same features as the hysteresis on Ag(111) (see Fig. 6.39). This suggests that the interpretation that was given earlier to explain the hysteresis is the same for both metals. This means that the three tip-molecule configurations that were assumed to be observed while manipulating molecules on Ag(111) are also observed when the manipulation is done on Au(111).

In Fig. 6.54 the generic behaviors for manipulations assigned to class A on Au(111) are plotted. No conductance was recorded for manipulations of class A on NTCD. Frequency shift measurement of class A exist, as at the beginning of the study a few manipulations were made where only the frequency shift was measured. From the generic behaviors of class A it is found that the conductance of PTCD and TTCD evolve remarkably parallel. Further it is found that in comparison to the manipulations with silver electrodes the differences in the conductance behavior between class A and class B on gold are negligible. This means, that the transport through molecules contacted by gold electrodes is less influenced by the exact geometry of the contact than in the case of silver electrodes. Again, no peak in the conductance is observed, in contrast to the observation on Ag(111).

Again, two points  $P_1$  and  $P_3$  are defined and a linear regression is made to get the decay constants for the contact tunneling regime. As for the manipulations of class B

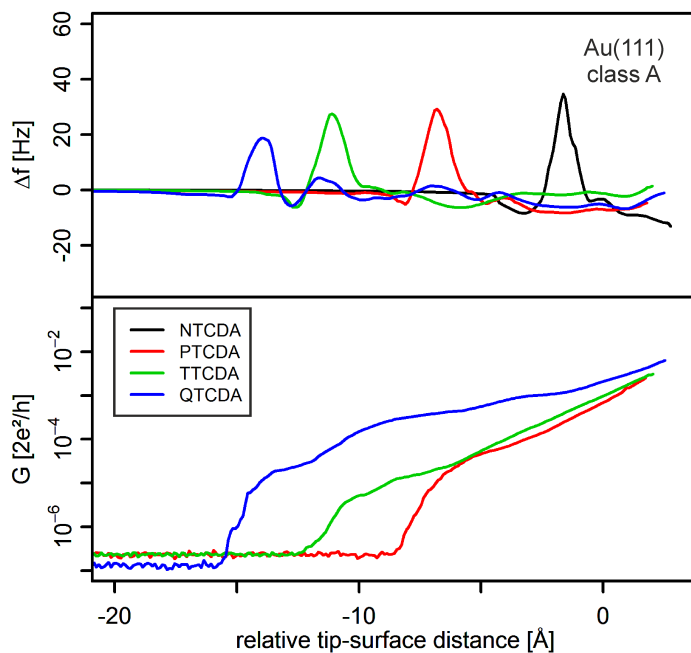


Figure 6.54: The generic behaviors assigned to class A for manipulations on Au(111). No zero-bias differential conductance was recorded for manipulations of class A with NTCDA. The hysteresis shows the same features as were observed with silver electrodes. The conductance behavior of class A is not very different to the one observed for class B. This means that in the case of gold electrodes the transport through the molecule is much less influenced by the exact tip-molecule contact geometry.

on Au(111) no clear transition is observed between two transport regimes, in contrast to the observation made on Ag(111). In Fig. A.59 in chapter A the two points and the linear regression are plotted together with the generic behaviors. The two points  $P_1$  and  $P_3$  were defined by the following criteria:

- $P_1$  Conductance  $G_{\text{start}}$  at the closest z-position relative to the substrate.
- $P_3$  The conductance  $G_{\text{wire}}$  at the knee in the conductance data in the region of the global frequency shift peak.

Molecule	$P_1$ [ $\text{\AA}, 2e^2/h$ ]	$P_3$ [ $\text{\AA}, 2e^2/h$ ]
NTCDA	no data	no data
PTCDA	$(1.74, 2.52 \times 10^{-3})$	$(-6.00, 2.35 \times 10^{-5})$
TTCDA	$(2.04, 3.10 \times 10^{-3})$	$(-7.49, 1.57 \times 10^{-5})$
QTCDA	$(2.53, 6.32 \times 10^{-3})$	$(-14.00, 1.08 \times 10^{-5})$

Table 6.15: The coordinates of the points  $P_1$  and  $P_3$  for the analysis of the class A manipulations on Au(111).

### 6.5.2.1 Transport in class A manipulations on Au(111)

In Fig. 6.55 the decay constants of the contact tunneling regime of both classes on Au(111) are plotted versus the length of the molecules. For class A no data was measured for NTCDA. For the other three molecules probed it is found that the decay constants do not differ a lot between both classes. Together with the earlier made observation upon the generic behavior, that the conductance behavior is very similar for both classes the following can be concluded: The different geometric tip-molecule configurations leading to the observation of two well distinguishable manipulation behaviors have little impact on the conductance behavior in the case of Au(111).

In Fig. 6.56 the conductance values of the molecule standing upright in the junction, i.e. in the wire configuration for both classes on Au(111) are plotted. Again the conductance of QTCDA is disregarded as it is unclear if intact single isolated QTCDA molecules were probed on Au(111). As no conductance data was measured for NTCDA the decay constant of class A on Au(111) has to be determined by two points. As observed for the two classes on Ag(111) (see Fig. 6.46) the conductance of the wires assigned to class B are larger than the ones assigned to class A. A decay constants of  $\beta_{\text{wire}} = 0.1 \text{ \AA}^{-1}$  is found for the wire conductance on Au(111) of manipulations of class A and  $\beta_{\text{wire}} = 0.22 \text{ \AA}^{-1}$  for the

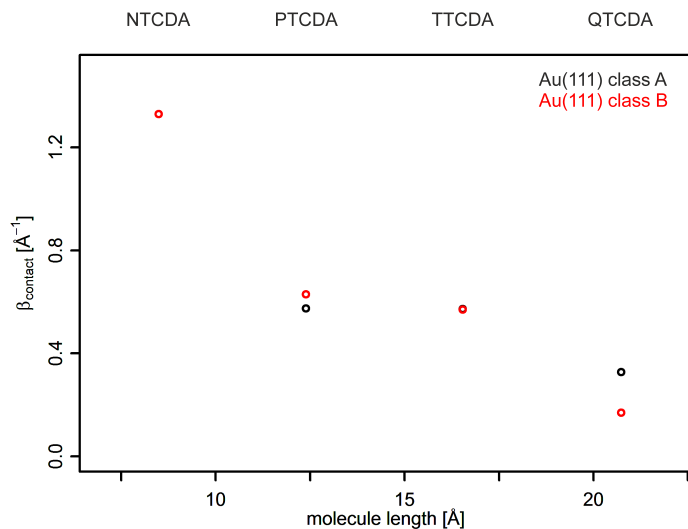


Figure 6.55: Decay constant of the contact tunneling regime of class A and class B on Au(111). Both classes show very similar behaviors. This means, that the different tip-molecule geometries observed influence the conductance less when the molecule is contacted by gold electrodes compared to silver electrodes.

manipulations of class B. This means that both decay constants differ in contrast to the observation made on Ag(111). The reason might be, that only two molecules are taken into account to determine the decay constant of class A.

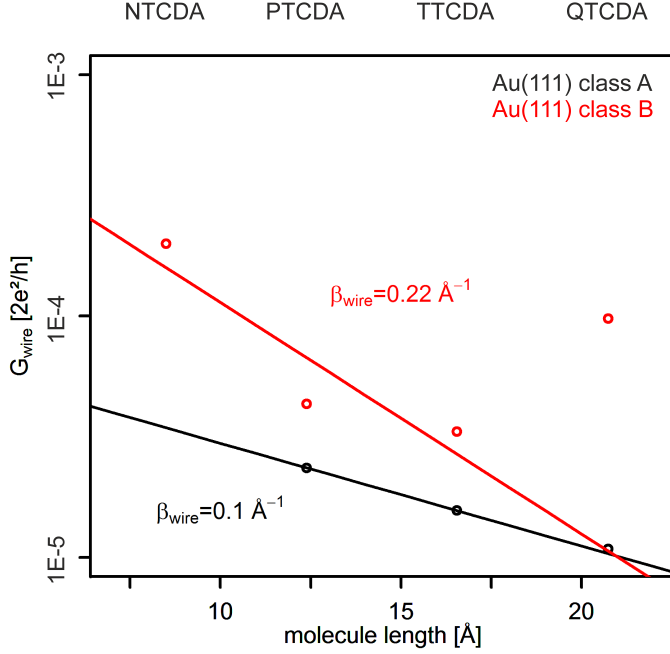


Figure 6.56: Conductance of the molecule in the wire configuration of class A and class B on Au(111). As observed on Ag(111) the conductance of class B is higher than the conductance of class A.

### 6.5.2.2 Influence of the electrodes material on the frequency shift

After discussing the influence of the electrode material on the conductance the frequency shift is investigated. It is observed that the height of the global peak of the frequency shift on Ag(111) (feature B) is always larger than the corresponding one observed on Au(111). Further to the absolute height of the peak, the difference between the peak heights of both electrode materials  $\Delta P_{\text{peak}}$  can be determined. In Fig. 6.57 the difference of the peak heights  $\Delta P_{\text{peak}}$  of feature B of manipulations on silver and gold is plotted

versus the molecule length for class A and class B. The two lines indicate the average difference between the peak heights, while again neglecting the differences for QTCDA. This shows that the peak height difference  $\Delta P_{\text{peak}}$  is much more pronounced between the class B manipulations of both substrates. In table 6.16 the heights of the peaks of feature B in the frequency shift for the manipulations on Ag(111) and Au(111) are listed together with the peak height differences  $\Delta P_{\text{peak}}$ .

Molecule	classA		
	$P_{\text{peak}}(\text{Au}(111))$ [Hz]	$P_{\text{peak}}(\text{Ag}(111))$ [Hz]	$\Delta P_{\text{peak}}$ [Hz]
NTCDA	35	43	8
PTCDA	29	50	21
TTCDA	28	35	7
QTCDA	19	55	36

---

Molecule	classB		
	$P_{\text{peak}}(\text{Au}(111))$ [Hz]	$P_{\text{peak}}(\text{Ag}(111))$ [Hz]	$\Delta P_{\text{peak}}$ [Hz]
NTCDA	20	68	48
PTCDA	42	73	31
TTCDA	38	84	46
QTCDA	20	53	33

Table 6.16: Height of the peak  $P_{\text{peak}}$  in the frequency shift for both metal electrodes and the differences between both peak heights  $\Delta P_{\text{peak}}$  for all manipulations assigned to class A and class B.

By integrating the frequency shift two times the potential energy in the junction can be determined (see chapter 5). The height of the peak in the frequency shift is then related to the energy needed to remove the molecule from the substrate. Since the height is always found to be larger on Ag(111) this means that the interaction between the silver electrode and the molecule is larger than the interaction between the gold electrodes and the molecule. This is the result of the larger coupling between the carboxylic oxygen and the substrate in the case of silver.



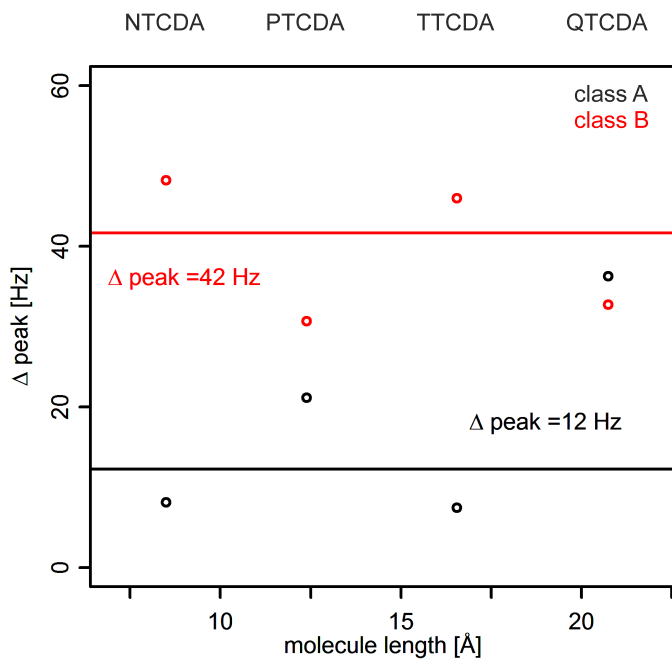


Figure 6.57: Differences of the peak heights  $\Delta \text{ peak}$  of feature B between manipulations on silver and gold assigned to class A or class B. The peak height of manipulations on Ag(111) is always larger than the peak height of manipulations on Au(111). Further the peak height differences are much more pronounced for class B.

## 6.6 Conclusions

In this chapter a systematic study on molecules of different length contacted by two types of electrodes was presented. A method was introduced which allows highly reproducible simultaneous measurement of the zero-bias differential conductance and the frequency shift in the junction tip-molecule-substrate during the manipulation of a single molecule. Further an analysis was presented, which based on the extraction of generic behaviors of the physical quantities measured. It was found that the total statistic can be separated into several classes. Two classes named class A and class B were analyzed in depth. The analysis showed that the transport through the junction not only depends on the electrode material but also on the geometrical configuration of the tip-molecule contact.

In the first part of the chapter the measurement routine and data processing was introduced. Manipulations were performed which allowed it to gain large statistic for all eight systems probed (NTCDA, PTCDA, TTCDA and QTCDA on Ag(111) and Au(111)). For the analysis every individual lifting or lowering curve was assigned to a class. The individual curves had to be assigned to different classes, as two very well distinguishable behaviors were observed. These classes of curves were then eventually shifted and histograms were plotted. From these histograms, generic behaviors for the two physical quantities, the zero-bias differential conductance and the frequency shift were extracted by calculating arithmetic means for class A manipulations and determining the correlation between each curve for class B manipulations. With these generic behaviors the further analysis was performed. The class A was characterized by a hysteresis between the data measured while lifting the molecule and the data while lowering the molecule. This was attributed to a switching event in a bistable junction geometry, which leads to two different tip-molecule contact geometries for class A. It was assumed that this switching event is the consequence of a unsymmetrical d-orbital at the tip originating from a platinum or iridium atom at the tip apex. The second class observed, class B, was characterized by a very stable junction geometry, this was attributed to a symmetric s-orbital at the tip originating from a silver atom at the tip apex. This stable junction geometry made it possible to measure highly reproducible data sets.

In the following first the result of the manipulations of molecules by silver electrodes were presented. It was found that the transport through the molecules contacted by silver can be split into two transport regimes. The first transport regime is observed as long as the molecule or part of it are still in contact with the substrate and was called

contact tunneling regime. The second transport regime is identified as tunneling through the ruptured junction and is called vacuum tunneling regime. This separation into two transport regimes was made upon features found in the frequency shift and differential conductance data. The decay constant of both transport regimes were calculated. It was assumed that in both regimes tunneling is observed. A dependence of the contact tunneling decay constant on the molecule length was observed. The longer the molecule is the smaller is its (normalized) decay constant. This was explained by the bending of the molecules during the lifting process. This bending was also observed in the force-field simulations. It was further shown that the decay constants of the vacuum tunneling regime are larger than the decay constants of the conductance of the bare metal tip approaching the surface before making contact to the molecule. From this it was concluded that the work function of the junction is increased as a molecule is bound to the tip.

For manipulations of both classes on Ag(111) a conductance peak was observed in the generic zero-bias differential conductance curves. This peak in the conductance always coincided with a dip in the frequency shift which is a signature of the removal of the last naphthalene unit. With differential conductance spectra in the junction the electronic structure was probed during the manipulation. For class A manipulations of PTCDA and TTCDA a Kondo resonance could be identified through a peak at the Fermi level. In class B NTCD and PTCDA showed Kondo characteristics, while for TTCDA and QTCDA no Kondo signature was observed. This means that at least two different mechanism are responsible for the conductance peak.

The analysis of the manipulations on Au(111) revealed the same two classes A and B. In contrast to the manipulations with silver electrodes the transition between the two transport regimes is observed in a different junction configuration. The transition is observed after the removal of the last naphthalene unit. This indicates that no electric interaction is present between the oxygen atoms and the gold substrate. The generic frequency shift curves showed well pronounced dips, which were assigned to the removal of the naphthalene units. The conductance behavior of the two classes A and B showed no significant differences. From this it follows, that the exact junction configuration has less influence on the transport through the molecule when it is contacted by gold electrodes in contrast to silver electrodes. Further no peak in the conductance was observed.

The electronic structure of the gold junction was also probed by making differential conductance spectra while lifting the molecule. It was shown that no change is ob-

servable in the junction upon the manipulation with gold electrodes. No orbital is crossing the Fermi level. This missing electron density at the Fermi level is responsible for the about one order of magnitude smaller conductance through molecules contacted by gold in contrast to molecules contacted by silver electrodes. This finding is the opposite observation to what was found for many molecular junctions with thiolated molecules.

In summary it can be stated that a method was developed which allows the highly reproducible probing of the transport through molecular junctions. By comparing this transport information to the geometry recorded by measuring the frequency shift a very detailed analysis of the junction physics is possible. Together with transport spectroscopy a lot of assumptions about the physics in the junction can be made.

## 7 Summary

In this thesis the quantum transport through molecular wires was systematically investigated. To this purpose a method was developed which allowed the controlled manipulations of molecules contacted by metal electrodes with a combined LT-STM/AFM. During these manipulations the frequency shift to monitor the mechanical properties in the junction was measured with the AFM. To achieve the superior control of the junction the frequency shift measured by the AFM was compared to force-field simulations which allowed gaining structural information. The zero-bias differential conductance to probe the transport was measured with the STM. Further transport spectroscopy was performed by STS.

A homologous series of  $\pi$ -conjugated molecules was probed on the two different metals Ag(111) and Au(111). Before performing the transport measurements some preliminary experiments were done. First the molecular islands deposited on the two metals were investigated. In the process it was observed that the QTCDA molecules were always deposited together with another type of particle. On Ag(111) this second type of particles could be separated from the QTCDA molecules which allowed to create pure QTCDA islands. On Au(111) this separation was not possible. As a consequence only for seven of the eight systems the unit cells were determined.

Next to the geometrical structure of the adsorbed molecules the electronic structure was investigated. This was done by performing STS measurements. It was found that in the case of molecules adsorbed on Ag(111) the LUMO of the molecules shifts to negative energies upon adsorption and that the energy of the LUMO and the size of the molecules show a linear relation. This dependence between LUMO and molecule size was explained by the change of the work function when the molecule adsorbs. In the case of adsorption on Au(111) the LUMO of the molecules is not shifted to negative values. This means that in the case of adsorption on Au(111) physisorption is observed, contrary to the chemisorption which is observed on Ag(111). But also on Au(111) a linear dependence between the LUMO energy and the molecule length was observed. Again the work function change was used to explain this observation.

## 7 Summary

While investigating NTCDA on Ag(111) three different geometric phases were observed. Thereby it was found that NTCDA molecules on Ag(111) can be distinguished by two different electronic structures. It was observed that every second molecule, called type A, showed a Kondo resonance at the Fermi energy, while the type B molecule showed no Kondo resonance. Next to this resonance signatures of coupling between a molecular vibration and electrons were identified. By performing DFT calculations this vibration was identified. Further it was shown that the formation of the Kondo state is determined by the adsorption site. By measuring differential conductance maps it was shown that the type B molecules can also show the Kondo resonance when they are lifted up by 1 Å from the surface.

The method to control the junction geometry was introduced earlier in the two letters “Force-controlled lifting of molecular wires” by Fournier *et al.* [42] and “Measurement of the Binding Energies of the Organic-Metal Perylene-Teracarboxylic-Dianhydride/Au(111) Bonds by Molecular Manipulation Using an Atomic Force Microscope” by Wagner *et al.* [43]. In the letter by Fournier *et al.* [42] it was shown that by measuring the frequency shift with an AFM and comparing these experimental measurements to simulations the geometry in the junction can be determined at any moment of the manipulation process. In the letter by Wagner *et al.* [43] the simulation and the frequency shift measurement were used to determine the adsorption energies of the systems NTCDA on Au(111) (1.7 eV) and PTCDA on Au(111) (2.5 eV). This new method allows the measurement of the adsorption energies of systems which could not be probed with classical methods as e.g. temperature programmed desorption (TPD).

In the main chapter of this thesis the systematic transport measurement on eight different molecule-metal systems were presented. Based on the knowledge of the electronic and geometric structure of the systems an interpretation of the experimental data was given. Therefore an extensive data processing and statistical analysis had to be developed. It was found that the manipulations can be split into two main classes. The statistical analysis was based on generic behaviors which were extracted from 2D histograms of the measured data. Two approaches were chosen. The first one was applied to the manipulations assigned to class A and was based on the determination of generic behaviors by calculating arithmetic means. The second one was applied to the manipulations of class B and was based on a correlation analysis. The generic curve was defined as the measured curve with the highest correlation in respect to all other measured curves of the same class.

First the molecular manipulations with silver electrodes were discussed. It was found that

## 7 Summary

the two classes mentioned earlier can be related to different tip-molecule configurations. The class A manipulations are characterized by a hysteresis in the experimental data between the lifting and lowering of the molecule. This was explained by a geometrical switching at the tip-molecule contact in a bistable junction triggered by an unsymmetrical d-orbital on the tip apex resulting from a platinum or iridium atom. In contrast to this the manipulations of class B are characterized by a stable junction configuration resulting from the symmetrical s-orbital of a silver atom at the tip apex. This stable junction configuration allowed very reproducible manipulations. The transport through molecules on Ag(111) is characterized by a sharp transition between two transport regimes. The first one, named contact tunneling regime, is observed as long as the molecule is in contact with the two electrodes tip and surface. The second transport regime, named vacuum tunneling regime, was identified as tunneling through the ruptured metal-molecule-metal junction. Decay constants for both transport regimes were measured. It was found that the decay constant of the contact tunneling regime decreases the longer the molecule is. Even when this decay constants are normalized by the length of the molecule they decrease the longer the molecule is. This was explained by the fact that the longer the molecule is, the more flexible it is and thus is bending more towards the surface. As a consequence the transport orbital of the longer molecule is longer in contact with the surface. The decay constant of the vacuum tunneling regime is found to not depend on the length of the molecule, with an average  $\beta_{\text{vacuum}} = 2.8 \text{ \AA}^{-1}$ . This vacuum tunneling decay constant was compared to the decay constant determined while manipulating the bare metal tip over the molecules, which was found to be smaller (in average  $\beta_{\text{silver tip}} = 1.93 \text{ \AA}^{-1}$ ). This difference was explained by the change of the work function by the oxygen-metal bond when the molecule is bound to the tip.

In manipulations of both classes a peak is observed in the conductance data. By transport spectroscopy measurements on the manipulated molecules it was shown that the peak in class A manipulations on Ag(111) is always originating from a Kondo resonance at the Fermi level. The peak in the class B manipulation on Ag(111) on the other hand is not always originating from a Kondo resonance. Only for the two smallest molecules, NTCDA and PTCDA, the transport spectroscopy measurements revealed Kondo behavior, i.e. a peak at the Fermi level. The reason for this different behavior is not yet clear. By comparing the conductance of the upright standing molecules in the junction an exponential dependence between the molecule length and the conductance was found. This suggests that off-resonant coherent tunneling is the underlying transport mechanism in the junction.

## 7 Summary

Next to the manipulations on Ag(111) manipulations on Au(111) were discussed. It was shown that the same geometrical configurations as found on Ag(111) are also present upon manipulation with gold electrodes, i.e. the classes A and B are also observed while manipulating molecules on Au(111). The distinction between two transport regimes as observed on Ag(111) is not so well pronounced on Au(111), instead a smooth transition at the position where the molecule stands upright in the junction is observed. This could be a consequence of the weaker metal-oxygen bond on Au(111). Further it was shown by transport spectroscopy measurement that the electronic structure of the junction is not changing significantly upon manipulation. No orbital is crossing the Fermi level while lifting the molecule from the substrate and no Kondo behavior is observed. The weaker metal-oxygen bond on Au(111) explains the about two magnitudes lower conductance measured on molecules contacted by gold electrodes. In the frequency shift data of the manipulation on Au(111) oscillations, which were attributed to the removal of the naphthalene units, were identified. Further it was shown that the global peak in the frequency shift data measured on Ag(111) is significantly higher than on Au(111) as a consequence of the higher interaction of the molecules with the metal.

The most important achievement of this thesis was to introduce a new method which allows the analysis of molecular wires. It was shown that very reproducible data can be measured by this method. The knowledge about the junction structure during manipulation was used to interpret the transport characteristics. Now, theoretical calculations are needed to validate the assumptions made in this thesis. Also a more profound analysis of single lifting events is desirable, as these show intrinsic features which were not discussed yet in detail. The new experimental method should be applied further to different molecule/metal systems. In the context of our study it would be especially interesting to study the influence of different functional groups on the transport behavior through the molecules.



# A Supplemental materials

In chapter 6 the processing of the data was shown exemplary on the system QTCDA on Ag(111); in this appendix all the data is shown. The complete 2D histograms of all eight systems are shown in Figs. A.9, A.14, A.19, A.24, A.29, A.34, A.39 and A.44. Further the 2D histograms of all lifting and lowering curves assigned to a particular class app, A, B and C, together with the generic curves are presented (Figs. A.1 to A.8, A.10 to A.13, A.15 to A.18, A.20 to A.23, A.25 to A.28, A.30 to A.33, A.35 to A.38, A.40 to A.43 and A.45 to A.48). The 2D histograms are plotted with the counts on a logarithmic scale as can be seen from the corresponding legends. In the caption to each 2D histogram the bin sizes are given. For the frequency shift the bin size of the  $z$ -axis (relative tip-surface distance) in Å and the  $y$ -axis ( $\Delta f$ ) in Hz are given. For the conductance the bin size of the  $z$ -axis (relative tip-surface distance) in Å and two bin sizes for the  $y$ -axis ( $G$ ) in  $2e^2/h$  are given. Two bin sizes have to be given, as the conductance is plotted on a logarithmic size and consequently the size of the bins vary. The first bin size  $\min(y)$  refers to the smallest bin, the second bin size  $\max(y)$  to the largest bin.

The histogram of the correlation values as defined in section 6.3.3.2 are shown in Figs. A.49 to A.56. Further the points  $P_1$ ,  $P_2$ ,  $P_3$ ,  $P_4$  and  $P_5$  determined to analyze the transport through the molecular wires are shown together with the generic curves and the linear regressions in Figs. A.57 to A.60. The generic curves used for the analysis in chapter 6 are plotted on a linear scale in Figs. A.61 to A.64. Finally the results of the transport spectroscopy experiments described in section 6.4.1.2 are presented in Figs. A.65 to A.72.

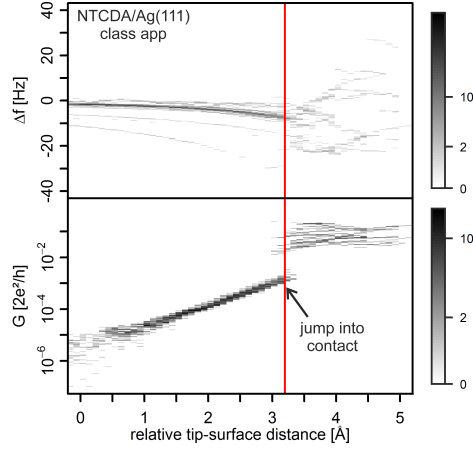


Figure A.1: Approach and jump into contact of NTCDA/Ag(111). Bin size of  $\Delta f$ :  $z = 0.1 \text{ \AA}$ ,  $y = 0.3 \text{ Hz}$ ; bin size of  $G$ :  $z = 0.1 \text{ \AA}$ ,  $\min(y) = 4.8 \times 10^{-9} 2e^2/h$ ,  $\max(y) = 1.2 \times 10^{-2} 2e^2/h$ .

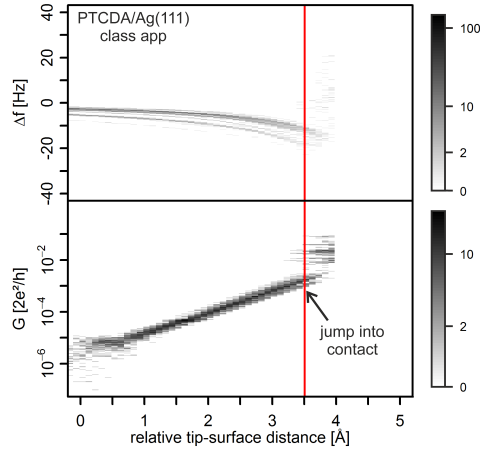


Figure A.2: Approach and jump into contact of PTCDA/Ag(111). Bin size of  $\Delta f$ :  $z = 0.1 \text{ \AA}$ ,  $y = 0.1 \text{ Hz}$ ; bin size of  $G$ :  $z = 0.1 \text{ \AA}$ ,  $\min(y) = 6.0 \times 10^{-10} 2e^2/h$ ,  $\max(y) = 5.9 \times 10^{-3} 2e^2/h$ .

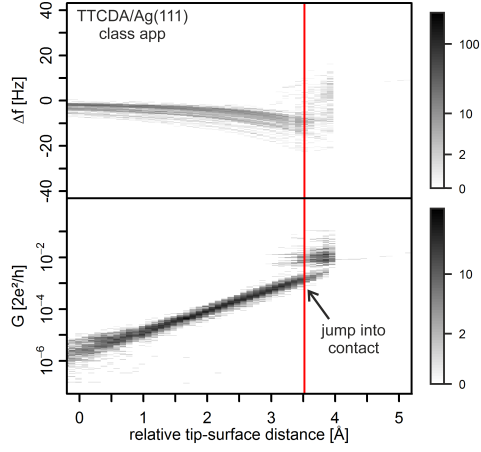


Figure A.3: Approach and jump into contact of TTCDA/Ag(111). Bin size of  $\Delta f$ :  $z = 0.1 \text{ \AA}$ ,  $y = 0.1 \text{ Hz}$ ; bin size of  $G$ :  $z = 0.1 \text{ \AA}$ ,  $\min(y) = 3.9 \times 10^{-10} 2e^2/h$ ,  $\max(y) = 4.2 \times 10^{-3} 2e^2/h$ .

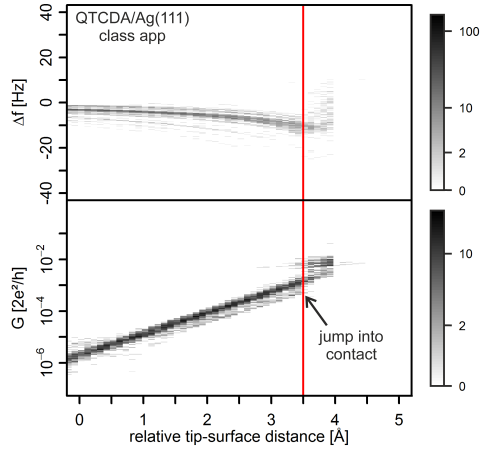


Figure A.4: Approach and jump into contact of QTCDA/Ag(111).  $0.1 \text{ \AA}$ ,  $0.2 \text{ Hz}$ ,  $0.1 \text{ \AA}$ ,  $2.0 \times 10^{-10} 2e^2/h$ ,  $1.7 \times 10^{-3} 2e^2/h$ .

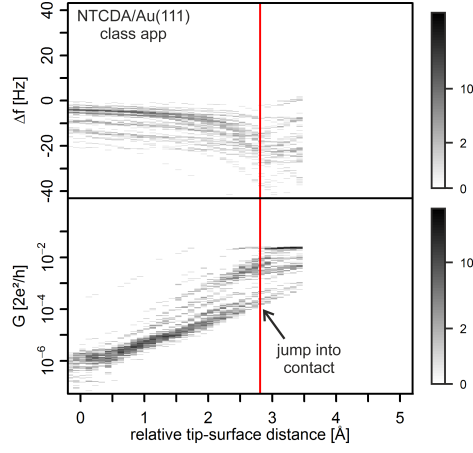


Figure A.5: Approach and jump into contact of NTCDA/Au(111).  $0.1 \text{ \AA}$ ,  $0.2 \text{ Hz}$ ,  $0.1 \text{ \AA}$ ,  $5.2 \times 10^{-10} 2e^2/h$ ,  $1.3 \times 10^{-3} 2e^2/h$ .

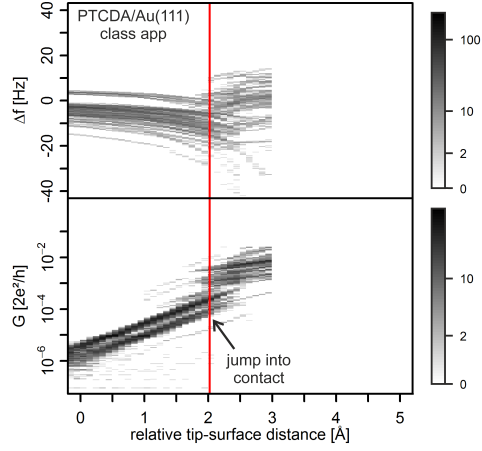


Figure A.6: Approach and jump into contact of PTCDA/Au(111).  $0.1 \text{ \AA}$ ,  $0.3 \text{ Hz}$ ,  $0.1 \text{ \AA}$ ,  $2.8 \times 10^{-10} 2e^2/h$ ,  $1.4 \times 10^{-3} 2e^2/h$ .

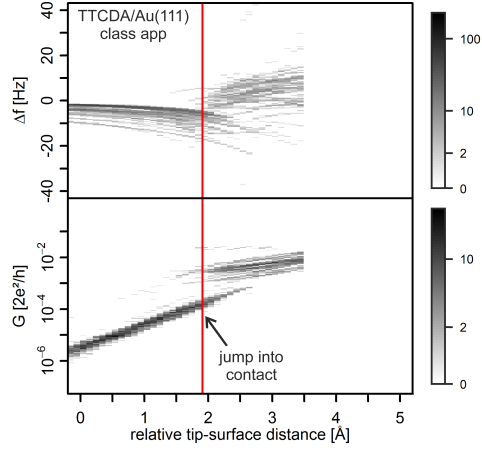


Figure A.7: Approach and jump into contact of TTCD/Au(111).  $0.1 \text{ \AA}$ ,  $0.4 \text{ Hz}$ ,  $0.1 \text{ \AA}$ ,  $3.9 \times 10^{-10} 2e^2/h$ ,  $9.7 \times 10^{-4} 2e^2/h$ .

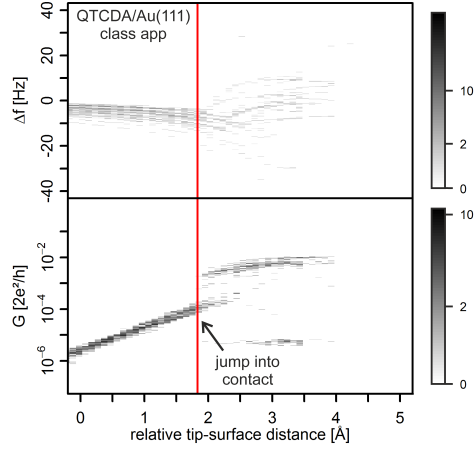


Figure A.8: Approach and jump into contact of QTCD/Au(111).  $0.1 \text{ \AA}$ ,  $0.2 \text{ Hz}$ ,  $0.1 \text{ \AA}$ ,  $1.9 \times 10^{-10} 2e^2/h$ ,  $4.0 \times 10^{-4} 2e^2/h$ .

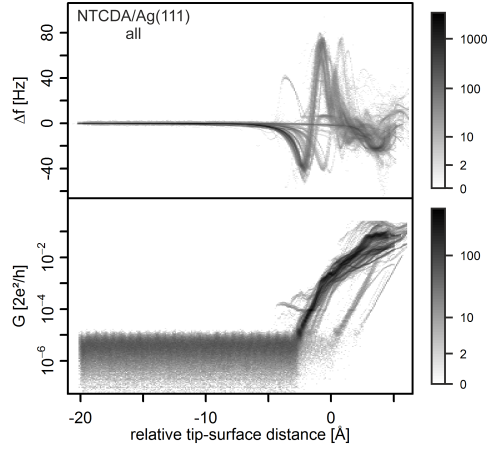


Figure A.9: All lifting and lowering curves of NTCDA/Ag(111). Bin size of  $\Delta f$ :  $z = 0.1 \text{ \AA}$ ,  $y = 0.6 \text{ Hz}$ ; bin size of  $G$ :  $z = 0.1 \text{ \AA}$ ,  $\min(y) = 3.0 \times 10^{-12} 2e^2/h$ ,  $\max(y) = 1.8 \times 10^{-2} 2e^2/h$ .

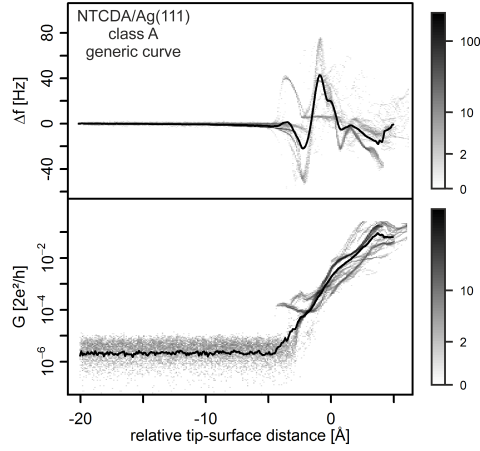


Figure A.10: NTCDA/Ag(111) lifting and lowering curves of class A. Bin size of  $\Delta f$ :  $z = 0.1 \text{ \AA}$ ,  $y = 0.5 \text{ Hz}$ ; bin size of  $G$ :  $z = 0.1 \text{ \AA}$ ,  $\min(y) = 1.9 \times 10^{-11} 2e^2/h$ ,  $\max(y) = 2.0 \times 10^{-2} 2e^2/h$ .

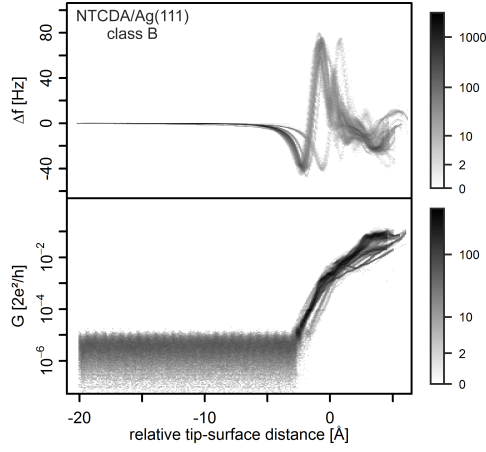


Figure A.11: NTCDA/Ag(111) lifting and lowering curves of class B. Bin size of  $\Delta f$ :  $z = 0.1 \text{ \AA}$ ,  $y = 0.5 \text{ Hz}$ ; bin size of  $G$ :  $z = 0.1 \text{ \AA}$ ,  $\min(y) = 3.6 \times 10^{-12} 2e^2/h$ ,  $\max(y) = 1.8 \times 10^{-2} 2e^2/h$ .

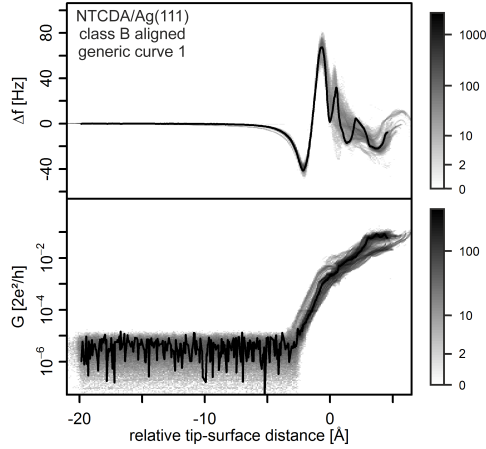


Figure A.12: NTCDA/Ag(111) lifting and lowering curves of class B aligned with the generic curve 1. Bin size of  $\Delta f$ :  $z = 0.1 \text{ \AA}$ ,  $y = 0.5 \text{ Hz}$ ; bin size of  $G$ :  $z = 0.1 \text{ \AA}$ ,  $\min(y) = 3.3 \times 10^{-12} 2e^2/h$ ,  $\max(y) = 1.7 \times 10^{-2} 2e^2/h$ .

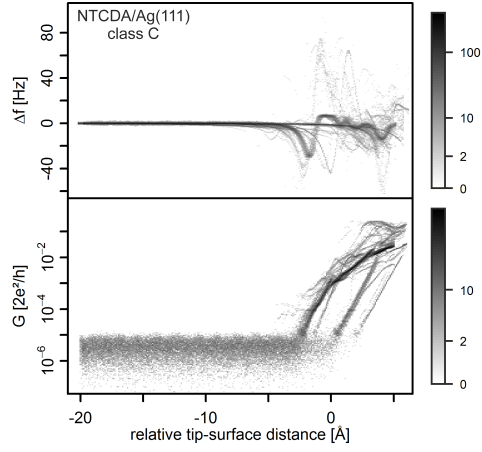


Figure A.13: NTCDA/Ag(111) lifting and lowering curves of class C. Bin size of  $\Delta f$ :  $z = 0.1 \text{ Å}$ ,  $y = 0.7 \text{ Hz}$ ; bin size of  $G$ :  $z = 0.1 \text{ Å}$ ,  $\min(y) = 2.6 \times 10^{-11} 2e^2/h$ ,  $\max(y) = 1.9 \times 10^{-2} 2e^2/h$ .

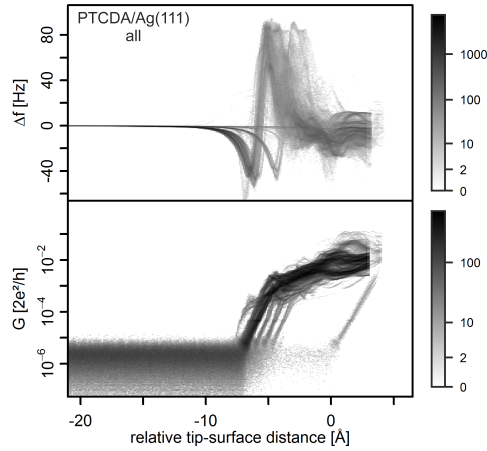


Figure A.14: All lifting and lowering curves of PTCDA/Ag(111). Bin size of  $\Delta f$ :  $z = 0.1 \text{ Å}$ ,  $y = 0.5 \text{ Hz}$ ; bin size of  $G$ :  $z = 0.1 \text{ Å}$ ,  $\min(y) = 5.4 \times 10^{-13} 2e^2/h$ ,  $\max(y) = 8.6 \times 10^{-3} 2e^2/h$ .



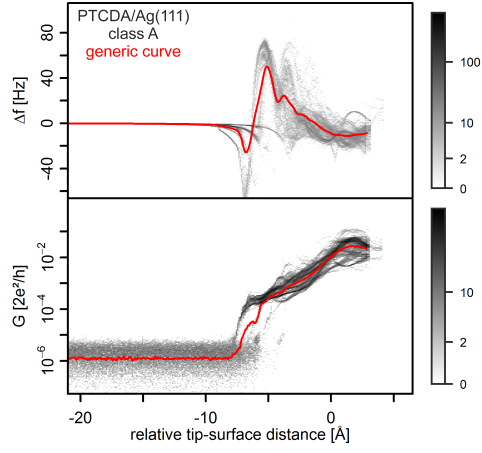


Figure A.15: PTCDA/Ag(111) lifting and lowering curves of class A. Bin size of  $\Delta f$ :  $z = 0.1 \text{ Å}$ ,  $y = 0.5 \text{ Hz}$ ; bin size of  $G$ :  $z = 0.1 \text{ Å}$ ,  $\min(y) = 5.4 \times 10^{-13} 2e^2/h$ ,  $\max(y) = 8.6 \times 10^{-3} 2e^2/h$ .

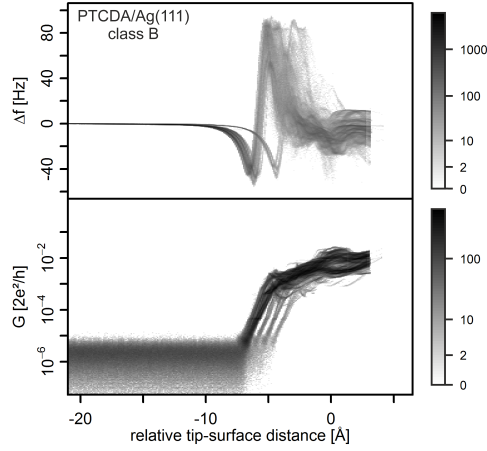


Figure A.16: PTCDA/Ag(111) lifting and lowering curves of class B. Bin size of  $\Delta f$ :  $z = 0.1 \text{ Å}$ ,  $y = 0.5 \text{ Hz}$ ; bin size of  $G$ :  $z = 0.1 \text{ Å}$ ,  $\min(y) = 7.4 \times 10^{-13} 2e^2/h$ ,  $\max(y) = 1.7 \times 10^{-3} 2e^2/h$ .

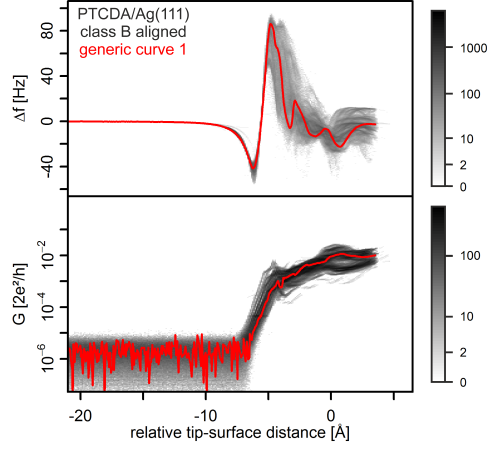


Figure A.17: PTCDA/Ag(111) lifting and lowering curves of class B aligned with the generic curve 1. Bin size of  $\Delta f$ :  $z = 0.1 \text{ \AA}$ ,  $y = 0.4 \text{ Hz}$ ; bin size of  $G$ :  $z = 0.1 \text{ \AA}$ ,  $\min(y) = 6.9 \times 10^{-13} 2e^2/h$ ,  $\max(y) = 1.6 \times 10^{-3} 2e^2/h$ .

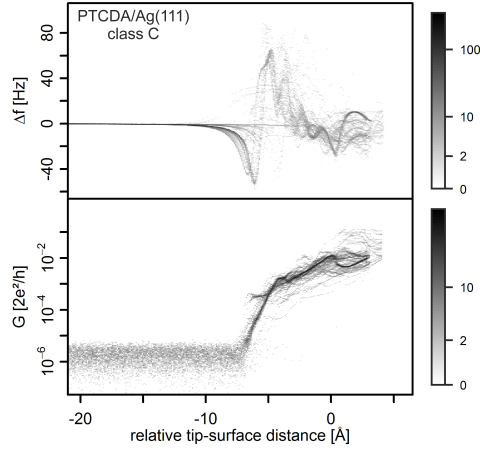


Figure A.18: PTCDA/Ag(111) lifting and lowering curves of class C. Bin size of  $\Delta f$ :  $z = 0.1 \text{ \AA}$ ,  $y = 0.5 \text{ Hz}$ ; bin size of  $G$ :  $z = 0.1 \text{ \AA}$ ,  $\min(y) = 1.6 \times 10^{-11} 2e^2/h$ ,  $\max(y) = 7.3 \times 10^{-3} 2e^2/h$ .

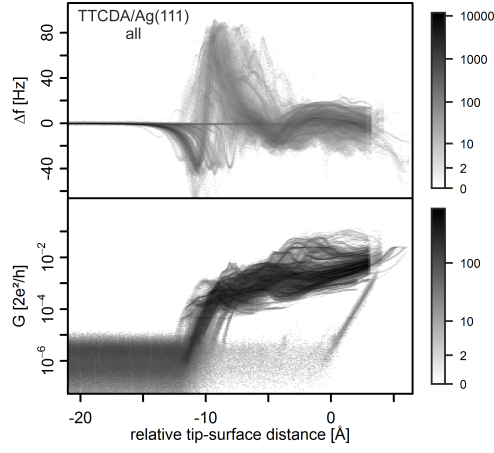


Figure A.19: All lifting and lowering curves of TTCDA/Ag(111). Bin size of  $\Delta f$ :  $z = 0.1 \text{ \AA}$ ,  $y = 0.4 \text{ Hz}$ ; bin size of  $G$ :  $z = 0.1 \text{ \AA}$ ,  $\min(y) = 3.1 \times 10^{-13} 2e^2/h$ ,  $\max(y) = 7.2 \times 10^{-3} 2e^2/h$ .

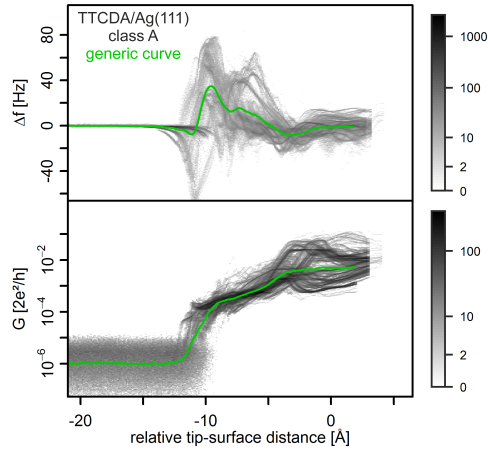


Figure A.20: TTCDA/Ag(111) lifting and lowering curves of class A. Bin size of  $\Delta f$ :  $z = 0.1 \text{ \AA}$ ,  $y = 0.4 \text{ Hz}$ ; bin size of  $G$ :  $z = 0.1 \text{ \AA}$ ,  $\min(y) = 3.3 \times 10^{-13} 2e^2/h$ ,  $\max(y) = 7.6 \times 10^{-3} 2e^2/h$ .

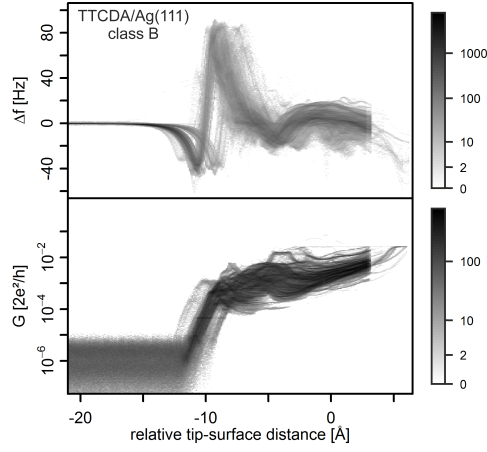


Figure A.21: TTCDA/Ag(111) lifting and lowering curves of class B. Bin size of  $\Delta f$ :  $z = 0.1 \text{ \AA}$ ,  $y = 0.4 \text{ Hz}$ ; bin size of  $G$ :  $z = 0.1 \text{ \AA}$ ,  $\min(y) = 4.4 \times 10^{-13} 2e^2/h$ ,  $\max(y) = 4.0 \times 10^{-3} 2e^2/h$ .

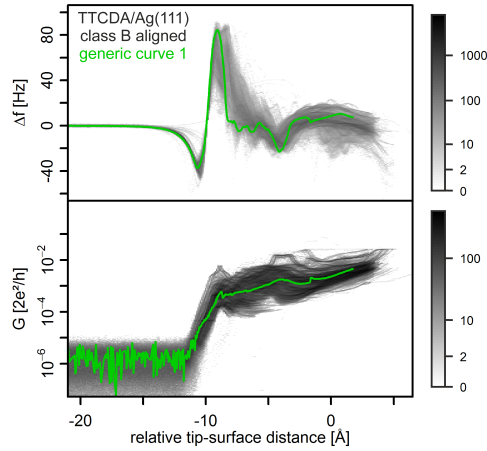


Figure A.22: TTCDA/Ag(111) lifting and lowering curves of class B aligned with the generic curve 1. Bin size of  $\Delta f$ :  $z = 0.1 \text{ \AA}$ ,  $y = 0.4 \text{ Hz}$ ; bin size of  $G$ :  $z = 0.1 \text{ \AA}$ ,  $\min(y) = 3.9 \times 10^{-13} 2e^2/h$ ,  $\max(y) = 3.6 \times 10^{-3} 2e^2/h$ .

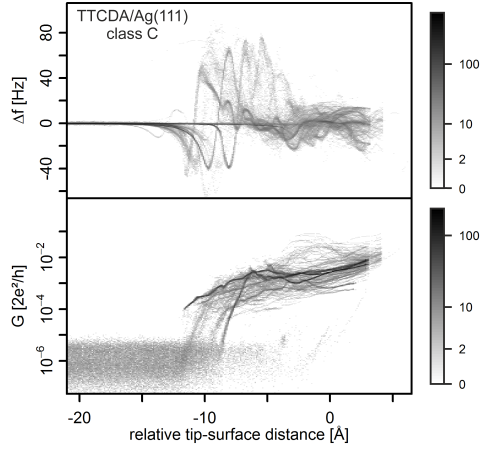


Figure A.23: TTCDA/Ag(111) lifting and lowering curves of class C. Bin size of  $\Delta f$ :  $z = 0.1 \text{ Å}$ ,  $y = 0.4 \text{ Hz}$ ; bin size of  $G$ :  $z = 0.1 \text{ Å}$ ,  $\min(y) = 1.7 \times 10^{-12} 2e^2/h$ ,  $\max(y) = 4.3 \times 10^{-3} 2e^2/h$ .

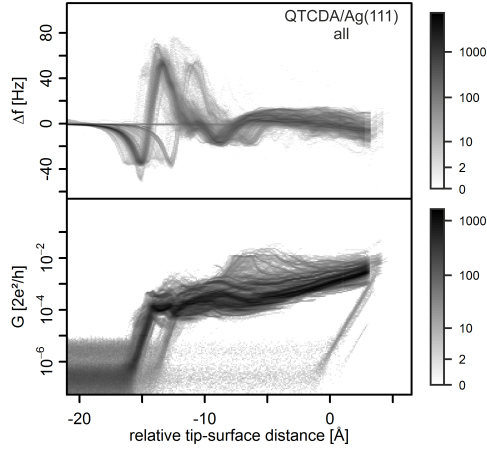


Figure A.24: All lifting and lowering curves of QTCD/Ag(111). Bin size of  $\Delta f$ :  $z = 0.1 \text{ Å}$ ,  $y = 0.4 \text{ Hz}$ ; bin size of  $G$ :  $z = 0.1 \text{ Å}$ ,  $\min(y) = 2.8 \times 10^{-21} 2e^2/h$ ,  $\max(y) = 1.6 \times 10^{-3} 2e^2/h$ .

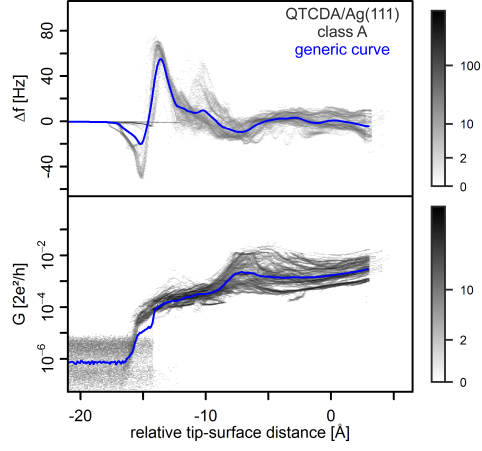


Figure A.25: QTCDA/Ag(111) lifting and lowering curves of class A. Bin size of  $\Delta f$ :  $z = 0.1 \text{ \AA}$ ,  $y = 0.4 \text{ Hz}$ ; bin size of  $G$ :  $z = 0.1 \text{ \AA}$ ,  $\min(y) = 1.6 \times 10^{-12} 2e^2/h$ ,  $\max(y) = 1.6 \times 10^{-3} 2e^2/h$ .

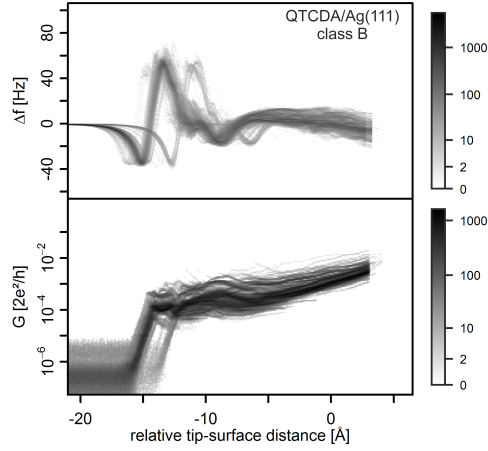


Figure A.26: QTCDA/Ag(111) lifting and lowering curves of class B. Bin size of  $\Delta f$ :  $z = 0.1 \text{ \AA}$ ,  $y = 0.3 \text{ Hz}$ ; bin size of  $G$ :  $z = 0.1 \text{ \AA}$ ,  $\min(y) = 2.8 \times 10^{-21} 2e^2/h$ ,  $\max(y) = 1.9 \times 10^{-3} 2e^2/h$ .

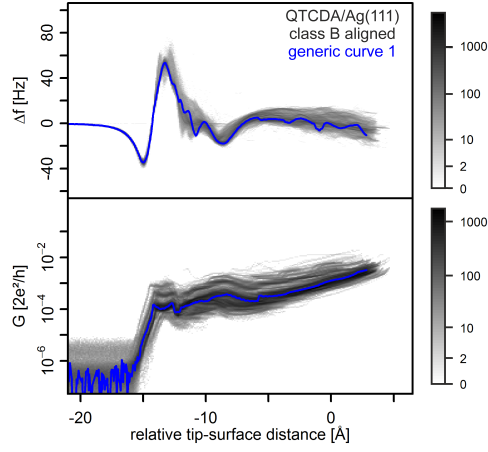


Figure A.27: QTCDA/Ag(111) lifting and lowering curves of class B aligned with the generic curve 1. Bin size of  $\Delta f$ :  $z = 0.1 \text{ \AA}$ ,  $y = 0.3 \text{ Hz}$ ; bin size of  $G$ :  $z = 0.1 \text{ \AA}$ ,  $\min(y) = 2.6 \times 10^{-21} 2e^2/h$ ,  $\max(y) = 1.8 \times 10^{-3} 2e^2/h$ .

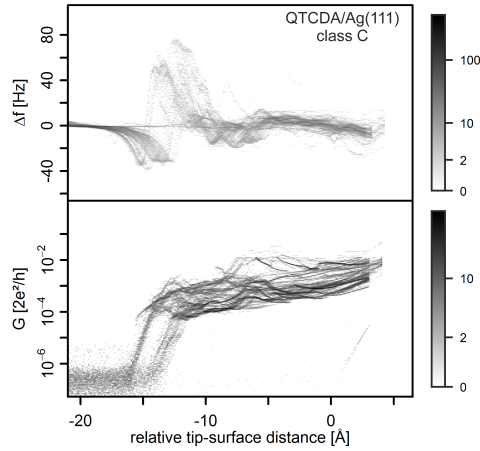


Figure A.28: QTCDA/Ag(111) lifting and lowering curves of class C. Bin size of  $\Delta f$ :  $z = 0.1 \text{ \AA}$ ,  $y = 0.4 \text{ Hz}$ ; bin size of  $G$ :  $z = 0.1 \text{ \AA}$ ,  $\min(y) = 1.3 \times 10^{-12} 2e^2/h$ ,  $\max(y) = 2.8 \times 10^{-3} 2e^2/h$ .

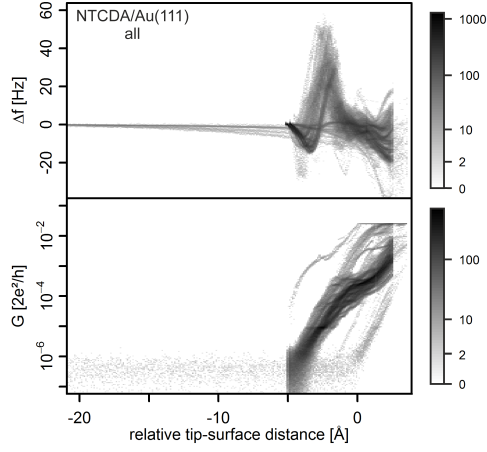


Figure A.29: All lifting and lowering curves of NTCDA/Au(111). Bin size of  $\Delta f$ :  $z = 0.1 \text{ \AA}$ ,  $y = 0.4 \text{ Hz}$ ; bin size of  $G$ :  $z = 0.1 \text{ \AA}$ ,  $\min(y) = 3.5 \times 10^{-12} 2e^2/h$ ,  $\max(y) = 1.7 \times 10^{-3} 2e^2/h$ .

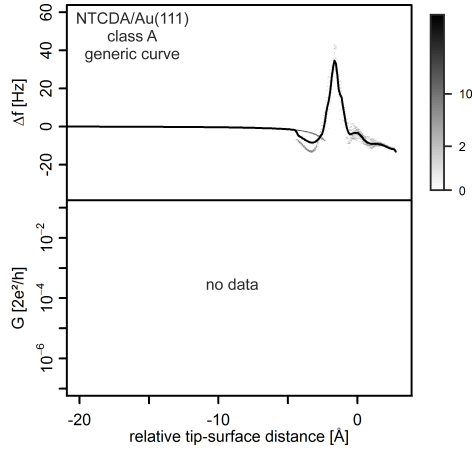


Figure A.30: NTCDA/Au(111) lifting and lowering curves of class A. Bin size of  $\Delta f$ :  $z = 0.1 \text{ \AA}$ ,  $y = 0.2 \text{ Hz}$



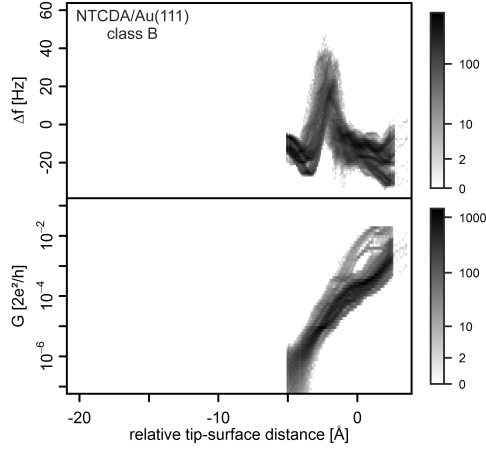


Figure A.31: NTCDA/Au(111) lifting and lowering curves of class B. Bin size of  $\Delta f$ :  $z = 0.1 \text{ \AA}$ ,  $y = 1.0 \text{ Hz}$ ; bin size of  $G$ :  $z = 0.1 \text{ \AA}$ ,  $\min(y) = 2.3 \times 10^{-11} 2e^2/h$ ,  $\max(y) = 5.2 \times 10^{-3} 2e^2/h$ .

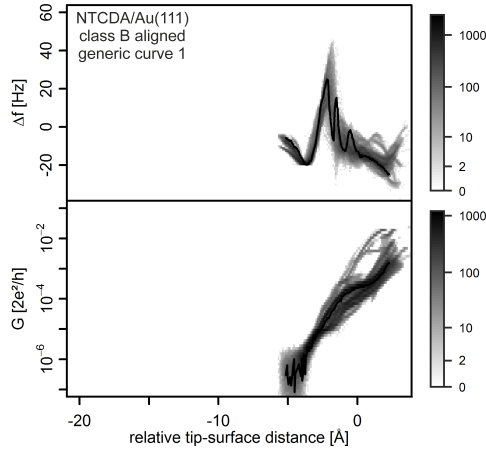


Figure A.32: NTCDA/Au(111) lifting and lowering curves of class B aligned with the generic curve 1. Bin size of  $\Delta f$ :  $z = 0.1 \text{ \AA}$ ,  $y = 0.9 \text{ Hz}$ ; bin size of  $G$ :  $z = 0.1 \text{ \AA}$ ,  $\min(y) = 2.0 \times 10^{-11} 2e^2/h$ ,  $\max(y) = 4.7 \times 10^{-3} 2e^2/h$ .

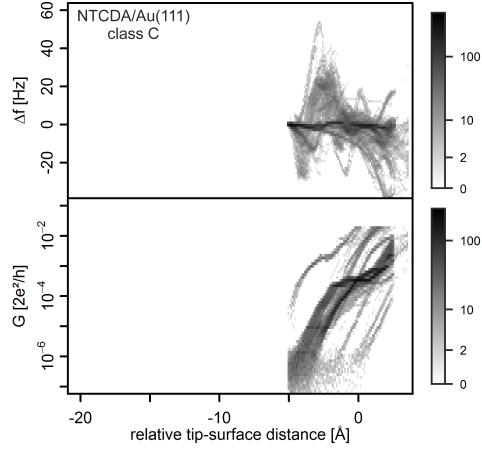


Figure A.33: NTCDA/Au(111) lifting and lowering curves of class C. Bin size of  $\Delta f$ :  $z = 0.1 \text{ \AA}$ ,  $y = 1.2 \text{ Hz}$ ; bin size of  $G$ :  $z = 0.1 \text{ \AA}$ ,  $\min(y) = 6 \times 10^{-11} 2e^2/h$ ,  $\max(y) = 4.9 \times 10^{-3} 2e^2/h$ .

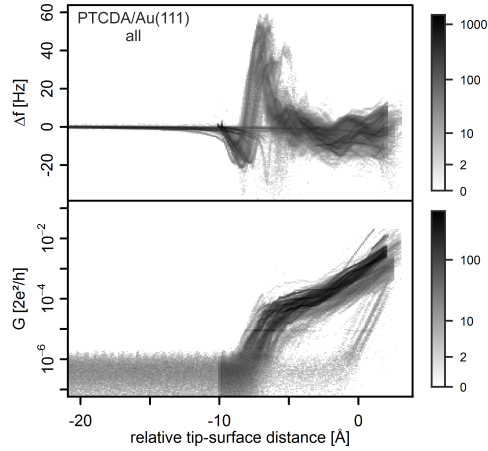


Figure A.34: All lifting and lowering curves of PTCDA/Au(111). Bin size of  $\Delta f$ :  $z = 0.1 \text{ \AA}$ ,  $y = 0.6 \text{ Hz}$ ; bin size of  $G$ :  $z = 0.1 \text{ \AA}$ ,  $\min(y) = 3.3 \times 10^{-13} 2e^2/h$ ,  $\max(y) = 2 \times 10^{-3} 2e^2/h$ .

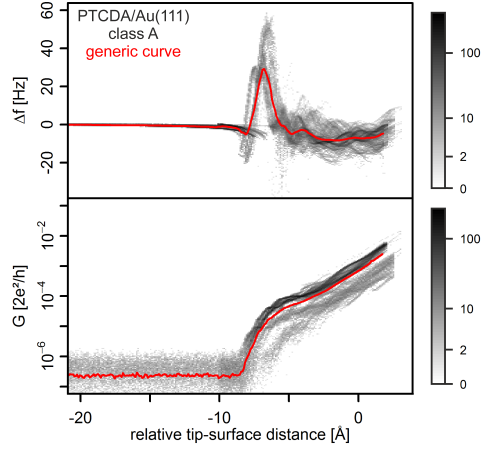


Figure A.35: PTCDA/Au(111) lifting and lowering curves of class A. Bin size of  $\Delta f$ :  $z = 0.1 \text{ Å}$ ,  $y = 0.5 \text{ Hz}$ ; bin size of  $G$ :  $z = 0.1 \text{ Å}$ ,  $\min(y) = 3.4 \times 10^{-12} 2e^2/h$ ,  $\max(y) = 9.6 \times 10^{-4} 2e^2/h$ .

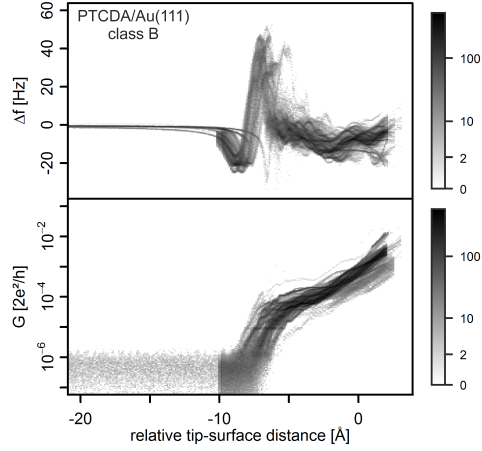


Figure A.36: PTCDA/Au(111) lifting and lowering curves of class B. Bin size of  $\Delta f$ :  $z = 0.1 \text{ Å}$ ,  $y = 0.4 \text{ Hz}$ ; bin size of  $G$ :  $z = 0.1 \text{ Å}$ ,  $\min(y) = 3.3 \times 10^{-13} 2e^2/h$ ,  $\max(y) = 2.0 \times 10^{-3} 2e^2/h$ .

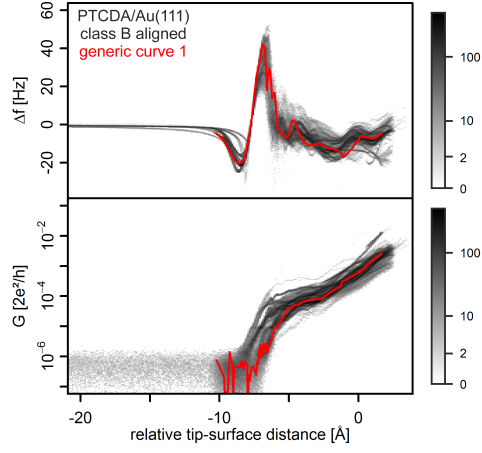


Figure A.37: PTCDA/Au(111) lifting and lowering curves of class B aligned with the generic curve 1. Bin size of  $\Delta f$ :  $z = 0.1 \text{ \AA}$ ,  $y = 0.3 \text{ Hz}$ ; bin size of  $G$ :  $z = 0.1 \text{ \AA}$ ,  $\min(y) = 3.1 \times 10^{-13} 2e^2/h$ ,  $\max(y) = 1.9 \times 10^{-3} 2e^2/h$ .

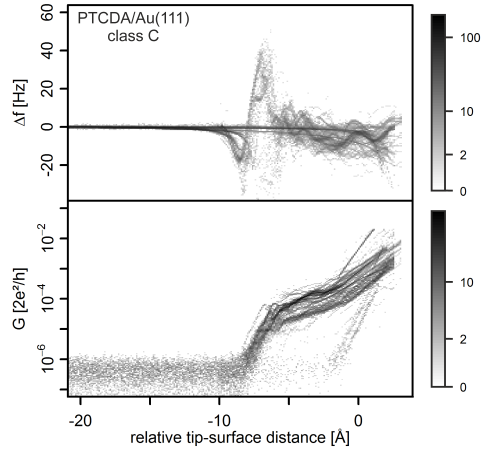


Figure A.38: PTCDA/Au(111) lifting and lowering curves of class C. Bin size of  $\Delta f$ :  $z = 0.1 \text{ \AA}$ ,  $y = 0.6 \text{ Hz}$ ; bin size of  $G$ :  $z = 0.1 \text{ \AA}$ ,  $\min(y) = 1.2 \times 10^{-12} 2e^2/h$ ,  $\max(y) = 1.9 \times 10^{-3} 2e^2/h$ .

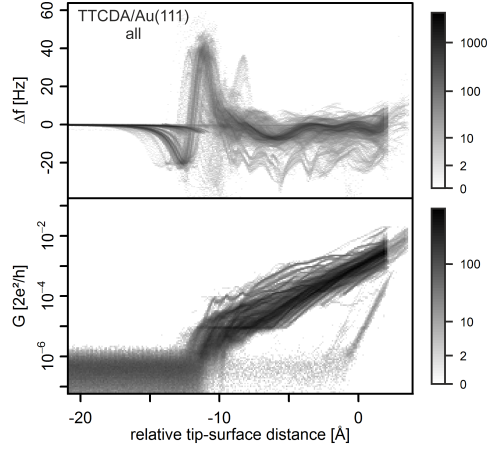


Figure A.39: All lifting and lowering curves of TTCDA/Au(111). Bin size of  $\Delta f$ :  $z = 0.1 \text{ \AA}$ ,  $y = 0.4 \text{ Hz}$ ; bin size of  $G$ :  $z = 0.1 \text{ \AA}$ ,  $\min(y) = 1.6 \times 10^{-21} 2e^2/h$ ,  $\max(y) = 2.7 \times 10^{-3} 2e^2/h$ .

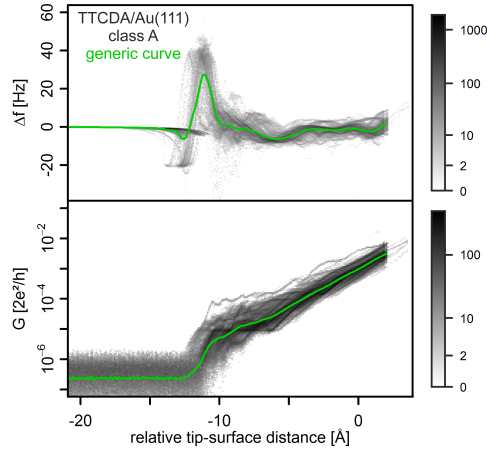


Figure A.40: TTCDA/Au(111) lifting and lowering curves of class A. Bin size of  $\Delta f$ :  $z = 0.1 \text{ \AA}$ ,  $y = 0.3 \text{ Hz}$ ; bin size of  $G$ :  $z = 0.1 \text{ \AA}$ ,  $\min(y) = 5.6 \times 10^{-21} 2e^2/h$ ,  $\max(y) = 2.6 \times 10^{-3} 2e^2/h$ .

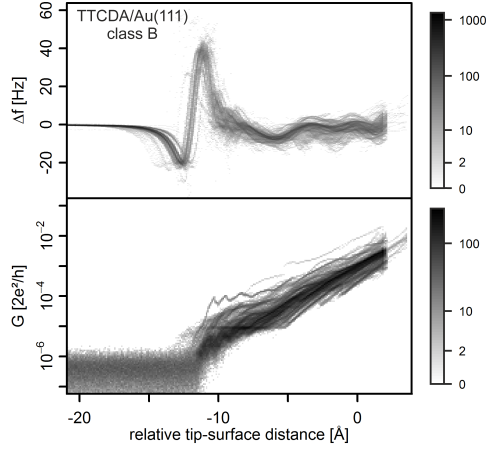


Figure A.41: TTCDA/Au(111) lifting and lowering curves of class B. Bin size of  $\Delta f$ :  $z = 0.1 \text{ \AA}$ ,  $y = 0.3 \text{ Hz}$ ; bin size of  $G$ :  $z = 0.1 \text{ \AA}$ ,  $\min(y) = 2.9 \times 10^{-21} 2e^2/h$ ,  $\max(y) = 2.6 \times 10^{-3} 2e^2/h$ .

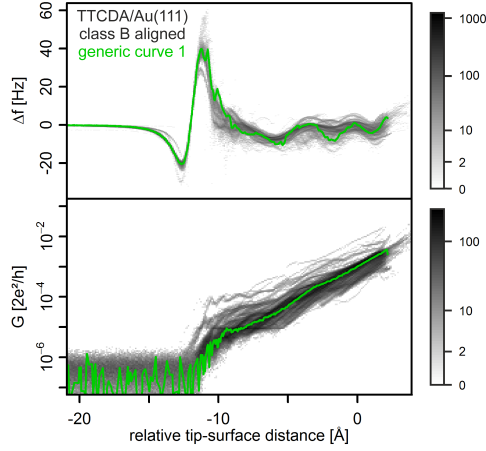


Figure A.42: TTCDA/Au(111) lifting and lowering curves of class B aligned with the generic curve 1. Bin size of  $\Delta f$ :  $z = 0.1 \text{ \AA}$ ,  $y = 0.3 \text{ Hz}$ ; bin size of  $G$ :  $z = 0.1 \text{ \AA}$ ,  $\min(y) = 2.7 \times 10^{-21} 2e^2/h$ ,  $\max(y) = 2.5 \times 10^{-3} 2e^2/h$ .

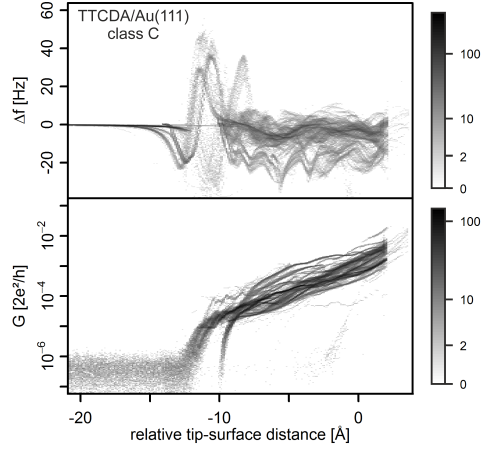


Figure A.43: TTCDA/Au(111) lifting and lowering curves of class C. Bin size of  $\Delta f$ :  $z = 0.1 \text{ \AA}$ ,  $y = 0.3 \text{ Hz}$ ; bin size of  $G$ :  $z = 0.1 \text{ \AA}$ ,  $\min(y) = 1.3 \times 10^{-12} 2e^2/h$ ,  $\max(y) = 1.4 \times 10^{-3} 2e^2/h$ .

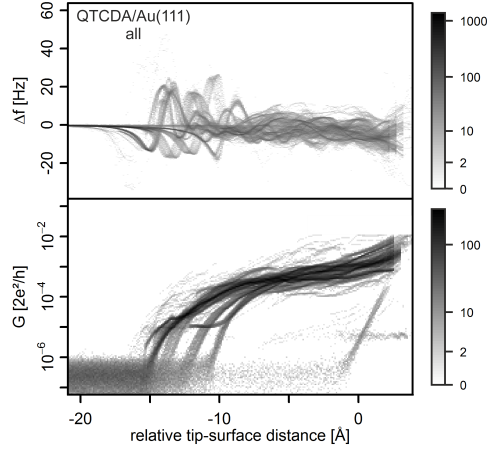


Figure A.44: All lifting and lowering curves of QTCD/Au(111). Bin size of  $\Delta f$ :  $z = 0.1 \text{ \AA}$ ,  $y = 0.3 \text{ Hz}$ ; bin size of  $G$ :  $z = 0.1 \text{ \AA}$ ,  $\min(y) = 2.1 \times 10^{-21} 2e^2/h$ ,  $\max(y) = 1.3 \times 10^{-3} 2e^2/h$ .

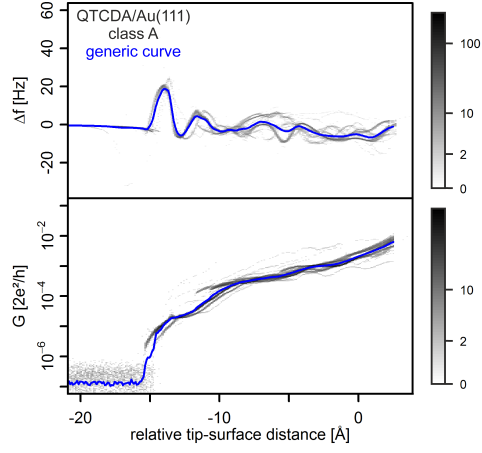


Figure A.45: QTCDA/Au(111) lifting and lowering curves of class A. Bin size of  $\Delta f$ :  $z = 0.1 \text{ \AA}$ ,  $y = 0.2 \text{ Hz}$ ; bin size of  $G$ :  $z = 0.1 \text{ \AA}$ ,  $\min(y) = 8.3 \times 10^{-13} 2e^2/h$ ,  $\max(y) = 6.3 \times 10^{-4} 2e^2/h$ .

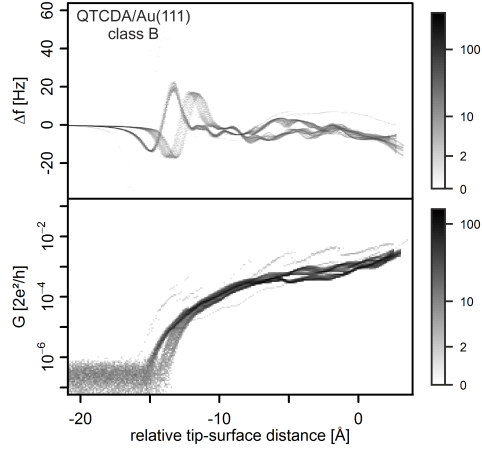


Figure A.46: QTCDA/Au(111) lifting and lowering curves of class B. Bin size of  $\Delta f$ :  $z = 0.1 \text{ \AA}$ ,  $y = 0.2 \text{ Hz}$ ; bin size of  $G$ :  $z = 0.1 \text{ \AA}$ ,  $\min(y) = 2.1 \times 10^{-21} 2e^2/h$ ,  $\max(y) = 8.0 \times 10^{-4} 2e^2/h$ .



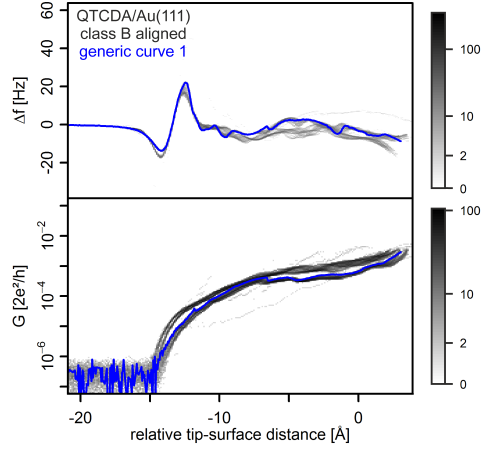


Figure A.47: QTCDA/Au(111) lifting and lowering curves of class B aligned with the generic curve 1. Bin size of  $\Delta f$ :  $z = 0.1 \text{ \AA}$ ,  $y = 0.2 \text{ Hz}$ ; bin size of  $G$ :  $z = 0.1 \text{ \AA}$ ,  $\min(y) = 1.9 \times 10^{-21} 2e^2/h$ ,  $\max(y) = 7.3 \times 10^{-4} 2e^2/h$ .

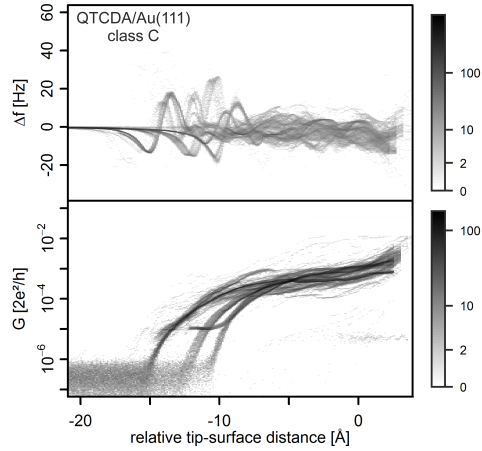


Figure A.48: QTCDA/Au(111) lifting and lowering curves of class C. Bin size of  $\Delta f$ :  $z = 0.1 \text{ \AA}$ ,  $y = 0.3 \text{ Hz}$ ; bin size of  $G$ :  $z = 0.1 \text{ \AA}$ ,  $\min(y) = 4.2 \times 10^{-13} 2e^2/h$ ,  $\max(y) = 6.7 \times 10^{-4} 2e^2/h$ .

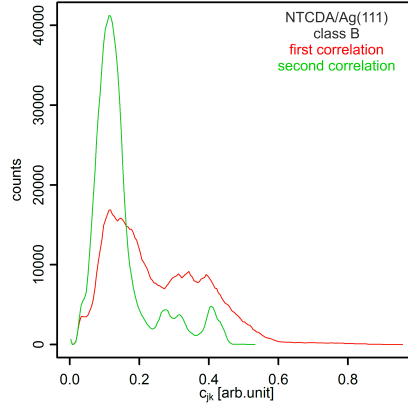


Figure A.49: Histogram of first and second correlation of NTCDA/Ag(111)

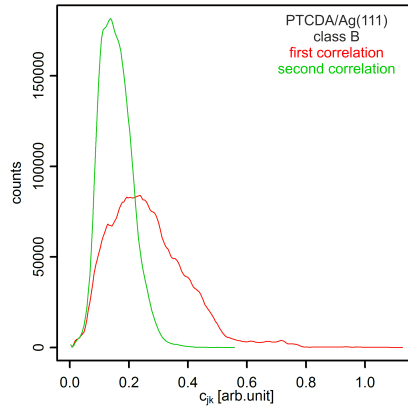


Figure A.50: Histogram of first and second correlation of PTCDA/Ag(111)

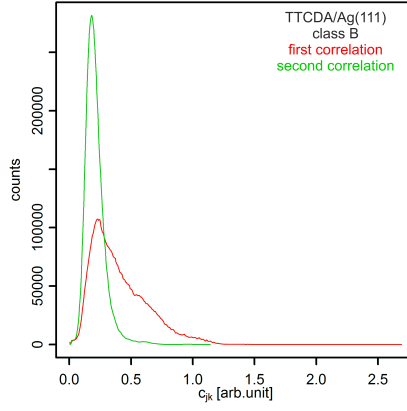


Figure A.51: Histogram of first and second correlation of TTCDA/Ag(111)

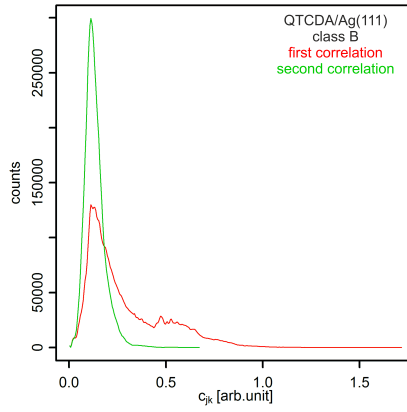


Figure A.52: Histogram of first and second correlation of QTCDA/Ag(111)

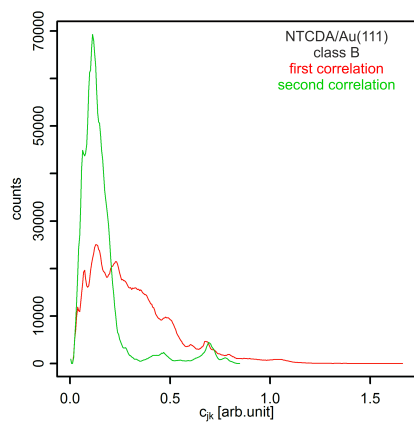


Figure A.53: Histogram of first and second correlation of NTCDA/Au(111)

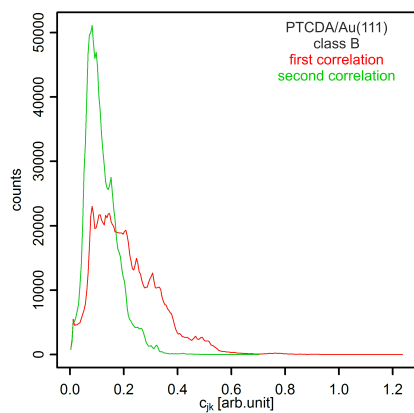


Figure A.54: Histogram of first and second correlation of PTCDA/Au(111)

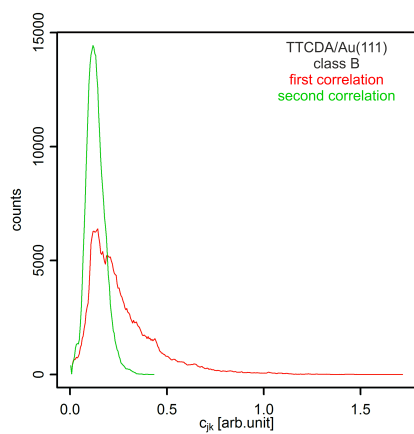


Figure A.55: Histogram of first and second correlation of TTCDA/Au(111)

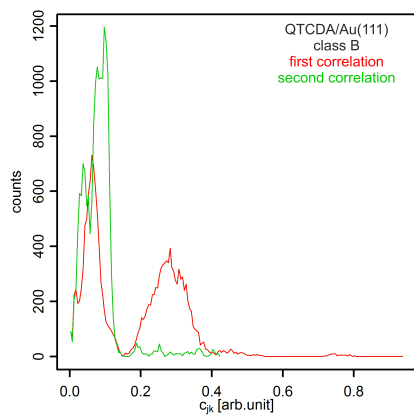


Figure A.56: Histogram of first and second correlation of QTCDA/Au(111)

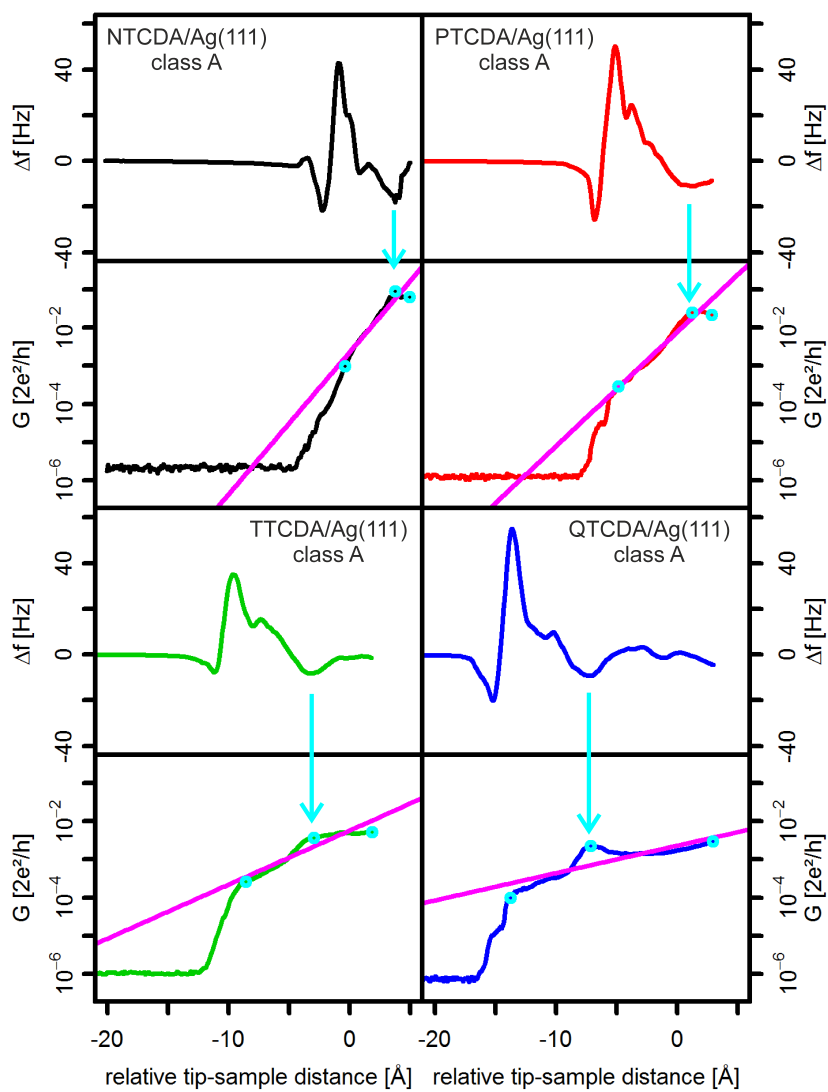


Figure A.57: Generic behavior with points, linear regressions and arrow of class A on Ag(111)

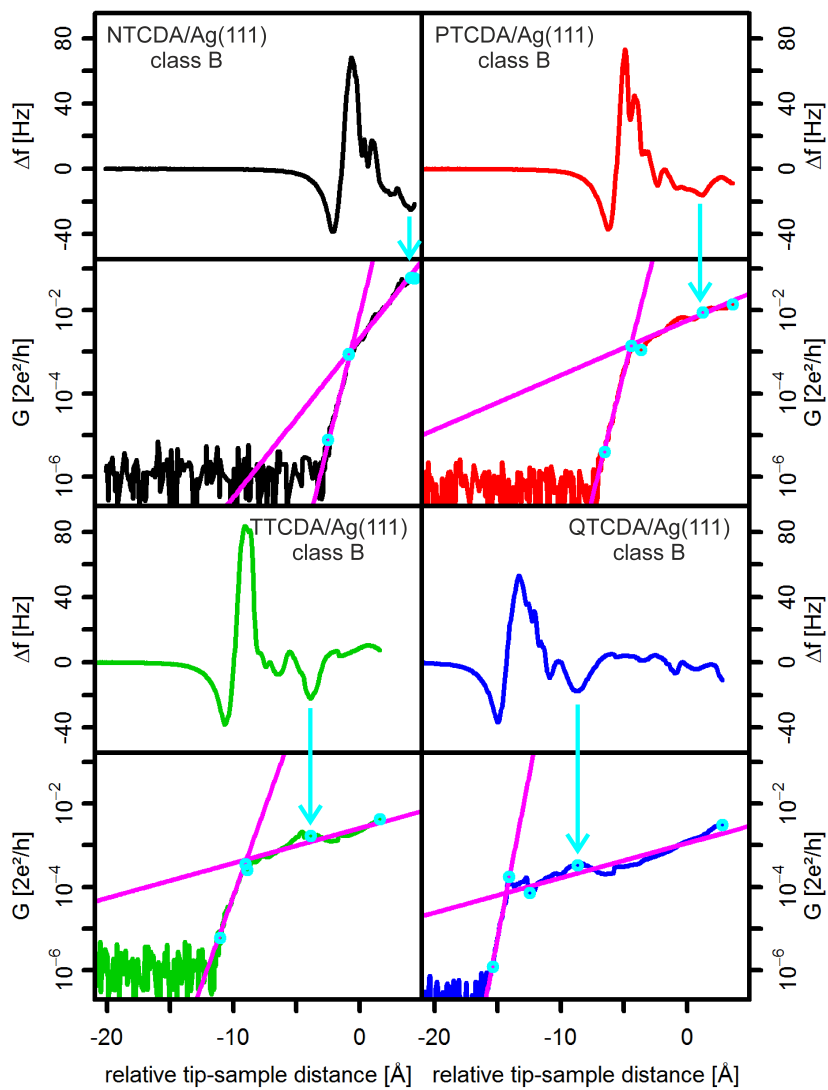


Figure A.58: Generic behavior with points, linear regression and arrow of class B on Ag(111)

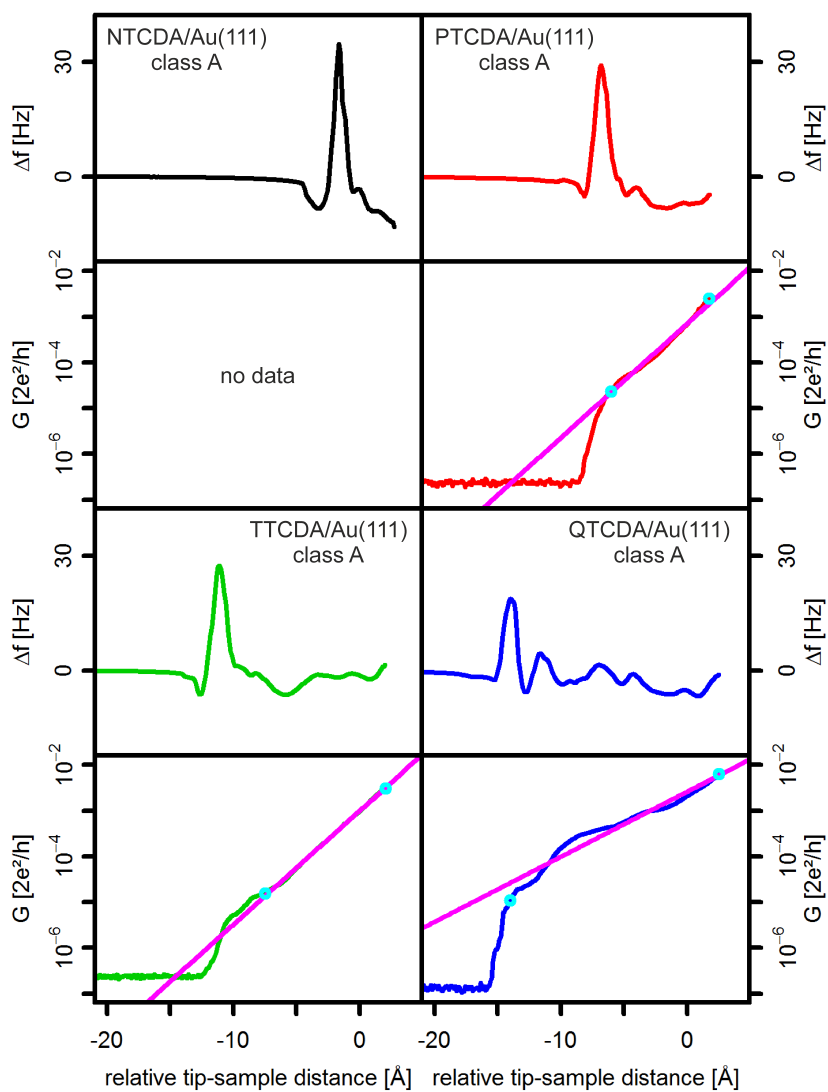


Figure A.59: Generic behavior with points and linear regression of class A on Au(111)



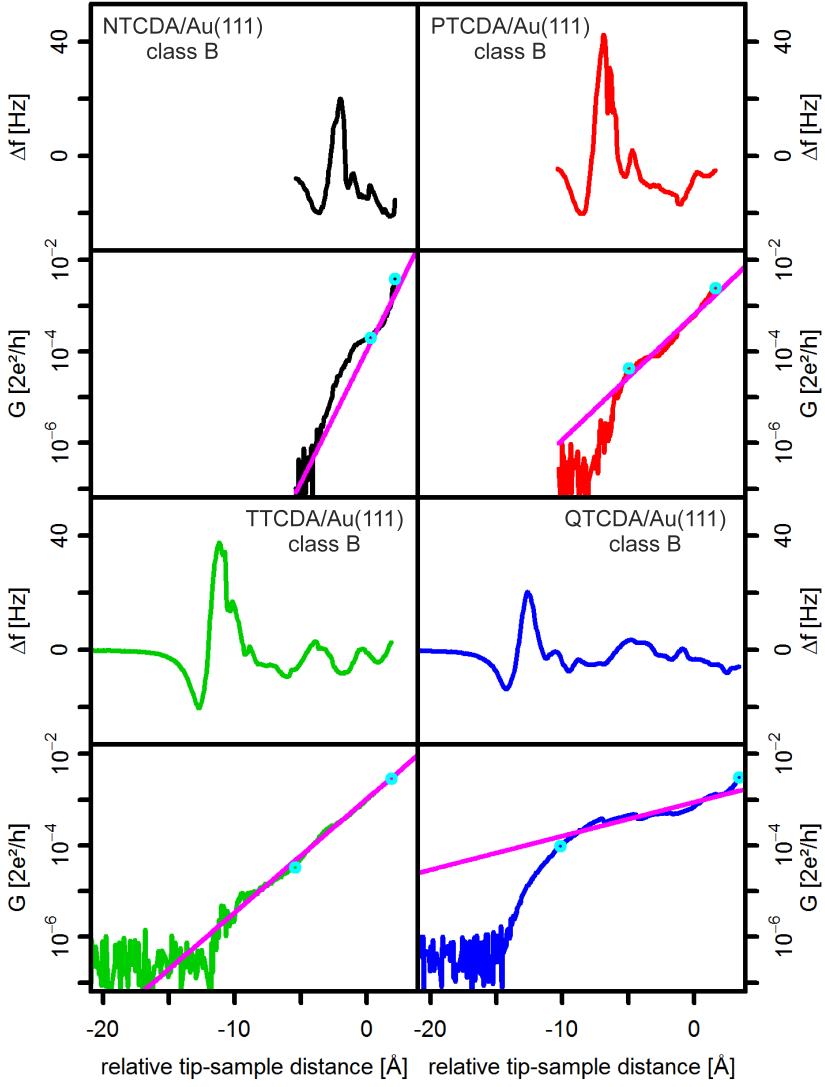


Figure A.60: Generic behavior with points and linear regression of class B on Au(111)

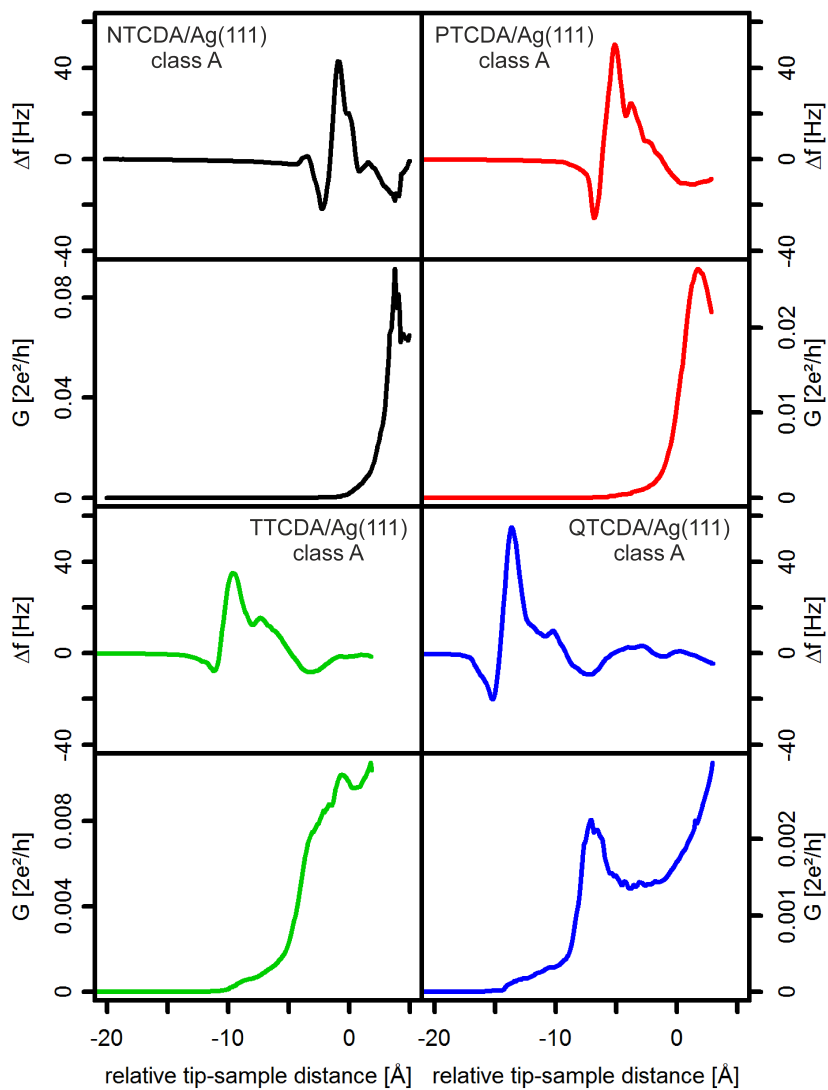


Figure A.61: Generic behavior with conductance on a linear scale of class A on Ag(111)

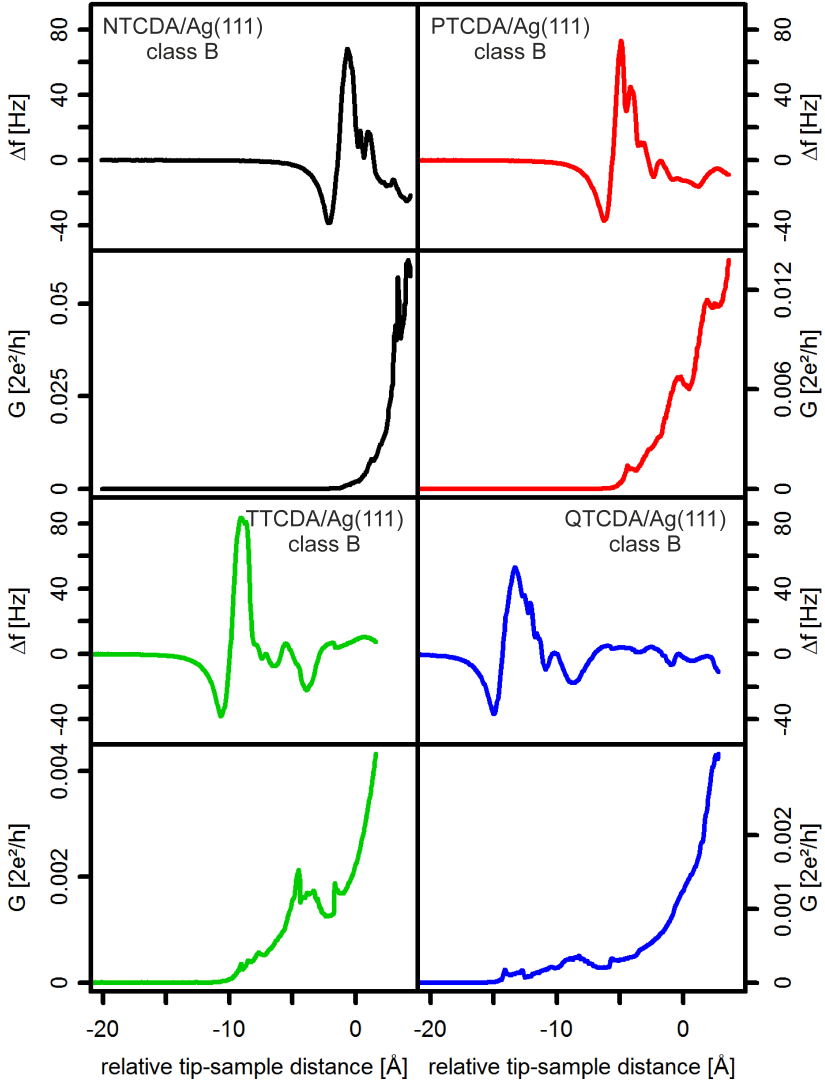


Figure A.62: Generic behavior with conductance on a linear scale of class B on Ag(111)

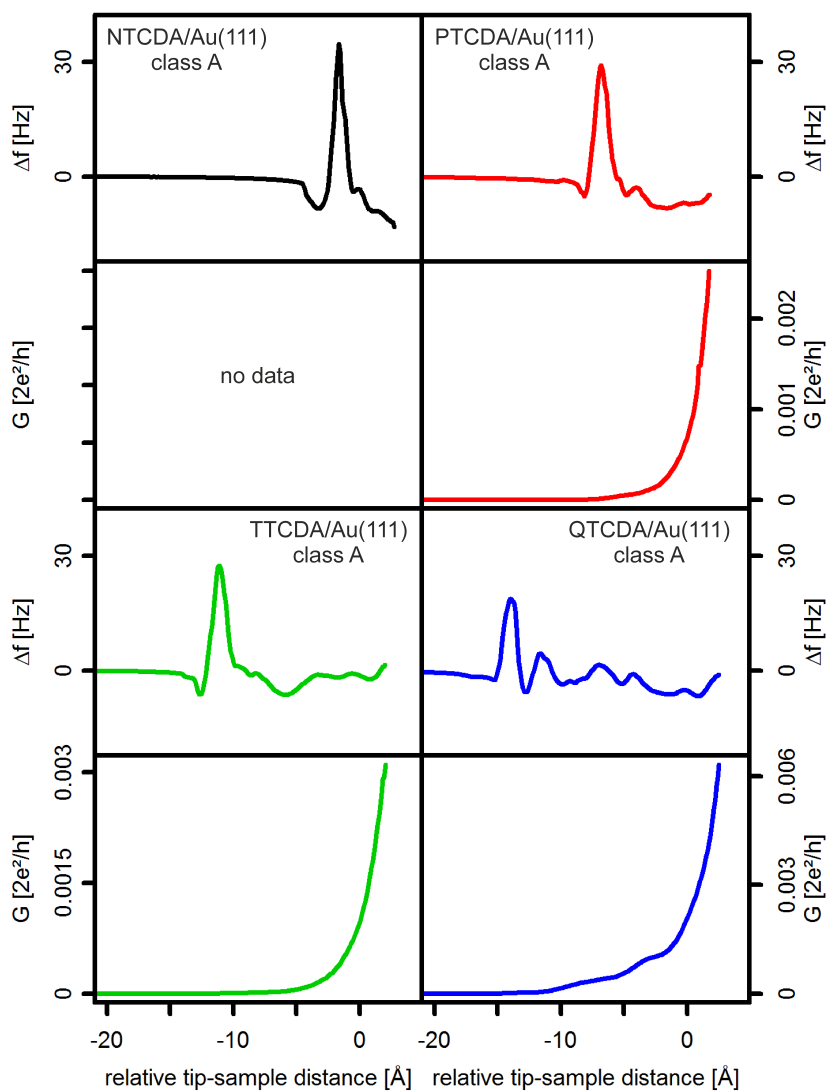


Figure A.63: Generic behavior with conductance on a linear scale of class A on Au(111)

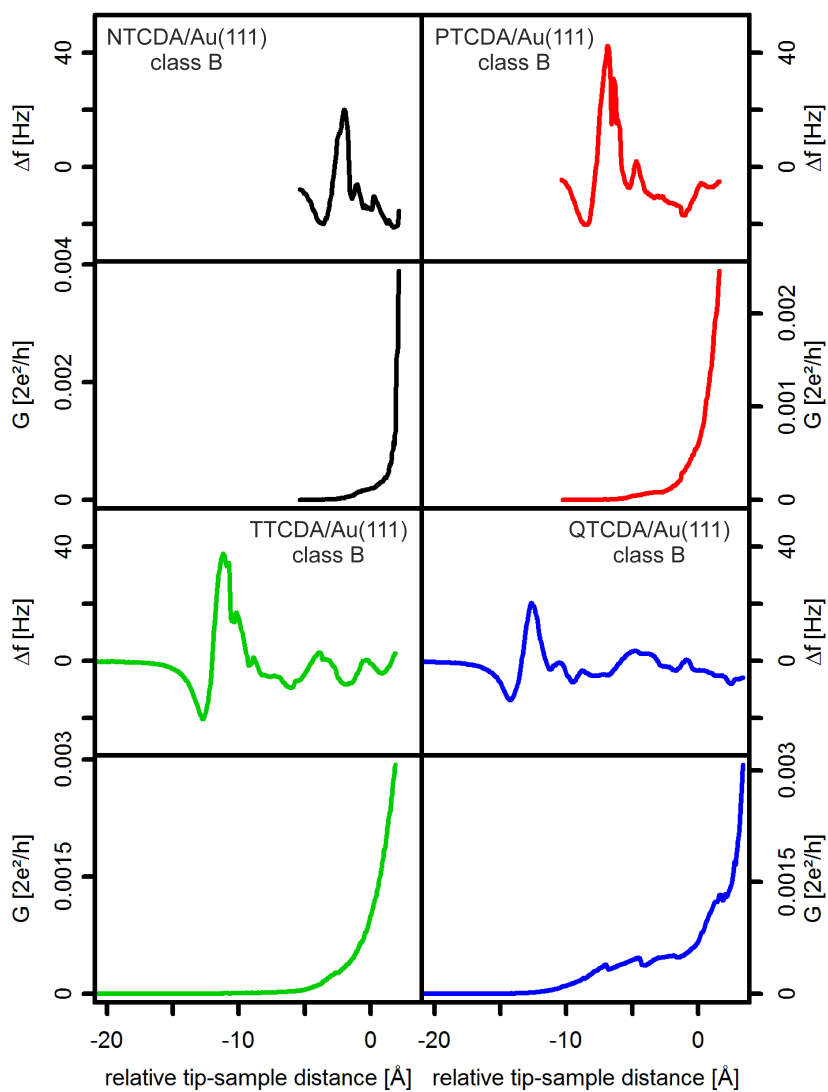


Figure A.64: Generic behavior with conductance on a linear scale of class B on Au(111)

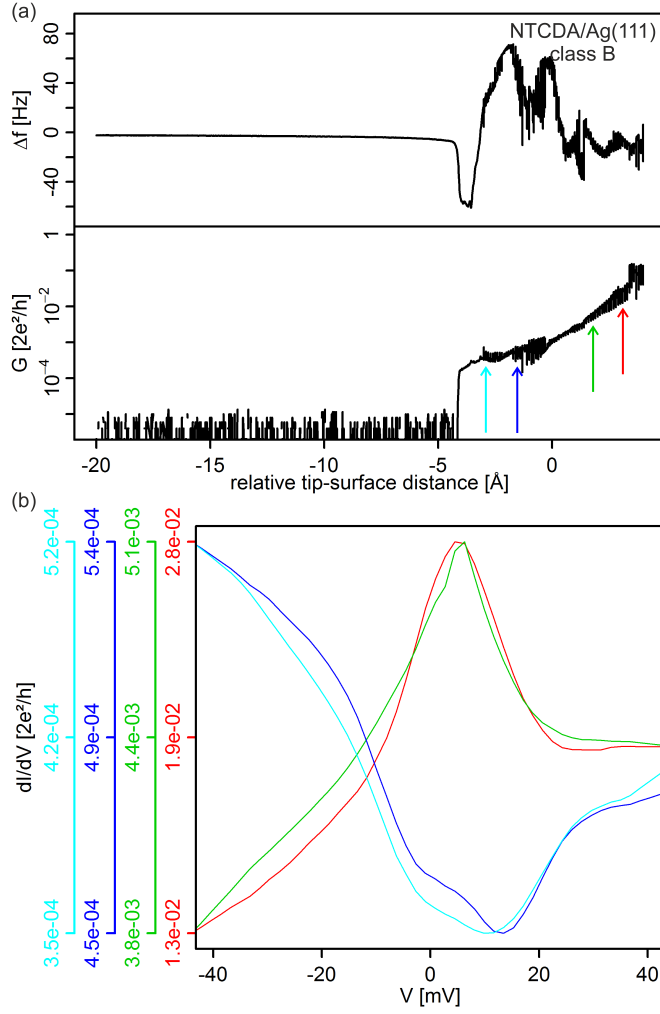


Figure A.65: Transport spectroscopy on NTCDA/Ag(111) junction of class B

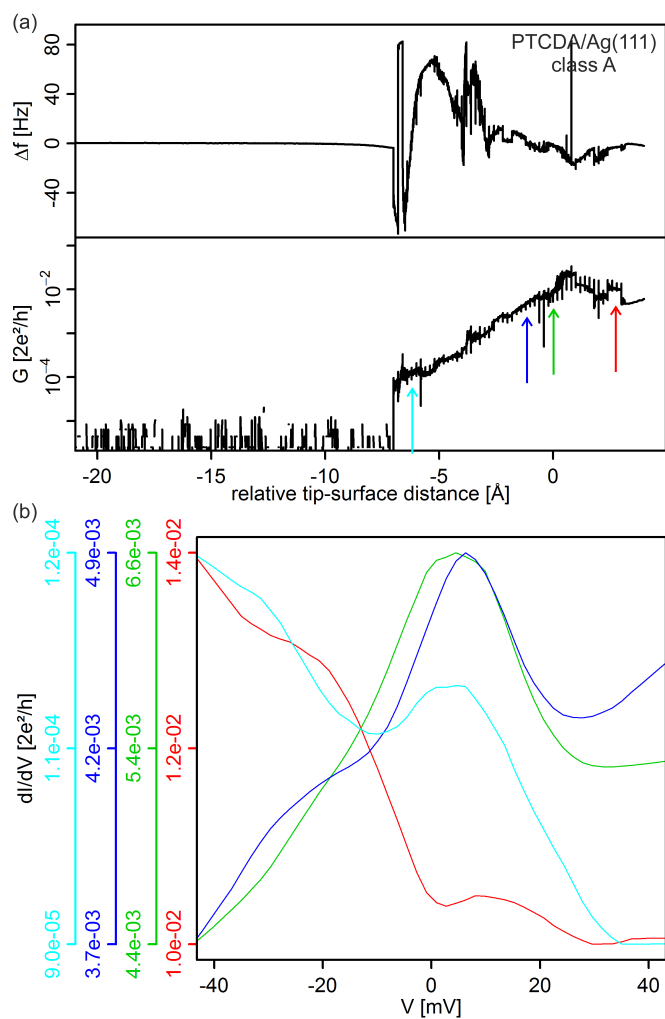


Figure A.66: Transport spectroscopy on PTCDA/Ag(111) junction of class A

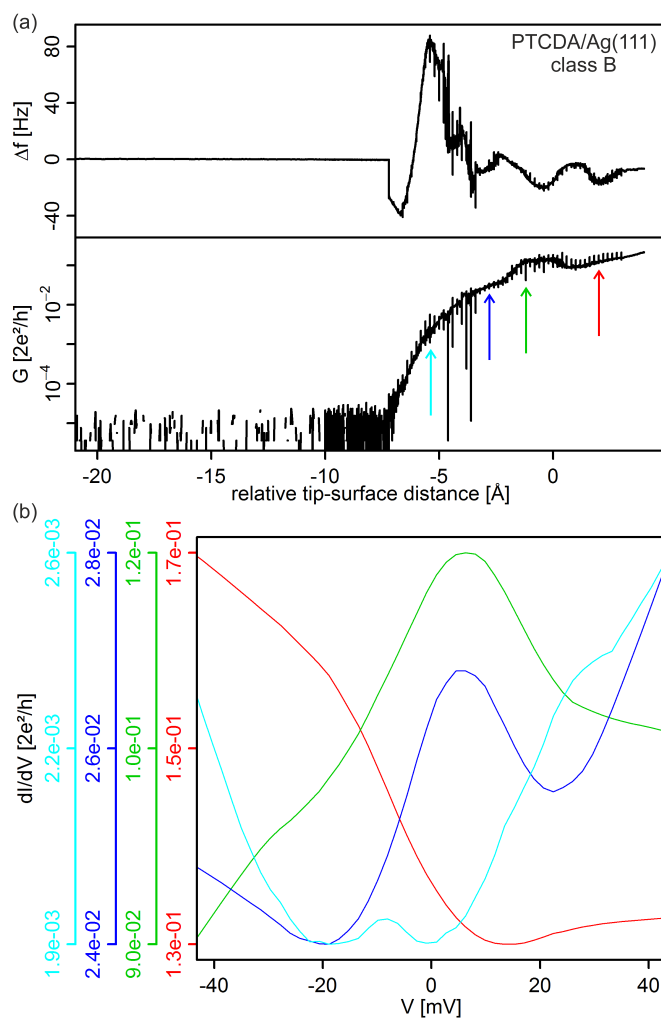


Figure A.67: Transport spectroscopy on PTCDA/Ag(111) junction of class B



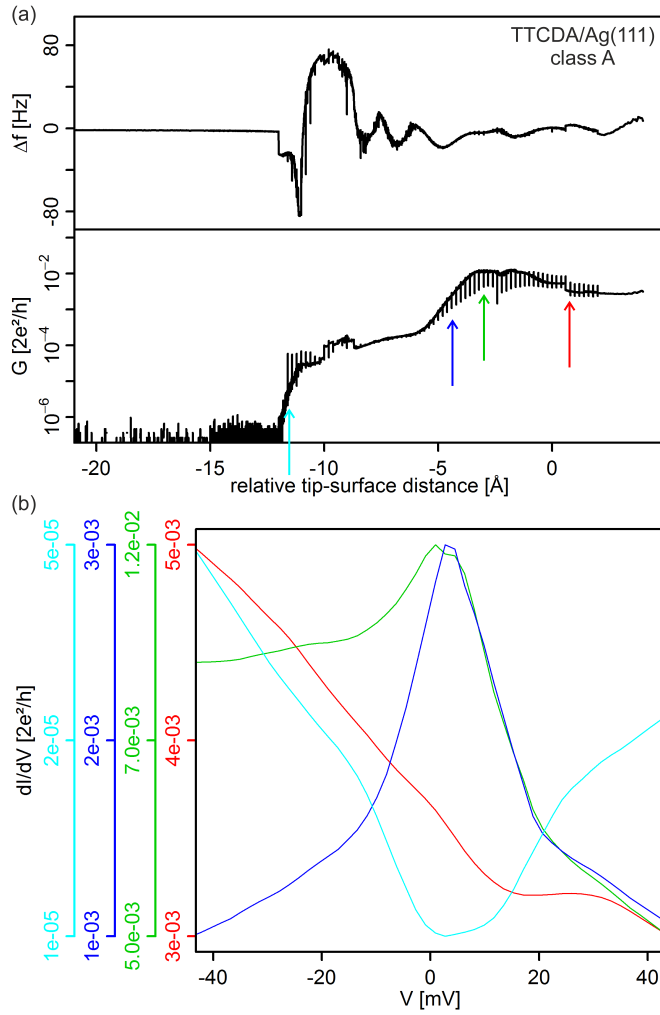


Figure A.68: Transport spectroscopy on TTcDA/Ag(111) junction of class A

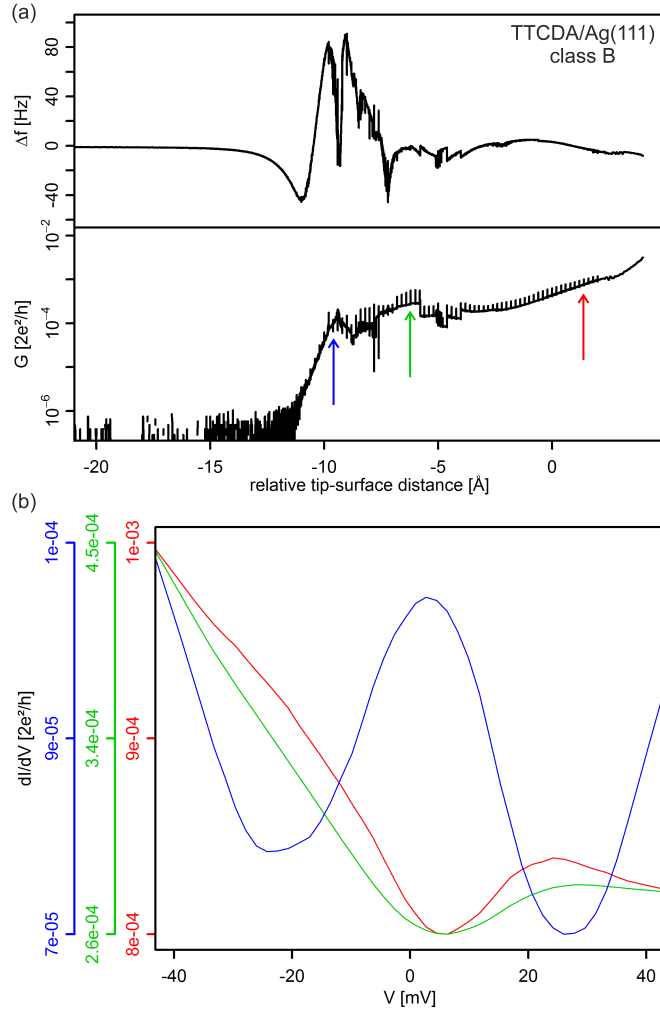


Figure A.69: Transport spectroscopy on TTCDA/Ag(111) junction of class B

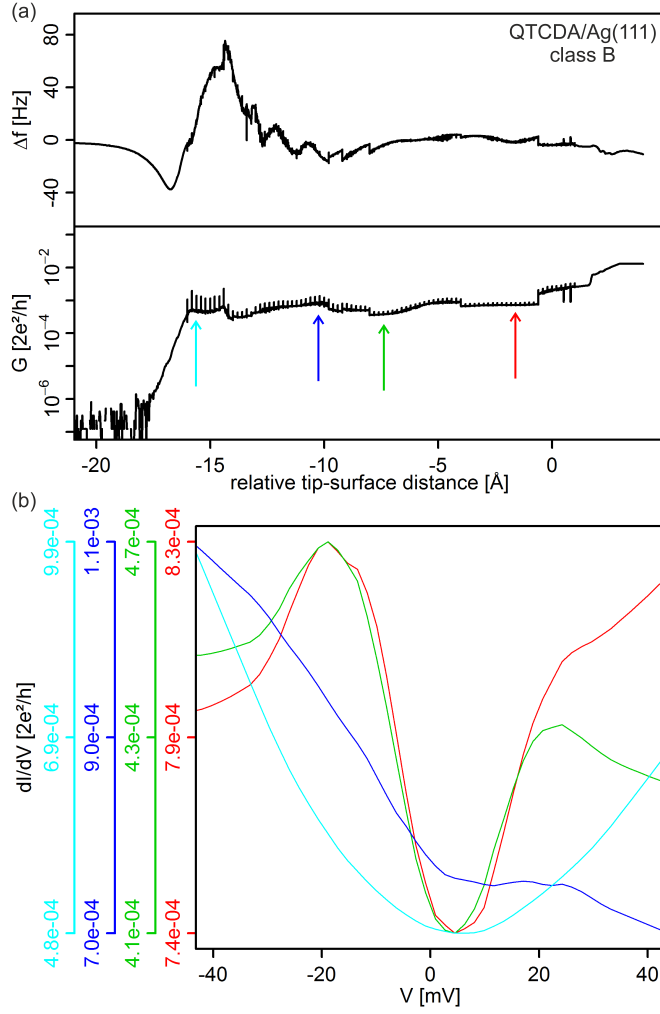


Figure A.70: Transport spectroscopy on QTCD/Ag(111) junction of class B

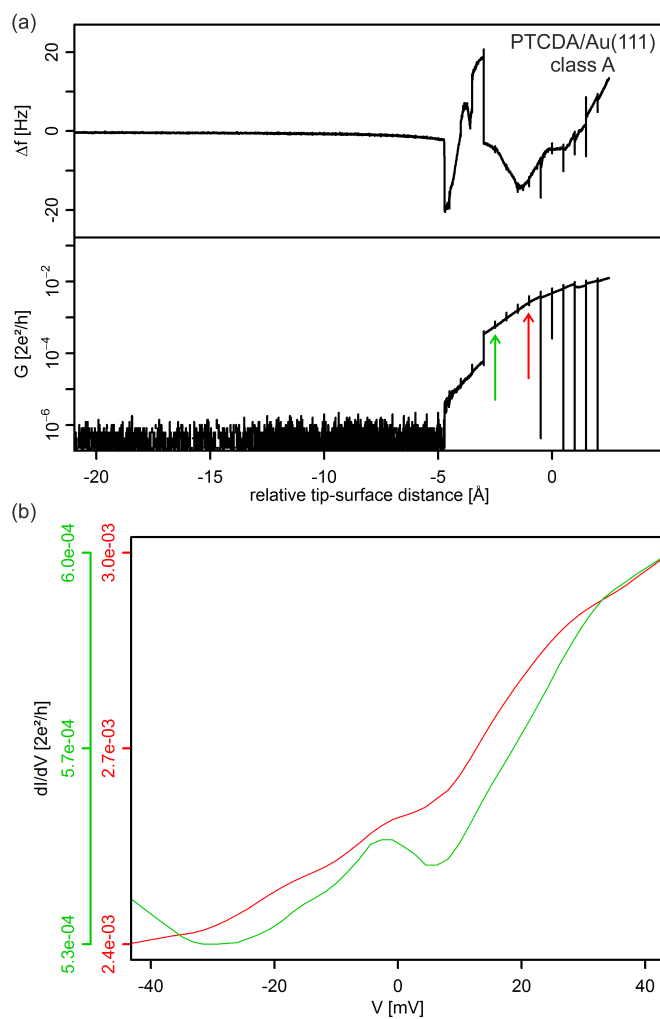


Figure A.71: Transport spectroscopy on PTCDA/Au(111) junction of class A

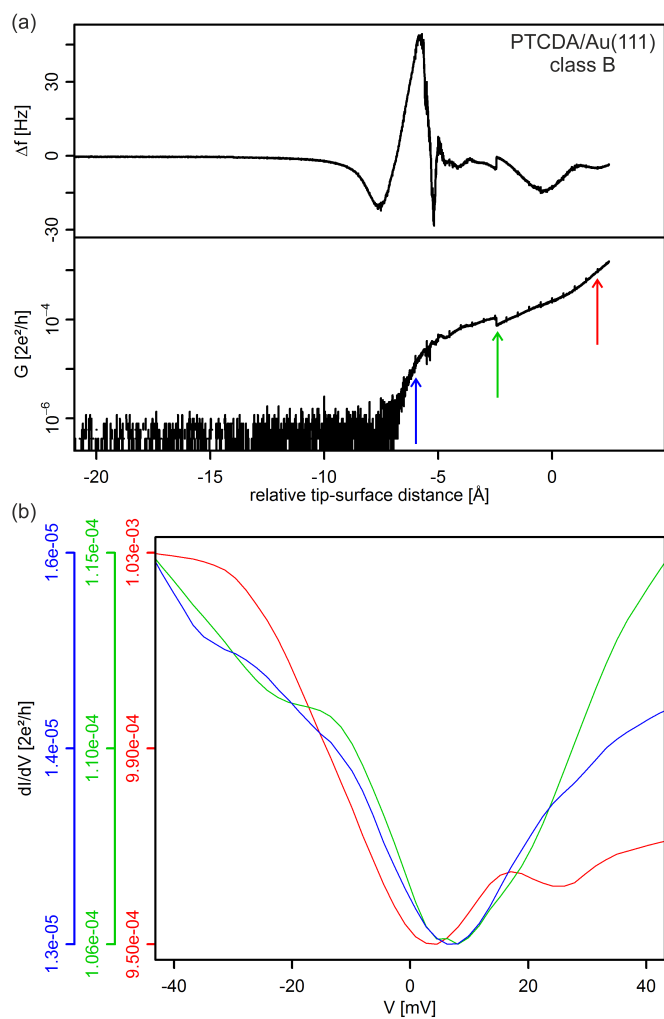


Figure A.72: Transport spectroscopy on PTCDA/Au(111) junction of class B



# List of Publications

## Journal publications

1. N. Fournier, C. Wagner, C. Weiss, R. Temirov and F.S. Tautz "Force-controlled lifting of molecular wires", PHYSICAL REVIEW B, 84:035435, JUL 2011
2. C. Wagner, N. Fournier, F.S. Tautz and R. Temirov "Measurement of the Binding Energies of the Organic-Metal Perylene-Tetracarboxylic-Dianhydride/Au(111) Bonds by Molecular Manipulation Using an Atomic Force Microscope", PHYSICAL REVIEW LETTERS, 109:076102, AUG 2012
3. C. Wagner, N. Fournier, F.S. Tautz and R. Temirov "The role of surface corrugation and tip oscillation in single-molecule manipulation with a non-contact atomic force microscope", BEILSTEIN JOURNAL OF NANOTECHNOLOGY, 5:202, FEB 2014
4. C. Wagner, N. Fournier, V.G. Ruiz, C. Li, M. Rohlfing, A. Tkatchenko, R. Temirov and F.S. Tautz "Non-additivity of molecule-surface van der Waals potentials from force measurements", NATURE COMMUNICATIONS, 2014, 5:5568, NOV 2014

## Oral presentations

1. N. Fournier, C. Wagner, C. Weiss, R. Temirov and F.S. Tautz "Measuring forces in a single-molecule transport junction", DPG Spring Meeting 2011, Dresden, March 13-18, 2011
2. N. Fournier, C. Wagner, C. Weiss, R. Temirov and F.S. Tautz "Force-controlled lifting of molecular wires", DPG Spring Meeting 2012, Berlin, March 25-30, 2012

## **Poster presentations**

1. N. Fournier, C. Wagner, C. Weiss, R. Temirov and F.S. Tautz "Measuring forces in a single-molecule junction", ElecMol10: 5th International Meeting on Molecular Electronics, Grenoble, December 6-10, 2010
2. C. Wagner, N. Fournier, C. Weiss, R. Temirov and F.S. Tautz "Force-controlled lifting of molecular wires", JARA FIT Science Days, Schleiden, October 28-29, 2011
3. N. Fournier, C. Wagner, C. Weiss, R. Temirov and F.S. Tautz "Force controlled lifting of molecular wires", 493. WE-Heraeus-Seminar on "Latest Developements in Scanning Probe Techniques focused on Nanotechnology", Bad Honnef, November 28 - December 1, 2011
4. N. Fournier, C. Wagner, R. Temirov and F.S. Tautz "Measuring the conductance of molecular wires by force-controlled lifting", Lorentz center workshop "Future directions of Molecular Electronics", Leiden, June 25-29 , 2012
5. N. Engels, N. Fournier, G. Kichin, S. Korte, C. Stampfer, F.S. Tautz, R. Temirov, B. Voigtländer, C. Wagner and C. Weiss "Nanoscale transport with STM", Peter Grünberg Institut Midterm Evaluation, Jülich, November 05 , 2012
6. N. Fournier, C. Wagner, R. Temirov and F.S. Tautz "STM-based quantum transport through molecular wires", Evaluation Panel Meeting: Helmholtz Young Investigators Group of Dr. Ruslan Temirov, Jülich, July 1, 2013



# Bibliography

- [1] C. Auth, “A 22 nm high performance and low-power CMOS technology featuring fully-depleted tri-gate transistors, self-aligned contacts and high density MIM capacitors,” tech. rep., Intel, 2012.
- [2] R. Smith, “Intel’s 2011 Investor Meeting - Intel’s Architecture Group: 14nm Airmont Atom In 2014,” May 2011.
- [3] V. Subramanian, “Multiple Gate Field-Effect Transistors for Future CMOS Technologies,” *IETE TECHNICAL REVIEW*, vol. 27, pp. 446–454, NOV-DEC 2010.
- [4] V. Khanna, “Physics of carrier-transport mechanisms and ultra-small scale phenomena for theoretical modelling of nanometer MOS transistors from diffusive to ballistic regimes of operation,” *PHYSICS REPORTS-REVIEW SECTION OF PHYSICS LETTERS*, vol. 398, pp. 67–131, AUG 2004.
- [5] D. Frank, “Power-constrained CMOS scaling limits,” *IBM JOURNAL OF RESEARCH AND DEVELOPMENT*, vol. 46, pp. 235–244, MAR-MAY 2002.
- [6] R. H. French and H. V. Tran, “Immersion Lithography: Photomask and Wafer-Level Materials,” *ANNUAL REVIEW OF MATERIALS RESEARCH*, vol. 39, pp. 93–126, 2009.
- [7] T. Fulton and G. Dolan, “Observation of single-electron charging effects in small tunnel-junctions,” *PHYSICAL REVIEW LETTERS*, vol. 59, pp. 109–112, JUL 6 1987.
- [8] S. Tans, A. Verschueren, and C. Dekker, “Room-temperature transistor based on a single carbon nanotube,” *NATURE*, vol. 393, pp. 49–52, MAY 7 1998.
- [9] S. Kubatkin, A. Danilov, M. Hjort, J. Cornil, J. Bredas, N. Stuhr-Hansen, P. Hedegard, and T. Bjornholm, “Single-electron transistor of a single organic molecule with access to several redox states,” *NATURE*, vol. 425, pp. 698–701, OCT 16 2003.

## Bibliography

- [10] C. Tang, "Two-layer organic photovoltaic cell," *APPLIED PHYSICS LETTERS*, vol. 48, pp. 183–185, JAN 13 1986.
- [11] A. Tsumura, H. Koezuka, and T. Ando, "Macromolecular electronic device: Field-effect transistor with a polythiophene thin film," *APPLIED PHYSICS LETTERS*, vol. 49, pp. 1210–1212, NOV 3 1986.
- [12] C. Tang and S. Vanslyke, "Organic electroluminescent diodes," *APPLIED PHYSICS LETTERS*, vol. 51, pp. 913–915, SEP 21 1987.
- [13] M. A. Green, K. Emery, Y. Hishikawa, W. Warta, and E. D. Dunlop, "Solar cell efficiency tables (version 41)," *PROGRESS IN PHOTOVOLTAICS*, vol. 21, pp. 1–11, JAN 2013.
- [14] J. Shaw and P. Seidler, "Organic electronics: Introduction," *IBM JOURNAL OF RESEARCH AND DEVELOPMENT*, vol. 45, pp. 3–9, JAN 2001.
- [15] J.-H. Jou, W.-B. Wang, M.-F. Hsu, J.-J. Shyue, C.-H. Chiu, I.-M. Lai, S.-Z. Chen, P.-H. Wu, C.-C. Chen, C.-P. Liu, and S.-M. Shen, "Extraordinarily High Efficiency Improvement for OLEDs with High Surface-Charge Polymeric Nanodots," *ACS NANO*, vol. 4, pp. 4054–4060, JUL 2010.
- [16] D. Mitzi, K. Chondroudis, and C. Kagan, "Organic-inorganic electronics," *IBM JOURNAL OF RESEARCH AND DEVELOPMENT*, vol. 45, pp. 29–45, JAN 2001.
- [17] R. M. Metzger, "Unimolecular electronics," *JOURNAL OF MATERIALS CHEMISTRY*, vol. 18, no. 37, pp. 4364–4396, 2008.
- [18] A. Aviram and M. Ratner, "Molecular rectifiers," *CHEMICAL PHYSICS LETTERS*, vol. 29, no. 2, pp. 277–283, 1974.
- [19] F. Chen, J. Hihath, Z. Huang, X. Li, and N. J. Tao, "Measurement of single-molecule conductance," *ANNUAL REVIEW OF PHYSICAL CHEMISTRY*, vol. 58, pp. 535–564, 2007.
- [20] J. Gimzewski and C. Joachim, "Nanoscale science of single molecules using local probes," *SCIENCE*, vol. 283, pp. 1683–1688, MAR 12 1999.
- [21] B. Stipe, M. Rezaei, and W. Ho, "Inducing and viewing the rotational motion of a single molecule," *SCIENCE*, vol. 279, pp. 1907–1909, MAR 20 1998.

## Bibliography

- [22] B. Xu, X. Li, X. Xiao, H. Sakaguchi, and N. Tao, "Electromechanical and conductance switching properties of single oligothiophene molecules," *NANO LETTERS*, vol. 5, pp. 1491–1495, JUL 2005.
- [23] T. Albrecht, A. Guckian, J. Ulstrup, and J. Vos, "Transistor-like behavior of transition metal complexes," *NANO LETTERS*, vol. 5, pp. 1451–1455, JUL 2005.
- [24] J. Park, A. Pasupathy, J. Goldsmith, C. Chang, Y. Yaish, J. Petta, M. Rinkoski, J. Sethna, H. Abruna, P. McEuen, and D. Ralph, "Coulomb blockade and the Kondo effect in single-atom transistors," *NATURE*, vol. 417, pp. 722–725, JUN 13 2002.
- [25] W. Liang, M. Shores, M. Bockrath, J. Long, and H. Park, "Kondo resonance in a single-molecule transistor," *NATURE*, vol. 417, pp. 725–729, JUN 13 2002.
- [26] M. Reed, C. Zhou, C. Muller, T. Burgin, and J. Tour, "Conductance of a molecular junction," *SCIENCE*, vol. 278, pp. 252–254, OCT 10 1997.
- [27] J. Reichert, R. Ochs, D. Beckmann, H. Weber, M. Mayor, and H. von Lohneysen, "Driving current through single organic molecules," *PHYSICAL REVIEW LETTERS*, vol. 88, APR 29 2002.
- [28] D. Djukic, K. Thygesen, C. Untiedt, R. Smit, K. Jacobsen, and J. van Ruitenbeek, "Stretching dependence of the vibration modes of a single-molecule Pt-H-2-Pt bridge," *PHYSICAL REVIEW B*, vol. 71, APR 2005.
- [29] J. He, F. Chen, J. Li, O. Sankey, Y. Terazono, C. Herrero, D. Gust, T. Moore, A. Moore, and S. Lindsay, "Electronic decay constant of carotenoid polyenes from single-molecule measurements," *JOURNAL OF THE AMERICAN CHEMICAL SOCIETY*, vol. 127, pp. 1384–1385, FEB 9 2005.
- [30] L. Venkataraman, J. Klare, I. Tam, C. Nuckolls, M. Hybertsen, and M. Steigerwald, "Single-molecule circuits with well-defined molecular conductance," *NANO LETTERS*, vol. 6, pp. 458–462, MAR 2006.
- [31] X. Li, J. He, J. Hihath, B. Xu, S. Lindsay, and N. Tao, "Conductance of single alkanedithiols: Conduction mechanism and effect of molecule-electrode contacts," *JOURNAL OF THE AMERICAN CHEMICAL SOCIETY*, vol. 128, pp. 2135–2141, FEB 15 2006.
- [32] A. Nitzan and M. Ratner, "Electron transport in molecular wire junctions," *SCIENCE*, vol. 300, pp. 1384–1389, MAY 30 2003.

## Bibliography

- [33] Z. Li and D. S. Kosov, “Nature of well-defined conductance of amine-anchored molecular junctions: Density functional calculations,” *PHYSICAL REVIEW B*, vol. 76, JUL 2007.
- [34] I. Diez-Perez, J. Hihath, T. Hines, Z.-S. Wang, G. Zhou, K. Muellen, and N. Tao, “Controlling single-molecule conductance through lateral coupling of  $\pi$  orbitals,” *NATURE NANOTECHNOLOGY*, vol. 6, pp. 226–231, APR 2011.
- [35] A. Danilov, S. Kubatkin, S. Kafanov, P. Hedegard, N. Stuhr-Hansen, K. Moth-Poulsen, and T. Bjornholm, “Electronic transport in single molecule junctions: Control of the molecule-electrode coupling through intramolecular tunneling barriers,” *NANO LETTERS*, vol. 8, pp. 1–5, JAN 2008.
- [36] K. Moth-Poulsen and T. Bjornholm, “Molecular electronics with single molecules in solid-state devices,” *NATURE NANOTECHNOLOGY*, vol. 4, pp. 551–556, SEP 2009.
- [37] S. Schmaus, A. Bagrets, Y. Nahas, T. K. Yamada, A. Bork, M. Bowen, E. Beaurepaire, F. Evers, and W. Wulfhekkel, “Giant magnetoresistance through a single molecule,” *NATURE NANOTECHNOLOGY*, vol. 6, pp. 185–189, MAR 2011.
- [38] S. Barraza-Lopez, M. C. Avery, and K. Park, “First-principles study of a single-molecule magnet Mn(12) monolayer on the Au(111) surface,” *PHYSICAL REVIEW B*, vol. 76, DEC 2007.
- [39] R. Temirov, A. Lassise, F. B. Anders, and F. S. Tautz, “Kondo effect by controlled cleavage of a single-molecule contact,” *NANOTECHNOLOGY*, vol. 19, p. 065401, FEB 13 2008.
- [40] C. Toher, R. Temirov, A. Greuling, F. Pump, M. Kaczmariski, G. Cuniberti, M. Rohlfing, and F. S. Tautz, “Electrical transport through a mechanically gated molecular wire,” *PHYSICAL REVIEW B*, vol. 83, p. 155402, APR 2011.
- [41] A. Greuling, M. Rohlfing, R. Temirov, F. S. Tautz, and F. B. Anders, “*Ab initio* study of a mechanically gated molecule: From weak to strong correlation,” *PHYSICAL REVIEW B*, vol. 84, p. 125413, SEP 2011.
- [42] N. Fournier, C. Wagner, C. Weiss, R. Temirov, and F. S. Tautz, “Force-controlled lifting of molecular wires,” *PHYSICAL REVIEW B*, vol. 84, p. 035435, JUL 2011.

## Bibliography

- [43] C. Wagner, N. Fournier, F. S. Tautz, and R. Temirov, “Measurement of the binding energies of the organic-metal perylene-teracarboxylic-dianhydride/au(111) bonds by molecular manipulation using an atomic force microscope,” *PHYSICAL REVIEW LETTERS*, vol. 109, p. 076102, AUG 2012.
- [44] I. Giaever, “Energy gap in superconductors measured by electron tunneling,” *PHYSICAL REVIEW LETTERS*, vol. 5, pp. 147–148, Aug 1960.
- [45] I. Giaever, “Electron tunneling between two superconductors,” *PHYSICAL REVIEW LETTERS*, vol. 5, pp. 464–466, Nov 1960.
- [46] J. Nicol, S. Shapiro, and P. H. Smith, “Direct measurement of the superconducting energy gap,” *PHYSICAL REVIEW LETTERS*, vol. 5, pp. 461–464, Nov 1960.
- [47] J. Bardeen, “Tunnelling from a many-particle point of view,” *PHYSICAL REVIEW LETTERS*, vol. 6, pp. 57–59, Jan 1961.
- [48] G. Binnig, H. Rohrer, C. Gerber, and E. Weibel, “Surface studies by scanning tunneling microscopy,” *PHYSICAL REVIEW LETTERS*, vol. 49, pp. 57–61, JUL 1982.
- [49] G. Binnig, G., H. Rohrer, H., C. Gerber, C., and E. Weibel, “Tunneling through a controllable vacuum gap,” *APPLIED PHYSICS LETTERS*, vol. 40, no. 2, pp. 178–180, 1982.
- [50] J. Tersoff and D. Hamann, “Theory and application for the scanning tunneling microscope,” *PHYSICAL REVIEW LETTERS*, vol. 50, no. 25, pp. 1998–2001, 1983.
- [51] J. Tersoff and D. Hamann, “Theory of the scanning tunneling microscope,” *PHYSICAL REVIEW B*, vol. 31, no. 2, pp. 805–813, 1985.
- [52] L. Gross, N. Moll, F. Mohn, A. Curioni, G. Meyer, F. Hanke, and M. Persson, “High-Resolution Molecular Orbital Imaging Using a p-Wave STM Tip,” *PHYSICAL REVIEW LETTERS*, vol. 107, AUG 15 2011.
- [53] C. Chen, “Theory of scanning tunneling spectroscopy,” *JOURNAL OF VACUUM SCIENCE & TECHNOLOGY A-VACUUM SURFACES AND FILMS*, vol. 6, pp. 319–322, MAR-APR 1988.
- [54] C. Chen, “Tunneling matrix-elements in 3-dimensional space: The derivate rule and the sum rule,” *PHYSICAL REVIEW B*, vol. 42, pp. 8841–8857, NOV 15 1990.

## Bibliography

- [55] C. Chen, *Introduction to Scanning Tunneling Microscopy*. Oxford University Press, 1993.
- [56] O. Dulub, W. Hebenstreit, and U. Diebold, “Imaging cluster surfaces with atomic resolution: The strong metal-support interaction state of Pt supported on TiO<sub>2</sub>(110),” *PHYSICAL REVIEW LETTERS*, vol. 84, pp. 3646–3649, APR 17 2000.
- [57] J. Tao, T. Luttrell, and M. Batzill, “A two-dimensional phase of TiO<sub>2</sub> with a reduced bandgap,” *NATURE CHEMISTRY*, vol. 3, pp. 296–300, APR 2011.
- [58] L. Tapaszto, T. Dumitrica, S. J. Kim, P. Nemes-Incze, C. Hwang, and L. P. Biro, “Breakdown of continuum mechanics for nanometre-wavelength rippling of graphene,” *NATURE PHYSICS*, vol. 8, pp. 739–742, OCT 2012.
- [59] K. Besocke, “An easily operable scanning tunneling microscope,” *SURFACE SCIENCE*, vol. 181, pp. 145–153, MAR 1987.
- [60] J. Lindahl, T. Takanen, and L. Montelius, “Easy and reproducible method for making sharp tips of Pt/Ir,” *JOURNAL OF VACUUM SCIENCE & TECHNOLOGY B*, vol. 16, pp. 3077–3081, NOV-DEC 1998.
- [61] B. Rogers, J. Shapter, W. Skinner, and K. Gascoigne, “A method for production of cheap, reliable Pt-Ir tips,” *REVIEW OF SCIENTIFIC INSTRUMENTS*, vol. 71, pp. 1702–1705, APR 2000.
- [62] W. Escovitz, T. Fox, and R. Levisetti, “Scanning transmission ion microscope with a field ion source,” *PROCEEDINGS OF THE NATIONAL ACADEMY OF SCIENCES OF THE UNITED STATES OF AMERICA*, vol. 72, no. 5, pp. 1826–1828, 1975.
- [63] J. Orloff and L. Swanson, “Study of a field-ionization source for microprobe applications,” *JOURNAL OF VACUUM SCIENCE & TECHNOLOGY*, vol. 12, no. 6, pp. 1209–1213, 1975.
- [64] R. Seliger, J. Ward, V. Wang, and K. R.L., “A high-intensity scanning ion probe with submicrometer spot size,” *APPLIED PHYSICS LETTERS*, vol. 34, p. 310, 1979.
- [65] S. Reyntjens and R. Puers, “A review of focused ion beam applications in microsystem technology,” *JOURNAL OF MICROMECHANICS AND MICROENGINEERING*, vol. 11, pp. 287–300, JUL 2001.

## Bibliography

- [66] R. Temirov, S. Soubatch, A. Luican, and F. S. Tautz, “Free-electron-like dispersion in an organic monolayer film on a metal substrate,” *NATURE*, vol. 444, pp. 350–353, NOV 16 2006.
- [67] R. Temirov, S. Soubatch, A. Lassise, and F. S. Tautz, “Bonding and vibrational dynamics of a large  $\pi$ -conjugated molecule on a metal surface,” *JOURNAL OF PHYSICS: CONDENSED MATTER*, vol. 20, no. 22, p. 224010, 2008.
- [68] K. J. Franke and J. I. Pascual, “Effects of electron-vibration coupling in transport through single molecules,” *JOURNAL OF PHYSICS-CONDENSED MATTER*, vol. 24, OCT 3 2012.
- [69] B. Koslowski, T. A., M. N., and Z. P., “4,4'-Dithiopyridine on Au(111) A combined STM, STS and DFT study,” *JOURNAL OF PHYSICAL CHEMISTRY C*, vol. 117, pp. 20060–20067, 2013.
- [70] P. King, A. Borg, B. Kim, P. Pianetta, I. Lindau, G. Knapp, and M. Keenlyside, “Small area photoemission and photoadsorption measurements using a photoelectron microscope,” *PHYSICA SCRIPTA*, vol. 41, pp. 413–417, APR 1990.
- [71] K. Horiba, Y. Nakamura, N. Nagamura, S. Toyoda, H. Kumigashira, M. Oshima, K. Amemiya, Y. Senba, and H. Ohashi, “Scanning photoelectron microscope for nanoscale three-dimensional spatial-resolved electron spectroscopy for chemical analysis,” *REVIEW OF SCIENTIFIC INSTRUMENTS*, vol. 82, NOV 2011.
- [72] N. Lang, “Spectroscopy of single atoms in the scanning tunneling microscope,” *PHYSICAL REVIEW B*, vol. 34, pp. 5947–5950, OCT 15 1986.
- [73] J. M. Beebe, B. Kim, J. W. Gadzuk, C. D. Frisbie, and J. G. Kushmerick, “Transition from direct tunneling to field emission in metal-molecule-metal junctions,” *PHYSICAL REVIEW LETTERS*, vol. 97, JUL 14 2006.
- [74] P. Echenique, J. Osma, M. Machado, V. Silkin, E. Chulkov, and J. Pitarke, “Surface-state electron dynamics in noble metals,” *PROGRESS IN SURFACE SCIENCE*, vol. 67, pp. 271–283, MAY-AUG 2001. 20th International Seminar on Surface Physics, KUDOWA ZDROJ, POLAND, JUN 19-24, 2000.
- [75] L. Burgi, N. Knorr, H. Brune, M. Schneider, and K. Kern, “Two-dimensional electron gas at noble-metal surfaces,” *APPLIED PHYSICS A-MATERIALS SCIENCE & PROCESSING*, vol. 75, pp. 141–145, JUL 2002.

## Bibliography

- [76] M. Everson, R. Jaklevic, and W. Shen, "Measurement of the local density of states on a metal-surface: Scanning tunneling spectroscopic imaging of au(111)," *JOURNAL OF VACUUM SCIENCE & TECHNOLOGY A-VACUUM SURFACES AND FILMS*, vol. 8, pp. 3662–3665, SEP-OCT 1990.
- [77] W. Chen, V. Madhavan, T. Jamneala, and M. Crommie, "Scanning tunneling microscopy observation of an electronic superlattice at the surface of clean gold," *PHYSICAL REVIEW LETTERS*, vol. 80, pp. 1469–1472, FEB 16 1998.
- [78] N. Lorente and M. Persson, "Theory of Single Molecule Vibrational Spectroscopy and Microscopy," *PHYSICAL REVIEW LETTERS*, vol. 85, pp. 2997–3000, Oct 2000.
- [79] C. Caroli, C. R. N. P, and S.-J. D, "Direct calculation of tunneling current: IV. Electron-phonon interaction effects," *JOURNAL OF PHYSICS PART C SOLID STATE PHYSICS*, vol. 5, no. 1, pp. 21–42, 1972.
- [80] Stanford Research Systems, *About Lock-in Amplifiers*.
- [81] N. Agrait, A. Yeyati, and J. van Ruitenbeek, "Quantum properties of atomic-sized conductors," *PHYSICS REPORTS-REVIEW SECTION OF PHYSICS LETTERS*, vol. 377, pp. 81–279, APR 2003.
- [82] G. Binnig, C. F. Quate, and C. Gerber, "Atomic force microscope," *PHYSICAL REVIEW LETTERS*, vol. 56, pp. 930–933, MAR 1986.
- [83] G. Binnig, C. Gerber, E. Stoll, T. Albrecht, and C. F. Quate, "Atomic resolution with atomic force microscope," *EUROPHYSICS LETTERS*, vol. 3, pp. 1281–1286, JUN 15 1987.
- [84] G. F.J. and G. Binnig, "Investigation of the (111) cleavage plane of potassium-bromide with an atomic force microscope at 4.2k in ultra-high-vacuum," *ULTRA-MICROSCOPY*, vol. 42, pp. 281–289, JUL 1992. 6TH INTERNATIONAL CONF ON SCANNING TUNNELING MICROSCOPY ( STM 91 ), INTERLAKEN, SWITZERLAND, AUG 12-16, 1991.
- [85] F. Giessibl, "Atomic resolution of the silicon (111)-(7x7) surface by atomic force microscopy," *SCIENCE*, vol. 267, pp. 68–71, JAN 6 1995.
- [86] F. J. Giessibl, "AFM's path to atomic resolution," *MATERIALS TODAY*, vol. 8, pp. 32–41, MAY 2005.



## Bibliography

- [87] F. Giessibl, S. Hembacher, M. Herz, C. Schiller, and J. Mannhart, "Stability considerations and implementation of cantilevers allowing dynamic force microscopy with optimal resolution: the qPlus sensor," *NANOTECHNOLOGY*, vol. 15, pp. S79–S86, FEB 2004. 6th International Conference on Non-contact Atomic Force Microscopy, Dingle, IRELAND, AUG 31-SEP 03, 2003.
- [88] F. Giessibl, "Atomic resolution on Si(111)-(7x7) by noncontact atomic force microscopy with a force sensor based on a quartz tuning fork," *APPLIED PHYSICS LETTERS*, vol. 76, pp. 1470–1472, MAR 13 2000.
- [89] Y. Seo and W. Jhe, "Atomic force microscopy and spectroscopy," *REPORTS ON PROGRESS IN PHYSICS*, vol. 71, JAN 2008.
- [90] G. H. Simon, M. Heyde, and H.-P. Rust, "Recipes for cantilever parameter determination in dynamic force spectroscopy: spring constant and amplitude," *NANOTECHNOLOGY*, vol. 18, JUN 27 2007.
- [91] C. Woll, S. Chiang, R. Wilson, E., and P. Lippel, "Determination of atom positions at stacking-fault dislocations on au(111) by scanning tunneling microscopy," *PHYSICAL REVIEW B*, vol. 39, pp. 7988–7991, APR 15 1989.
- [92] U. Stahl, D. Gador, A. Soukopp, R. Fink, and E. Umbach, "Coverage-dependent superstructures in chemisorbed NTCDA monolayers: a combined LEED and STM study," *SURFACE SCIENCE*, vol. 414, pp. 423–434, SEP 19 1998.
- [93] K. Glocker, C. Seidel, A. Soukopp, M. Sokolowski, E. Umbach, M. Bohringer, R. Berndt, and W. Schneider, "Highly ordered structures and submolecular scanning tunnelling microscopy contrast of PTCDA and DM-PBDCI monolayers on Ag(111) and Ag(110)," *SURFACE SCIENCE*, vol. 405, pp. 1–20, MAY 12 1998.
- [94] L. Kilian, E. Umbach, and M. Sokolowski, "Molecular beam epitaxy of organic films investigated by high resolution low energy electron diffraction (SPA-LEED): 3,4,9,10-perylenetetracarboxylicacid-dianhydride (PTCDA) on Ag(111)," *SURFACE SCIENCE*, vol. 573, pp. 359–378, DEC 20 2004.
- [95] T. SchmitzHubsch, T. Fritz, F. Sellam, R. Staub, and K. Leo, "Epitaxial growth of 3,4,9,10-perylene-tetracarboxylic-dianhydride on Au(111): A STM and RHEED study," *PHYSICAL REVIEW B*, vol. 55, pp. 7972–7976, MAR 15 1997.
- [96] I. Chizhov, A. Kahn, and G. Scoles, "Initial growth of 3,4,9,10-perylenetetracarboxylic-dianhydride (PTCDA) on Au(111): a scanning tunneling

## Bibliography

- microscopy study,” *JOURNAL OF CRYSTAL GROWTH*, vol. 208, pp. 449–458, JAN 2000.
- [97] P. Fenter, F. Schreiber, L. Zhou, P. Eisenberger, and S. Forrest, “In situ studies of morphology, strain, and growth modes of a molecular organic thin film,” *PHYSICAL REVIEW B*, vol. 56, pp. 3046–3053, AUG 1 1997.
- [98] R. Temirov, S. Soubatch, O. Neucheva, A. C. Lassise, and F. S. Tautz, “A novel method achieving ultra-high geometrical resolution in scanning tunnelling microscopy,” *NEW JOURNAL OF PHYSICS*, vol. 10, MAY 12 2008.
- [99] C. Weiss, C. Wagner, C. Kleimann, M. Rohlfing, F. S. Tautz, and R. Temirov, “Imaging pauli repulsion in scanning tunneling microscopy,” *PHYSICAL REVIEW LETTERS*, vol. 105, p. 086103, AUG 2010.
- [100] C. Weiss, C. Wagner, R. Temirov, and F. S. Tautz, “Direct Imaging of Intermolecular Bonds in Scanning Tunneling Microscopy,” *JOURNAL OF THE AMERICAN CHEMICAL SOCIETY*, vol. 132, pp. 11864–11865, SEP 1 2010.
- [101] S. Datta, *Electronic Transport in Mesoscopic Systems*. Cambridge University Press, 1997.
- [102] L. Bogani and W. Wernsdorfer, “Molecular spintronics using single-molecule magnets,” *NATURE MATERIALS*, vol. 7, pp. 179–186, MAR 2008.
- [103] G. Nazin, S. Wu, and W. Ho, “Tunneling rates in electron transport through double-barrier molecular junctions in a scanning tunneling microscope,” *PROCEEDINGS OF THE NATIONAL ACADEMY OF SCIENCES OF THE UNITED STATES OF AMERICA*, vol. 102, pp. 8832–8837, JUN 21 2005.
- [104] L. Chang, L. Esaki, and R. Tsu, “Resonant tunneling in semiconductor double barriers,” *APPLIED PHYSICS LETTERS*, vol. 24, no. 12, pp. 593–595, 1974.
- [105] M. Galperin, M. A. Ratner, and A. Nitzan, “Molecular transport junctions: vibrational effects,” *JOURNAL OF PHYSICS-CONDENSED MATTER*, vol. 19, MAR 14 2007.
- [106] C. Huang, M. Paulus, C. Bozada, S. Dudley, K. Evans, C. Stutz, R. Jones, and M. Cheney, “AlGaAs/GaAs double barrier diodes with high peak-to-valley current ratio,” *APPLIED PHYSICS LETTERS*, vol. 51, pp. 121–123, JUL 13 1987.

## Bibliography

- [107] F. Chevoir and B. Vinter, "Scattering-assisted tunneling in double-barrier diodes: Scattering rates and valley currents," *PHYSICAL REVIEW B*, vol. 47, pp. 7260–7274, MAR 15 1993.
- [108] O. Tal, M. Krieger, B. Leerink, and J. M. van Ruitenbeek, "Electron-vibration interaction in single-molecule junctions: From contact to tunneling regimes," *PHYSICAL REVIEW LETTERS*, vol. 100, MAY 16 2008.
- [109] B. Stipe, M. Rezaei, and W. Ho, "Single-molecule vibrational spectroscopy and microscopy," *SCIENCE*, vol. 280, pp. 1732–1735, JUN 12 1998.
- [110] D. Wegner, R. Yamachika, X. Zhang, Y. Wang, M. F. Crommie, and N. Lorente, "Adsorption site determination of a molecular monolayer via inelastic tunneling," *NANO LETTERS*, vol. 13, no. 0, pp. 2346–2350, 2013.
- [111] R. Jaklevic and J. Lambe, "Molecular vibration spectra by electron tunneling," *PHYSICAL REVIEW LETTERS*, vol. 17, no. 22, pp. 1139–&, 1966.
- [112] W. De Haas, J. De Boer, and G. Van Den Berg, "The electrical resistance of gold, copper and lead at low temperatures," *PHYSICA*, vol. 1, pp. 1115–1124, 1934.
- [113] M. Sarachik, E. Corenzwit, and L. Longinotti, "Resistivity of Mo-Nb + Mo-Re Alloys Containing 1% Fe," *PHYSICAL REVIEW A-GENERAL PHYSICS*, vol. 135, no. 4A, pp. 1041–1045, 1964.
- [114] J. Kondo, "Resistance minimum in dilute magnetic alloys," *PROGRESS OF THEORETICAL PHYSICS*, vol. 32, no. 1, pp. 37–&, 1964.
- [115] J. Li, W. Schneider, R. Berndt, and B. Delley, "Kondo scattering observed at a single magnetic impurity," *PHYSICAL REVIEW LETTERS*, vol. 80, pp. 2893–2896, MAR 30 1998.
- [116] D. Goldhaber-Gordon, H. Shtrikman, D. Mahalu, D. Abusch-Magder, U. Meirav, and M. Kastner, "Kondo effect in a single-electron transistor," *NATURE*, vol. 391, pp. 156–159, JAN 8 1998.
- [117] J. J. Parks, A. R. Champagne, G. R. Hutchison, S. Flores-Torres, H. D. Abruña, and D. C. Ralph, "Tuning the kondo effect with a mechanically controllable break junction," *PHYSICAL REVIEW LETTERS*, vol. 99, p. 026601, Jul 2007.

- [118] Y. Jiang, Y. N. Zhang, J. X. Cao, R. Q. Wu, and W. Ho, “Real-Space Imaging of Kondo Screening in a Two-Dimensional O-2 Lattice,” *SCIENCE*, vol. 333, pp. 324–328, JUL 15 2011.
- [119] F. S. Tautz, “Structure and bonding of large aromatic molecules on noble metal surfaces: The example of PTCDA,” *PROGRESS IN SURFACE SCIENCE*, vol. 82, pp. 479–520, SEP-DEC 2007.
- [120] M. Rohlfling, R. Temirov, and F. S. Tautz, “Adsorption structure and scanning tunneling data of a prototype organic-inorganic interface: Ptcda on ag(111),” *PHYSICAL REVIEW B*, vol. 76, p. 115421, SEP 2007.
- [121] A. Kraft, R. Temirov, S. K. M. Henze, S. Soubatch, M. Rohlfling, and F. S. Tautz, “Lateral adsorption geometry and site-specific electronic structure of a large organic chemisorbate on a metal surface,” *PHYSICAL REVIEW B*, vol. 74, p. 041402, JUL 2006.
- [122] L. Romaner, D. Nabok, P. Puschnig, E. Zojer, and C. Ambrosch-Draxl, “Theoretical study of PTCDA adsorbed on the coinage metal surfaces, Ag(111), Au(111) and Cu(111),” *NEW JOURNAL OF PHYSICS*, vol. 11, p. 053010, MAY 22 2009.
- [123] O. Bauer, G. Mercurio, M. Willenbockel, W. Reckien, C. Heinrich Schmitz, B. Fiedler, S. Soubatch, T. Bredow, F. S. Tautz, and M. Sokolowski, “Role of functional groups in surface bonding of planar  $\pi$ -conjugated molecules,” *PHYSICAL REVIEW B*, vol. 86, p. 235431, Dec 2012.
- [124] C. Stadler, S. Hansen, A. Schoell, T.-L. Lee, J. Zegenhagen, C. Kumpf, and E. Umbach, “Molecular distortion of NTCDA upon adsorption on Ag(111): a normal incidence x-ray standing wave study,” *NEW JOURNAL OF PHYSICS*, vol. 9, MAR 5 2007.
- [125] V. Gobre and A. Tkatchenko, “Scaling law for van der Waals interactions in nanostructured materials,” *NATURE COMMUNICATIONS*, vol. 4, p. 2341, 2013.
- [126] C. Wagner, N. Fournier, V. G. Ruiz, C. Li, K. Muellen, M. Rohlfling, A. Tkatchenko, R. Temirov, and F. S. Tautz, “Non-additivity of molecule-surface van der Waals potentials from force measurements,” *NATURE COMMUNICATIONS*, vol. 5, 2014.
- [127] S. Braun, W. R. Salaneck, and M. Fahlman, “Energy-Level Alignment at Organic/Metal and Organic/Organic Interfaces,” *ADVANCED MATERIALS*, vol. 21, pp. 1450–1472, APR 20 2009.

- [128] L. Kilian, U. Stahl, I. Kossev, M. Sokolowski, R. Fink, and E. Umbach, "The commensurate-to-incommensurate phase transition of an organic monolayer: A high resolution LEED analysis of the superstructures of NTCDA on Ag(111)," *SURFACE SCIENCE*, vol. 602, pp. 2427–2434, JUL 15 2008.
- [129] R. Strohmaier, J. Petersen, B. Gompf, and W. Eisenmenger, "A systematic STM study of planar aromatic molecules on inorganic substrates - I. Submolecular image contrast," *SURFACE SCIENCE*, vol. 418, pp. 91–104, NOV 27 1998.
- [130] L. Kilian, A. Hauschild, R. Temirov, S. Soubatch, A. Schöll, A. Bendounan, F. Reinert, T.-L. Lee, F. S. Tautz, M. Sokolowski, and E. Umbach, "Role of intermolecular interactions on the electronic and geometric structure of a large  $\pi$ -conjugated molecule adsorbed on a metal surface," *PHYSICAL REVIEW LETTERS*, vol. 100, p. 136103, APR 2008.
- [131] M. Willenbockel, B. Stadtmueller, K. Schoenauer, F. C. Bocquet, D. Lueftner, E. M. Reinisch, T. Ules, G. Koller, C. Kumpf, S. Soubatch, P. Puschnig, M. G. Ramsey, and F. S. Tautz, "Energy offsets within a molecular monolayer: the influence of the molecular environment," *NEW JOURNAL OF PHYSICS*, vol. 15, MAR 13 2013.
- [132] J. Hahn, H. Lee, and W. Ho, "Electronic resonance and symmetry in single-molecule inelastic electron tunneling," *PHYSICAL REVIEW LETTERS*, vol. 85, pp. 1914–1917, AUG 28 2000.
- [133] I. Fernandez-Torrente, K. J. Franke, and J. I. Pascual, "Vibrational Kondo Effect in Pure Organic Charge-Transfer Assemblies," *PHYSICAL REVIEW LETTERS*, vol. 101, NOV 21 2008.
- [134] L. Yu and D. Natelson, "The Kondo effect in C-60 single-molecule transistors," *NANO LETTERS*, vol. 4, pp. 79–83, JAN 2004.
- [135] K. J. Franke, G. Schulze, and J. I. Pascual, "Excitation of Jahn-Teller Active Modes during Electron Transport through Single C-60 Molecules on Metal Surfaces," *JOURNAL OF PHYSICAL CHEMISTRY LETTERS*, vol. 1, pp. 500–504, JAN 21 2010.
- [136] P. Weibel, E. M. Grioni, D. Malterre, B. Dardel, Y. Baer, and M. Besnus, "Temperature-dependence of the kondo peak in photoemission spectra of ybagcu4," *ZEITSCHRIFT FUR PHYSIK B-CONDENSED MATTER*, vol. 91, pp. 337–341, JUL 1993.

## Bibliography

- [137] D. Goldhaber-Gordon, J. Gores, M. Kastner, H. Shtrikman, D. Mahalu, and U. Meirav, “From the Kondo regime to the mixed-valence regime in a single-electron transistor,” *PHYSICAL REVIEW LETTERS*, vol. 81, pp. 5225–5228, DEC 7 1998.
- [138] S. Amasha, I. Gelfand, M. Kastner, and A. Kogan, “Kondo temperature dependence of the Kondo splitting in a single-electron transistor,” *PHYSICAL REVIEW B*, vol. 72, JUL 2005.
- [139] E. Scheer, T. Böhler, S. Egle, A. Erbe, and T. Pietsch, “Switchable zero-bias anomaly in individual  $C_{60}$  molecules contacted with tunable aluminium electrodes,” *LOW TEMPERATURES PHYSICS*, vol. 39, pp. 259–264, 2013.
- [140] P. Wahl, L. Diekhoner, G. Wittich, L. Vitali, M. Schneider, and K. Kern, “Kondo effect of molecular complexes at surfaces: Ligand control of the local spin coupling,” *PHYSICAL REVIEW LETTERS*, vol. 95, OCT 14 2005.
- [141] T. Hanke, M. Bode, S. Krause, L. Berbil-Bautista, and R. Wiesendanger, “Temperature-dependent scanning tunneling spectroscopy of Cr(001): Orbital Kondo resonance versus surface state,” *PHYSICAL REVIEW B*, vol. 72, AUG 2005.
- [142] K. Nagaoka, T. Jamneala, M. Grobis, and M. Crommie, “Temperature dependence of a single Kondo impurity,” *PHYSICAL REVIEW LETTERS*, vol. 88, FEB 18 2002.
- [143] M. Ternes, A. J. Heinrich, and W.-D. Schneider, “Spectroscopic manifestations of the Kondo effect on single adatoms,” *JOURNAL OF PHYSICS-CONDENSED MATTER*, vol. 21, FEB 4 2009.
- [144] P. W. Anderson, “Localized magnetic states in metals,” *Phys. Rev.*, vol. 124, pp. 41–53, Oct 1961.
- [145] T. Costi, A. Hewson, and V. Zlatic, “Transport coefficients of the Anderson model via the numerical renormalization group,” *JOURNAL OF PHYSICS-CONDENSED MATTER*, vol. 6, pp. 2519–2558, MAR 28 1994.
- [146] T. Esat. private communication, 2013.
- [147] B. M. F. de Resende and E. Vernek, “Parity oscillations of Kondo temperature in a single molecule break junction,” *APPLIED PHYSICS LETTERS*, vol. 100, MAY 21 2012.

- [148] V. Iancu, A. Deshpande, and S. Hla, “Manipulating Kondo temperature via single molecule switching,” *NANO LETTERS*, vol. 6, pp. 820–823, APR 2006.
- [149] L. Gao, W. Ji, Y. B. Hu, Z. H. Cheng, Z. T. Deng, Q. Liu, N. Jiang, X. Lin, W. Guo, S. X. Du, W. A. Hofer, X. C. Xie, and H.-J. Gao, “Site-specific Kondo effect at ambient temperatures in iron-based molecules,” *PHYSICAL REVIEW LETTERS*, vol. 99, SEP 7 2007.
- [150] J. J. Parks, A. R. Champagne, T. A. Costi, W. W. Shum, A. N. Pasupathy, E. Neuscamman, S. Flores-Torres, P. S. Cornaglia, A. A. Aligia, C. A. Balseiro, G. K. L. Chan, H. D. Abruna, and D. C. Ralph, “Mechanical Control of Spin States in Spin-1 Molecules and the Underscreened Kondo Effect,” *SCIENCE*, vol. 328, pp. 1370–1373, JUN 11 2010.
- [151] C. Wagner, N. Fournier, F. S. Tautz, and R. Temirov, “The role of surface corrugation and tip oscillation in single-molecule manipulation with a non-contact atomic force microscope,” *Beilstein Journal of Nanotechnology*, vol. 5, pp. 202–209, 2014.
- [152] C. Bruot, J. Hihath, and N. Tao, “Mechanically controlled molecular orbital alignment in single molecule junctions,” *NATURE NANOTECHNOLOGY*, vol. 7, pp. 35–40, JAN 2012.
- [153] L. Lafferentz, F. Ample, H. Yu, S. Hecht, C. Joachim, and L. Grill, “Conductance of a Single Conjugated Polymer as a Continuous Function of Its Length,” *SCIENCE*, vol. 323, pp. 1193–1197, FEB 27 2009.
- [154] T. Hines, I. Diez-Perez, J. Hihath, H. Liu, Z.-S. Wang, J. Zhao, G. Zhou, K. Muellen, and N. Tao, “Transition from Tunneling to Hopping in Single Molecular Junctions by Measuring Length and Temperature Dependence,” *JOURNAL OF THE AMERICAN CHEMICAL SOCIETY*, vol. 132, pp. 11658–11664, AUG 25 2010.
- [155] N. Koch, “Electronic structure of interfaces with conjugated organic materials,” *PHYSICA STATUS SOLIDI-RAPID RESEARCH LETTERS*, vol. 6, pp. 277–293, JUL 2012.
- [156] A. Bilic, Z. Crljen, B. Gumhalter, J. D. Gale, I. Rungger, and S. Sanvito, “Conductance of a phenylene-vinylene molecular wire: Contact gap and tilt angle dependence,” *PHYSICAL REVIEW B*, vol. 81, APR 15 2010.

## Bibliography

- [157] J. Krans, J. van Ruitenbeek, V. Fisun, I. Yanson, and L. de Jongh, "The signature of conductance quantization in metallic point contacts," *NATURE*, vol. 375, pp. 767–769, JUN 29 1995.
- [158] V. Engelkes, J. Beebe, and C. Frisbie, "Length-dependent transport in molecular junctions based on SAMs of alkanethiols and alkanedithiols: Effect of metal work function and applied bias on tunneling efficiency and contact resistance," *JOURNAL OF THE AMERICAN CHEMICAL SOCIETY*, vol. 126, pp. 14287–14296, NOV 3 2004.
- [159] X. Xiao, B. Xu, and N. Tao, "Conductance titration of single-peptide molecules," *JOURNAL OF THE AMERICAN CHEMICAL SOCIETY*, vol. 126, pp. 5370–5371, MAY 5 2004.
- [160] R. Cohen, K. Stokbro, J. M. L. Martin, and M. A. Ratner, "Charge transport in conjugated aromatic molecular junctions: Molecular conjugation and molecule-electrode coupling," *JOURNAL OF PHYSICAL CHEMISTRY C*, vol. 111, pp. 14893–14902, OCT 11 2007.
- [161] S. Y. Quek, H. J. Choi, S. G. Louie, and J. B. Neaton, "Length Dependence of Conductance in Aromatic Single-Molecule Junctions," *NANO LETTERS*, vol. 9, pp. 3949–3953, NOV 2009.
- [162] G. Peng, M. Strange, K. S. Thygesen, and M. Mavrikakis, "Conductance of Conjugated Molecular Wires: Length Dependence, Anchoring Groups, and Band Alignment," *JOURNAL OF PHYSICAL CHEMISTRY C*, vol. 113, pp. 20967–20973, DEC 10 2009.
- [163] C. Wang, A. S. Batsanov, M. R. Bryce, S. Martin, R. J. Nichols, S. J. Higgins, V. M. Garcia-Suarez, and C. J. Lambert, "Oligoyne Single Molecule Wires," *JOURNAL OF THE AMERICAN CHEMICAL SOCIETY*, vol. 131, pp. 15647–15654, NOV 4 2009.
- [164] M. Kamenetska, S. Y. Quek, A. C. Whalley, M. L. Steigerwald, H. J. Choi, S. G. Louie, C. Nuckolls, M. S. Hybertsen, J. B. Neaton, and L. Venkataraman, "Conductance and Geometry of Pyridine-Linked Single-Molecule Junctions," *JOURNAL OF THE AMERICAN CHEMICAL SOCIETY*, vol. 132, pp. 6817–6821, MAY 19 2010.



- [165] S. T. Schneebeli, M. Kamenetska, Z. Cheng, R. Skouta, R. A. Friesner, L. Venkataraman, and R. Breslow, "Single-Molecule Conductance through Multiple pi-pi-Stacked Benzene Rings Determined with Direct Electrode-to-Benzene Ring Connections," *JOURNAL OF THE AMERICAN CHEMICAL SOCIETY*, vol. 133, pp. 2136–2139, FEB 23 2011.
- [166] Z.-L. Peng, Z.-B. Chen, X.-Y. Zhou, Y.-Y. Sun, J.-H. Liang, Z.-J. Niu, X.-S. Zhou, and B.-W. Mao, "Single Molecule Conductance of Carboxylic Acids Contacting Ag and Cu Electrodes," *JOURNAL OF PHYSICAL CHEMISTRY C*, vol. 116, pp. 21699–21705, OCT 18 2012.
- [167] T. Kim, V. H., M. Hybertsen, and L. Venkataraman, "Conductance of molecular junctions formed with silver electrodes," *NANO LETTERS*, vol. 10, p. 1021, 2013.
- [168] L. Luo, S. H. Choi, and C. D. Frisbie, "Probing Hopping Conduction in Conjugated Molecular Wires Connected to Metal Electrodes," *CHEMISTRY OF MATERIALS*, vol. 23, pp. 631–645, FEB 8 2011.
- [169] X. Zhao, C. Huang, M. Gulcur, A. S. Batsanov, M. Baghernejad, W. Hong, M. R. Bryce, and T. Wandlowski, "Oligo(aryleneethynylene)s with Terminal Pyridyl Groups: Synthesis and Length Dependence of the Tunneling-to-Hopping Transition of Single-Molecule Conductances," *CHEMISTRY OF MATERIALS*, vol. 25, pp. 4340–4347, NOV 12 2013.
- [170] Z. Donhauser, B. Mantooth, K. Kelly, L. Bumm, J. Monnell, J. Stapleton, D. Price, A. Rawlett, D. Allara, J. Tour, and P. Weiss, "Conductance switching in single molecules through conformational changes," *SCIENCE*, vol. 292, pp. 2303–2307, JUN 22 2001.
- [171] A. Blum, J. Kushmerick, D. Long, C. Patterson, J. Yang, J. Henderson, Y. Yao, J. Tour, R. Shashidhar, and B. Ratna, "Molecularly inherent voltage-controlled conductance switching," *NATURE MATERIALS*, vol. 4, pp. 167–172, FEB 2005.
- [172] A. V. Danilov, S. E. Kubatkin, S. G. Kafanov, K. Flensberg, and T. Bjornholm, "Electron transfer dynamics of bistable single-molecule junctions," *NANO LETTERS*, vol. 6, pp. 2184–2190, OCT 11 2006.
- [173] M. L. Trouwborst, E. H. Huisman, S. J. van der Molen, and B. J. van Wees, "Bistable hysteresis and resistance switching in hydrogen-gold junctions," *PHYSICAL REVIEW B*, vol. 80, AUG 2009.

## Bibliography

- [174] S. Y. Quek, M. Kamenetska, M. L. Steigerwald, H. J. Choi, S. G. Louie, M. S. Hybertsen, J. B. Neaton, and L. Venkataraman, "Mechanically controlled binary conductance switching of a single-molecule junction," *NATURE NANOTECHNOLOGY*, vol. 4, pp. 230–234, APR 2009.
- [175] H. Basch, R. Cohen, and M. Ratner, "Interface geometry and molecular junction conductance: Geometric fluctuation and stochastic switching," *NANO LETTERS*, vol. 5, pp. 1668–1675, SEP 2005.
- [176] A. Grigoriev, J. Skoldberg, G. Wendin, and Z. Crljen, "Critical roles of metal-molecule contacts in electron transport through molecular-wire junctions," *PHYSICAL REVIEW B*, vol. 74, JUL 2006.
- [177] D. Dulic, F. Pump, S. Campidelli, P. Lavie, G. Cuniberti, and A. Filoramo, "Controlled Stability of Molecular Junctions," *ANGEWANDTE CHEMIE-INTERNATIONAL EDITION*, vol. 48, no. 44, pp. 8273–8276, 2009.
- [178] W. R. French, C. R. Iacovella, I. Rungger, A. M. Souza, S. Sanvito, and P. T. Cummings, "Atomistic simulations of highly conductive molecular transport junctions under realistic conditions," *NANOSCALE*, vol. 5, no. 9, pp. 3654–3659, 2013.
- [179] H. Basch and M. Ratner, "Binding at molecule/gold transport interfaces. I. Geometry and bonding," *JOURNAL OF CHEMICAL PHYSICS*, vol. 119, pp. 11926–11942, DEC 8 2003.
- [180] S. Sek, "Two metal-molecule binding modes for peptide molecular junctions," *JOURNAL OF PHYSICAL CHEMISTRY C*, vol. 111, pp. 12860–12865, AUG 30 2007.
- [181] C. R. Arroyo, E. Leary, A. Castellanos-Gomez, G. Rubio-Bollinger, M. Teresa Gonzalez, and N. Agrait, "Influence of Binding Groups on Molecular Junction Formation," *JOURNAL OF THE AMERICAN CHEMICAL SOCIETY*, vol. 133, pp. 14313–14319, SEP 14 2011.
- [182] S. Bilan, L. A. Zotti, F. Pauly, and J. C. Cuevas, "Theoretical study of the charge transport through C-60-based single-molecule junctions," *PHYSICAL REVIEW B*, vol. 85, MAY 2 2012.
- [183] Y. Li, P. Wei, M. Bai, Z. Shen, S. Sanvito, and S. Hou, "Contact geometry and electronic transport properties of Ag-benzene-Ag molecular junctions," *CHEMICAL PHYSICS*, vol. 397, pp. 82–86, MAR 13 2012.

## Bibliography

- [184] L. A. Zotti, E. Leary, M. Soriano, J. Carlos Cuevas, and J. Jose Palacios, "A Molecular Platinum Cluster Junction: A Single-Molecule Switch," *JOURNAL OF THE AMERICAN CHEMICAL SOCIETY*, vol. 135, pp. 2052–2055, FEB 13 2013.
- [185] S. K. M. Henze, O. Bauer, T. L. Lee, M. Sokolowski, and F. S. Tautz, "Vertical bonding distances of ptcda on au(111) and ag(111): Relation to the bonding type," *SURFACE SCIENCE*, vol. 601, pp. 1566–1573, MAR 15 2007.
- [186] M. Mura, A. Gulans, T. Thonhauser, and L. Kantorovich, "Role of van der Waals interaction in forming molecule-metal junctions: flat organic molecules on the Au(111) surface," *PHYSICAL CHEMISTRY CHEMICAL PHYSICS*, vol. 12, no. 18, pp. 4759–4767, 2010.
- [187] S. Yaliraki, M. Kemp, and M. Ratner, "Conductance of molecular wires: Influence of molecule-electrode binding," *JOURNAL OF THE AMERICAN CHEMICAL SOCIETY*, vol. 121, pp. 3428–3434, APR 14 1999.
- [188] J. W. Lawson and C. W. Bauschlicher, Jr., "Transport in molecular junctions with different metallic contacts," *PHYSICAL REVIEW B*, vol. 74, SEP 2006.
- [189] H. Kondo, J. Nara, H. Kino, and T. Ohno, "Transport properties of a biphenyl-based molecular junction system-the electrode metal dependence," *JOURNAL OF PHYSICS-CONDENSED MATTER*, vol. 21, FEB 11 2009. 2nd International Conference on Quantum Simulators and Design, Tokyo, JAPAN, MAY 31-JUN 03, 2008.
- [190] Z.-L. Peng, Y.-Y. Sun, Z. X.Y., Y. Wang, D. Han, Z. Niu, and X. Zhou, "The influence of conjugated bond on single molecule conductance of carboxylic acids measured by electrochemical jump-to-contact scanning tunneling microscopy break junction," *INTERNATIONAL JOURNAL OF ELECTROCHEMICAL SCIENCE*, vol. 8, p. 6544, 2013.



# List of Figures

2.1	Tunneling barrier . . . . .	6
2.2	Planar tunneling barrier . . . . .	7
2.3	Schematic representation of a STM . . . . .	10
2.4	SEM image of Pt/Ir tip . . . . .	11
2.5	Creating a single TTCDA molecule on Ag(111) . . . . .	14
2.6	Schematic representation of a tunneling barrier . . . . .	16
2.7	STS of bare metal surfaces . . . . .	17
2.8	Tunneling processes by electron-vibration coupling . . . . .	18
2.9	Step in $dI/dV$ . . . . .	19
2.10	Electronic transition by electron-vibration coupling . . . . .	20
2.11	Lock-in amplifier . . . . .	21
2.12	qPlus sensor . . . . .	25
2.13	Molecular islands on Ag(111) . . . . .	32
2.14	Molecular islands on Au(111) . . . . .	33
2.15	STHM images . . . . .	35
3.1	Ballistic conductor . . . . .	38
3.2	Transmission probability . . . . .	42
3.3	Molecule in tunneling junction . . . . .	50
3.4	Resonant tunneling . . . . .	51
3.5	Resonant condition . . . . .	52
3.6	Scattering . . . . .	52
3.7	Kondo . . . . .	56
4.1	The four molecules . . . . .	58
4.2	STS of molecules on Ag(111) . . . . .	60
4.3	LUMO position on Ag(111) . . . . .	63
4.4	LUMO shift on Ag(111) . . . . .	64
4.5	STS of molecules on Au(111) . . . . .	65

## List of Figures

4.6	LUMO position on Au(111) . . . . .	66
4.7	STM image of the three phases of NTCDA on Ag(111) . . . . .	70
4.8	STM image of the commensurate phase of NTCDA on Ag(111) . . . . .	71
4.9	STS of the type A and B molecules . . . . .	72
4.10	STM image of four NTCDA molecules forming a diamond . . . . .	74
4.11	STS on every third molecule in the incommensurate phase . . . . .	75
4.12	STS on a type A molecule . . . . .	78
4.13	DFT calculations I . . . . .	80
4.14	DFT calculations II . . . . .	81
4.15	Kondo replica I . . . . .	83
4.16	Kondo replica II . . . . .	85
4.17	STS on a type B molecule . . . . .	87
4.18	Temperature dependent STS on NTCDA on Ag(111) . . . . .	90
4.19	Full width at half maximum $K_{FWHM}$ of the Kondo resonance vs. the sample temperature $T_{sample}$ . . . . .	92
4.20	Absolute tip height . . . . .	96
4.21	Differential conductance map of a type A molecule . . . . .	97
4.22	Differential conductance map of a type B molecule . . . . .	98
4.23	STS vs. conductance maps . . . . .	99
6.1	Manipulation procedure . . . . .	120
6.2	Lifting a single QTCDA molecule (Ag(111), Class B) . . . . .	122
6.3	Different classes found for QTCDA (Ag(111), class B) . . . . .	125
6.4	2D histogram of QTCDA (Ag(111), all) . . . . .	127
6.5	2D histogram of QTCDA (Ag(111), class B) . . . . .	129
6.6	2D histogram of QTCDA (Ag(111), class A) . . . . .	131
6.7	Different manipulation scenarios . . . . .	132
6.8	Shifted 2D histogram of QTCDA (Ag(111), class B) . . . . .	134
6.9	2D histogram of QTCDA with the generic behavior (Ag(111), class A) . . . . .	136
6.10	First correlation matrix of the aligned QTCDA/Ag(111) curves (class B) . . . . .	140
6.11	Sum of first correlation matrix of the aligned QTCDA/Ag(111) curves (class B) . . . . .	141
6.12	Best representing curve of the aligned QTCDA/Ag(111) curves (class B) . . . . .	142
6.13	Histogram of multiplication factors (Ag(111),class B) . . . . .	144
6.14	Histogram of multiplication factors (Au(111),class B) . . . . .	145

## List of Figures

6.15	Second correlation matrix of the aligned and shifted QTCDA/Ag(111) curves (class B) . . . . .	146
6.16	Comparing the first and second correlation values of QTCDA/Ag(111) (class B) . . . . .	147
6.17	Sum of second correlation matrix of the aligned QTCDA/Ag(111) curves (class B) . . . . .	148
6.18	Best representing curve of the aligned and shifted QTCDA/Ag(111) curves (class B) . . . . .	149
6.19	NTCDA/Ag(111) of class B aligned and generic curve 2 . . . . .	150
6.20	PTCDA/Ag(111) of class B aligned and generic curve 2 . . . . .	150
6.21	TTCDA/Ag(111) of class B aligned and generic curve 2 . . . . .	151
6.22	NTCDA/Au(111) of class B aligned and generic curve 2 . . . . .	151
6.23	PTCDA/Au(111) of class B aligned and generic curve 2 . . . . .	152
6.24	TTCDA/Au(111) of class B aligned and generic curve 2 . . . . .	152
6.25	QTCDA/Au(111) of class B aligned and generic curve 2 . . . . .	153
6.26	Different types of decay constants . . . . .	154
6.27	All generic curves (Ag(111), class B) . . . . .	157
6.28	QTCDA with conductance on linear scale (Ag(111), class B) . . . . .	158
6.29	Generic frequency shift and force (QTCDA/Ag(111), class B) . . . . .	159
6.30	Generic curve of QTCDA with points (Ag(111), class B) . . . . .	161
6.31	The two transport regimes of QTCDA (Ag(111), class B) . . . . .	163
6.32	Decay constant of the contact tunneling regime (Ag(111), class B) . . . .	165
6.33	Bending of different molecules . . . . .	167
6.34	Decay constant of the vacuum tunneling regime (Ag(111), class B) . . . .	168
6.35	Decay constant of the bare metal tips before contact (Ag(111) and Au(111))	169
6.36	STS on a TTCDA molecule (Ag(111), class B) . . . . .	172
6.37	Decay constant of the conductance peak (Ag(111), class B) . . . . .	173
6.38	Conductance of the molecule in the wire configuration (Ag(111), class B) .	175
6.39	Hysteresis in class A manipulations (Ag(111), class A) . . . . .	179
6.40	Origin of hysteresis (Ag(111), class A) . . . . .	180
6.41	Different junction configurations . . . . .	181
6.42	All generic curves (Ag(111), class A) . . . . .	183
6.43	Decay constants of the contact tunneling regime (Ag(111), class A and class B) . . . . .	184
6.44	STS on a TTCDA molecule (Ag(111), class A) . . . . .	186
6.45	Decay constant of the conductance peak (Ag(111), class A and class B) . .	188

## List of Figures

6.46	Conductance of the molecule in the wire configuration (Ag(111), class A and class B) . . . . .	190
6.47	Position of jump into contact (Au(111) and Ag(111), class app) . . . . .	192
6.48	All generic curves (Au(111), class B) . . . . .	195
6.49	Different wire geometries on Ag(111) and Au(111) . . . . .	196
6.50	Dips in the frequency shift (Au(111), class B) . . . . .	197
6.51	STS on a PTCDA molecule (Au(111), class B) . . . . .	199
6.52	Decay constant of the contact tunneling regime (Au(111) and Ag(111), class B) . . . . .	201
6.53	Conductance of the molecular wires (Au(111) and Ag(111), class B) . . .	202
6.54	All generic curves (Au(111), class A) . . . . .	204
6.55	Decay constant of the contact tunneling regime (Au(111), class A and class B) . . . . .	206
6.56	Conductance of the wire (Au(111), class A and class B) . . . . .	207
6.57	Peak height differences (Au(111) and Ag(111), class B) . . . . .	209
A.1	Approach on NTCDa/Ag(111) . . . . .	218
A.2	Approach on PTCDA/Ag(111) . . . . .	218
A.3	Approach on TTCDA/Ag(111) . . . . .	219
A.4	Approach on QTCDA/Ag(111) . . . . .	219
A.5	Approach on NTCDa/Au(111) . . . . .	220
A.6	Approach on PTCDA/Au(111) . . . . .	220
A.7	Approach on TTCDA/Au(111) . . . . .	221
A.8	Approach on QTCDA/Au(111) . . . . .	221
A.9	NTCDa/Ag(111) . . . . .	222
A.10	NTCDa/Ag(111) of class A . . . . .	222
A.11	NTCDa/Ag(111) of class B . . . . .	223
A.12	NTCDa/Ag(111) of class B aligned and generic curve 1 . . . . .	223
A.13	NTCDa/Ag(111) of class C . . . . .	224
A.14	PTCDA/Ag(111) . . . . .	224
A.15	PTCDA/Ag(111) of class A . . . . .	225
A.16	PTCDA/Ag(111) of class B . . . . .	225
A.17	PTCDA/Ag(111) of class B aligned and generic curve 1 . . . . .	226
A.18	PTCDA/Ag(111) of class C . . . . .	226
A.19	TTCDA/Ag(111) . . . . .	227
A.20	TTCDA/Ag(111) of class A . . . . .	227



# *List of Figures*

A.21 TTCDA/Ag(111) of class B . . . . .	228
A.22 TTCDA/Ag(111) of class B aligned and generic curve 1 . . . . .	228
A.23 TTCDA/Ag(111) of class C . . . . .	229
A.24 QTCDA/Ag(111) . . . . .	229
A.25 QTCDA/Ag(111) of class A . . . . .	230
A.26 QTCDA/Ag(111) of class B . . . . .	230
A.27 QTCDA/Ag(111) of class B aligned and generic curve 1 . . . . .	231
A.28 QTCDA/Ag(111) of class C . . . . .	231
A.29 NTCDA/Au(111) . . . . .	232
A.30 NTCDA/Au(111) of class A . . . . .	232
A.31 NTCDA/Au(111) of class B . . . . .	233
A.32 NTCDA/Au(111) of class B aligned and generic curve 1 . . . . .	233
A.33 NTCDA/Au(111) of class C . . . . .	234
A.34 PTCDA/Au(111) . . . . .	234
A.35 PTCDA/Au(111) of class A . . . . .	235
A.36 PTCDA/Au(111) of class B . . . . .	235
A.37 PTCDA/Au(111) of class B aligned and generic curve 1 . . . . .	236
A.38 PTCDA/Au(111) of class C . . . . .	236
A.39 TTCDA/Au(111) . . . . .	237
A.40 TTCDA/Au(111) of class A . . . . .	237
A.41 TTCDA/Au(111) of class B . . . . .	238
A.42 TTCDA/Au(111) of class B aligned and generic curve 1 . . . . .	238
A.43 TTCDA/Au(111) of class C . . . . .	239
A.44 QTCDA/Au(111) . . . . .	239
A.45 QTCDA/Au(111) of class A . . . . .	240
A.46 QTCDA/Au(111) of class B . . . . .	240
A.47 QTCDA/Au(111) of class B aligned and generic curve 1 . . . . .	241
A.48 QTCDA/Au(111) of class C . . . . .	241
A.49 Histogram of correlations of NTCDA/Ag(111) . . . . .	242
A.50 Histogram of correlations of PTCDA/Ag(111) . . . . .	242
A.51 Histogram of correlations of TTCDA/Ag(111) . . . . .	243
A.52 Histogram of correlations of QTCDA/Ag(111) . . . . .	243
A.53 Histogram of correlations of NTCDA/Au(111) . . . . .	244
A.54 Histogram of correlations of PTCDA/Au(111) . . . . .	244
A.55 Histogram of correlations of TTCDA/Au(111) . . . . .	245
A.56 Histogram of correlations of QTCDA/Au(111) . . . . .	245

*List of Figures*

A.57 Generic behavior with points (Ag(111), class A) . . . . .	246
A.58 Generic behavior with points (Ag(111), class B) . . . . .	247
A.59 Generic behavior with points (Au(111), class A) . . . . .	248
A.60 Generic behavior with points (Au(111), class B) . . . . .	249
A.61 Generic behavior with linear conductance (Ag(111), class A) . . . . .	250
A.62 Generic behavior with linear conductance (Ag(111), class B) . . . . .	251
A.63 Generic behavior with linear conductance (Au(111), class A) . . . . .	252
A.64 Generic behavior with linear conductance (Au(111), class B) . . . . .	253
A.65 Transport spectroscopy (NTCDA/Ag(111), class B) . . . . .	254
A.66 Transport spectroscopy (PTCDA/Ag(111), class A) . . . . .	255
A.67 Transport spectroscopy (PTCDA/Ag(111), class B) . . . . .	256
A.68 Transport spectroscopy (TTCDA/Ag(111), class A) . . . . .	257
A.69 Transport spectroscopy (TTCDA/Ag(111), class B) . . . . .	258
A.70 Transport spectroscopy (QTCDA/Ag(111), class B) . . . . .	259
A.71 Transport spectroscopy (PTCDA/Au(111), class A) . . . . .	260
A.72 Transport spectroscopy (PTCDA/Au(111), class B) . . . . .	261

# List of Tables

2.1	Sample preparation parameters . . . . .	28
2.2	Molecule deposition parameters . . . . .	29
2.3	Unit cell of different systems . . . . .	34
4.1	LUMO position of adsorbed molecules . . . . .	67
4.2	The three NTCDAs phases . . . . .	76
6.1	Total number of lifting and lowering curves . . . . .	128
6.2	Shifting parameters (Ag(111), class B) . . . . .	135
6.3	Correlation parameters (class B) . . . . .	138
6.4	Number of lifting and lowering curves (Ag(111), class A and class B) . . . .	156
6.5	Coordinates of the points $P_1$ , $P_2$ , $P_3$ , $P_4$ and $P_5$ (Ag(111), class B) . . . .	160
6.6	Decay constants of the two transport regimes (Ag(111), class B) . . . . .	169
6.7	Coordinates of the points $P_1$ , $P_2$ and $P_3$ (Ag(111), class A) . . . . .	177
6.8	Decay constants of the contact tunneling regime (Ag(111), class A and class B) . . . . .	185
6.9	Observation of Kondo physics in Ag(111) manipulations . . . . .	187
6.10	Coordinates of the conductance peaks (Ag(111), class A and class B) . . . .	188
6.11	Coordinates of the wire configuration (Ag(111), class A and class B) . . . .	189
6.12	Number of lifting and lowering curves (Au(111), class A and class B) . . . .	193
6.13	Coordinates of the points $P_1$ and $P_3$ (Au(111), class B) . . . . .	196
6.14	Conductance of the molecular wires (Au(111) and Ag(111), class B) . . . .	201
6.15	Coordinates of the points $P_1$ and $P_3$ (Au(111), class A) . . . . .	205
6.16	Height of peak in frequency shift (Au(111) and Ag(111)) . . . . .	208



# List of Acronyms

<b>AFM</b>	atomic force microscope
<b>DAC</b>	digital-to-analog converter
<b>DFT</b>	density functional theory
<b>DOS</b>	density of states
<b>FIB</b>	focused ion beam
<b>FWHM</b>	full width at half maximum
<b>HOMO</b>	highest occupied molecular orbital
<b>IETS</b>	inelastic electron tunneling spectroscopy
<b>LDOS</b>	local density of states
<b>LEED</b>	low-energy electron diffraction
<b>LUMO</b>	lowest unoccupied molecular orbital
<b>NTCDA</b>	1,4,5,8-naphthalene-tetracarboxylic-dianhydride
<b>PTCDA</b>	3,4,9,10-perylene-tetracarboxylic-dianhydride
<b>SPA-LEED</b>	spot profile analysis low-energy electron diffraction
<b>STM</b>	scanning tunneling microscope
<b>STHM</b>	scanning tunneling hydrogen microscope
<b>STS</b>	scanning tunneling spectroscopy
<b>TTCDA</b>	5,6,13,14-terrylene-tetracarboxylic-dianhydride
<b>QTCDA</b>	7,8,17,18-quatterylene-tetracarboxylic-dianhydride



# Curriculum Vitae

## **Norman Fournier**

born on April 27th, 1982 in Kehl am Rhein, Germany

Nationality: German and French

## **Higher Education**

2010 - 2014: PhD student at Forschungszentrum Jülich, Germany  
Peter Grünberg Institute 3: Functional Nanostructures at Surfaces  
Thesis title: "STM-based quantum transport through molecular wires"  
Supervisor: Prof. Dr. Stefan Tautz

2010: Diploma degree in Physics at Karlsruhe Institute of Technology, Germany  
Institute of Applied Physics  
Thesis Title: "Elektrochemische Herstellung von  
Quantenpunktkontakten aus Nickel und Cobalt"  
Supervisor: Prof. Dr. Thomas Schimmel

2002 - 2010: Physics studies at Karlsruhe Institute of Technology, Germany

## **Military service**

2001 - 2002: Basic military service at Panzergrenadierbatallion 294  
in Stetten am kalten Markt, Germany

## **Education**

1992 - 2001: Abitur at Einstein Gymnasium in Kehl am Rhein, Germany

Jülich, March 26, 2014





Band / Volume 95

**2-Steps in 1-pot: enzyme cascades for the synthesis of chiral vicinal amino alcohols**

T. Sehl (2014), XIV, 167 pp

ISBN: 978-3-95806-001-2

Band / Volume 96

**Immunohistochemical and electrophysiological characterization of the mouse model for Retinitis Pigmentosa, *rd10***

S. Biswas (2014), XII, 119 pp

ISBN: 978-3-95806-011-1

Band / Volume 97

**Single molecule localization microscopy: Imaging of cellular structures and a new three-dimensional localization technique**

X. Fan (2014), XII, 92 pp

ISBN: 978-3-95806-014-2

Band / Volume 98

**Cryogenic Break-Junction Characterization of Single Organic Molecules**

T. Grellmann (2014), VI, 86 pp

ISBN: 978-3-95806-015-9

Band / Volume 99

**Interacting Interactions: A Study on the Interplay of Molecule-Molecule and Molecule-Substrate Interactions at Metal-Organic Interfaces**

M. Willenbockel (2014), IX, 245 pp

ISBN: 978-3-95806-018-0

Band / Volume 100

**Microwire crossbar arrays for chemical, mechanical, and thermal stimulation of cells**

P. Rinklin (2015), xii, 184 pp

ISBN: 978-3-95806-022-7

Band / Volume 101

**Modification and characterization of potential bioelectronic interfaces**

K. Greben (2015), 76 pp

ISBN: 978-3-95806-028-9

Band / Volume 102

**Extending the precision and efficiency of the all-electron full-potential linearized augmented plane-wave density-functional theory method**

G. Michalíček (2015), 195 pp

ISBN: 978-3-95806-031-9

Band / Volume 103

**Metabolic engineering of *Escherichia coli* for the production of plant phenylpropanoid derived compounds**

P. V. van Summeren-Wesenhagen (2015), V, 92 pp

ISBN: 978-3-95806-039-5

Band / Volume 104

**Spin-reorientation transition in epitaxial  $\text{Ni}_x\text{Pd}_{1-x}$  films on Cu(001): a microscopic analysis**

D. Gottlob (2015), x, 134 pp

ISBN: 978-3-95806-049-4

Band / Volume 105

**Resonant Magnetic Scattering Studies using Synchrotron Radiation and Laser-Generated Extreme Ultraviolet Light**

C. M. Weier (2015), vii, 143 pp

ISBN: 978-3-95806-052-4

Band / Volume 106

**Neutron Scattering**

Lectures of the JCNS Laboratory Course held at Forschungszentrum Jülich and at the Heinz-Maier-Leibnitz Zentrum Garching

edited by Th. Brückel, D. Richter, G. Roth, A. Wischnewski and R. Zorn (2015), ca 300 pp

ISBN: 978-3-95806-055-5

Band / Volume 107

**Neutron Scattering**

Experimental Manuals of the JCNS Laboratory Course held at Forschungszentrum Jülich and at the Heinz-Maier-Leibnitz Zentrum Garching

edited by Th. Brückel, D. Richter, G. Roth, A. Wischnewski and R. Zorn (2015), ca 150 pp

ISBN: 978-3-95806-056-2

Band / Volume 108

**STM-based quantum transport through molecular wires**

N. Fournier (2015), ix, 295 pp

ISBN: 978-3-95806-059-3

Weitere **Schriften des Verlags im Forschungszentrum Jülich** unter  
<http://wwwzb1.fz-juelich.de/verlagextern1/index.asp>



**Schlüsseltechnologien /**  
**Key Technologies**  
**Band / Volume 108**  
**ISBN 978-3-95806-059-3**

